

**Macroscopic and microscopic  
deformation of the piezoelectric  
 $\text{Li}_2\text{SO}_4 \cdot \text{H}_2\text{O}$ ,  $\text{Li}_2\text{SeO}_4 \cdot \text{H}_2\text{O}$  and  $\text{BiB}_3\text{O}_6$   
crystals under an external electric field**

DISSERTATION

zur Erlangung des Grades eines Doktors  
der Naturwissenschaften

vorgelegt von

Dipl.-Phys. Oleg Schmidt

geb. am 12.07.1981 in Toparski/Karaganda (SU)

eingereicht beim Fachbereich Physik  
der Universität Siegen

Siegen 2010

Gutachter: Prof. Dr. Ullrich Pietsch  
Prof. Dr. Ladislav Bohatý

Tag der mündlichen Prüfung: 24.09.2010

# Contents

<b>Introduction</b>	<b>1</b>
<b>1 Elastic, piezoelectric and dielectric properties of crystals</b>	<b>3</b>
1.1 Elasticity . . . . .	3
1.2 Electric polarization . . . . .	4
1.2.1 Pyroelectric and ferroelectric crystals . . . . .	6
1.3 Piezoelectricity . . . . .	6
<b>2 X-ray diffraction by crystals under an static external electric field</b>	<b>9</b>
2.1 X-ray diffraction by unperturbed crystals . . . . .	9
2.2 Electron density distribution in crystals . . . . .	11
2.2.1 Multipole refinement of the electron density . . . . .	11
2.2.2 DFT calculations of the electron density . . . . .	12
2.2.3 Topological analysis of the electron density . . . . .	13
2.3 External and internal strain of a crystal induced by an applied electric field	14
2.3.1 Determination of the piezoelectric constants of a crystal by means of X-ray diffraction . . . . .	16
2.3.2 Refinement of the electric-field-induced atomic displacements in a crystal . . . . .	20
<b>3 Description of the field-switching X-ray diffraction experiments</b>	<b>25</b>
3.1 Setup of the static field-switching experiment . . . . .	25
3.2 Setup of the time-resolved experiment . . . . .	27
3.2.1 Physical origin of the Bragg peak oscillations . . . . .	31
<b>4 Electric-field-induced response of <math>\text{Li}_2\text{SO}_4\cdot\text{H}_2\text{O}</math>, <math>\text{Li}_2\text{SeO}_4\cdot\text{H}_2\text{O}</math> and <math>\text{BiB}_3\text{O}_6</math> single crystals</b>	<b>33</b>
4.1 Lithium sulfate monohydrate, $\text{Li}_2\text{SO}_4\cdot\text{H}_2\text{O}$ . . . . .	33
4.1.1 Multipole-model refinement of the electron density and properties of the chemical bonds . . . . .	34
4.1.2 X-ray diffraction study of $\text{Li}_2\text{SO}_4\cdot\text{H}_2\text{O}$ under the influence of an applied external electric field . . . . .	40
4.1.3 Model used for the description of the electric-field-induced atomic displacements . . . . .	42
4.1.4 Refinement of the piezoelectric constants $d_{2jk}$ and atomic displace- ments . . . . .	44
4.1.5 Discussion . . . . .	48
4.2 Lithium selenate monohydrate, $\text{Li}_2\text{SeO}_4\cdot\text{H}_2\text{O}$ . . . . .	48
4.2.1 Properties of the chemical bonds . . . . .	49
4.2.2 Electric-field-induced atomic rearrangement . . . . .	54

4.2.3	Comparison of the bond-selective response strength of different piezo-electric crystals . . . . .	57
4.3	Bismuth triborate, $\text{BiB}_3\text{O}_6$ . . . . .	59
4.3.1	X-ray determination of the piezoelectric constants . . . . .	60
4.3.2	Internal strain induced in $\text{BiB}_3\text{O}_6$ by external electric fields applied in different crystallographic directions . . . . .	62
4.3.3	Neutron diffraction study of the internal strain . . . . .	68
<b>5</b>	<b>Time-resolved X-ray diffraction study of the dynamic piezoelectric response of crystals</b>	<b>73</b>
5.1	Measurements with the first rectangular $\text{Li}_2\text{SO}_4\cdot\text{H}_2\text{O}$ (010) crystal plate . .	74
5.1.1	Discussion . . . . .	80
5.2	Measurements with the second rectangular $\text{Li}_2\text{SO}_4\cdot\text{H}_2\text{O}$ (010) crystal plate	83
5.3	X-ray diffraction investigations of the piezoelectrically induced crystal vibrations . . . . .	84
5.3.1	Supplementary measurements performed with other $\text{Li}_2\text{SO}_4\cdot\text{H}_2\text{O}$ and $\text{BiB}_3\text{O}_6$ crystal plates . . . . .	87
<b>6</b>	<b>Summary</b>	<b>89</b>
	<b>Appendix</b>	<b>91</b>
A.1	Publications arising from the thesis . . . . .	91
A.2	Talks given at conferences, colloquiums and workshops . . . . .	91
A.3	Financing . . . . .	92
A.4	All $(\Delta I/I)_a$ data observed and calculated for $\text{Li}_2\text{SO}_4\cdot\text{H}_2\text{O}$ , $\text{Li}_2\text{SeO}_4\cdot\text{H}_2\text{O}$ and $\text{BiB}_3\text{O}_6$ . . . . .	92
A.5	VHDL source code . . . . .	97
	<b>Bibliography</b>	<b>105</b>
	<b>Acknowledgments</b>	<b>113</b>

# Introduction

X-ray diffraction is the major experimental tool for the investigation of the microscopic structure of crystals. A highly redundant set of Bragg intensities can be collected almost automatically with high precision and can be used to obtain accurate atomic positions, atomic displacement parameters and electron-density distributions in crystals. In general, these quantities describe a crystal at the static equilibrium, *i.e.* in the absence of any external influences. However, probing the microscopic response of the crystal to an external perturbation is still a challenge for modern X-ray structure analysis. The main aim of such experiments is to understand how the specific features of the structural network are responsible for the physical properties of a crystal and how the crystal structural parameters can be tuned to control the property of interest.

The types of perturbations which are usually applied to a crystal in an X-ray diffraction experiment are high pressure, high or low temperature, laser irradiation and external high voltage [1, 2, 3, 4]. The specific response of the crystal to such perturbations defines its intrinsic physical properties, *e.g.* the development of the macroscopic polarization under the influence of an applied electric field is known as dielectricity, whereas the formation of the mechanical strains is referred to as the converse piezoelectric effect [5, 6]. Although many technical applications are essentially based on both of these phenomena, their microscopic nature is not yet well understood. Starting with the pioneering work by Fujimoto (1978) [7] on  $\text{LiNbO}_3$ , the atomistic origin of the piezoelectric effect has so far been investigated for only a very narrow class of compounds, such as  $\text{AgGaS}_2$  [8],  $\text{KD}_2\text{PO}_4$  [9, 10],  $\text{KH}_2\text{PO}_4$  [11],  $\text{GaAs}$  [4],  $\text{ZnSe}$  [4],  $\alpha\text{-SiO}_2$  [12, 13] and  $\alpha\text{-GaPO}_4$  [14]. In this context, X-ray diffraction under an external electric perturbation has turned out to be a promising experimental tool for obtaining an understanding of the piezoelectric effect at the microscopic level. Nevertheless, till now the fundamental relationship between the atomic arrangement, the electron density distribution and the piezoelectric properties of a crystal could not be explained in full detail for any single structure [15]. The great advantage of the X-ray diffraction technique is that the atomic redistribution within the unit cell of a crystal caused by an applied electric field and the corresponding macroscopic deformation (pure lattice strain keeping the atomic fractional coordinates constant) of the crystal can be simultaneously and separately studied using one and the same sample. The small displacements of the atomic positions ( $\Delta R \sim 10^{-4}$  Å, [14]) may be evaluated from Bragg intensity changes. At the same time, the lattice strain manifests itself as small angular shifts of diffraction curves ( $\Delta\omega \sim 10^{-3^\circ}$ , [16]).

The aim of this work consists of three parts: First of all, the investigations of the bond-selective response of piezoelectric crystals ought to be extended on the  $\text{Li}_2\text{SO}_4\cdot\text{H}_2\text{O}$ ,  $\text{Li}_2\text{SeO}_4\cdot\text{H}_2\text{O}$  (is isostructural with  $\text{Li}_2\text{SO}_4\cdot\text{H}_2\text{O}$ ) and  $\text{BiB}_3\text{O}_6$  compounds. In particular, the behavior of the  $\text{LiO}_4$ ,  $\text{SO}_4$ ,  $\text{SeO}_4$ ,  $\text{BO}_4$ ,  $\text{BO}_3$  and  $\text{BiO}_6$  structural units under an external electric field should be analyzed and compared with the results obtained for crystal structures built up from similar atomic groups. Thus, the first part of this work represents a continuation of the measurements that have proved to be successful in previous studies on the microscopic response of a crystal to an external electric perturbation. Normally,

the measurement of the time dependence of the processes initiated in a crystal by a fast change of an applied electric field enables deeper insights into the nature of the physical properties of the crystal. But from the beginning the experimental technique used for switching the external electric fields was not designed to generate dynamic processes in crystals, as the static (*i.e.* time-averaged) properties of the crystals were of interest only. This disadvantage of the old field-switching technique is the origin of the second subject of this thesis that deals with further developments of the experiment to the time-resolved measurements of the dynamic processes in crystals. Finally, within the scope of this work the time evolution of the piezoelectrically induced lattice strain and of the atomic displacements in  $\text{Li}_2\text{SO}_4\cdot\text{H}_2\text{O}$  crystals should be investigated on the nanosecond time scale.

The present work is structured as follows: In chapters 1 and 2 the basic theoretical principles are discussed. Chapter 3 deals with the employed field-switching technique in terms of the old four-step modulation-demodulation method and new FPGA-based data acquisition system being suitable for the time-resolved measurements of the angular shifts and intensity variations of diffraction curves under the influence of an external electric field. The results obtained for the  $\text{Li}_2\text{SO}_4\cdot\text{H}_2\text{O}$ ,  $\text{Li}_2\text{SeO}_4\cdot\text{H}_2\text{O}$  and  $\text{BiB}_3\text{O}_6$  crystals from the performed X-ray (neutron) diffraction experiments are presented in chapter 4. In chapter 5 the time-resolved measurements of the piezoelectric response of rectangular plane-parallel  $\text{Li}_2\text{SO}_4\cdot\text{H}_2\text{O}$  crystal plates are introduced.

All experiments were performed with crystals grown and prepared for measurements in the form of thin plane-parallel plates by L. Bohatý and P. Becker who are from the Institute of Crystallography belonging to the University of Cologne.

# 1 Elastic, piezoelectric and dielectric properties of crystals

In the next sections the macroscopic description of the physical properties of crystals related to elasticity, electric polarization and piezoelectricity is briefly reviewed. The treatment of these physical phenomena mainly follows the text books by Nye (1984) [5], Haussühl (2007) [6] and Brandt & Dahmen (1997) [17] and is strongly reduced to the subjects that are relevant for this work.

## 1.1 Elasticity

Within the limits of Hooke's law each component,  $\sigma_{ij}$ , of the homogeneous stress applied to a non-piezoelectric crystal is linearly related to all components,  $\varepsilon_{ij}$ , of the induced homogeneous strain by

$$\sigma_{ij} = c_{ijkl}\varepsilon_{kl}, \quad (1.1)$$

where  $c_{ijkl}$  are the elastic constants of the crystal and the Einstein summation convention is used ( $i, j, k, l = 1, 2, 3$ ). In contrast to the description of the static processes in crystals by (1.1), the propagation of the elastic waves in a crystal is described by the theory of elastodynamics. Provided that an excited elastic wave has a harmonic time dependence, the corresponding wave equation is

$$\rho\omega^2\hat{u}_i + c_{ijkl}\frac{\partial^2\hat{u}_k}{\partial x_j\partial x_l} = 0. \quad (1.2)$$

Here  $\hat{u}_i$  refer to as the components of the displacement vector,

$$\hat{u}_i(\mathbf{x}, t) = u_i(\mathbf{x}) \exp(i\omega t), \quad (1.3)$$

and  $\rho$  is the mass density of the crystal. As the crystal is not in a static equilibrium, for its kinetic energy density, KE, one has

$$\text{KE} = \frac{1}{2}\rho\frac{\partial\hat{u}_i}{\partial t}\frac{\partial\hat{u}_i}{\partial t} = \frac{1}{2}\rho\omega^2\hat{u}_i\hat{u}_i \quad (1.4)$$

and its potential (strain) energy density, PE, is given by

$$\text{PE} = \frac{1}{2}c_{ijkl}\varepsilon_{ij}\varepsilon_{kl} = \frac{1}{2}c_{ijkl}\frac{\partial\hat{u}_i}{\partial x_j}\frac{\partial\hat{u}_k}{\partial x_l}. \quad (1.5)$$

The Lagrangian,  $L$ , of an arbitrary shaped crystal with the free-surface (free of external stress) boundary conditions,

$$n_j\sigma_{ij} = 0, \quad (1.6)$$

and a volume  $V$  has the form [18]

$$L = \int_V (\text{KE} - \text{PE}) dV, \quad (1.7)$$

in (1.6)  $\mathbf{n}$  is a unit vector normal to the crystal surface,  $S$ . Usually, for an expansion of the time-independent part,  $u_i(\mathbf{x})$  (1.3), of the displacement vector a set of power functions of the type

$$\Phi_\lambda = x^l y^m z^n \quad (1.8)$$

is employed [19]:

$$u_i = \sum_\lambda a_{i\lambda} \Phi_\lambda, \quad (1.9)$$

where  $x$ ,  $y$  and  $z$  denote the Cartesian coordinates and  $l$ ,  $m$  and  $n$  are positive integers defining the function label,  $\lambda = (l, m, n)$ . With expression (1.9) the Lagrangian (1.7) becomes ([19, 20])

$$L = \left( \frac{1}{2} \omega^2 \mathbf{a}^T [E] \mathbf{a} - \frac{1}{2} \mathbf{a}^T [\Gamma] \mathbf{a} \right) \exp(2i\omega t). \quad (1.10)$$

Both matrices  $[E]$ ,

$$E_{\lambda i \lambda' i'} = \delta_{ii'} \int_V \Phi_{\lambda\rho} \Phi_{\lambda'} dV, \quad (1.11)$$

and  $[\Gamma]$ ,

$$\Gamma_{\lambda i \lambda' i'} = C_{ij i' j'} \int_V \frac{\partial \Phi_\lambda}{\partial x_j} \frac{\partial \Phi_{\lambda'}}{\partial x'_j} dV, \quad (1.12)$$

are symmetric, square and dependent on the shape of a crystal. The order,  $R$ , of  $[E]$  and  $[\Gamma]$  arises from the truncation condition  $l + m + n \leq N$  that is applied to limit the number of basis functions (1.8):

$$R = \frac{(N + 3)!}{2N!}. \quad (1.13)$$

According to Hamilton's principle [18], in the case of the crystal vibrations that satisfy the elastic wave equation (1.2) the Lagrangian (1.10) is stationary for any arbitrary variations of the displacements  $u_i$  (1.9) in  $V$  and on  $S$  of the crystal. This condition is equivalent to ([20])

$$\frac{\partial L}{\partial \mathbf{a}} = \omega^2 \mathbf{a}^T [E] - \mathbf{a}^T [\Gamma] = \mathbf{0} \quad (1.14)$$

and results in the eigenvalue problem

$$\omega^2 [E] \mathbf{a} = [\Gamma] \mathbf{a}. \quad (1.15)$$

Using the program *RUS* [20] that is based on the introduced approach, the frequency spectrum of the resonant normal-modes and the mode shapes (eigenvectors  $\mathbf{a}$ ) of the vibrations of a plane-parallel crystal plate having free boundaries were calculated.

## 1.2 Electric polarization

An external electric field induces in a non-conducting crystal an electric polarization that is associated with the rearrangement of charges within the crystal. In general, for the

characterization of the dielectric properties of a crystal one makes use of the electric displacement,  $\mathbf{D}$ :

$$\mathbf{D} = \epsilon_0 \mathbf{E} + \mathbf{P}, \quad (1.16)$$

here  $\mathbf{E}$  is the static electric field strength within the crystal and  $\epsilon_0$  is the absolute dielectric constant. The vector  $\mathbf{P}$  denotes the electric polarization of the crystal and is defined as the dipole moment per unit volume. The divergence of  $\mathbf{D}$  is equal to the external charge density,  $\rho_{\text{ext}}$ , outside the crystal:

$$\nabla \cdot \mathbf{D} = \rho_{\text{ext}}. \quad (1.17)$$

The density  $\rho_{\text{ext}}$  produces the external electric field,  $\mathbf{E}_{\text{ext}}$ , at the crystal. In contrast, the divergence of  $\mathbf{E}$  determines the total charge density,  $\rho$ , in the crystal. Thus,  $\rho$  is a sum of  $\rho_{\text{ext}}$  and the polarization charge density,  $\rho_P$ :

$$\epsilon_0 (\nabla \cdot \mathbf{E}) = \rho = \rho_{\text{ext}} + \rho_P. \quad (1.18)$$

Both  $\rho_{\text{ext}}$  and  $\rho_P$  stand for the charge densities averaged over a microscopic distribution of point charges in a sufficiently large crystal volume.

Macroscopically, the electric polarization of a crystal is described by the tensor equation

$$P_i = \epsilon_0 (\epsilon_{ij} - \delta_{ij}) E_j = \epsilon_0 \chi_{ij} E_j, \quad (1.19)$$

where  $[\epsilon_{ij}]$  is the symmetrical dielectric permittivity tensor and  $[\chi_{ij}]$  is the electric susceptibility tensor. The electric field created by  $\rho_P$  within the crystal is denoted as the depolarization field,  $\mathbf{E}_P$ , the direction of which is opposite to  $\mathbf{P}$ :

$$\epsilon_0 \mathbf{E}_P = -\mathbf{P}. \quad (1.20)$$

Hence, according to expression (1.16) and with

$$\mathbf{D} = \epsilon_0 \mathbf{E}_{\text{ext}} \quad (1.21)$$

the total electric field within the crystal is given by

$$\mathbf{E} = \mathbf{E}_{\text{ext}} + \mathbf{E}_P. \quad (1.22)$$

Assuming that the electric-field-induced atomic displacements,  $\Delta \mathbf{R}_\mu$ , in a crystal provide the main contribution to the electric polarization,  $\hat{\mathbf{P}}$ , of the unit cell of the crystal, one may express  $\hat{\mathbf{P}}$  as

$$\hat{\mathbf{P}} = \frac{1}{V} \sum_{\mu} Q_{\mu} \Delta \mathbf{R}_{\mu}. \quad (1.23)$$

Above,  $Q_{\mu}$  is the pseudoatomic charge (see section 2.2 in chapter 2 for definition) of the  $\mu$ -th atom within the unit cell and  $V$  is the unit-cell volume. On the other hand, the macroscopic electric polarization ( $\mathbf{P}$ ) of the crystal is defined by its relative dielectric constants ( $\epsilon_{ij}$ ), as shown in equation (1.19). On the assumption that  $\mathbf{P}$  is homogeneous throughout a crystal, the microscopic approach (1.23) is equal to the macroscopic treatment (1.19) of the electric polarization and therefore, one has [14]:

$$\epsilon_0 ([\epsilon] - 1) \mathbf{E} = \frac{1}{V} \sum_{\mu} Q_{\mu} \Delta \mathbf{R}_{\mu}. \quad (1.24)$$

Since the constants  $\epsilon_{ij}$  were known for the investigated  $\text{Li}_2\text{SO}_4 \cdot \text{H}_2\text{O}$ ,  $\text{Li}_2\text{SeO}_4 \cdot \text{H}_2\text{O}$  and  $\text{BiB}_3\text{O}_6$  crystals, the above condition was used as an additional constraint in the refinements of the atomic displacements. The charges of the pseudoatoms in the crystals were either theoretically calculated or experimentally determined. Equation (1.24) is very important, as it links the microscopic structural changes of a crystal to its macroscopic dielectric properties.

### 1.2.1 Pyroelectric and ferroelectric crystals

The tensor equation (1.19) represents a linear relation between the components of the electric polarization and the components of the electric field within a crystal and is normally well applicable for not too large electric field strengths. In addition, in this section pyroelectric and ferroelectric crystals are introduced, the dielectric properties of which differ from those described by (1.19).

Pyroelectric crystals exhibit a change,  $\Delta\mathbf{P}$ , in the electric polarization when their temperature is changed. In the case of uniform and sufficiently small temperature variations,  $\Delta T$ , within a certain interval  $\Delta\mathbf{P}$  is given by

$$\Delta\mathbf{P} = \mathbf{p}\Delta T, \quad (1.25)$$

where  $\mathbf{p}$  is the pyroelectric vector of the crystal. Consequently, in comparison with expression (1.19), pyroelectric crystals may have an electric polarization in the absence of an external electric field.

In ferroelectric crystals the dependence of the electric polarization on the applied electric field is described by a hysteresis behavior. Thus, these crystals possess both a saturation polarization and a remanent polarization. Therefore, by an application of an electric field it is possible to polarize a ferroelectric crystal that has not had a permanent electric polarization before or to reverse the direction of its polarization vector. Besides, to a ferroelectric crystal a transition temperature, so-called Curie temperature, may be assigned above that the ferroelectric properties of the crystal vanish and the crystal takes on the paraelectric phase.

## 1.3 Piezoelectricity

Under application of a mechanical stress piezoelectric crystals change their electric polarization,  $\mathbf{P}$ . This physical phenomenon is expressed by means of

$$\Delta P_i = d_{ijk}\sigma_{jk} + d_{ijklm}\sigma_{jk}\sigma_{lm} + \dots \quad (1.26)$$

and is denoted as the direct piezoelectric effect. Here  $[\sigma_{jk}]$  is the stress tensor, the third-rank tensor  $[d_{ijk}]$  describes the linear piezoelectric effect and  $[d_{ijklm}]$  stands for the quadratic piezoelectric effect *etc.* Due to the usually small contribution of the quadratic piezoelectric effect, we considered in the analysis of experimental data the linear piezoelectric effect only. Since  $[\sigma_{jk}]$  is symmetric, the piezoelectric tensor  $[d_{ijk}]$  has to be symmetric in the indices  $j$  and  $k$ . Thus, for the components  $d_{ijk}$  one has:  $d_{ijk} = d_{ikj}$ . Furthermore, owing to the transformation law for tensors, all crystals with an inversion center are not piezoelectric, as this symmetry operation implies the vanishing of all components of odd-rank tensors. Assuming that uniaxial stress is applied to a piezoelectric crystal in the direction along a vector  $\mathbf{e}$ , the induced change of the electric polarization of the crystal parallel to  $\mathbf{e}$  is referred to as the longitudinal piezoelectric effect and perpendicular to  $\mathbf{e}$  as the transverse piezoelectric effect.

The converse piezoelectric effect, also known as the first-order electrostriction, describes the occurrence of a deformation of piezoelectric crystals when they are subjected to an external electric field:

$$\varepsilon_{ij} = \hat{d}_{ijk}E_k. \quad (1.27)$$

Accordingly, the components,  $E_k$ , of the applied electric field are linearly related to the components,  $\varepsilon_{ij}$ , of the strain tensor by the first-order electrostriction tensor,  $[\hat{d}_{ijk}]$ . As  $[\varepsilon_{ij}]$  represents the symmetric part of the displacement tensor,  $[e_{ij}]$ , of a crystal,

$$\varepsilon_{ij} = \frac{1}{2} (e_{ij} + e_{ji}), \quad (1.28)$$

$[\hat{d}_{ijk}]$  is symmetric in the second and third index position. Based on a thermodynamical approach to piezoelectricity, one can derive that the components of the piezoelectric and electrostriction tensor are exactly equal:

$$d_{kij} = \hat{d}_{ijk}. \quad (1.29)$$

Consequently, as it was stated by Hansen *et al.* (2004) [15], one has:

Equation (1.29) implies that we may determine the piezoelectric constants from different experiments but it does not mean that the same state may be obtained, either from applying an electric field or from a mechanical stress. In both cases, the final state depends on the piezoelectric properties but in the former it also depends on the dielectric polarizability whereas it depends on the elastic constants in the latter, and these two properties are not related in any simple way.

Since  $\text{Li}_2\text{SO}_4 \cdot \text{H}_2\text{O}$ ,  $\text{Li}_2\text{SeO}_4 \cdot \text{H}_2\text{O}$  and  $\text{BiB}_3\text{O}_6$  crystallize in the point group 2, the piezoelectric tensor of these crystals in total has eight independent components:

$$d_{ij} = \begin{pmatrix} 0 & 0 & 0 & d_{14} & 0 & d_{16} \\ d_{21} & d_{22} & d_{23} & 0 & d_{25} & 0 \\ 0 & 0 & 0 & d_{34} & 0 & d_{36} \end{pmatrix}, \quad (1.30)$$

where the Voigt notation of  $[d_{ijk}]$  is shown.

The description of the elastic and dielectric behavior of piezoelectric crystals requires basic equations that differ from those introduced in sections 1.1 [see eq. (1.1)] and 1.2 [see eqs. (1.16) and (1.19)], as the piezoelectric coupling between propagating elastic and electromagnetic waves has to be considered. This phenomenon results in the following equations

$$\sigma_{ij} = c_{ijkl}^E \varepsilon_{kl} - e_{mij} E_m \quad \text{and} \quad (1.31)$$

$$D_i = e_{ikl} \varepsilon_{kl} + \epsilon_{im}^E E_m, \quad (1.32)$$

where  $[\sigma_{ij}]$  and  $[c_{ijkl}^E]$  denote the stress tensor and the elastic tensor at constant electric field, respectively. The quantities  $e_{mij} = -c_{ijkl}^E d_{mkl}$  stand for the components of the piezoelectric  $e$ -tensor and  $\epsilon_{im}^E$  are the relative dielectric constants at constant mechanical deformation.  $\mathbf{E}$  is the internal electric field and  $\mathbf{D}$  is the internal electric displacement accompanying an acoustic wave in piezoelectric media. Thus, the wave equation describing the propagation of a plane elastic wave along the direction  $\mathbf{g}$  in a piezoelectric crystal is given by

$$(-\rho v^2 \delta_{ik} + c_{ijkl}^D g_j g_l) u_i = 0 \quad \text{with} \quad (1.33)$$

$$c_{ijkl}^D = c_{ijkl}^E + \frac{e_{mij} e_{nkl}}{\epsilon_{rs}^E g_r g_s} g_m g_n. \quad (1.34)$$

Here  $[\delta_{ij}]$  is the Kronecker symbol,  $\mathbf{u}$  designates the mechanical displacement vector and the superscript  $D$  means: at constant electric displacement. The form of (1.33) is identical to that of equation (1.2) for non-piezoelectric crystals, merely the elastic tensor  $[c_{ijkl}]$  was replaced by  $[c_{ijkl}^D]$ .



## 2 X-ray diffraction by crystals under an static external electric field

Firstly, in the context of this chapter it will be derived how the piezoelectric constants of a crystal are related to the measured angular shifts of Bragg peak positions. Secondly, a theoretical relation between the atomic displacements in a crystal induced by an applied electric field and the simultaneously observed changes of the integrated intensities of Bragg peaks will be reviewed (atomistic description of the electric polarization). But first of all, this chapter begins with the X-ray diffraction by unperturbed crystals.

### 2.1 X-ray diffraction by unperturbed crystals

The main theories of the X-ray diffraction by crystals, such as kinematical and dynamical diffraction, are described in detail in many text books, as for instance [21, 22, 23, 24], whereas the concept of extinction is discussed in numerous scientific publications, *e.g.* in the works by Zachariasen (1967) [25], Coppens & Hamilton (1970) [26], Becker & Coppens (1974) [27] and Sabine (1988) [28]. Because of that, in the following discussion the most important results that are necessary for understanding the motivation and the challenge of this work and the data analysis will be introduced only.

The structure factor,  $F$ , of a crystal that is not subjected to an external perturbation is given by

$$F(\mathbf{H}) = \sum_{\mu} \left[ f_{\mu}(\mathbf{H}) + f'_{\mu}(\lambda) + i f''_{\mu}(\lambda) \right] T_{\mu}(\mathbf{H}) \exp(2\pi i \mathbf{H} \mathbf{R}_{\mu}), \quad (2.1)$$

where  $\mathbf{H}$  is a reciprocal-lattice vector,  $f_{\mu}$  is the scattering factor,  $f'_{\mu}$  and  $f''_{\mu}$  are the anomalous dispersion corrections,  $T_{\mu}$  represents the temperature factor and  $\mathbf{R}_{\mu}$  denotes the position of an atom  $\mu$ . The sum is taken over all atoms within the unit cell of the crystal. In the structure factor calculations for a  $\mathbf{H}$  the scattering factor of an atom

$$f(\mathbf{H}) = \int_{\text{atom}} \rho(\mathbf{r}) \exp(2\pi i \mathbf{H} \mathbf{r}) d\mathbf{r}, \quad (2.2)$$

which is the Fourier transform of the spherical electron density of the atom being in the ground state, was taken from [29]. For  $f'$  and  $f''$  numerically calculated values, based on the relativistic second-order S-matrix approach [30], provided by [31] were used. Besides, in order to describe the thermal motion of an atom in a crystal the anisotropic harmonic temperature factor of the form

$$T(\mathbf{H}) = \exp \left( -\beta^{jk} h_j h_k \right) \quad (2.3)$$

was considered, here  $[\beta^{jk}]$  is the thermal atomic displacement tensor.

The kinematical diffraction theory is based on the assumption that the interaction of propagating electromagnetic waves with matter is very weak (weak-scattering limit).

According to this theory the integrated intensity,  $I$ , of a crystal reflection is proportional to the square of the absolute value of the structure factor:

$$I \sim |F(\mathbf{H})|^2. \quad (2.4)$$

The exact expression for  $I$  depends, among other parameters, on the properties of the incident beam, the shape of the crystal and the diffraction geometry. This approach applies to so-called ideally imperfect crystals that are composed of widely misoriented small mosaic blocks of perfect crystals.

The dynamical theory describes the X-ray diffraction by macroscopic perfect crystals. In this theory multiple scattering effects of the electromagnetic waves in a crystal are taken into account by allowing for the reflection and transmission of the waves at each lattice plane that they pass through within the crystal. As a result, the integrated intensity of an X-ray reflection of a perfect crystal is proportional to the absolute value of  $F$  (2.1):

$$I \sim |F(\mathbf{H})|. \quad (2.5)$$

In this context, the extinction depth ( $\Lambda_{\text{ext}}$ ) refers to the thickness of a crystal that reduces the intensity of an incident X-ray beam (due to the scattering by planes of atoms) by the factor  $1/e$ , see Als-Nielsen (2000) [23]:

$$\Lambda_{\text{ext}} = \frac{VH}{4r_0|F(\mathbf{H})|}, \quad (2.6)$$

whereat the beam attenuation arising from the absorption processes in the crystal was neglected. In the expression presented above  $r_0$  is the Thomson scattering length,  $V$  is the volume of the unit cell and  $H$  denotes the modulus of the scattering vector  $\mathbf{H}$ . In general, the longer the extinction depth for a reflection is compared to the absorption depth,

$$\Lambda_{\text{abs}} = \frac{\sin \theta}{2\mu}, \quad (2.7)$$

(this definition is only valid for symmetrical Bragg reflections,  $\mu$  is the linear absorption coefficient of a crystal) the better the approximation of the kinematical diffraction is. The same conclusion may be drawn on the relation between  $\Lambda_{\text{ext}}$  and the crystal thickness.

Normally, the diffraction by real imperfect macroscopic crystals does not agree with the predictions of the kinematical approximation in terms of the  $F^2$ -dependence of the measured integrated intensities that for few strong reflections are smaller than predicted by the theory. This discrepancy between experiment and theory can be explained by the mosaic structure of crystals. On the one hand, the diffraction intensity of a reflection is reduced when the mosaic blocks in the crystal are not sufficiently small and therefore scatter according to the dynamical theory. This effect leads to the model of the primary extinction. On the other hand, if the disorientation of the blocks is not large enough it may occur that several successive blocks have an identical orientation. In this case the incident X-ray intensity is mostly reflected by the highest lying blocks in the crystal and consequently, only much weaker intensity reaches the remaining underlying blocks. This is the origin of the secondary extinction.

In the crystal structure study and determination of the electron density in a crystal the recorded diffraction intensities are analyzed on the basis of the kinematical approximation by means of a simultaneous correction of the experimental data for extinction effects. At this, the extinction factor,  $y$ , is defined by

$$I_{\text{obs}} = yI_{\text{kin}}, \quad (2.8)$$

where  $I_{\text{obs}}$  is the integrated intensity of a Bragg reflection observed in an experiment and  $I_{\text{kin}}$  stands for the intensity calculated applying the kinematical theory. The introduced quantity  $y$  depends on the Bragg angle, on the dimensions of the crystal and its microstructure and on the average size and angular distribution of the mosaic blocks in the crystal. Since analytical expressions for  $y$  can be derived (as shown in the theoretical approaches [25, 26, 27]), using experimental data it becomes possible to include the primary and secondary extinction in the least-squares refinements of the structural and charge density properties of a crystal.

## 2.2 Electron density distribution in crystals

In this work in order to analyze the properties of the chemical bonds and to calculate the pseudoatomic charges in the crystals probed both experimentally determined and theoretically calculated electron densities were considered.

### 2.2.1 Multipole refinement of the electron density

According to the formalism introduced by Hansen & Coppens (1978) [32] the nucleus-centered aspherical electron density of an atom within a crystal is modeled as

$$\rho(\mathbf{r}) = \rho_{\text{core}}(r) + P_{\text{val}}\kappa'^3\rho_{\text{val}}(\kappa'r) + \sum_{l=0}^{l_{\text{max}}} \kappa''^3 R_l(\kappa''r) \sum_{m=0}^l P_{lm\pm} d_{lm\pm}(\mathbf{r}/r). \quad (2.9)$$

Here the spherical core ( $\rho_{\text{core}}$ ) and valence ( $\rho_{\text{val}}$ ) density of a pseudoatom are calculated from non-relativistic ground state Hartree-Fock wave functions for isolated atoms [33].  $P_{\text{val}}$  and  $P_{lm}$  denote the multipole population coefficients. The radial expansion and contraction of multipoles is described by the parameters  $\kappa'$  and  $\kappa''$ .  $R_l$  are the Slater-type radial functions [22]

$$R_l(r) = \kappa''^3 \frac{\zeta^{n_l+3}}{(n_l+2)!} (\kappa''r)^{n_l} \exp(-\kappa''\zeta_l r) \quad (2.10)$$

and  $d_{lm\pm}$  stand for the real spherical harmonics. In above expression  $\zeta_l$  are the energy-optimized single- $\zeta$  Slater values for the electron subshells of unperturbed atoms [22, 34]. The choice of the  $n_l$  values in (2.10) ( $n_l \geq l$ ) depends on the type of orbitals of an atom, as discussed in [22, 32]. In the multipole refinement of the electron density (ED) in a crystal  $P_{\text{val}}$ ,  $P_{lm}$ ,  $\kappa'$  and  $\kappa''$  represent the atomic ED parameters which are refined for each of the symmetry-independent atoms within the crystal unit cell.

For instance, because of the phase problem that may occur for non-centrosymmetric crystals [35], the analysis of the refined experimental electron densities with respect to their physical significance is done by means of the difference ED maps [22],

$$\Delta\rho(\mathbf{r}) = V^{-1} \sum_{\mathbf{H}} (|F_{\text{OBS}}(\mathbf{H})|e^{i\phi_{\text{MULT}}} - |F_{\text{IAM}}(\mathbf{H})|e^{i\phi_{\text{IAM}}})e^{-2\pi i\mathbf{H}\mathbf{r}}, \quad (2.11)$$

that visualize the difference between the crystal ED (multipole density) determined in an experiment and the ED calculated by a superposition of isolated atoms (IAM density). In doing so, the ED accumulation in the chemical bonds and lone-pair regions become visible. Another possibility to check whether the ED distribution in a crystal could be

adequately described with the model of the aspherical-atom expansion of the ED represent the residual ED maps [22],

$$\Delta\rho(\mathbf{r}) = V^{-1} \sum_{\mathbf{H}} (|F_{\text{OBS}}(\mathbf{H})| - |F_{\text{MULT}}(\mathbf{H})|) e^{i\phi_{\text{MULT}}} e^{-2\pi i\mathbf{H}\mathbf{r}}. \quad (2.12)$$

The features of the residual density maps give some indication of possible shortcomings in modeling the ED of especially heavier atoms.

## 2.2.2 DFT calculations of the electron density

For all crystals investigated in this work *ab initio* calculations of the ED based on the Density Functional Theory (DFT) [36, 37] were performed using the program package *WIEN2k* [38].

The DFT provides a quantum mechanical approach for solving the many-electron problem of a crystal in the Born-Oppenheimer approximation, *i.e.* by neglecting the movements of the nuclei. As specified by the theorem of Hohenberg & Kohn (1964) [39], the ground-state energy,  $E$ , of a many-electron system

$$E_{V_{\text{ext}}}[\rho] = F_{\text{HK}}[\rho] + \int \rho(\mathbf{r})V_{\text{ext}}(\mathbf{r}) d\mathbf{r} \quad (2.13)$$

is a functional of the ground-state density,  $\rho$ . Here  $V_{\text{ext}}$  is the external potential of the nuclei, which are at fixed positions, in that the inhomogeneous electron gas in a crystal moves and  $F_{\text{HK}}$  denotes the Hohenberg-Kohn density functional. In general, the ED resulting from the solution of the Kohn-Sham equation [40]

$$\left( -\frac{\hbar^2}{2m_e} \nabla_i^2 + \frac{e^2}{4\pi\epsilon_0} \int \frac{\rho(\mathbf{r}')}{|\mathbf{r} - \mathbf{r}'|} d\mathbf{r}' + V_{\text{xc}} + V_{\text{ext}} \right) \phi_i(\mathbf{r}) = \epsilon_i \phi_i(\mathbf{r}) \quad (2.14)$$

minimizes the energy functional  $E_{V_{\text{ext}}}$  (2.13). Whereat  $V_{\text{xc}}$  is the  $\rho$ -dependent exchange-correlation potential and  $\rho$  is defined by  $N$  single-electron wave functions,  $\phi_i$  [37]:

$$\rho(\mathbf{r}) = \sum_{i=1}^N \phi_i^*(\mathbf{r})\phi_i(\mathbf{r}). \quad (2.15)$$

In order to solve the self-consistent problem (2.14) in the first step based on an approximation of the ED,  $\rho_0$ , the eigenfunctions  $\phi_i$  are determined and then with (2.15) a new ED,  $\rho_1$ , is calculated. Finally,  $\rho_0$  and  $\rho_1$  are compared with each other and in the case of disagreement within applied certain criteria  $\rho_1$  is used in the second iteration as the starting ED. This procedure is repeated until there is a convergence to an ED,  $\rho_c$ , that corresponds to the searched ground-state density in the crystal.

The functions  $\phi_i$  from (2.15), which are employed to model the ED in a crystal, have the form [37]

$$\phi_i(\mathbf{r}) = \sum_{\mathbf{G}} c_{\mathbf{G}}^{n,\mathbf{k}} \exp[i(\mathbf{k} + \mathbf{G})\mathbf{r}] \equiv \phi_{\mathbf{k}}^n(\mathbf{r}) \quad (2.16)$$

that satisfies the periodicity of the crystal lattice. Here  $\mathbf{k}$  is the wave vector inside the first Brillouin zone,  $\mathbf{G}$  indicates a reciprocal lattice vector ( $\mathbf{G} = 2\pi \times \mathbf{H}$ ) and  $n$  denotes the band index. The Fourier expansion (2.16) of the functions  $\phi_{\mathbf{k}}^n$  is due to the necessary large number of the plane wave basis functions needed for an accurate description of the

ED in crystals not efficient for computational methods. Therefore, a more optimized set of basis functions is considered by taking into account that the inner electrons of an atom may be modeled by atomic-like functions, whereas the outer electrons being not tightly bound are described by plane waves. This adaption is realized by subdividing the unit cell of a crystal into non-overlapping and nucleus-centered atomic spheres (so-called muffin tin spheres) and interstitial regions. In this context, the APW+lo approach [38] provides the most accurate and efficient method for calculating the ED in crystals. In this method the basis functions used to expand the single-electron wave functions  $\phi_{\mathbf{k}}^n$  (2.16) are given by

$$\psi_{\mathbf{k}}^n(\mathbf{r}) = \begin{cases} \sum_{lm} A_{lm}^{n\mathbf{k}\mathbf{G}}(r) Y_{lm}(\mathbf{k}/r) & \text{inside a muffin thin sphere} \\ \frac{1}{\sqrt{V}} \exp[i(\mathbf{k} + \mathbf{G})\mathbf{r}] & \text{outside a muffin thin sphere,} \end{cases} \quad (2.17)$$

where  $V$  is the volume of the unit cell and  $Y_{lm}$  are the spherical harmonics. The product  $K_{\max} \times R_{\min}$  consisting of the absolute value of the largest wave vector,  $K_{\max}$ , and the smallest radius,  $R_{\min}$ , of all muffin tin spheres defines the accuracy of a basis set.

### 2.2.3 Topological analysis of the electron density

The formalism introduced by Bader (1990) [41] treats the ED in a crystal as being composed of different nucleus-centered density fragments that are referred to as the atomic basins. The boundary surface,  $\Omega$ , (surface of zero flux) of the basins is defined by [22]

$$\nabla\rho(\mathbf{r}) \cdot \mathbf{n}(\mathbf{r}) = 0, \quad (2.18)$$

where  $\mathbf{n}(\mathbf{r})$  is the normal of  $\Omega$  at a point  $\mathbf{r}$ . The integration of the ED over the volume,  $V(\Omega)$ , of a pseudoatom gives its Bader charge in the crystal

$$Q = e \left( Z - \int_{V(\Omega)} \rho(\mathbf{r}) d\mathbf{r} \right). \quad (2.19)$$

The differences between the Bader approach and other space partitioning methods in terms of the obtained values of the pseudoatomic charges in a crystal are discussed in [22]. In this work the Bader method was used exclusively.

The classification of the chemical bonds in crystals is based on several quantities, such as ED, Laplacian of the ED ( $\nabla^2\rho$ ) and electronic energy density [eq. (2.22)], considered at the bond critical points ( $\mathbf{r}_b$ ) where the gradient vector of  $\rho$  vanishes [22, 36, 41]:

$$\nabla\rho(\mathbf{r}_b) = 0. \quad (2.20)$$

At the so-called (3, -1) critical point ( $\mathbf{r}_c$ ) that is located between two bonded atoms the ED along the corresponding bond path takes its minimum value. Simultaneously,  $\rho$  attains its maximum in the plane that is perpendicular to the bond path and goes through  $\mathbf{r}_c$ . Consequently, the eigenvalues of the Hessian matrix,  $\lambda_1$ ,  $\lambda_2$  and  $\lambda_3$ , defining the curvature of  $\rho$  at  $\mathbf{r}_c$  have the following signs: According to the definition usually used, the third principal axis of the  $\rho$  curvature lies along the bond path, therefore the eigenvalue  $\lambda_3$  is positive while  $\lambda_1$  and  $\lambda_2$  are negative. Besides, the value of  $\nabla^2\rho$  at  $\mathbf{r}_c$  is equal to the sum of the Hessian matrix eigenvalues:

$$\nabla^2\rho(\mathbf{r}_c) = \lambda_1 + \lambda_2 + \lambda_3. \quad (2.21)$$

The local energy density,  $h$ , of an electron distribution at a point  $\mathbf{r}$  in a crystal is defined as [22, 36]

$$h(\mathbf{r}) = g(\mathbf{r}) + v(\mathbf{r}), \quad (2.22)$$

where  $g$  is the electronic kinetic energy density and  $v$  is referred to as the potential energy density. In addition,  $h$  is related to the Laplacian of  $\rho$  through the equation

$$h(\mathbf{r}) = \frac{1}{2} [v(\mathbf{r}) + (\hbar^2/4m)\nabla^2\rho(\mathbf{r})]. \quad (2.23)$$

Thus,  $h$  is completely determined by the features of the ED, the Laplacian of the ED and the external nuclear potential.

In general, one distinguishes three different types of chemical bonding [22, 42]. Firstly, in the case of the closed-shell atomic interactions the values of  $\nabla^2\rho$  and  $h$  are both positive at the (3, -1) bond critical points. Secondly, a positive  $\nabla^2\rho$  and a negative  $h$  at a  $\mathbf{r}_c$  point indicate an intermediate atomic interaction that is neither a pure closed-shell nor a shared interaction. Finally, negative values of  $\nabla^2\rho(\mathbf{r}_c)$  and  $h(\mathbf{r}_c)$  are typical for the shared atomic interactions describing the covalent bonds. Furthermore, either the magnitude of the ED or of the bond degree (BD) parameter,

$$\text{BD} = h(\mathbf{r})/\rho(\mathbf{r}), \quad (2.24)$$

at  $\mathbf{r}_c$  is regarded as a measure of the strength of a chemical bond [43]. Therefore, the greater the value of  $\rho(\mathbf{r}_c)$  is the stronger the interaction is between two atoms.

## 2.3 External and internal strain of a crystal induced by an applied electric field

An external electric field applied to a piezoelectric crystal induces both a change of the crystal lattice parameters, denoted as the external strain, and a redistribution of the atomic positions within the unit cell, referred to as the internal strain [44]. The first phenomenon results in the macroscopic homogeneous deformation of the crystal under an electric field and is known as the converse piezoelectric effect, see chapter 1. In an X-ray diffraction experiment the external strain manifests itself in a change of the angular positions of Bragg peaks, as shown in Fig. 2.1. In contrast, the internal strain describes the response of a crystal to an external electric perturbation on the atomic scale and is associated with the macroscopic electric polarization of the crystal media. The internal strain leads to a variation of diffraction intensities (see Fig. 2.1), as the atomic fractional coordinates change in the unit cell.

Employing a field-switching technique, which will be introduced in chapter 3, the angular shift and the variation of the integrated intensity of a reflection can be measured simultaneously, as demonstrated in Fig. 2.1 for the  $\bar{2}57$  reflection of a  $\text{Li}_2\text{SO}_4 \cdot \text{H}_2\text{O}$  (010) crystal plate. Furthermore, the big advantage of such measurements is that one gets a unique possibility to distinguish the effect of the internal strain on the crystal structure from that of the external strain in a clear way. Consequently, from one and the same experimental data set both the piezoelectric constants of a crystal and the induced relative atomic displacements within the unit cell can be deduced.

Besides, especially in the case of very strong Bragg reflections, which are the most sensitive to the primary and secondary extinction effects (as described in section 2.1),

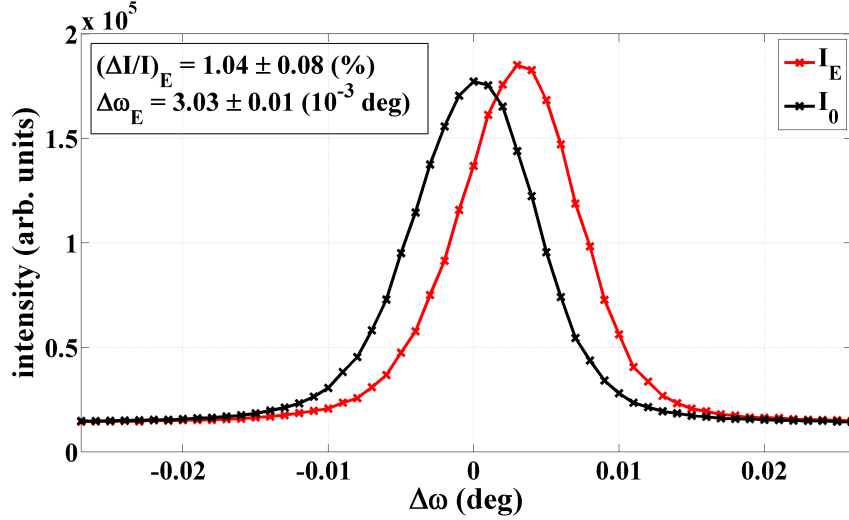


**Figure 2.1:** Change of the integrated intensity and angular shift of the peak position of the  $\bar{2}57$  reflection of a  $\text{Li}_2\text{SO}_4\cdot\text{H}_2\text{O}$  (010) crystal plate induced by an external electric field of the magnitude  $E = 5.9 \text{ kV mm}^{-1}$ ,  $\lambda = 0.6 \text{ \AA}$ . The reflection profiles were recorded in the  $\omega$  scan mode, whereat the  $I_0$  curve corresponds to the zero-field state.

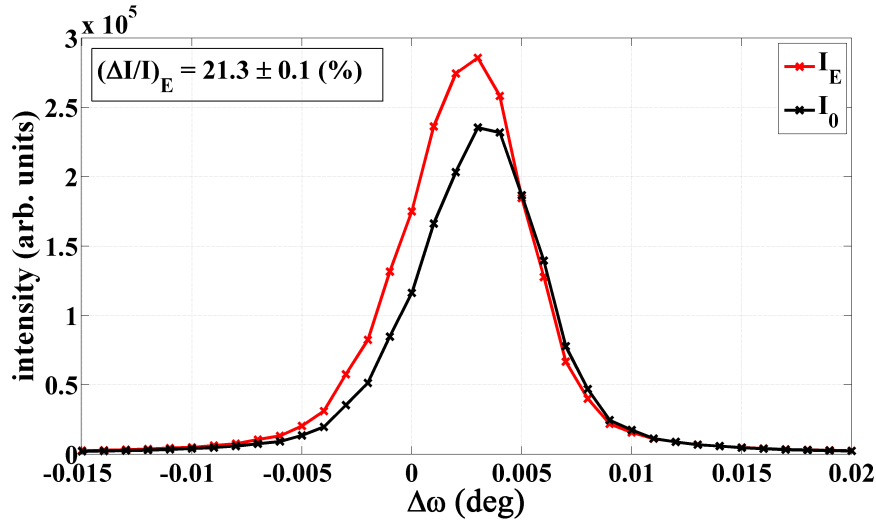


**Figure 2.2:** Extinction-affected huge change of the integrated intensity of the very strong  $\bar{1}44$  reflection of a  $\text{Li}_2\text{SO}_4\cdot\text{H}_2\text{O}$  (001) crystal plate measured under an external electric field of the magnitude  $E = 5.0 \text{ kV mm}^{-1}$ ,  $\lambda = 0.6 \text{ \AA}$ .

under an applied electric field the widths of the diffraction profiles may change as well as the diffraction intensities. Both effects result in a huge variation of the integrated intensity of a reflection, see Fig. 2.2. This phenomenon has its origin in the electric-field-caused modification of the mosaic structure of a crystal and is not related to the rearrangement of atoms in the unit cell. Since no theory exists allowing for a description of the influence of an external electric field on the crystal mosaicity, all reflections for that the observed change of diffraction intensities was affected by extinction effects have to be omitted from the data analysis. As there is no unambiguous way to define extinction-affected data, in order to reveal the atomic displacements in a crystal, it is essential that in an X-ray diffraction experiment under an external electric perturbation weak reflections are considered only.

### 2.3.1 Determination of the piezoelectric constants of a crystal by means of X-ray diffraction

Diffraction curves of a piezoelectric crystal measured in the  $\omega$  scan mode using a four-circle diffractometer in combination with an open X-ray point detector exhibit an angular shift of the rocking curve positions under an external electric field, as displayed in Fig. 2.3. Measurements of the effect for a large number of reflections allow for the determination of all piezoelectric constants,  $d_{ijk}$ , of a crystal.

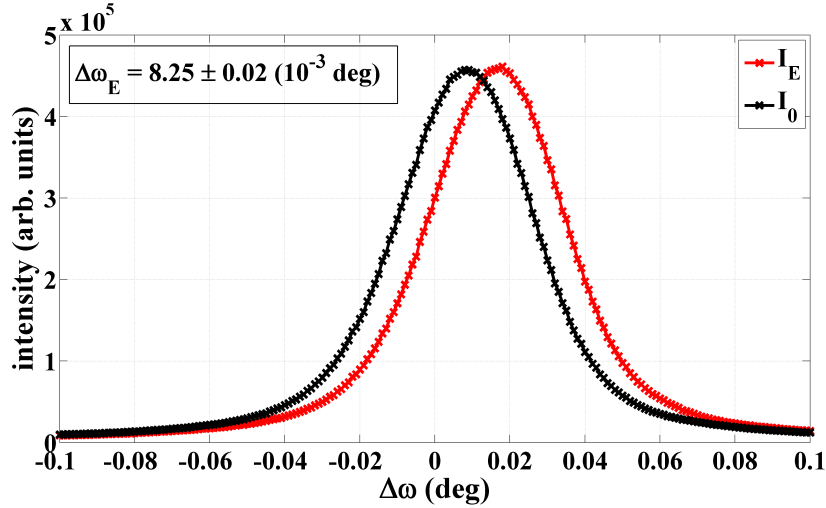


**Figure 2.3:** Angular shift of the  $\omega$  rocking curve position of the  $\text{BiB}_3\text{O}_6$  (010) crystal plate 087 reflection arising from the piezoelectric lattice deformation. In comparison with the black curve the red one was recorded during the crystal was subjected to an external electric field of the magnitude  $E = 3.8 \text{ kV mm}^{-1}$ ,  $\lambda = 0.93 \text{ \AA}$ .

A theoretical equation relating the tensor coefficients  $d_{ijk}$  with the piezoelectrically induced changes in the Bragg angle of X-ray reflections was derived for the first time by Barsch [45]. However, Barsch did not consider the rotation of the lattice due to the external electric perturbation and therefore, his equation can be used only if different series of harmonic reflections are recorded. Such measurements were performed for example with  $\alpha$ -quartz [12, 13] and monoclinic (point group  $m$ ) 2-methyl 4-nitroaniline [16]. Finally, it was Graafsma [46] who introduced a more general approach for the X-ray determination of all components of the piezoelectric tensor of a crystal with an arbitrary symmetry.

Following the ideas of Graafsma [46], the Ewald construction (see Fig. 2.4) is the best method to visualize how the electric-field-induced deformation of a crystal affects the angular position of the  $\omega$  rocking curve of a reflection. As the piezoelectric deformation is homogeneous throughout the crystal, it may be described in terms of the distortion of the crystal lattice vectors:

$$\mathbf{a}_i(\mathbf{E}) = \mathbf{a}_i(0) + \Delta\mathbf{a}_i(\mathbf{E}) \text{ and } \mathbf{b}_i(\mathbf{E}) = \mathbf{b}_i(0) + \Delta\mathbf{b}_i(\mathbf{E}). \quad (2.25)$$

Here  $\mathbf{a}_i(\mathbf{E})$  and  $\Delta\mathbf{a}_i(\mathbf{E})$  ( $i = 1, 2, 3$ ) are the lattice basis vectors and their changes under the influence of an applied electric field, respectively. The corresponding reciprocal basis vectors and their changes are denoted as  $\mathbf{b}_i(\mathbf{E})$  and  $\Delta\mathbf{b}_i(\mathbf{E})$ , respectively. Normally, as illustrated in Fig. 2.4, under  $\mathbf{E}$  a reciprocal lattice vector ( $\mathbf{H} = h\mathbf{b}_1 + k\mathbf{b}_2 + l\mathbf{b}_3$ ) is displaced from the Ewald sphere:

$$\mathbf{H}_E = \mathbf{H} + \Delta\mathbf{H}, \quad (2.26)$$

where  $\mathbf{H}_E$  and  $\mathbf{H}$  are the positions of the reciprocal lattice point with and without the external electric field, respectively. Besides,  $\Delta\mathbf{H}$  designates the change in  $\mathbf{H}$ :

$$\Delta\mathbf{H} = h\Delta\mathbf{b}_1 + k\Delta\mathbf{b}_2 + l\Delta\mathbf{b}_3. \quad (2.27)$$

Assuming that  $\mathbf{H}$  of a reflection lies exactly on the Ewald sphere, thus fulfills the Bragg condition, in order to return  $\mathbf{H}_E$  back into the reflection position the crystal has to be rotated around the main  $\omega$  axis of the diffractometer by an angle  $\Delta\omega$ . Consequently, the deformation of the crystal is visible as an angular shift of the rocking curve from its field-free position. Usually, the aperture ( $\sim 0.5^\circ$ ) of a point detector is wide enough with respect to  $\Delta\omega$  ( $\Delta\omega < 0.01^\circ$ ) and therefore, during an  $\omega$  scan it is not necessary to change the  $2\theta$  angle of the detector.

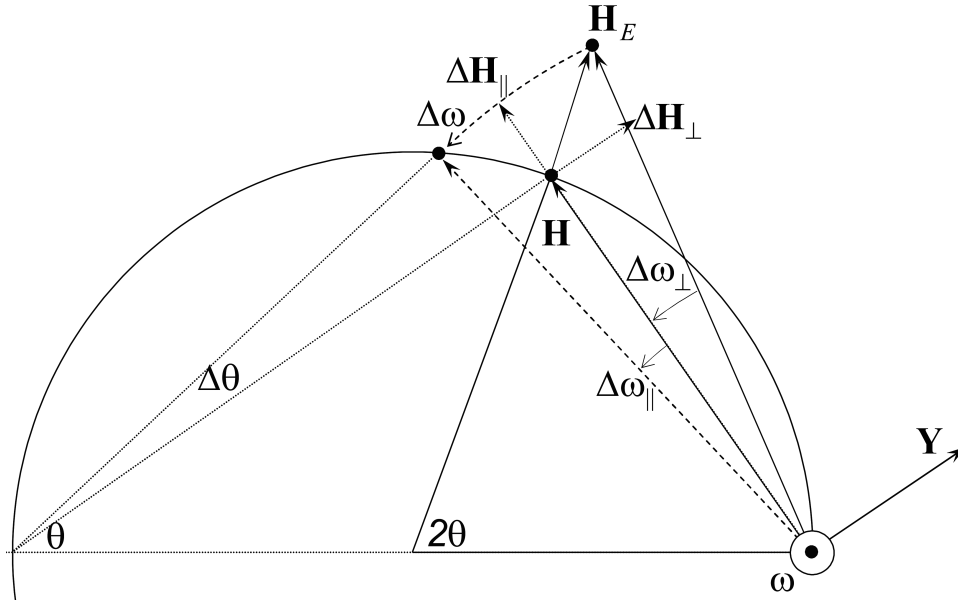


**Figure 2.4:** Reciprocal space reconstruction of the piezoelectrically induced displacement of the peak position of an  $\omega$  rocking curve, as shown in Fig. 2.3. Due to the influence of an external electric field, the reciprocal lattice point  $\mathbf{H}$  is displaced from the reflection position to  $\mathbf{H}_E$ .

As stated in chapter 1 by equation (1.27), the pure piezoelectric deformation of a crystal is described by a symmetric strain tensor,  $[\varepsilon_{ij}]$ . But in general, an applied electric field can also induce a rotation of the crystal, an effect that is captured by an antisymmetric rotation tensor,  $[r_{ij}]$ . The tensor coefficients  $r_{ij}$  are related to those of the electric field vector by the components of the third rank tensor  $[R_{kij}]$ :

$$r_{ij} = R_{kij}E_k, \quad \text{with } R_{kij} = -R_{kji}. \quad (2.28)$$

$[R_{kij}]$  does not represent a pure intrinsic crystal property, because due to the individual clamping conditions of a crystal sample on a diffractometer head, the values of the components  $R_{kij}$  have their physical significance only for an individual sample with its own characteristic experimental setup conditions. All tensor and vector quantities in (2.28) are referred to the crystal Cartesian system.

In terms of the strain and rotation tensor the change of the unit cell basis vectors of a crystal under  $\mathbf{E}$  is given by

$$\mathbf{a}_i(\mathbf{E}) = (1 + [\varepsilon] + [r]) \mathbf{a}_i(0). \quad (2.29)$$

Considering that the reciprocal lattice vectors are connected with the direct lattice through  $\mathbf{a}_i \mathbf{b}_j = \delta_{ij}$ , one can write

$$\mathbf{b}_i(\mathbf{E}) = (1 + [\varepsilon]^T + [r]^T)^{-1} \mathbf{b}_i(0) = (1 + [\varepsilon] - [r])^{-1} \mathbf{b}_i(0) = (1 - [\varepsilon] + [r]) \mathbf{b}_i(0), \quad (2.30)$$

where the relations  $[\varepsilon]^T = [\varepsilon]$  and  $[r]^T = -[r]$  were applied. In the last term is was taken into account that within the approximation of the linear theory of elasticity the displacements are small. Consequently, with

$$\Delta \mathbf{b}_i(\mathbf{E}) = (-[\varepsilon] + [r]) \mathbf{b}_i(0) \quad (2.31)$$

the shift of a reciprocal lattice point described by (2.27) can be expressed as

$$\Delta \mathbf{H} = (-[\varepsilon] + [r]) \mathbf{H}. \quad (2.32)$$

Using equations (1.27) and (2.28), the components of  $\Delta \mathbf{H}$  referred to the crystal Cartesian system are

$$\Delta H_i = (-d_{kij} + R_{kij}) E_k H_j. \quad (2.33)$$

A decomposition of the vector  $\Delta \mathbf{H}$  into a longitudinal,  $\Delta \mathbf{H}_{\parallel}$ , and transverse,  $\Delta \mathbf{H}_{\perp}$ , component (as demonstrated in Fig. 2.4) facilitates the derivation of a theoretical expression for the induced angular shift of an  $\omega$  rocking curve. At this,  $\Delta \mathbf{H}_{\parallel}$  is associated with the pure elongation of  $\mathbf{H}$  and hence, its absolute value is given by

$$\Delta H_{\parallel} = \left( \Delta \mathbf{H} \cdot \frac{\mathbf{H}}{H} \right) = -d_{kij} E_k H_i H_j / H. \quad (2.34)$$

In contrast,  $\Delta \mathbf{H}_{\perp}$  represents the pure rotation of  $\mathbf{H}$  without changing its length plus the additional rotation of the whole crystal. The absolute value of  $\Delta \mathbf{H}_{\perp}$  is equal to

$$\Delta H_{\perp} = (\Delta \mathbf{H} \cdot \mathbf{Y}) = -d_{kij} E_k Y_i H_j + R_{kij} E_k Y_i H_j, \quad (2.35)$$

where  $\mathbf{Y} = (\mathbf{H} \times \hat{\omega})/H$  has unit length and is perpendicular to both  $\mathbf{H}$  and the unit vector  $\hat{\omega}$  along the main  $\omega$  rotation axis of the diffractometer. The components  $\omega_i$  in the crystal Cartesian system depend on the diffractometer setting angles, the matrix  $\mathbf{B}$  transforming the crystal Cartesian system into the crystal reciprocal basic system and the orientation matrix  $\mathbf{M}$  of the crystal [47]. In the case of the axial system defined for the HUBER 4-circle diffractometer at the HASYLAB beamline D3 [48]  $\hat{\omega}$  can be calculated from

$$\hat{\omega} = (M \cdot B)^{-1} \begin{pmatrix} -\sin \chi \cos \phi \\ \sin \chi \sin \phi \\ \cos \chi \end{pmatrix}. \quad (2.36)$$

According to Fig. 2.4, the angular shift ( $\Delta \omega_{\parallel}$ ) of a rocking curve position owing to the contribution of  $\Delta \mathbf{H}_{\parallel}$  is equivalent to the change ( $\Delta \theta$ ) of the scattering angle. Together with the Bragg equation

$$H = 2 \sin \theta / \lambda \quad (2.37)$$

and (2.34) one gets

$$\Delta \omega_{\parallel} = \Delta \theta = \tan \theta \Delta H_{\parallel} / H = -\tan \theta d_{kij} E_k H_i H_j / H^2. \quad (2.38)$$

### 2.3 External and internal strain of a crystal induced by an applied electric field

Whereas, the angle  $\Delta\omega_{\perp}$ ,

$$\Delta\omega_{\perp} = \Delta H_{\perp}/H = -d_{kij}E_k Y_i H_j/H + R_{kij}E_k Y_i H_j/H, \quad (2.39)$$

stems from the  $\Delta\mathbf{H}_{\perp}$  (2.35) contribution. Finally, adding the equations (2.38) and (2.39) results in the total electric-field-induced angular displacement of the peak position of a diffraction curve:

$$\Delta\omega = \Delta\omega_{\parallel} + \Delta\omega_{\perp} = -\tan\theta d_{kij}E_k H_i H_j/H^2 - d_{kij}E_k Y_i H_j/H + R_{kij}E_k Y_i H_j/H, \quad (2.40)$$

where Barsch derived in his work [45] the first term only. As depicted in Fig. 2.5, affirming the theory (2.40),  $\Delta\omega$  exhibits a linear dependence on the external electric field applied to the crystal.

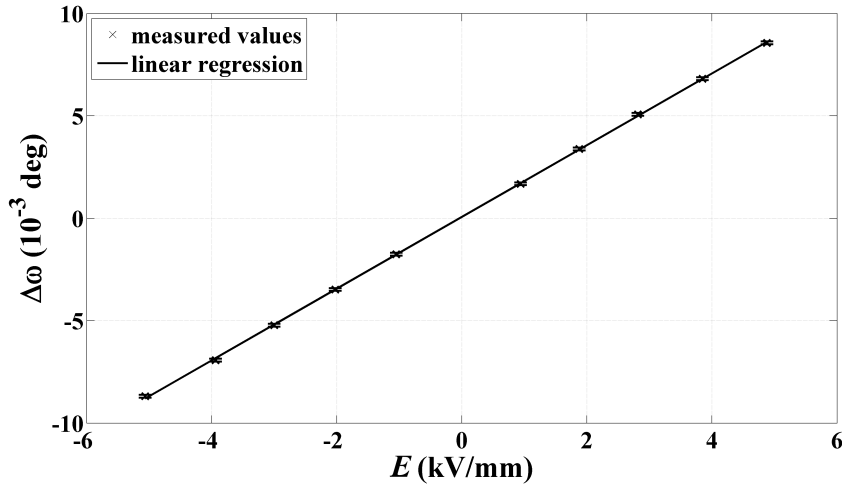


**Figure 2.5:** Bragg peak shift of the  $\text{BiB}_3\text{O}_6$  (010) crystal plate  $\bar{7}510$  reflection as a function of  $\mathbf{E} = E \times \mathbf{e}_2$ . In agreement with the theory (2.40) the  $\Delta\omega$  values are linear dependent on  $E$ .

In the general approach introduced in this section the piezoelectric tensor of a crystal is determined by the X-ray diffraction technique using equation (2.40) as the theoretical basis. In detail, with the  $\Delta\omega$  values measured for a set of arbitrarily chosen reflections one obtains a system of linear equations with the piezoelectric,  $d_{kij}$ , and rotation,  $R_{kij}$ , constants as unknown parameters. The advantage of the presented method is that in an experiment one can concentrate on those reflections being the most sensitive to the variation of the atomic structure of a crystal. In doing so, both the atomic rearrangement in the unit cell and the  $d_{kij}$  constants of the crystal can be determined simultaneously.

The individual  $\omega$  diffraction curves,  $I(\omega)$ , of a reflection were fitted by the pseudo-Voigt (PV) function [49],

$$\text{PV}(\omega) = \frac{I\eta\Gamma}{2\pi(\omega - \omega_0)^2 + \Gamma^2} + \frac{2I(1 - \eta)(\ln 2)^{1/2}}{\Gamma\pi^{1/2}} \exp \left[ - \left( \frac{2(\omega - \omega_0)(\ln 2)^{1/2}}{\Gamma} \right)^2 \right], \quad (2.41)$$

by taking account of a linear background,  $f_b(\omega) = b\omega + a$ . That way, the angular peak position,  $\omega_0$ , of a  $I(\omega)$  profile,

$$I(\omega) = \text{PV}(\omega) + b\omega + a, \quad (2.42)$$

was extracted. In equation (2.41) the parameter  $I$  is the integrated intensity of a curve,  $\Gamma$  corresponds to the full width of the curve at half-maximum (FWHM) and  $\eta$  is a parameter

that mixes the Gaussian ( $\eta = 0$ ) and Lorentzian ( $\eta = 1$ ) functions. The profile fitting was implemented in a *MATLAB* script based on the function *nlinfit* [50] from the statistic toolbox. The number of counts ( $N$ ) collected for each  $\omega$  angle was weighted according to the Poisson distribution with  $w = 1/\sigma^2 = 1/N$ .

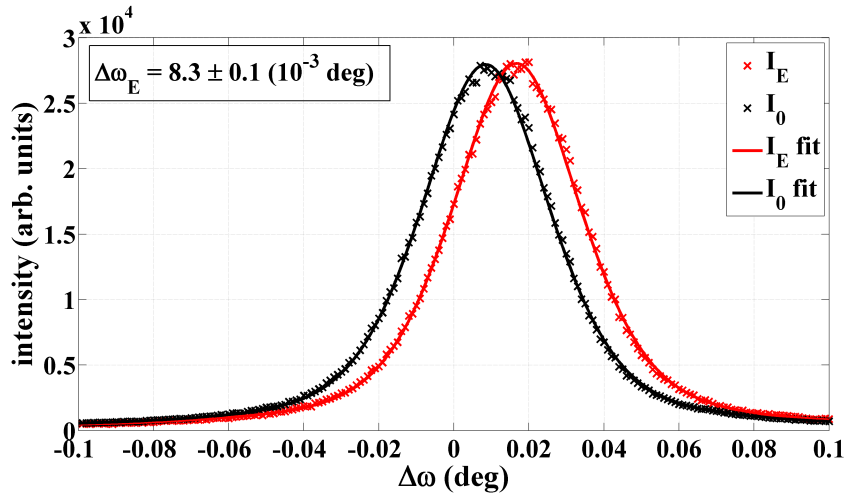


**Figure 2.6:** Rocking curves of the  $\text{BiB}_3\text{O}_6$  (010) crystal plate  $08\bar{7}$  reflection compared with the fitted profile functions (2.42). In contrast to this example, in Fig. 2.3 the complete measurement of the reflection consisting of a sum of 14 single  $\omega$  profiles recorded consecutively is presented.

Figure 2.6 displays the profile functions (2.42) fitted to the measured rocking curves of the  $\text{BiB}_3\text{O}_6$  (010) crystal plate  $08\bar{7}$  reflection. Almost all diffraction profiles could be well described by the PV function (2.41) (as shown in Fig. 2.6), otherwise the rocking curves were omitted from the data analysis. Normally, in order to achieve high counting statistics, for a reflection much more than one single  $\omega$  scan were performed. Therefore, for each scan the recorded rocking curves were fitted by (2.42), then their angular shift,

$$\Delta\omega = \omega_0(E) - \omega_0(E = 0), \quad (2.43)$$

was determined and finally, all  $\Delta\omega$  values of a complete measurement were averaged.

### 2.3.2 Refinement of the electric-field-induced atomic displacements in a crystal

The intensity of the X-ray diffraction by a crystal in the presence of an applied external electric field has been analyzed by Tsirelson *et al.* (2003) [51] and Gorfman *et al.* (2005) [52]. They showed that the change of the kinematical diffraction intensities, as illustrated in Fig. 2.7, is mainly due to the electric-field-induced displacements of atoms within the crystal unit cell. The contribution of the polarization of the electron subsystem was estimated as 100 times smaller and therefore can be neglected. Accordingly, the structure factor (2.1) of a crystal that is subjected to an external electric perturbation takes the form

$$\begin{aligned} F_E(\mathbf{H}) &= \sum_{\mu} \left[ f_{\mu}(\mathbf{H}) + f'_{\mu}(\lambda) + i f''_{\mu}(\lambda) \right] T_{\mu}(\mathbf{H}) \exp(2\pi i \mathbf{H} \mathbf{R}_{\mu}) \exp [2\pi i \mathbf{H} \Delta \mathbf{R}_{\mu}(\mathbf{E})] \\ &\equiv \sum_{\mu} f_{\mu}^a(\mathbf{H}) \exp [2\pi i \mathbf{H} \Delta \mathbf{R}_{\mu}(\mathbf{E})], \end{aligned} \quad (2.44)$$

where  $\Delta\mathbf{R}_\mu$  are the atomic displacement vectors. In a linear approximation the vector components  $\Delta R_\mu^i$  referred to the crystallographic coordinate system and marked with the superscript  $i$  are described by

$$\Delta R_\mu^i = a_j^i(\mu)E^j, \quad (2.45)$$

here the Einstein summation convention is used. The displacement tensor  $[a_j^i(\mu)]$  of an atom  $\mu$  and its dependence on the microscopic parameters of the crystal, such as phonon spectra and ED distribution, were discussed by Gorfman *et al.* (2006) [14]. Note that  $[a_j^i(\mu^*)]$  of an atom  $\mu^*$  that is related to the atom  $\mu$  by the symmetry operation  $\{\mathbf{S}, \mathbf{d}\}$  ( $\mathbf{S}$  is a rotation matrix and  $\mathbf{d}$  is a translation vector) is given by

$$[a_j^i(\mu^*)] = \mathbf{S} [a_j^i(\mu)] \mathbf{S}^{-1}. \quad (2.46)$$

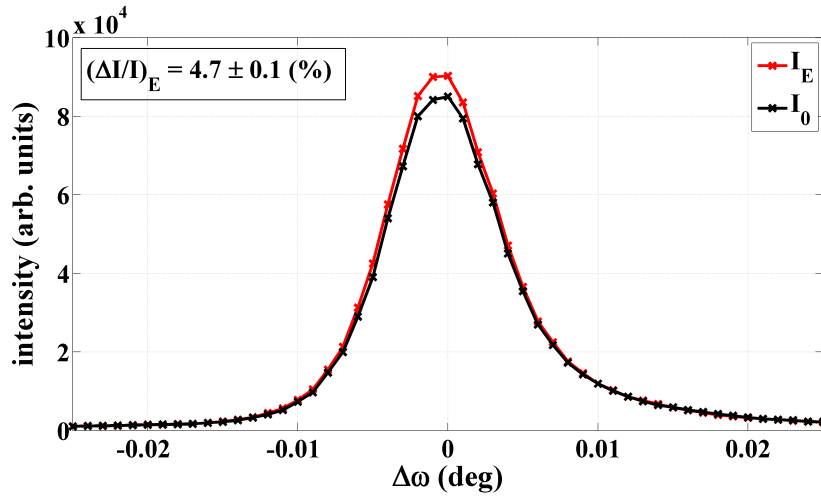


**Figure 2.7:** Electric-field-induced change of the diffraction intensity,  $I_E$  curve, of the  $\bar{1},0,10$  reflection of a  $\text{Li}_2\text{SeO}_4 \cdot \text{H}_2\text{O}$  (010) crystal plate measured at  $\lambda = 0.98 \text{ \AA}$  and under  $E = 3.9 \text{ kV mm}^{-1}$ . The  $I_0$  curve represents the unperturbed diffraction intensity.

The relative intensity change,

$$\frac{\Delta I}{I} = \frac{I_E - I_0}{I_0}, \quad (2.47)$$

of an X-ray reflection ( $I_E$  denotes the integrated intensity measured under  $\mathbf{E}$  and  $I_0$  is the unperturbed intensity, see Fig. 2.7) under the influence of an electric perturbation applied to the crystal can be modeled as

$$(\Delta I/I)_{\text{MOD}} = \frac{|F_E|^2 - |F_0|^2}{|F_0|^2}. \quad (2.48)$$

Consequently, the recorded diffraction intensities do not have to be corrected for polarization and absorption effects. Besides, the time dependence of the incident beam flux does not have to be considered in the data analysis. In expression (2.48) the tensor coefficients  $a_j^i(\mu)$  from (2.45) are the model parameters that are determined by fitting the  $(\Delta I/I)_{\text{MOD}}$  values to the observed X-ray ones,  $(\Delta I/I)_{\text{OBS}}$  values. In detail, using the *MATLAB* function *fminunc* [53] from the optimization toolbox, the  $a_j^i(\mu)$  constants were refined by minimizing the error sum

$$\chi^2 = \sum_{\mathbf{H}} \left[ \frac{(\Delta I/I)_{\text{OBS}} - (\Delta I/I)_{\text{MOD}}}{\sigma(\Delta I/I)} \right]^2. \quad (2.49)$$

Based on the agreement indices, such as  $R$  factor [14],

$$R = \frac{\sum_i |(\Delta I/I)_{i\text{OBS}} - (\Delta I/I)_{i\text{MOD}}|}{\sum_i |(\Delta I/I)_{i\text{OBS}}|}, \quad (2.50)$$

and weighted  $R_w$  factor [14],

$$R_w = \left[ \frac{\sum_i w_i |(\Delta I/I)_{i\text{OBS}} - (\Delta I/I)_{i\text{MOD}}|^2}{\sum_i w_i |(\Delta I/I)_{i\text{OBS}}|^2} \right]^{1/2} \quad \text{with } w_i = \frac{1}{\sigma^2 (\Delta I/I)_i}, \quad (2.51)$$

the quality of the performed refinements was estimated. The better the model (2.48) fits the experimental data the smaller the values of  $R$  and  $R_w$  are.

Normally, in an external electric field ( $\mathbf{E} = E \times \hat{\mathbf{e}}$ ) the displacement of an atom in a piezoelectric crystal is of the order of  $|\Delta \mathbf{R}| \sim 10^{-3} - 10^{-4} \text{ \AA}$  [8-14]. Thus,  $|F_E|^2$  defined by (2.44) can be approximated as follows

$$\begin{aligned} |F_E(\mathbf{H})|^2 &\approx \left| \sum_{\mu} f_{\mu}^a(\mathbf{H}) [1 + 2\pi i \mathbf{H} \Delta \mathbf{R}_{\mu}(\mathbf{E})] \right|^2 = \left| \sum_{\mu} f_{\mu}^a(\mathbf{H}) [1 + 2\pi i \mathbf{H} [a(\mu)] \mathbf{E}] \right|^2 \\ &= |F_0(\mathbf{H}) + 2\pi i \sum_{\mu} f_{\mu}^a(\mathbf{H}) \mathbf{H} [a(\mu)] \mathbf{E}|^2 = |F_0(\mathbf{H})|^2 (1 + \alpha E), \end{aligned} \quad (2.52)$$

with the introduced new quantity  $\alpha$ ,

$$\alpha(\mathbf{H}) = -4\pi \text{Im} \left\{ F_0(\mathbf{H})^* \sum_{\mu} f_{\mu}^a(\mathbf{H}) \mathbf{H} [a(\mu)] \hat{\mathbf{e}} \right\} / |F_0(\mathbf{H})|^2. \quad (2.53)$$

Substituting  $|F_E|^2$  in (2.48) by expression (2.52) results in

$$(\Delta I/I)_{\text{MOD}} \approx \alpha(\mathbf{H}) E \quad (2.54)$$

and therefore, in good approximation the relative variation of the integrated intensity of a reflection should be proportional to  $E$ . This behavior of  $\Delta I/I$  was well confirmed by experimental data, see the measurements of the  $\text{Li}_2\text{SeO}_4 \cdot \text{H}_2\text{O}$  (010) crystal plate  $2, \bar{3}, \bar{1}0$  reflection displayed in Fig. 2.8.

Because of the used four-step modulation-demodulation technique (see next chapter) in an experiment  $\Delta I/I$  is measured simultaneously for each crystal reflection as a function of two opposite directions of an applied electric field:  $\mathbf{E} = \pm E \times \hat{\mathbf{e}}$ . For this reason by verifying the linear requirement (2.54), one can quite easily check the quality of the recorded data, which is another big advantage of the employed high-voltage modulation. In particular, all reflections for that  $\Delta I/I$  did not show a clear linear dependence on  $\mathbf{E}$  were discarded.

In general, in an experiment under an electric field only a limited number of reflections of a crystal exhibit variations in the integrated intensity that are large enough to be measured using the intense synchrotron radiation with a reasonable accuracy within a few hours [52]. Thus, for the first-ever measurements with a new crystal it is absolutely necessary to estimate those reflections that are the most sensitive to the electric-field-induced rearrangement of atoms within the unit cell. As shown by Gorfman *et al.* (2005) [52], such calculations may be done by applying a model of independent atomic vibrations. According to this simplified model, the components,  $\Delta R_{\mu}^i$ , of the displacement vector of

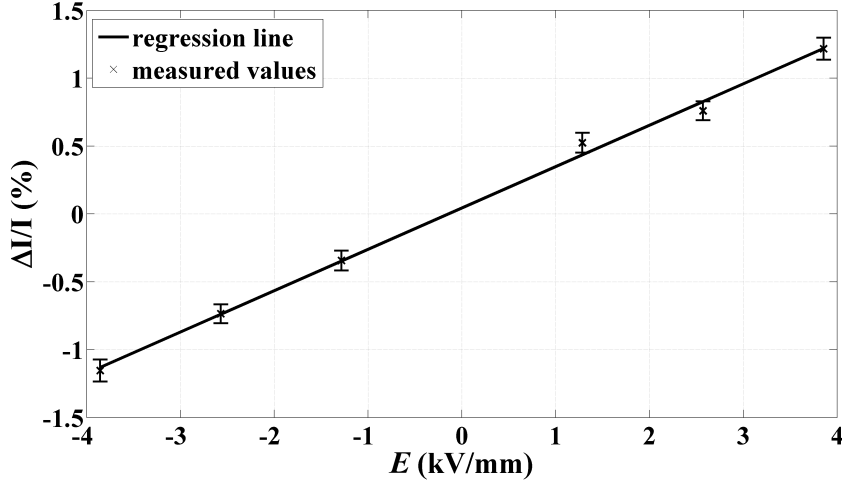


**Figure 2.8:** Relative intensity change,  $\Delta I/I$  [see equation (2.47)], of the  $2\bar{3}10$  reflection of a  $\text{Li}_2\text{SeO}_4 \cdot \text{H}_2\text{O}$  (010) crystal plate measured at  $\lambda = 0.99 \text{ \AA}$  and as a function of the external electric field  $\mathbf{E} = E \times \mathbf{e}_2$ . As shown in this example, within the considered electric field range  $\Delta I/I$  is linear dependent on  $E$ .

an atom  $\mu$  are related to its pseudoatomic charge,  $Q_\mu$ , its thermal displacement tensor,  $[\beta_\mu^{ik}]$ , and the metric tensor coefficients,  $g_{kj} = \mathbf{a}_k \mathbf{a}_j$ , of the crystal lattice by

$$\Delta R_\mu^i = \sum_j \frac{Q_\mu \beta_\mu^{ik} g_{kj}}{2\pi^2 k_B T} E^j, \quad (2.55)$$

where  $T$  denotes the temperature of the crystal and  $k_B$  is the Boltzmann constant.

In order to make use of expression (2.55) for *a priori* estimations of the most promising reflections of the  $\text{Li}_2\text{SO}_4 \cdot \text{H}_2\text{O}$ ,  $\text{Li}_2\text{SeO}_4 \cdot \text{H}_2\text{O}$  and  $\text{BiB}_3\text{O}_6$  crystals, the atomic  $Q$  values were calculated with the program package *WIEN2k* [38]. The tensors components  $\beta^{ik}$  for single atoms were known from previous X-ray structure studies of these crystals [54, 55, 56]. That way, in the case of the  $\text{Li}_2\text{SO}_4 \cdot \text{H}_2\text{O}$  and  $\text{Li}_2\text{SeO}_4 \cdot \text{H}_2\text{O}$  (010) crystal plate during the first beamtime of a week at HASYLAB sufficiently many reflections could be collected to refine on the basis of these experimental data a new better list of reflections. For  $\text{BiB}_3\text{O}_6$  the approach (2.55) has turned out to be less successful, because for this crystal the observed change in the diffraction intensities was normally relatively small, as it will be discussed in section 4.3.2.

The integrated intensity,  $I$ , of a reflection was extracted by adding up all counts recorded at each  $\omega$  angle of a scan:

$$I = N_s = \sum_{\text{steps}} N(\omega). \quad (2.56)$$

Considering that the counting statistics of an X-ray scintillation counter follows the Poisson distribution, the experimental error,  $\sigma$ , of  $I$  amounts to

$$\sigma(I) = \sqrt{I}. \quad (2.57)$$

Using (2.47) together with the approximation  $I_E \approx I_0$  and by taking account of above expression, for the error  $\sigma(\Delta I/I)$  one has:

$$\sigma(\Delta I/I) = \sqrt{\frac{3}{2I_0}}, \quad (2.58)$$

## 2 X-ray diffraction by crystals under an static external electric field

where it was considered that  $I_0$  is measured twice in a four-step field-switching experiment, see chapter 3. Thus,  $\sigma(I_0)$  is equal to

$$\sigma(I_0) = \sqrt{\frac{I_0}{2}}. \quad (2.59)$$

## 3 Description of the field-switching X-ray diffraction experiments

Two different X-ray diffraction experiments, both based on the field-switching technique [15], were performed to probe the response of the  $\text{Li}_2\text{SO}_4\cdot\text{H}_2\text{O}$ ,  $\text{Li}_2\text{SeO}_4\cdot\text{H}_2\text{O}$  and  $\text{BiB}_3\text{O}_6$  crystals to an external electric field. With the first experiment the induced macroscopic and microscopic deformation of the crystals averaged over a period of 11 ms were investigated, while the second experiment allowed for measuring the time evolution of both strains generated by a fast change of an applied electric field on the nanosecond scale.

For the X-ray diffraction investigations of the piezoelectric crystals under an external electric perturbation thin crystal plates were prepared, see for example the  $\text{BiB}_3\text{O}_6$  (010) crystal plate shown in Fig. 3.1. Then each crystal sample had to be fixed with some wax in the groove on top of a Plexiglas slab which in turn was attached to a goniometer head. A homogeneous external electric field normal to the surface of a crystal plate was created by supplying a high voltage (HV) to sputtered thin gold contacts lying exactly in line with each other on opposite faces of the plate.

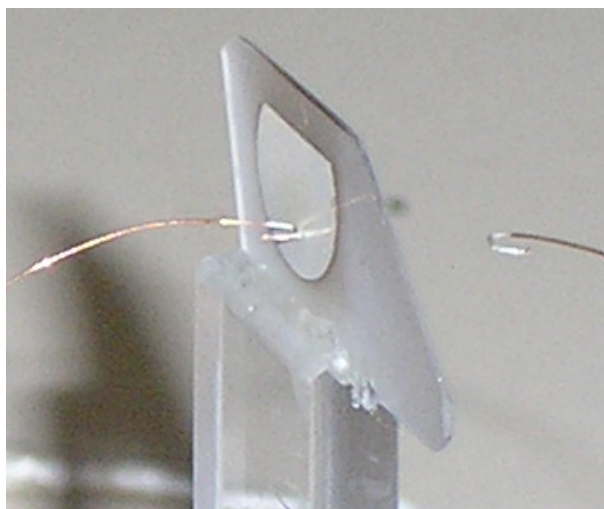


**Figure 3.1:** A  $\text{BiB}_3\text{O}_6$  (010) crystal plate fixed with some wax in the groove on top of a Plexiglas slab which in turn was attached to a goniometer head. In order to apply high voltage to the crystal plate thin gold contacts lying exactly in line with each other were sputtered on opposite faces of the plate.

### 3.1 Setup of the static field-switching experiment

This experiment was performed exclusively with the synchrotron radiation of the HASYLAB bending magnet D3 beamline [48] which is equipped with a HUBER four-circle diffractometer. As an X-ray detector we used a relatively slow open NaI scintillation counter with that in the range where the effect of the counting system dead-time is negligible rates up to  $5 \times 10^4$  counts/s can be counted. Since usually weak reflections are the most sensitive to the internal strain in a crystal, the “slow” X-ray detection system of the beamline did not impair our measurements. At this beamline the wavelength of the

### 3 Description of the field-switching X-ray diffraction experiments

incident X-ray beam can be tuned to a value in the range from 0.3 to 2.3 Å. All rocking curves of reflections were recorded in the  $\omega$  scan mode using the  $\omega$  step width of  $0.001^\circ$ .

The HV applied to crystals was modulated periodically with a frequency of 18 Hz, which equals to a period length of 56 ms, through alternating positive ( $U_+$ ), zero ( $U_0$ ), negative ( $U_- = -U_+$ ), and zero ( $U_0$ ) HV step states, as depicted in Fig. 3.2. In this context, the fast HV modulation employed in an experiment is essential to prevent charge migration in crystals. For instance, after a couple of hours under a constant external electric field both the  $\text{Li}_2\text{SO}_4 \cdot \text{H}_2\text{O}$  and  $\text{Li}_2\text{SeO}_4 \cdot \text{H}_2\text{O}$  (010) crystal plate became conducting, but under an alternating electric field these pyroelectric crystals behaved at room temperature like insulators, which is in agreement with the work [57]. Thus, the response of both crystals to an electric field could be investigated on the atomic scale. In the experiments HV up to  $\pm 3$  kV was applied to crystal samples. Higher HV values were not accessible, as they might destroy the electronics used for switching the HV. The digital pulses of the point detector were distributed continuously over four counting channels that in turn were synchronized with the HV modulation. This so-called modulation-demodulation technique is based on the experimental method introduced for the first time by Puget & Godefroy (1975) [58] and Fujimoto (1978) [7] for the study of the electric-field-induced structural changes in crystals. Besides, because of the time required for charging and especially discharging a crystal plate the first 3 ms of each of the four HV states were excluded from the data collection, see Fig. 3.2. Therefore, the measurements for a single HV state took 11 ms.

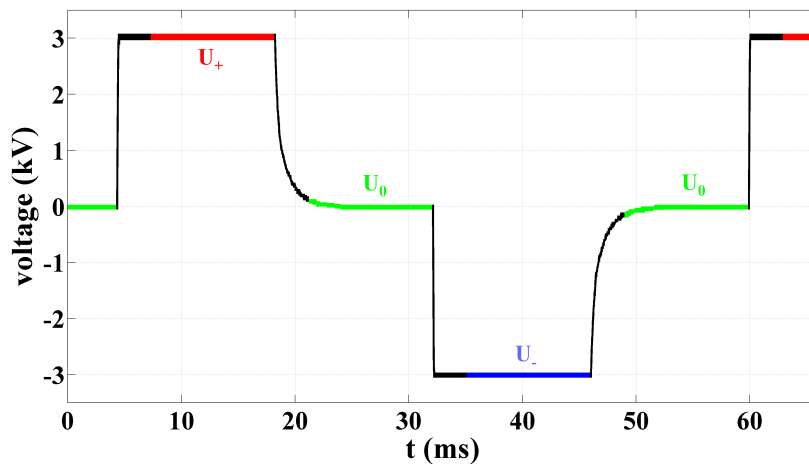


**Figure 3.2:** Schematic view of the used four-step modulation of the HV consisting of successive  $U_+$ ,  $U_0$ ,  $U_- = -U_+$  and  $U_0$  step states applied periodically to a crystal plate. The HV modulated that way was employed for the quasi-simultaneous measurements of reflection profiles as a function of  $U_+$ ,  $U_0$  and  $U_-$ . As shown, the time needed for charging and especially discharging a crystal plate is excluded from the data collection.

The measurement period chosen for each angular step of an  $\omega$  scan determines the number of repetitions of the basic HV period. Since the diffraction intensity was collected for each  $\omega$  position over more than 100 HV cycles, the experimental data was not affected by short-term oscillations of the intensity of the incident X-ray beam. That way, the rocking curves of a reflection could be measured quasi-simultaneously for each of the three different electric field states, as illustrated in Fig. 3.3. Consequently, very small relative changes in the diffraction intensity,  $\Delta I/I < 1\%$ , became measurable. Furthermore, particularly for the weakest reflections the profiles had to be remeasured in the

worst case more than 20 and 30 times until reasonable counting statistics was achieved. An experimental procedure that makes this experiment even at the synchrotron beamlines very time consuming, as normally at least 30 – 50 reflections of a crystal showing a significantly large effect in  $\Delta I/I$  have to be collected for a reliable refinement of the induced atomic displacements in the crystal.

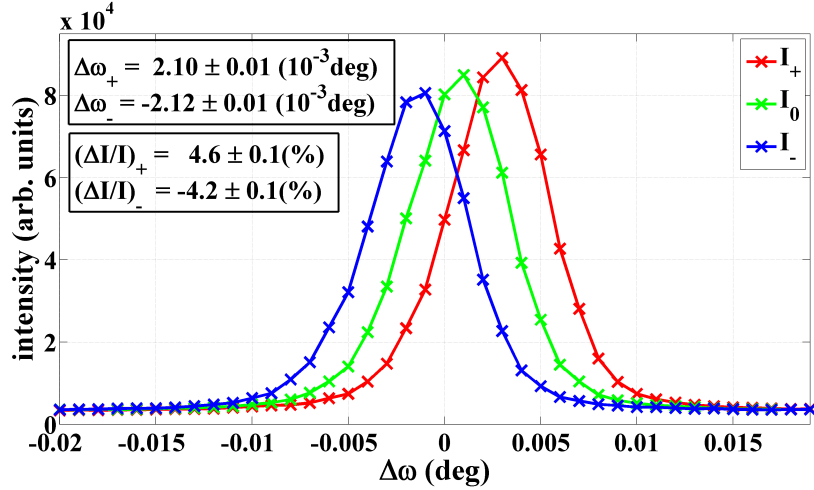


**Figure 3.3:** Three rocking curves,  $I_+$ ,  $I_0 = \langle I_{0+}, I_{0-} \rangle$  and  $I_-$ , of the  $\text{Li}_2\text{SO}_4 \cdot \text{H}_2\text{O}$  (010) crystal plate 0,1,12 reflection measured simultaneously in the  $\omega$  scan mode using the four-step field-switching technique, as shown in Fig. 3.2. The reflection profiles correspond to the  $U_+$ ,  $U_0$  and  $U_-$  HV states,  $|U_{\pm}| = 3$  kV, which result in  $E = 5.1$  kV  $\text{mm}^{-1}$  applied to the crystal.

For further data analysis both rocking curves  $I_{0+}$  and  $I_{0-}$  corresponding to the zero HV states were averaged to a single curve  $I_0 = \langle I_{0+}, I_{0-} \rangle$ . In addition, the observed angular shifts and relative intensity variations of reflections were normalized to the values referred to the positive direction ( $\mathbf{E}_+ = E \times \hat{\mathbf{e}}$ ), with respect to the crystal Cartesian system, of an applied electric field:

$$\Delta\omega_a = \langle \Delta\omega_{E_+}, -\Delta\omega_{E_-} \rangle, \quad (3.1)$$

$$(\Delta I/I)_a = \langle (\Delta I/I)_{E_+}, -(\Delta I/I)_{E_-} \rangle. \quad (3.2)$$

Finally, from the  $\Delta\omega_a$  and  $(\Delta I/I)_a$  data the piezoelectric constants of a crystal and the displacements of atoms were refined, respectively (see chapter 4).

## 3.2 Setup of the time-resolved experiment

This experiment was conducted at the Swiss-Norwegian beamline (BM01A) of ESRF. At this beamline a KUMA six-circle diffractometer, an area ONYX detector and a scintillation counter are available. The CCD operation mode was used exclusively for the determination of the crystal orientation, whereas all measurements of reflection profiles were performed with the point detector. Additional measurements were carried out in the home X-ray laboratory employing high-resolution diffraction.

A data acquisition (DAQ) system based on a commercial Xilinx Virtex-4 FPGA (Field Programmable Gate Array) board, which uses the ML405 evaluation platform [59], was developed for the realization of the time-resolved X-ray measurements. This board is equipped with a 100 MHz clock oscillator resulting in a single tact period of 10 ns. With

### 3 Description of the field-switching X-ray diffraction experiments

this technique the following experimental requirements can be met: Firstly, it becomes possible to adjust in an easy and flexible way the time resolution of an experiment to any value in a broad time range only having 20 ns as bottom limit. Secondly, the FPGA board enables us to process the incoming detector signals with respect to the time structure and periodicity of the external perturbation applied to a crystal. Finally, compared to the pump-probe experiments [60] we do not have to exploit the time structure of the synchrotron radiation in order to reach a time resolution of 20 ns, we can do it in an intrinsic way. All this makes our measurements, which we can run for days to collect higher counting statistics, much faster.

Based on the software code written by Marc von Kozierowski within the scope of his bachelor thesis, I implemented the control of an on-board SRAM (Static Random-Access Memory) by the FPGA chip, see an extract of the relevant source code attached in the appendix. Besides, by optimizing the internal processes running on the FPGA I could increase the accessible time resolution of the DAQ system from 20  $\mu$ s to 20 ns.

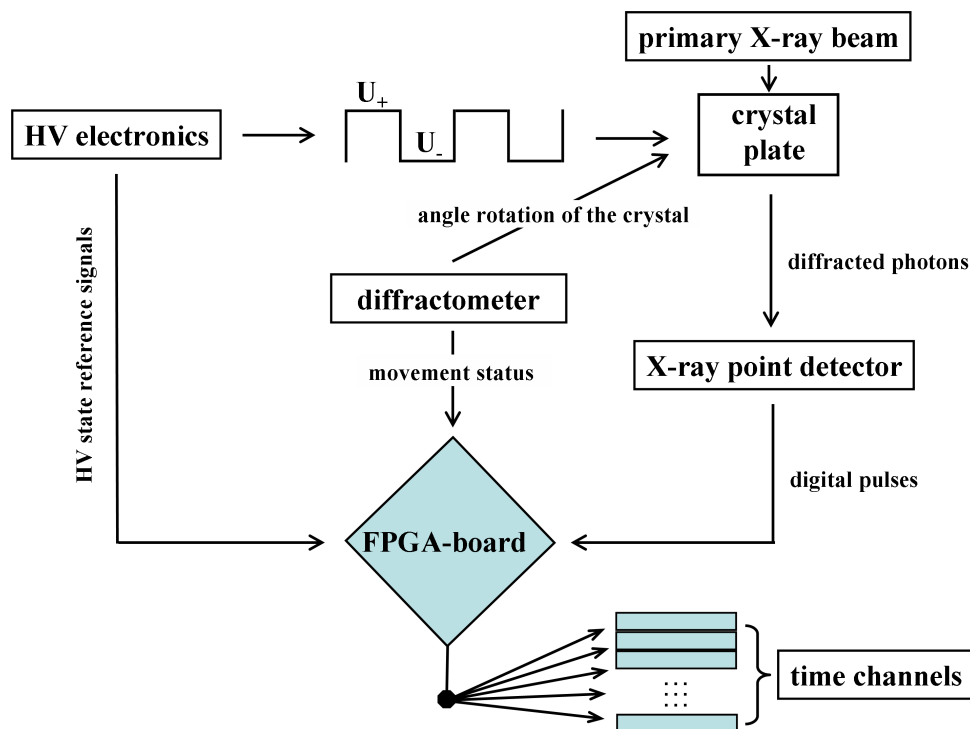


**Figure 3.4:** Flow chart of the data acquisition system developed for the time-resolved X-ray diffraction studies of the response of a piezoelectric crystal to a fast periodic change of an applied external electric field.

The time resolution of an experiment is defined by a fixed number of FPGA clock cycles. To synchronize the DAQ system with the time structure of the HV applied periodically to a crystal, digital signals modulated according to the respective active HV state are generated. These signals are routed directly to the FPGA board, as depicted on the flow chart in Fig. 3.4. The rising edge of the positive voltage (see Fig. 3.5) is used to trigger the starting point of the fragmentation of the HV cycles into well-defined consecutive time intervals. Employing a memory device, such as SRAM, to each of the time intervals one single counter can be assigned in that the number of all pulses of an X-ray point detector fed into the FPGA board in the respective time window is stored. Due to the periodicity of the HV, it is only necessary to initiate the counters for the first HV cycle, so that for the next cycles one has just to increment their values.

In particular, because of the read and write timing of the synchronous pipelined on-board SRAM in total 7 clock cycles are required to control a single write operation followed by a read operation. A procedure that limits the smallest time resolution of this DAQ system to 70 ns. At the same time the SRAM, having in total 18 address pins, can be used as a counter with possible  $2^{18}$  channels of that each one has a memory width of 4 byte. The digital clock manager of the Xilinx ISE software [59] provides a simply tool to generate several output clocks that have specific phase shifts (the phase of the SRAM clock has to be shifted relative to that of the FPGA clock) and frequencies. But due to the available speed grade of the SRAM, it does not run with a double frequency of 200 MHz. In this mode the small memory of the FPGA chip with a depth of 14 bit and a width of 2 byte can be addressed only, however in this manner a time resolution of 20 ns can be reached. Concerning a fast X-ray detector, such as avalanche photo-diode (APD) [61] (that can be adjusted to produce pulse widths of 30, 20, 10 and 5 ns), the clock frequency of a FPGA is the crucial limiting parameter. With a 100 MHz clock pulses with a width of 20 ns can be processed only. This limitation strongly affects the dead time of an APD and thus, the saturation threshold of this detector decreases.

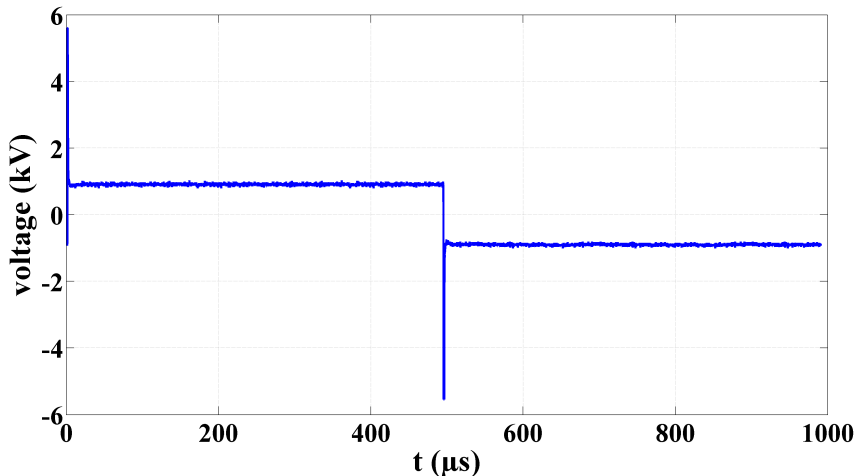


**Figure 3.5:** Representation of the 2-step modulated HV ( $U_{\pm} = \pm 1$  kV) applied periodically to single crystal plates. In this example the HV frequency amounts to 1 kHz and the switching time between  $U_{\pm}$  and  $U_{\mp}$  equals nearly to 200 ns. The HV spikes of the magnitudes up to  $\pm 6$  kV arise from the fast HV switching process.

In order to accomplish fast periodic back and forth switching of the HV special electronics was developed by the electronic workshop of the University of Siegen. In detail, the HV electronics is based on two cascades of high voltage MOSFETs which are potential-separately gated. Both cascades are interconnected to a half bridge, that way using two HV power supplies positive and negative HV up to  $\pm 3$  kV can be switched within a few 10 ns. Optionally, by adding further cascades it becomes possible to realize zero HV states, so that the two-step modulation of the HV can be easily changed to the four-step mode, see Fig. 3.2 in section 3.1. In an experiment the HV is switched from  $U_{+}$  to  $U_{-} = -U_{+}$  and from  $U_{-}$  to  $U_{+}$  within a period of about 200 ns, respectively. As illustrated in Fig. 3.5, the short and high HV spikes of the magnitudes up to  $\pm 6$  kV that accompany the HV jumps could not be suppressed. But owing to the  $RC$  time constant of the sample capacitor, the HV spikes do not reach the crystals and therefore are not reproduced by the experimental data, see Figs. 3.6 and 3.7. Concerning the HV frequency, which is set with an external digital pulse generator, charging and discharging current has to be taken into

### 3 Description of the field-switching X-ray diffraction experiments

account. For the system introduced the highest possible current through the electronic devices is limited to 2 mA, a value that for instance in the case of  $U_{\pm} = \pm 1.5$  kV results in the upper HV frequency of 1.5 kHz.

Furthermore, in order to perform for each angle of an  $\omega$  step scan independent time-resolved measurements, additional feedback signals containing the information about the movement status of the crystal referred to the  $\omega$  angle rotation of the diffractometer are needed. It has to be ensured that a DAQ run is started only if the diffractometer, thus the crystal, is in a non-moving state. In this context, the big advantage of a programmable FPGA chip becomes really visible in its function as the main interface where the reference signals about the active HV state at the crystal and the diffractometer movement status are analyzed synchronously in terms of the processing of the incoming detector pulses, as demonstrated in Fig. 3.4.

The data processing described in this section was realized by transforming a VHDL (Very High Speed Integrated Circuit Hardware Description Language) software code to integrated circuits on the FPGA chip. A serial interface was implemented for the communication between the FPGA board and a control computer that was used to transmit the individual parameters of an experiment to the FPGA chip and to control the data readout process.

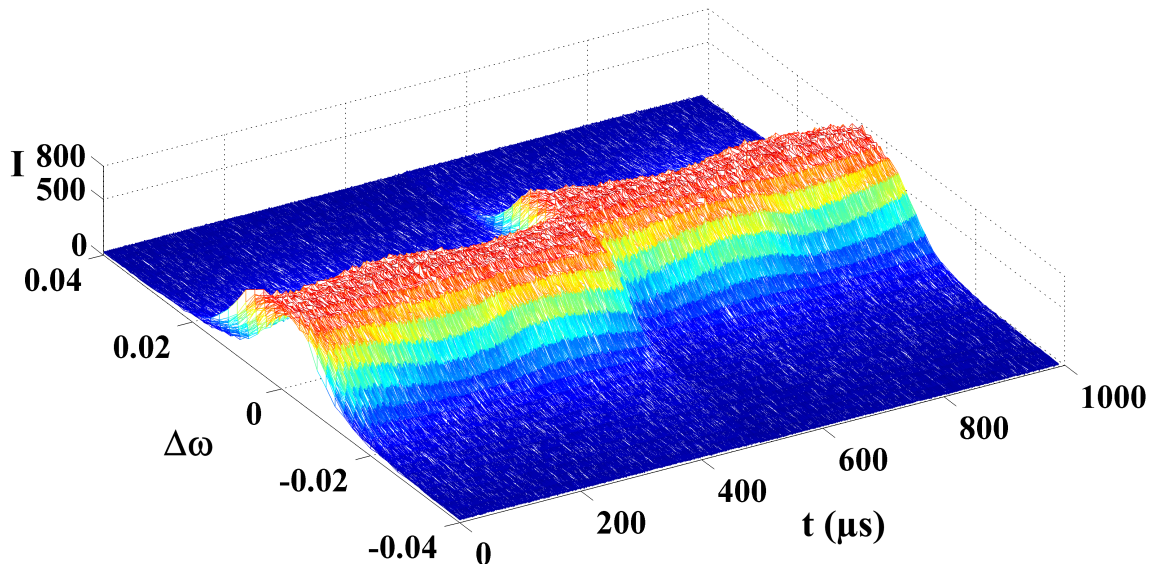


**Figure 3.6:** Representation of the time-resolved measurements of the  $\text{BiB}_3\text{O}_6$  (010) crystal plate 392 reflection. The diffraction intensity was recorded with a time resolution of 100 ns. These raw data correspond to the applied HV basic period displayed in Fig. 3.5.

In Fig. 3.6 the raw data of the time-resolved scanning of the diffraction intensity of the  $\text{BiB}_3\text{O}_6$  (010) crystal plate 392 reflection within the two-step modulated basic HV period (see Fig. 3.5) applied to the crystal are shown. These measurements were carried out with a time resolution of 100 ns, were repeated 5 times to increase the counting statistics of the data and then merged together. The width of the  $\omega$  steps was fixed to  $2 \times 10^{-3}^\circ$ . First of all, the pronounced discontinuity of the angular peak position of the 392 reflection approximately at  $500 \mu\text{s}$  within the basic HV period strikes the eyes. An accurate analysis of the time evolution of  $\Delta\omega$  is displayed in Fig. 3.7. The distinctive behavior of the function  $\Delta\omega(t)$  (jumps at 0 and  $496 \mu\text{s}$ ) exactly reflects the fast  $U_- - U_+$  and  $U_+ - U_-$  changes within the HV period. In addition, both HV jumps have induced the

same dynamic response of the crystal plate comprising at least two different superimposed oscillations of the Bragg peak position. In summary, the measurements of the  $\text{BiB}_3\text{O}_6$  392 reflection present a good example of the capability of the introduced experimental technique for probing the electric-field-induced dynamic processes in piezoelectric crystals.

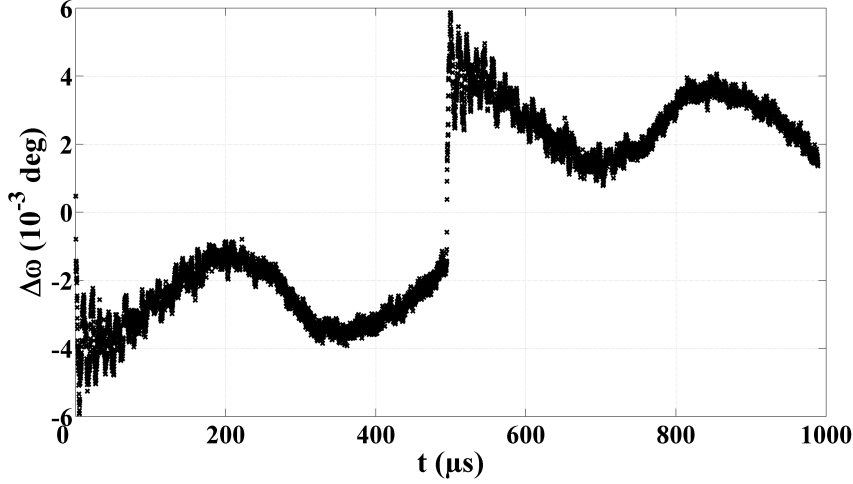


**Figure 3.7:** Angular shift,  $\Delta\omega$ , of the Bragg peak position of the  $\text{BiB}_3\text{O}_6$  (010) crystal plate 392 reflection as a function of the time within the two-step modulated basic HV period, see Fig. 3.5. The function  $\Delta\omega(t)$  was extracted from the raw data shown in Fig. 3.6.

### 3.2.1 Physical origin of the Bragg peak oscillations

In general, a periodic square function,  $f(t)$ , with  $f(t) = -f(t + \pi)$  and  $f(0) = 0$  can be represented by a Fourier series of the form

$$f(t) = \sum_{k=1}^{\infty} \frac{4}{(2k-1)\pi} \sin[(2k-1)t] \quad (3.3)$$

containing an infinite number of increasing frequencies,  $\nu = (2k-1)/2\pi$  ( $k = 1, 2, 3, \dots$ ). Because of that, the used fast-modulated periodic HV (see Fig. 3.5) is describable by equation (3.3) applying an appropriate normalization so that it becomes apparent that the employed time-resolved experiment can be compared with the method of the resonant ultrasound spectroscopy (RUS) [62, 63]. In this method a crystal of well-defined shape is held almost freely between two piezoelectric transducers. One of the transducer acts as a generator of an elastic wave of constant amplitude but of varying frequencies in the specimen, while the another one serves as a detector of the induced mechanical resonances [62]. From the measured spectrum of resonance frequencies all elastic and piezoelectric constants of the sample can be deduced simultaneously [64]. In contrast to the RUS technique, because the different HV states are changed fast within a basic HV period, we generate an ultrasound signal consisting of a huge variety of discrete frequencies that are applied to a crystal. For instance, in Fig. 3.8 the function  $f(t)$  (3.3) is plotted for  $k \leq 10$ . Accordingly, it is easily conceivable that in the large pool of the frequencies there are some that are close to the resonance frequencies of the crystal and thus, different vibrational modes of the sample may be excited in the experiment. If this assumption is true, then the induced vibrations of a crystal should be strongly dependent on the one hand on the used modulation frequency of the external HV and on the other hand on the switching

### 3 Description of the field-switching X-ray diffraction experiments

time between single HV states.

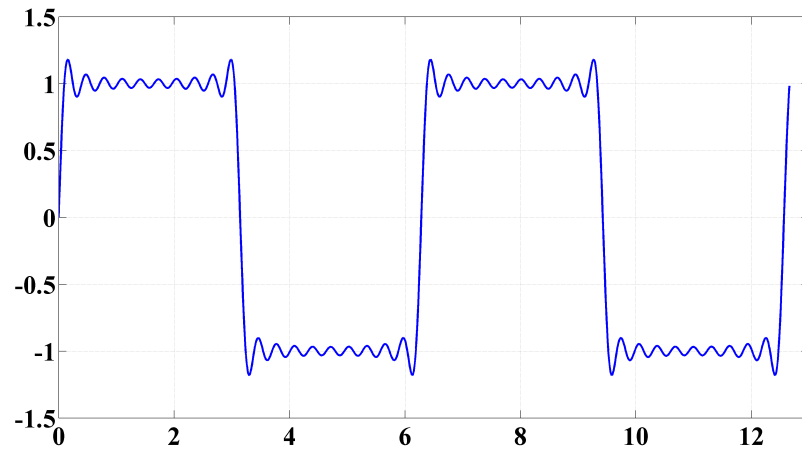


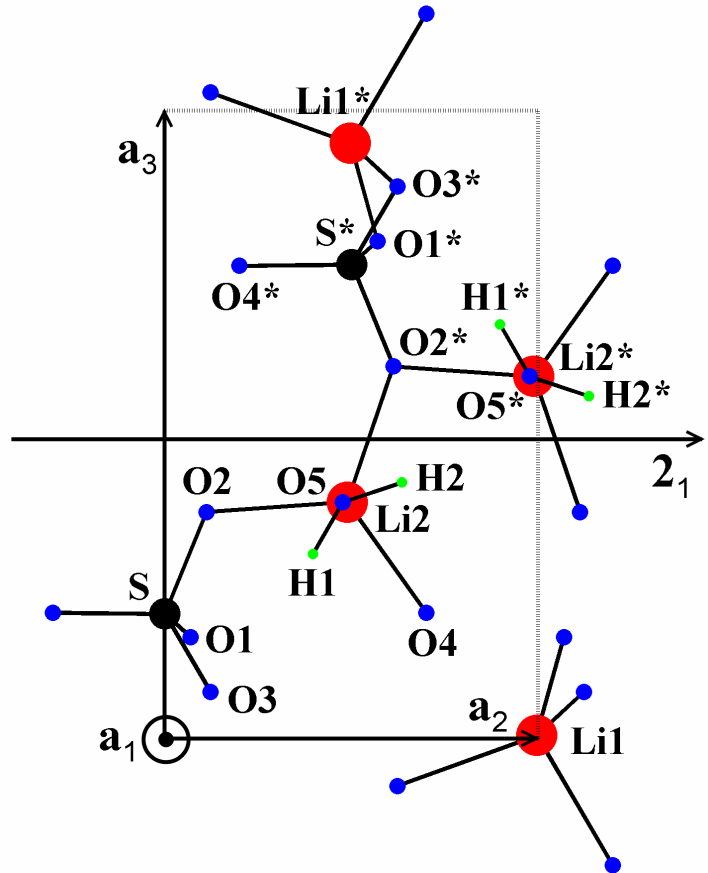
**Figure 3.8:** Graphical representation of the Fourier series (3.3) for  $k \leq 10$ .

# 4 Electric-field-induced response of $\text{Li}_2\text{SO}_4 \cdot \text{H}_2\text{O}$ , $\text{Li}_2\text{SeO}_4 \cdot \text{H}_2\text{O}$ and $\text{BiB}_3\text{O}_6$ single crystals

## 4.1 Lithium sulfate monohydrate, $\text{Li}_2\text{SO}_4 \cdot \text{H}_2\text{O}$

$\text{Li}_2\text{SO}_4 \cdot \text{H}_2\text{O}$  crystallizes in the space group  $P2_1$  [unit-cell parameters are:  $a_1 = 5.4553(1) \text{ \AA}$ ,  $a_2 = 4.8690(1) \text{ \AA}$ ,  $a_3 = 8.1761(1) \text{ \AA}$  and  $\alpha_2 = 107.337(2)^\circ$  (Karppinen *et al.*, 1986 [65])]. The asymmetric part of the unit cell consists of ten atoms: two Li atoms (Li1, Li2), one S atom (S), five O atoms (O1 to O5) and two H atoms (H1, H2). Each atom occupies a general (2a) position. The crystal structure is formed by  $\text{Li1O}_4$ ,  $\text{Li2O}_4 \equiv \text{Li2O}_3(\text{H}_2\text{O})$  and  $\text{SO}_4$  groups that are linked together by oxygen atoms to a three-dimensional tetrahedral framework, as shown in Fig. 4.1. All three structural units are basically regular tetrahedra that are only slightly distorted (see Table 4.1).

**Figure 4.1:** Arrangement of the  $\text{Li1O}_4$ ,  $\text{Li2O}_3(\text{H}_2\text{O})$  and  $\text{SO}_4$  tetrahedra in the  $\text{Li}_2\text{SO}_4 \cdot \text{H}_2\text{O}$  crystal structure viewed along the  $[100]$  crystallographic direction. The symmetry operation  $[-x, y + 1/2, -z]$  relates atoms with their symmetry equivalents, which are marked by stars. In addition, the direction of the two-fold screw axis parallel to  $[010]$ , the monoclinic basis vectors and the corresponding unit cell are shown.



The piezoelectric  $\text{Li}_2\text{SO}_4 \cdot \text{H}_2\text{O}$  is a polar crystal with interesting physical properties. It has the highest pyroelectric coefficient of all non-ferroelectric crystals ( $p_2 = 87(2) \times 10^{-6}$

$\text{C m}^{-2} \text{ K}^{-1}$  [57]). The highest piezoelectric constant of  $\text{Li}_2\text{SO}_4\cdot\text{H}_2\text{O}$  is the longitudinal component ( $d_{222} = 15.8(5) \text{ pC N}^{-1}$  [66]) which is about seven times larger than that of  $\alpha$ -quartz ( $d_{111} = 2.3 \text{ pC N}^{-1}$  [67]). Another reason why this crystal was chosen for the present studies is the availability of large single crystals of excellent quality grown from water solution [68].

**Table 4.1:** Selected geometric parameters of the tetrahedral structural units,  $\text{Li}_1\text{O}_4$ ,  $\text{Li}_2\text{O}_4$  and  $\text{SO}_4$ , of  $\text{Li}_2\text{SO}_4\cdot\text{H}_2\text{O}$ . The bond lengths ( $\mu - \text{O}$ ) and angles [ $\angle(\text{O} - \mu - \text{O})$ ] were calculated with respect to the cations  $\mu = \{\text{Li1, Li2, S}\}$  and  $\mathbf{D}_{\text{tetr}}$  is defined by (4.1).

Tetrahedron	$\langle\mu - \text{O}\rangle$ ( $\text{\AA}$ )	$\langle\angle(\text{O} - \mu - \text{O})\rangle$ ( $^\circ$ )	$ \mathbf{D}_{\text{tetr}} $ ( $\text{\AA}$ )
$\text{Li}_1\text{O}_4$	1.96 (4)	109.2 (71)	0.158 (2)
$\text{Li}_2\text{O}_4$	1.93 (3)	109.4 (42)	0.084 (2)
$\text{SO}_4$	1.47 (1)	109.5 (5)	0.014 (2)

The absolute value of the vector

$$\mathbf{D}_{\text{tetr}} = \frac{1}{4} \sum_{i=1}^4 \mathbf{R}(\text{O}_i) - \mathbf{R}(\mu) \quad (4.1)$$

characterizing the degree of the deformation of a tetrahedron is small for each of the three  $\text{Li}_1\text{O}_4$ ,  $\text{Li}_2\text{O}_4$  and  $\text{SO}_4$  groups, as given in Table 4.1.

#### 4.1.1 Multipole-model refinement of the electron density and properties of the chemical bonds

The experimental ED distribution in  $\text{Li}_2\text{SO}_4\cdot\text{H}_2\text{O}$  is required for the evaluation of the chemical-bond properties. The crystal structure and thermal parameters of  $\text{Li}_2\text{SO}_4\cdot\text{H}_2\text{O}$  have been reported in the works [54, 69, 70]. Although the ED in  $\text{Li}_2\text{SO}_4\cdot\text{H}_2\text{O}$  has already been studied by [65], no quantitative analysis of the particular properties of the Li–O and S–O chemical bonds has been made by means of modern tools, such as Bader topological analysis (see section 2.2).

For the ED determination a spherical sample with a radius of 0.12 (1) mm was prepared. The X-ray diffraction measurements were collected using an Enraf-Nonius CAD-4 diffractometer and Mo  $K\alpha$  radiation. The sample was cooled to a temperature of 90 (5) K by a  $\text{N}_2$  jet. The intensities of Bragg reflections were recorded with a point detector in an  $\omega$ - $2\theta$  scan mode. The measurement period for each rocking curve was individually adjusted to ensure that the uncertainty in the intensities was less than 1.0%. However, for weak reflections the period was restricted to 10 min. In total, over about three weeks 7853 reflections up to  $\sin \theta/\lambda = 1.2 \text{ \AA}^{-1}$  fulfilling the condition  $I(\mathbf{H}) > 3\sigma(I)$  were collected, as displayed in Table 4.2. Using the software *Jana2000* [71], the data were corrected for the decay, Lorentz-polarization and absorption effects, then the intensities of symmetry-equivalent reflections were merged and finally submitted to the refinement program *MOLLYN* [72]. For evaluating the quality of the data recorded the quantity  $R_{\text{sym}}$  defined according to [73] as

$$R_{\text{sym}} = \frac{\sum_i \sum_j^{n_i} |\bar{I}_i - I_j|}{\sum_i \sum_j^{n_i} I_j} \quad \text{with } \bar{I}_i = \frac{1}{n_i} \sum_j^{n_i} I_j \quad (4.2)$$

**Table 4.2:** Data collection and multipole refinement of the ED in  $\text{Li}_2\text{SO}_4\cdot\text{H}_2\text{O}$ .

Experimental parameters	
Radiation type	Mo $K\alpha$
Detection type	Point detector
Temperature (K)	90 (5)
Radius of crystal sphere (mm)	0.12 (1)
$\mu$ ( $\text{mm}^{-1}$ )	0.68 (1)
Recorded data	
$(\sin \theta/\lambda)_{\max}$ ( $\text{\AA}^{-1}$ )	1.2
Observed/unique reflections	7853/3930
Redundancy	2
$R_{\text{sym}}(I)$ [73]	0.014
Multipole refinement	
Number of ED parameters	48
Omitted reflections	65
$R_{\text{IAM}}(F)$	0.0150
$R(F)/R_w(F)$ [eqs. (2.50)/(2.51)]	0.0143/0.0179
Goodness of fit	5.18

**Table 4.3:** Refined atomic positions of  $\text{Li}_2\text{SO}_4\cdot\text{H}_2\text{O}$  at 90 (5) K. The unit-cell parameters are:  $a_1 = 5.4484(2)$   $\text{\AA}$ ,  $a_2 = 4.8339(2)$   $\text{\AA}$ ,  $a_3 = 8.1407(2)$   $\text{\AA}$  and  $\alpha_2 = 107.191(2)^\circ$ .

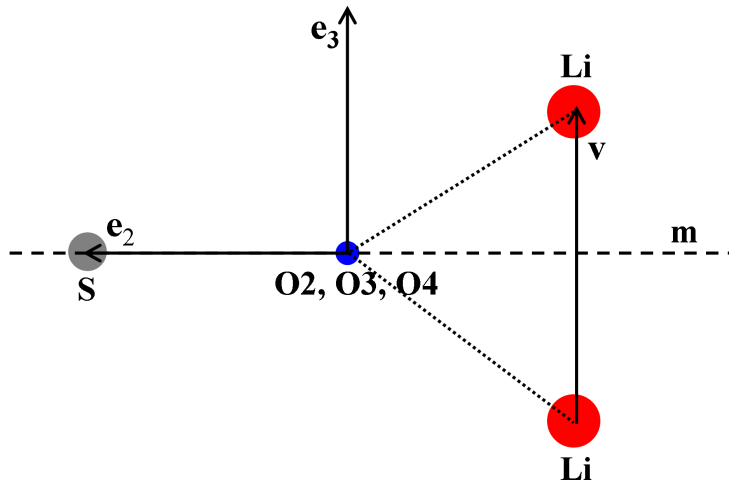
	$x$	$y$	$z$
S	0.29250 (1)	0	0.20806 (1)
Li1	0.30339 (16)	0.49641 (24)	0.99293 (11)
Li2	0.56016 (17)	0.48877 (24)	0.39517 (11)
O1	0.02096 (6)	0.07358 (8)	0.17099 (5)
O2	0.43702 (6)	0.11091 (6)	0.37855 (4)
O3	0.39822 (6)	0.12064 (6)	0.07650 (4)
O4	0.32514 (6)	-0.30371 (6)	0.20988 (4)
O5	0.91357 (8)	0.46525 (8)	0.40340 (6)
H1	0.9627 (44)	0.4006 (57)	0.3268 (30)
H2	0.9961 (48)	0.6032 (57)	0.4377 (31)

was considered. Here the summation  $i$  is over all symmetry-independent reflections and the index  $j$  runs over all to the  $i$ -th reflection symmetry-equivalent reflections.  $\bar{I}_i$  stands for the intensity of a reflection  $i$  averaged over the symmetry-related intensities and  $n_i$  denotes the number of reflections in a symmetry-equivalent group (multiplicity of the  $i$ -th reflection). Thus,  $R_{\text{sym}}$  is dependent on the redundancy of an X-ray diffraction data set. In the case of the measurements carried out the small value of  $R_{\text{sym}} = 1.4\%$ , which is distinctly smaller than 5%, indicates a good data quality, as reported in [73].

The initial values of the atomic positions and atomic displacement parameters (ADPs), the ADPs of the H atoms were fixed at their 80 K neutron-diffraction values [54], were taken from [65] and were further refined without any constraints, see the results presented in Tables 4.3 and 4.4. The primary and secondary extinction were refined in the isotropic

**Table 4.4:** Anisotropic thermal parameters ( $10^{-5} \text{ \AA}^2$ ) of  $\text{Li}_2\text{SO}_4\cdot\text{H}_2\text{O}$  at 90 (5) K. Stars denote neutron values that were taken from [54] and not refined.

	$U_{11}$	$U_{22}$	$U_{33}$	$U_{12}$	$U_{13}$	$U_{23}$
S	396 (2)	293 (2)	316 (1)	20 (3)	114 (2)	8 (2)
Li1	883 (19)	834 (22)	831 (8)	60 (48)	287 (20)	129 (34)
Li2	875 (19)	825 (25)	824 (8)	40 (45)	196 (20)	55 (30)
O1	404 (7)	944 (9)	746 (3)	117 (13)	110 (8)	-109 (9)
O2	756 (6)	560 (6)	415 (2)	-1232 (10)	33 (6)	-78 (7)
O3	863 (6)	590 (6)	636 (3)	109 (12)	462 (7)	178 (7)
O4	968 (7)	306 (6)	598 (3)	49 (10)	173 (7)	17 (6)
O5	862 (9)	1230 (12)	1352 (4)	-78 (14)	545 (9)	-228 (11)
H1*	2917 (38)	4547 (64)	2474 (34)	381 (41)	1481 (31)	-648 (40)
H2*	2727 (37)	2459 (47)	4090 (45)	-1091 (37)	944 (33)	-593 (40)

**Figure 4.2:** Next-neighbor coordination of the atoms O2, O3 and O4 in the  $\text{Li}_2\text{SO}_4\cdot\text{H}_2\text{O}$  structure and the choice of their respective local Cartesian coordinate system,  $\{\mathbf{e}_i\}$ . The axis  $\mathbf{e}_2$  is directed from an O to the corresponding S atom. The axis  $\mathbf{e}_3$  lies in the  $\mathbf{e}_2-\mathbf{v}$  plane ( $\mathbf{v}$  is a vector between the Li atoms) and defines the normal to the local non-crystallographic mirror plane. For the O2, O3 and O4 atom the angle between  $\mathbf{v}$  and  $\mathbf{e}_3$  is less than  $5^\circ$ .

approximation according to Becker & Coppens (1974) [27]. In total, 65 outlier reflections, those having  $|I_{\text{OBS}} - I_{\text{MOD}}|/\sigma(I_{\text{OBS}}) > 10$  and heavily affected by extinction [with an extinction factor  $y < 0.85$ , see equation (2.8)], were omitted from the data set. Using the scattering factors for isolated (non-bonded) atoms within the unit cell, the refinement of the structural parameters resulted in the reliability factor  $R_{\text{IAM}} = 1.50\%$ . The quantity “goodness of fit“ introduced in Table 4.2 is given by [72]

$$S = \sqrt{\frac{\sum_i w_i |F_{i\text{OBS}} - F_{i\text{MOD}}|^2}{n - p}} \quad \text{with } w_i = \frac{1}{\sigma^2(F_{i\text{OBS}})}, \quad (4.3)$$

where  $n$  is the number of used independent reflections ( $n = 3865$ ) and  $p$  is the number of parameters varied independently in the performed refinement of the aspherical-atom model ( $p = 127$ ). Since the value of  $S$  is with  $S = 5.18$  small enough, the model considered can be regarded as adequate for the description of the ED distribution in  $\text{Li}_2\text{SO}_4\cdot\text{H}_2\text{O}$ .

**Table 4.5:** Summary of all refined atomic population coefficients ( $P_{\text{val}}$ ,  $P_{lm}$ ) and radial parameters ( $\kappa'$ ,  $\kappa''$ ) together with the  $n_l$  and  $\zeta_l$  values used in the radial functions  $R_l$ , see eq. (2.10). The atomic  $P_{lm}$  marked by “\*\*” were not considered in the refinement of the ED distribution in  $\text{Li}_2\text{SO}_4 \cdot \text{H}_2\text{O}$  and those marked by “-” are forbidden according to the applied local symmetry operations. The corresponding structure factor file is deposited with the published article.

	S	Li1/Li2	O1	O2, O3, O4	O5	H1/H2
$P_{\text{val}}$	5.2 (2)	1.1 (1)	6.11 (6)	6.07 (6)	6.22 (7)	1.06 (4)
$P_{00}$	**	**	**	**	**	-
$P_{11}$	-	-	0.003 (20)	-0.003 (9)	0.02 (2)	-
$P_{1-1}$	-	-	0.06 (2)	-0.09 (2)	0.11 (2)	-
$P_{10}$	-	-	-0.08 (2)	-	-	-
$P_{20}$	-	-	-0.04 (2)	0.07 (2)	-0.09 (2)	-
$P_{21}$	-	-	0.01 (2)	-	-	-
$P_{2-1}$	-	-	0.01 (2)	-	-	-
$P_{22}$	-	-	-0.06 (2)	0.06 (1)	-0.05 (2)	-
$P_{2-2}$	-	-	-0.04 (2)	-0.03 (1)	-0.03 (2)	-
$P_{30}$	-	-	0.04 (2)	-	-	-
$P_{31}$	-	-	-0.01 (2)	-0.001 (11)	-0.11 (2)	-
$P_{3-1}$	-	-	0.001 (20)	-0.001 (11)	-0.11 (2)	-
$P_{32}$	-	-	0.01 (2)	-	-	-
$P_{3-2}$	-0.73 (6)	-0.11 (8)	-0.02 (2)	-	-	-
$P_{33}$	-	-	0.002 (20)	0.01 (1)	0.02 (2)	-
$P_{3-3}$	-	-	-0.02 (2)	-0.03 (1)	0.01 (2)	-
$P_{40}$	-0.34 (5)	-0.10 (8)	**	**	**	-
$P_{41}$	-	-	**	-	-	-
$P_{4-1}$	-	-	**	-	-	-
$P_{42}$	-	-	**	**	**	-
$P_{4-2}$	-	-	**	**	**	-
$P_{43}$	-	-	**	-	-	-
$P_{4-3}$	-	-	**	-	-	-
$P_{44}$	-0.25 (4)	-0.07 (7)	**	**	**	-
$P_{4-4}$	-	-	**	**	**	-
$\kappa'$	0.972 (8)	0.81 (9)	0.995 (3)	0.995 (3)	0.995 (3)	1.00
$\kappa''$	1.14 (3)	1.00	0.89 (5)	0.89 (5)	0.89 (5)	1.00
$n_0/\zeta_0$	4/3.851	2/1.279	2/4.466	2/4.466	2/4.466	0/0
$n_1/\zeta_1$	4/3.851	2/1.279	2/4.466	2/4.466	2/4.466	0/0
$n_2/\zeta_2$	4/3.851	2/1.279	2/4.466	2/4.466	2/4.466	0/0
$n_3/\zeta_3$	6/3.851	3/1.279	4/4.466	4/4.466	4/4.466	0/0
$n_4/\zeta_4$	8/3.851	4/1.279	4/4.466	4/4.466	4/4.466	0/0

In order to reduce the number of ED parameters, for the position of the Li1, Li2, S, O2, O3, O4 and O5 atom non-crystallographic local symmetry elements were included. In particular, since the S atom and both Li atoms occupy positions in the center of slightly distorted oxygen tetrahedra, only the multipoles allowed by the tetrahedral symmetry  $\bar{4}3m$  ( $P_{3-2}$  and  $P_{40} = 1.36 \times P_{44}$  [22]) were taken into account for these three atoms. Furthermore, for Li1 and Li2 equal multipole populations and contraction coefficients were used, but the refinement of  $\kappa''$  did not result in convergence, see Table 4.5. As

the O atoms O2, O3 and O4 are almost equally coordinated by one S atom and two Li atoms, they may be constrained to be chemically equivalent. Therefore, for these atoms one and the same set of multipole population coefficients was refined and only those ( $P_{11}$ ,  $P_{1-1}$ ,  $P_{20}$ ,  $P_{22}$ ,  $P_{2-2}$ ,  $P_{31}$ ,  $P_{3-1}$ ,  $P_{33}$  and  $P_{3-3}$  [22]) that are allowed under the local non-crystallographic mirror plane introduced in Fig. 4.2. The local Cartesian coordinate systems of the O2, O3 and O4 atoms were chosen in such a way that the  $Y$  axis ( $\mathbf{e}_2$ ) points from the respective O atom towards the corresponding S atom. The  $Z$  axis ( $\mathbf{e}_3$ ) is almost parallel to a line connection between the two next-neighbor Li atoms and normal to the local mirror plane, see Fig. 4.2. Because O5 is linked to one Li atom and two H atoms, it was treated in a similar way to O2, O3 and O4 with a non-crystallographic mirror plane located between the H atoms. For all O atoms only the  $P_{lm}$  up to  $l = 3$  were included in the multipole-model refinement; the inclusion of hexadecapoles did not improve the fit. For the two symmetry-independent H atoms only one (and the same) single valence-shell population coefficient ( $P_{\text{val}}$ ) was regarded. Since the total number of valence electrons of an atom is equal to the sum  $P_{\text{val}} + P_{00}$  [32], for all atoms not the monopole  $P_{00}$  but  $P_{\text{val}}$  was considered, as given in Table 4.5. With all these constraints the number of ED parameters could be reduced to 48.

The results of the multipole refinement are presented in Figs. 4.3 and 4.4 that show the difference ED maps containing the O1, S, O3 and O3, Li1, O4 atoms, respectively. The density accumulation in the S–O chemical bonds indicates the mainly covalent character of these bonds. As expected for the ionic Li–O bonds, the O multipoles are not oriented exactly along the direction of the Li–O bond paths. The pronounced features of the residual ED, those  $> 0.1 \text{ e } \text{\AA}^{-3}$  (see Fig. 4.5), are localized near the S atom. This particularity reflects the typical difficulties in the description of the inner-core electrons of heavy atoms [22].

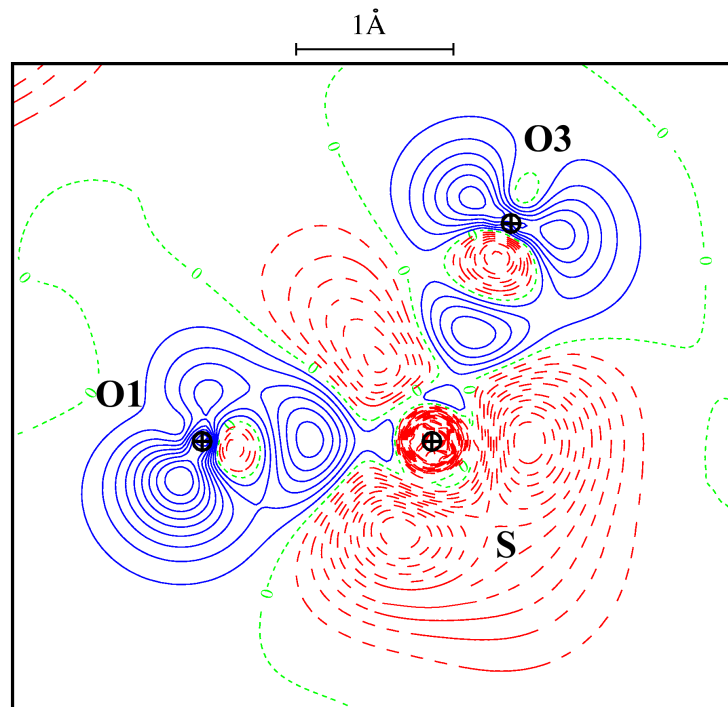


**Figure 4.3:** Difference ED within the O1–S–O3 plane. Contour intervals are at  $0.05 \text{ e } \text{\AA}^{-3}$ , broken red lines represent negative contours, whereas the blue lines indicate positive contours.

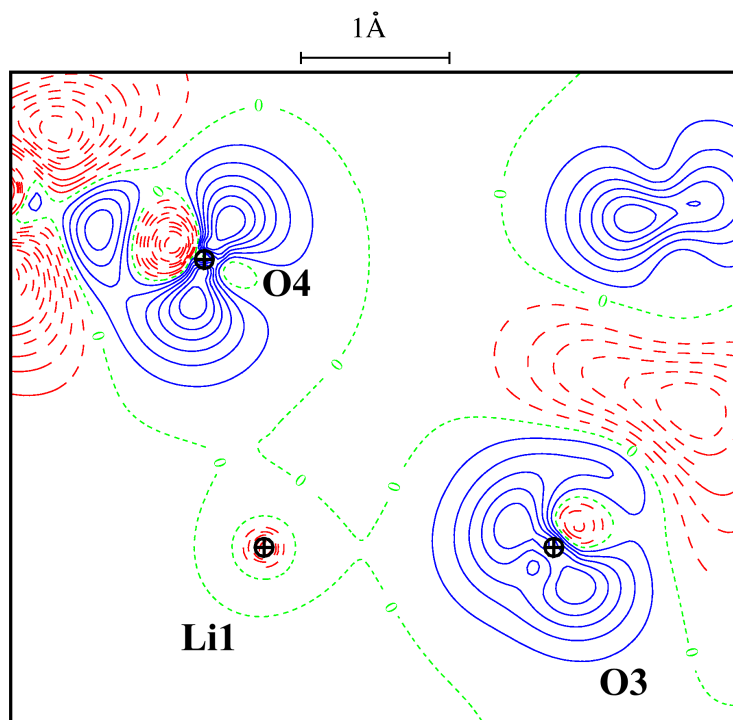


**Figure 4.4:** Difference ED within the O4–Li1–O3 plane. Contours are as in Fig. 4.3.

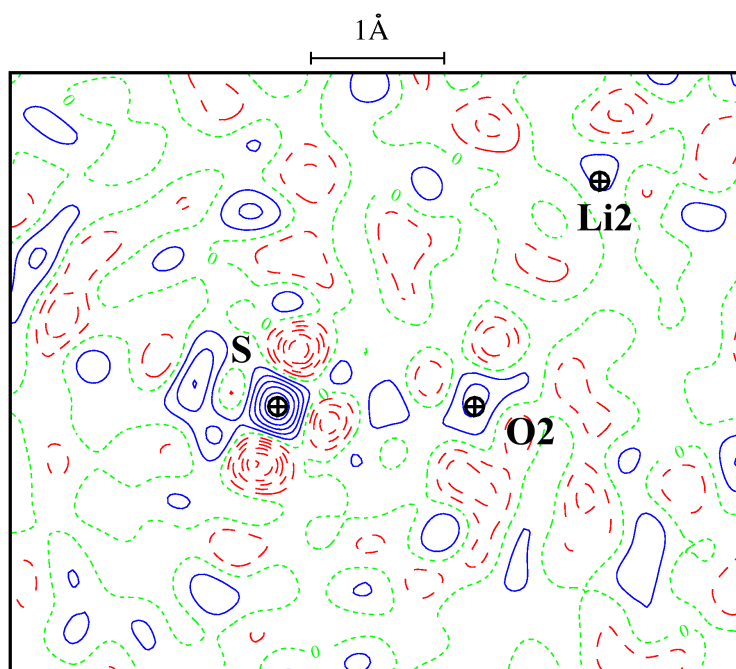


**Figure 4.5:** Residual ED map within the S–O2–Li2 plane (contours are as in Fig. 4.3).

The program *WinXPRO* [74] was used to perform the topological analysis of the experimental ED in  $\text{Li}_2\text{SO}_4 \cdot \text{H}_2\text{O}$ . The ED at the  $(3, -1)$  bond critical points ( $\mathbf{r}_c$ ) of the  $\text{SO}_4$ ,  $\text{Li}_1\text{O}_4$  and  $\text{Li}_2\text{O}_4$  groups (see Table 4.6) and the pseudoatomic charges (see Table 4.8) were determined according to the Bader formalism, as introduced in section 2.2. In addition, the Laplacian of the ED, the Hessian matrix eigenvalues ( $\lambda_1$ ,  $\lambda_2$  and  $\lambda_3$ ) and the electronic energy density ( $h$ ) were regarded at the  $\mathbf{r}_c$  points. All these features of the experimental

ED were crosschecked by the theoretical DFT calculations performed with *WIEN2k*. As shown in Tables 4.6, 4.7 and 4.8, the agreement between the theoretical and experimental results is reasonable. However, in the case of the S–O bonds there is a big discrepancy in the average value of  $\lambda_3$  and thus, the sign of the Laplacian ( $\nabla^2\rho = \lambda_1 + \lambda_2 + \lambda_3$ ) is different. For the second-row atoms, like S, such dominating influence of  $\lambda_3$  on the Laplacian was also noted by Coppens (1997) [22]. The negative sign of  $h$  at the S–O critical points indicates either covalent ( $\nabla^2\rho < 0$ , as follows from the *WIEN2k* calculations) or intermediate bond interactions [between closed-shell and shared interactions, as follows from the multipolar refinement ( $\nabla^2\rho > 0$ )]. A closed-shell type of interactions ( $h > 0$  and  $\nabla^2\rho > 0$ ) was deduced for the Li–O bonds.

**Table 4.6:** Experimental values of the ED ( $\text{e \AA}^{-3}$ ), Laplacian ( $\text{e \AA}^{-5}$ ), eigenvalues of the Hessian matrix ( $\text{e \AA}^{-5}$ ) and electronic energy density (a.u.) at the S–O, Li1–O, Li2–O bond critical points ( $\mathbf{r}_c$ ) averaged over the bonds within the  $\text{SO}_4$ ,  $\text{Li1O}_4$  and  $\text{Li2O}_4$  tetrahedra.

	$\langle\rho(\mathbf{r}_c)\rangle$	$\langle\nabla^2\rho(\mathbf{r}_c)\rangle$	$\langle\lambda_1\rangle$	$\langle\lambda_2\rangle$	$\langle\lambda_3\rangle$	$\langle h\rangle$
$\text{SO}_4$	1.90 (4)	8.5 (8)	−13.0 (1)	−12.8 (1)	34.3 (8)	−0.318 (9)
$\text{Li1O}_4$	0.15 (1)	4.5 (5)	−1.0 (1)	−0.9 (1)	6.4 (5)	0.011 (1)
$\text{Li2O}_4$	0.17 (1)	5.1 (2)	−1.2 (1)	−1.1 (1)	7.4 (2)	0.012 (1)

**Table 4.7:** Theoretical values of the ED ( $\text{e \AA}^{-3}$ ), Laplacian ( $\text{e \AA}^{-5}$ ), eigenvalues of the Hessian matrix ( $\text{e \AA}^{-5}$ ) and electronic energy density (a.u.) at the S–O, Li1–O, Li2–O bond critical points ( $\mathbf{r}_c$ ) averaged over the bonds within the  $\text{SO}_4$ ,  $\text{Li1O}_4$  and  $\text{Li2O}_4$  tetrahedra.

	$\langle\rho(\mathbf{r}_c)\rangle$	$\langle\nabla^2\rho(\mathbf{r}_c)\rangle$	$\langle\lambda_1\rangle$	$\langle\lambda_2\rangle$	$\langle\lambda_3\rangle$	$\langle h\rangle$
$\text{SO}_4$	1.99 (2)	−2.8 (6)	−13.5 (1)	−13.5 (1)	24.2 (6)	−0.384 (9)
$\text{Li1O}_4$	0.17 (1)	4.4 (16)	−1.0 (1)	−1.0 (1)	6.4 (16)	0.009 (5)
$\text{Li2O}_4$	0.19 (1)	6.3 (6)	−0.9 (1)	−1.1 (1)	8.3 (6)	0.014 (2)

**Table 4.8:** Pseudoatomic charges in  $\text{Li}_2\text{SO}_4\cdot\text{H}_2\text{O}$ . The values shown were calculated according to the Bader formalism (see section 2.2) on the basis of an experimental and theoretical ED.

	S	Li1	Li2	O1	O2	O3	O4	O5	H1	H2
$Q_{\text{EXP}}$ (e)	4.40	0.91	0.90	−1.34	−1.36	−1.42	−1.38	−1.59	0.45	0.48
$Q_{\text{WIEN2k}}$ (e)	4.13	0.86	0.86	−1.43	−1.46	−1.46	−1.45	−1.35	0.67	0.67

#### 4.1.2 X-ray diffraction study of $\text{Li}_2\text{SO}_4\cdot\text{H}_2\text{O}$ under the influence of an applied external electric field

The field-switching experiment, as described in section 3.1 of chapter 3, was conducted using a 0.590 (2) mm thick  $\text{Li}_2\text{SO}_4\cdot\text{H}_2\text{O}$  (010) crystal plate ( $1.5 \times 1.7$  cm surface area) cut from a large right-handed single crystal. The crystal morphology allows the distinction between the left and right forms, and physically the handedness can be recognized from the sign of the longitudinal piezoelectric constant  $d_{222}$ , see *e.g.* [75]. That way, it was ensured that the crystal investigated by X-ray diffraction under an external electric field had the same handedness as the crystal used for the ED studies in the previous section 4.1.1. All measurements, except those shown in Fig. 4.7, were carried out

with the maximum accessible HV values  $U_{\pm} = \pm 3$  kV resulting in the external electric fields  $\mathbf{E}_{\pm} = \pm 5.1 \times \mathbf{e}_2$  kV mm $^{-1}$  applied to the crystal sample. The relative variations of diffraction intensities were recorded solely at the wavelength  $\lambda = 0.6$  Å. In general, the measurement of a reflection was repeated until the total number of counts was high enough to provide  $\sigma(\Delta I/I)$  (see eq. 2.58) of the order of 0.1%.

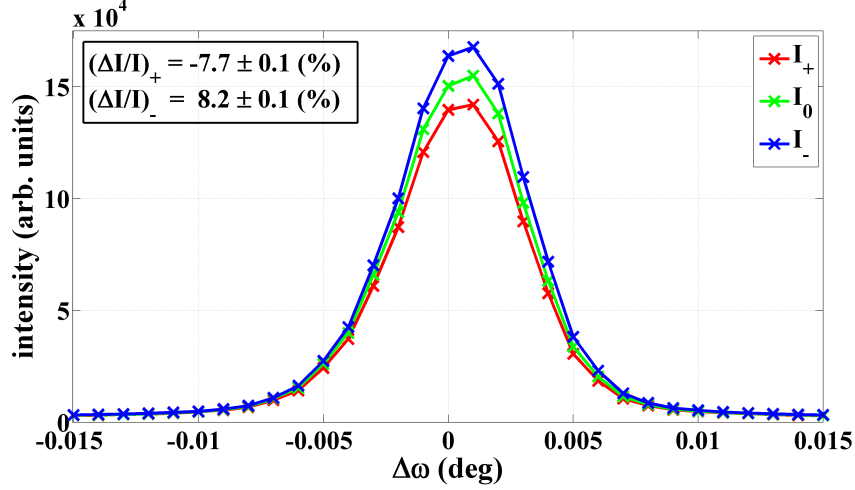


**Figure 4.6:** Three  $\omega$  rocking curves,  $I_+$ ,  $I_0$  and  $I_-$ , of the  $50\bar{6}$  reflection corresponding to the  $U_+$ ,  $U_0$  and  $U_-$  states of the HV,  $\mathbf{E} = \pm 5.1 \times \mathbf{e}_2$  kV mm $^{-1}$ . The structure factor of this reflection is unusually highly sensitive to the small displacements of the atomic positions in  $\text{Li}_2\text{SO}_4 \cdot \text{H}_2\text{O}$  induced by an external electric field applied parallel to the  $[010]$  direction.

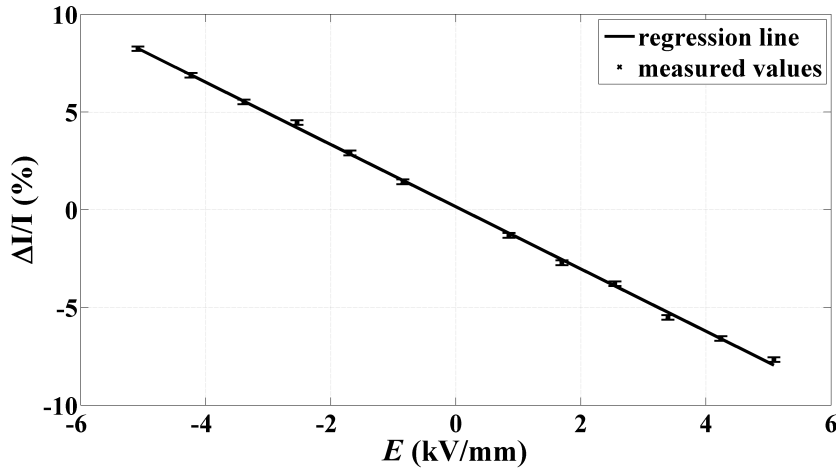


**Figure 4.7:** Relative intensity change,  $\Delta I/I$ , of the  $50\bar{6}$  reflection measured as a function of the magnitude of the applied electric field  $\mathbf{E} = E \times \mathbf{e}_2$ . These measurements confirm the assumption that the microscopic response of the crystal is linear with  $E$  within the range considered.

The intensities of selected Bragg reflections of the  $\text{Li}_2\text{SO}_4 \cdot \text{H}_2\text{O}$  (010) crystal plate were particularly sensitive to the electric-field-generated internal strain. For example, the reflection  $50\bar{6}$  exhibited an effect of  $\Delta I/I \simeq 8\%$  (see Fig. 4.6) which is remarkably high for this kind of experiment (usually the measured relative intensity variations are of the order of 1%). Furthermore, the  $\Delta I/I$  values of this reflection showed a good linear dependence on the magnitude of the external electric field  $\mathbf{E} = E \times \mathbf{e}_2$ , as displayed in Fig. 4.7. Note

that in this range of the electric field strength a linear behavior of  $\Delta I/I$  under  $\mathbf{E}$  was observed in almost all previous experiments [12, 14].

During the initial measurement period at HASYLAB based on *a priori* estimations of the sensitive reflections (applying equation (2.55) from section 2.3.2) 43 reflections showing a measurable effect in  $\Delta I/I$  could be collected. The average relative change,  $\langle |(\Delta I/I)_a| \rangle$  (eq. 3.2), of Bragg intensities was about 1.0%. These data of the first beamtime were exploited for a preliminary refinement of the atomic structural changes in  $\text{Li}_2\text{SO}_4\cdot\text{H}_2\text{O}$ . Using the roughly refined atomic displacements, a new list of reflections was created and in this way, 71 additional  $(\Delta I/I)_a$  values were collected (as summarized in Fig. 4.8;  $\langle |(\Delta I/I)_a| \rangle \simeq 2.1\%$ ). Finally, both sets were merged to a single data pool which was submitted to the final model refinement.

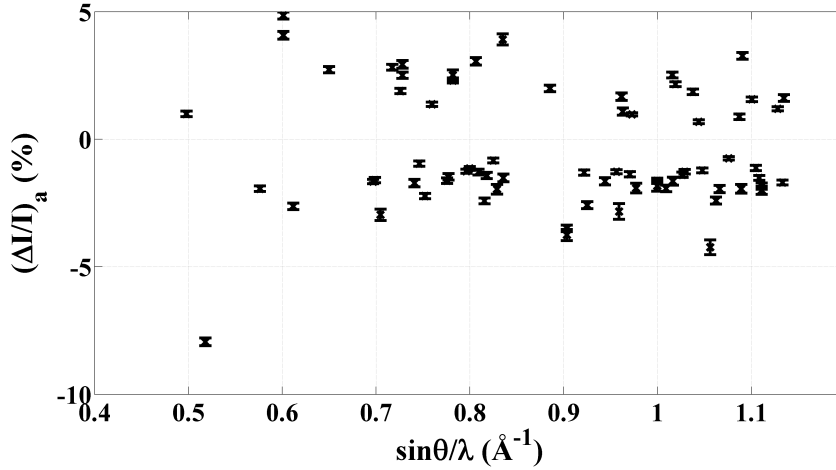


**Figure 4.8:** All  $(\Delta I/I)_a$  values (see eq. 3.2) that were recorded during the second measurement period at HASYLAB plotted against  $\sin\theta/\lambda$ .

### 4.1.3 Model used for the description of the electric-field-induced atomic displacements

In the case of  $\text{Li}_2\text{SO}_4\cdot\text{H}_2\text{O}$  the only symmetry operation that is not just a pure lattice translation is a  $2_1$  screw axis parallel to the lattice basis vector  $\mathbf{a}_2$ . Therefore, the components of the displacement tensor  $[a_j^i(\mu^*)]$  (as defined by eq. (2.46) in section 2.3.2) in the crystallographic coordinate system are given by

$$[a_j^i(\mu^*)] = \begin{pmatrix} a_1^1 & -a_2^1 & a_3^1 \\ -a_1^2 & a_2^2 & -a_3^2 \\ a_1^3 & -a_2^3 & a_3^3 \end{pmatrix} \text{ with } [a_j^i(\mu)] = \begin{pmatrix} a_1^1 & a_2^1 & a_3^1 \\ a_1^2 & a_2^2 & a_3^2 \\ a_1^3 & a_2^3 & a_3^3 \end{pmatrix}. \quad (4.4)$$

Since in the experiments  $\mathbf{E}$  was applied only in the  $[010]$  crystallographic direction, according to eq. (2.45) the parameters for a symmetry-independent atom that have to be refined are the elements of the second column,  $a_2^i(\mu)$ , of equation (4.4). Consequently, an unconstrained model should contain in total 30 independent parameters (three for each of the 10 atoms in the asymmetric unit of  $\text{Li}_2\text{SO}_4\cdot\text{H}_2\text{O}$ ).

The displacements of the H atoms were not refined ( $\Delta\mathbf{R}_{\text{H1}} = \Delta\mathbf{R}_{\text{H2}} = 0$ ), as their scattering power is too small to yield any significant results. The shifts of both Li atoms were constrained to be equal to each other and parallel to the external electric field:

$$\Delta\mathbf{R}_{\text{Li1}} = \Delta\mathbf{R}_{\text{Li2}} = a_{\text{Li}}\mathbf{E} \text{ with } \Delta\mathbf{R}_{\text{Li}} \parallel \mathbf{E} \parallel \mathbf{a}_2. \quad (4.5)$$

The reason behind the above assumption originates from the weak ionic Li–O bonds. The displacements (2.45) of the O atoms O2, O3 and O4 were restrained according to the local non-crystallographic mirror planes  $[\mathbf{m}(\mu) \perp \mathbf{e}_3(\mu)]$  related to the atomic positions, as illustrated in Fig. 4.2 in section 4.1.1:

$$[a_j^i(\mu)] = \mathbf{S} [a_j^i(\mu)] \mathbf{S}^{-1} \text{ with } \mathbf{S}_{m \perp \mathbf{e}_3} = \begin{pmatrix} 1 & 0 & 0 \\ 0 & 1 & 0 \\ 0 & 0 & -1 \end{pmatrix}. \quad (4.6)$$

In addition, the chemical-equivalence condition was imposed on these atoms. Thus, the components of the displacement tensors  $[a_j^i(\text{O2})]$ ,  $[a_j^i(\text{O3})]$  and  $[a_j^i(\text{O4})]$  are in the respective atomic local Cartesian coordinate system equal to each other and take the form

$$[a_{ij}(\text{O})] = \begin{pmatrix} \alpha_{11} & \alpha_{12} & 0 \\ \alpha_{21} & \alpha_{22} & 0 \\ 0 & 0 & \alpha_{33} \end{pmatrix}. \quad (4.7)$$

The special form of equation (4.7) arises from the constraint (4.6) applied to the tensor components  $a_j^i(\mu)$  of O2, O3 and O4. To express the coefficients of  $[a_{ij}(\text{O})]$  in the crystallographic coordinate system, the matrix of transformation,  $\mathbf{A}(\text{O}_\mu)$ , from the local Cartesian coordinate system of an atom  $\text{O}_\mu$  to the global crystallographic coordinate system,  $\{\mathbf{a}_i\}$ , was introduced:

$$[a_j^i(\text{O}_\mu)] = \mathbf{A}(\text{O}_\mu) [a_{ij}(\text{O})] \mathbf{A}^{-1}(\text{O}_\mu). \quad (4.8)$$

The five elements  $\alpha_{11}$ ,  $\alpha_{12}$ ,  $\alpha_{21}$ ,  $\alpha_{22}$  and  $\alpha_{33}$  from (4.7) are the only parameters in the refinement. Therefore, the number of variables describing the displacements of O2, O3 and O4 could be reduced from 9 to 5.

Furthermore, the fact that a translation of all atoms in the unit cell of a crystal by a lattice vector does not have effect on the absolute value of the structure factor  $F_E$  (2.44) was taken into account. To exclude this ambiguity in the results, an additional constraint was put on the quantities  $\Delta \mathbf{R}_\mu$  [14]:

$$\sum_{\mu} \Delta \mathbf{R}_\mu = 0. \quad (4.9)$$

Here the sum runs over all atoms within the unit cell. As follows from equation (4.4), the first and third components of the vector sum (4.9) (relative to the crystallographic coordinate system) automatically cancel for the displacements of a pair of symmetry-equivalent atoms, because for an electric field that is parallel to  $\mathbf{a}_2$  one has:

$$\Delta R^{1*} = -\Delta R^1, \quad \Delta R^{2*} = \Delta R^2 \text{ and } \Delta R^{3*} = -\Delta R^3. \quad (4.10)$$

Hence, the condition given in (4.9) is relevant for the second components of  $\Delta \mathbf{R}_\mu$  only and effectively reduces the number of free model parameters by one.

For calculating the right-hand side of equation (1.24), by means of which the dielectric constants of  $\text{Li}_2\text{SO}_4 \cdot \text{H}_2\text{O}$  are incorporated into the refinement, both H atoms were assumed to be rigidly shifted with the water oxygen O5. In total, including all constraints the electric-field-induced atomic displacements in  $\text{Li}_2\text{SO}_4 \cdot \text{H}_2\text{O}$  could be described by 13 parameters.

#### 4.1.4 Refinement of the piezoelectric constants $d_{2jk}$ and atomic displacements

As illustrated in Fig. 4.9, not more than 20 different reflections had to be submitted into the refinement procedure in order to get reliable values for the four piezoelectric constants  $d_{2jk}$  ( $d_{211}$ ,  $d_{222}$ ,  $d_{233}$  and  $d_{213}$ ) of  $\text{Li}_2\text{SO}_4\cdot\text{H}_2\text{O}$ . Adding further data did not change the refined values of the constants much. The piezoelectric constants  $d_{2jk}$  were refined separately for each of the two beamtimes at HASYLAB. The results are summarized in Table 4.9: In the first two rows the  $d_{211}$ ,  $d_{222}$ ,  $d_{233}$  and  $d_{213}$  values determined from the first and second set of measurements are presented, while in the third row the averaged values are displayed. In all, concerning the experimental conditions, both beamtimes can be regarded as equivalent to each other. In the last row of Table 4.9 the four independent constants  $d_{2jk}$  measured macroscopically using a dynamic pressure cell are given [66]. This data set is in quantitative agreement with the data obtained by the applied X-ray diffraction technique.

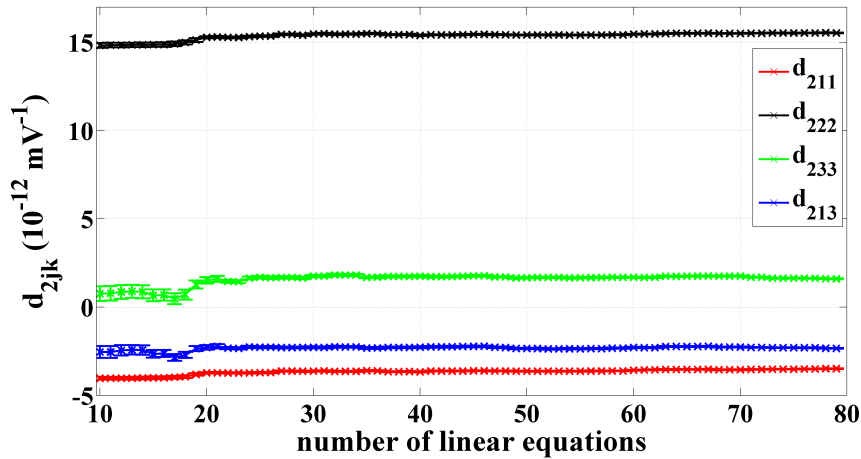


**Figure 4.9:** Four symmetry-allowed piezoelectric constants  $d_{2jk}$  ( $d_{211}$ ,  $d_{222}$ ,  $d_{233}$  and  $d_{213}$ ) of  $\text{Li}_2\text{SO}_4\cdot\text{H}_2\text{O}$  refined as a function of the number of linear equations (2.40) used at the same time in the refinement. In this example the data of the second set of measurements is analyzed.

**Table 4.9:** Piezoelectric constants ( $\text{pC N}^{-1}$ ) of  $\text{Li}_2\text{SO}_4\cdot\text{H}_2\text{O}$  determined in this work and macroscopically measured by means of a dynamic pressure cell [76] are compared.

	$d_{211}$	$d_{222}$	$d_{233}$	$d_{213}$
First data set	-3.26 (1)	15.17 (1)	1.16 (1)	-2.59 (1)
Second data set	-3.57 (1)	15.48 (1)	1.68 (1)	-2.29 (1)
$\langle 1^{\text{st}} \text{ set}, 2^{\text{nd}} \text{ set} \rangle$	-3.4 (3)	15.3 (2)	1.4 (3)	-2.4 (2)
Ochrombel (2007) [66]	-3.3 (2)	15.8 (5)	1.7 (1)	-2.2 (1)

In Fig. 4.10 the convergence behavior of the three non-vanishing components  $R_{212}$ ,  $R_{213}$  and  $R_{233}$  of the rotation tensor  $[R_{2jk}]$  [see third term in equation (2.40)], calculated simultaneously with the piezoelectric constants  $d_{211}$ ,  $d_{222}$ ,  $d_{233}$  and  $d_{213}$ , is demonstrated. The coefficients  $R_{212}$ ,  $R_{213}$  and  $R_{233}$  (Table 4.10) as well as the  $d_{2jk}$  constants (Table 4.9) were obtained by averaging over all refined values starting with the 20th linear equation, see Figs. 4.9 and 4.10. As shown in Table 4.10, the  $R_{212}$ ,  $R_{213}$  and  $R_{233}$  values are small and do not differ much between the first and second experiment.

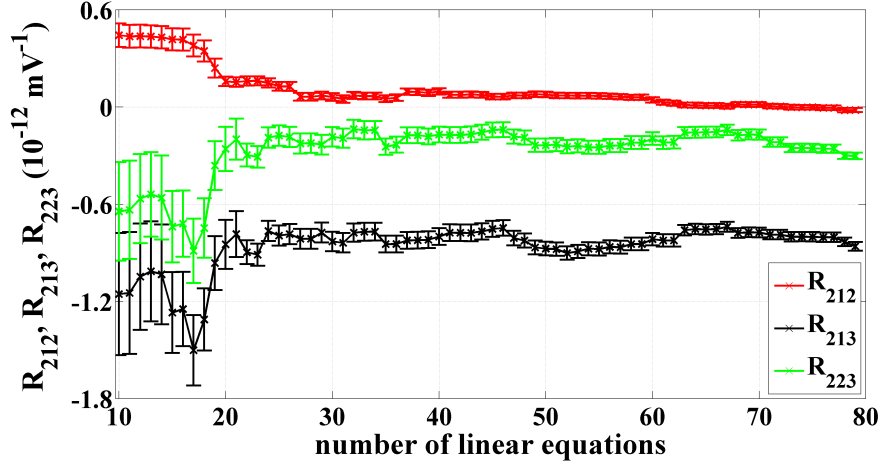


**Figure 4.10:** Rotation tensor coefficients  $R_{212}$ ,  $R_{213}$  and  $R_{233}$  calculated in dependence on the number of linear equations (2.40), here the second data set was used. With the four piezoelectric constants (see Fig. 4.9) there are in total seven parameters in the considered over-determined system of linear equations.

**Table 4.10:** Three independent components  $R_{212}$ ,  $R_{213}$  and  $R_{233}$  ( $\text{pC N}^{-1}$ ) of the rotation tensor  $[R_{2jk}]$  refined simultaneously with the piezoelectric constants  $d_{211}$ ,  $d_{222}$ ,  $d_{233}$  and  $d_{213}$  using the approach (2.40).

	$R_{212}$	$R_{213}$	$R_{233}$
First data set	0.28 (1)	-1.07 (1)	0.09 (1)
Second data set	0.04 (1)	-0.81 (1)	-0.22 (2)

The performed final refinement of the redistribution of atoms within the unit cell of  $\text{Li}_2\text{SO}_4 \cdot \text{H}_2\text{O}$  is summarized in Table 4.11. The data-to-variables ratio reaches a value of 9, which is quite high for such kind of experiment (see all considered symmetry-independent reflections in Table A.1 in the appendix). The quality of the fitting procedure including the model introduced in section 4.1.3 was characterized by means of the agreement factors  $R$  (2.50) and  $R_w$  (2.51).

**Table 4.11:** Main parameters of the refinement of the atomic structural changes in  $\text{Li}_2\text{SO}_4 \cdot \text{H}_2\text{O}$ : No.  $(\Delta I/I)_a$  denotes the number of the experimental data,  $R$  is the unweighted and  $R_w$  is the weighted agreement factor,  $\chi^2$  (eq. 2.49) is the error sum and  $\langle \sigma / |(\Delta I/I)_a| \rangle$  is the average relative standard deviation of  $|(\Delta I/I)_a|$ .

No. $(\Delta I/I)_a$	No. of variables	$R$	$R_w$	$\chi^2$	$\langle \sigma /  (\Delta I/I)_a  \rangle$
113	13	0.28	0.27	3198	0.13

A schematic representation of the obtained atomic rearrangement in  $\text{Li}_2\text{SO}_4 \cdot \text{H}_2\text{O}$  viewed along the  $\mathbf{a}_1$  axis is shown in Fig. 4.11. The determined true displacements of atoms are by a factor of 1500 smaller than visualized in the crystal structure plot. Especially the large shifts of the atoms Li1, Li2 and O5 catch the eye. As the  $\text{Li}^+$  ions having a very light mass are weakly bonded and because O5 is part of the water molecule, it is quite evident that the impact of an external electric field on these atoms is the largest in the structure of  $\text{Li}_2\text{SO}_4 \cdot \text{H}_2\text{O}$ . In contrast to the Li atoms, the O5 atom is displaced essentially opposite to  $\mathbf{E}_+$  ( $\mathbf{E}_+ \parallel \mathbf{a}_2$ ), which is in consistence with the expected response of a cation and anion to an electric field, respectively.

**Table 4.12:** Summary of the refined atomic displacements in  $\text{Li}_2\text{SO}_4\cdot\text{H}_2\text{O}$  induced by an applied electric field  $\mathbf{E}_+ = 5.1 \times \mathbf{e}_2 \text{ kV mm}^{-1}$ . The components of the displacement vectors,  $\Delta\mathbf{R}_\mu$ , are related to the crystallographic system.

Atom	$\Delta R^1 (10^{-5})$	$\Delta R^2 (10^{-5})$	$\Delta R^3 (10^{-5})$
S	2.59 (2)	-3.81 (14)	0.48 (2)
Li1	0	20.57 (13)	0
Li2	0	20.57 (13)	0
O1	1.12 (7)	-8.45 (90)	-3.72 (9)
O2	-1.70 (4)	-2.77 (10)	-0.54 (6)
O3	-1.65 (5)	-3.27 (16)	-1.33 (2)
O4	4.61 (13)	-0.95 (15)	1.32 (3)
O5	-1.87 (22)	-21.89 (37)	-5.28 (22)

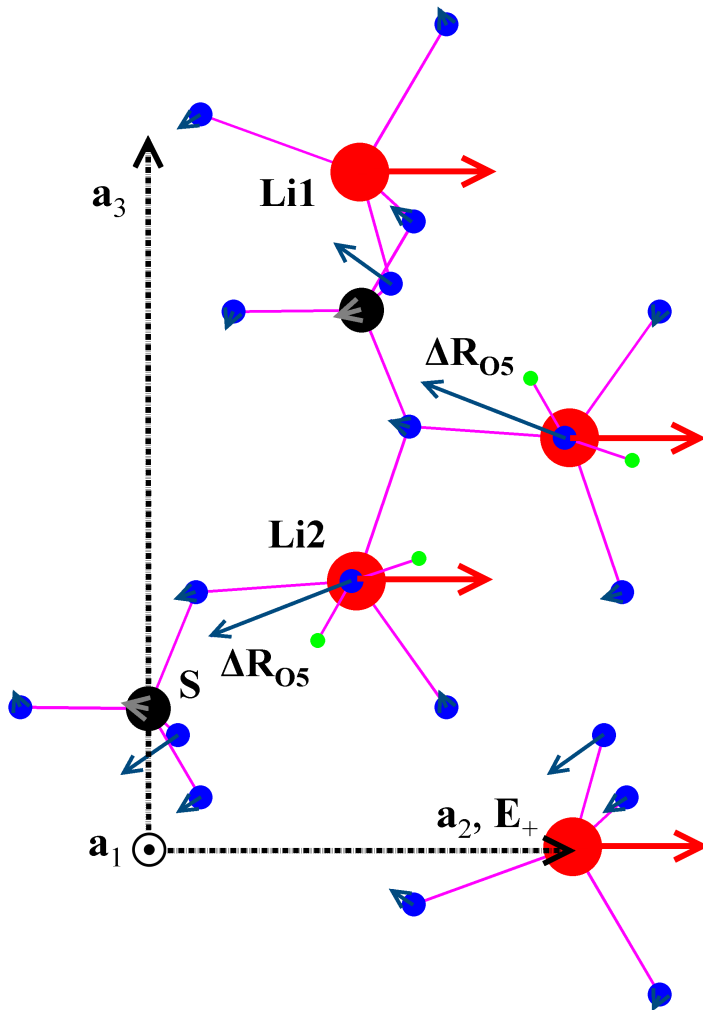


**Figure 4.11:** View of the induced rearrangement of atoms in  $\text{Li}_2\text{SO}_4\cdot\text{H}_2\text{O}$ , as presented in Table 4.12, along the  $\mathbf{a}_1$  crystallographic axis. In order to visualize the effect observed the true atomic displacements were multiplied by a factor of 1500. Especially striking are the large shifts of the atoms Li1, Li2 and O5 (O5 is a water oxygen) in and opposite to the direction of the applied electric field  $\mathbf{E}_+$  ( $\mathbf{E}_+ \parallel \mathbf{a}_2$ ), respectively.

The refined shifts of the symmetry-independent atoms of  $\text{Li}_2\text{SO}_4\cdot\text{H}_2\text{O}$ , as listed in Table 4.12, were used to evaluate the deformation of the Li1–O, Li2–O and S–O bond lengths. The variations of the individual bond lengths in the tetrahedral structural units  $\text{Li1O}_4$ ,  $\text{Li2O}_4$  and  $\text{SO}_4$  are presented in Table 4.13. There are huge differences in the effect observed within a tetrahedron, as the O atoms (O1, O2, O3 and O4, see Fig. 4.1) connecting the structural groups to a tetrahedral framework cannot follow the differently

large and differently oriented displacements of the cation atoms Li1, Li2 and S in a simple way, as illustrated in Fig. 4.11. The first row of Table 4.14 displays the average absolute values of the bond deformations  $\langle |\Delta(\mu - \text{O})| \rangle$  values with  $\mu = \{\text{Li1}, \text{Li2}, \text{S}\}$  arising from the change of the fractional atomic coordinates (internal strain). Since in a tetrahedral group the atomic shifts are correlated with each other, the standard deviation of  $\langle |\Delta(\mu - \text{O})| \rangle$  was not regarded. Because of that, the errors presented in Table 4.14 reflect the experimental uncertainty of the determined internal strain only. The second row of Table 4.14 shows the  $\langle |\Delta(\mu - \text{O})| \rangle$  values calculated by considering the contribution of the converse piezoelectric effect (external strain) to the internal strain. It is obvious that the major part of the deformation of the bond lengths in  $\text{Li}_2\text{SO}_4 \cdot \text{H}_2\text{O}$  is the internal strain. In conclusion, the ionic Li–O chemical bonds are significantly more strongly affected by an external electric field than the covalent S–O bonds.

**Table 4.13:** Change of the individual bond lengths ( $10^{-5}$  Å) in the  $\text{Li1O}_4$ ,  $\text{Li2O}_4$  and  $\text{SO}_4$  tetrahedra induced by  $\mathbf{E}_+ = 5.1 \times \mathbf{e}_2$  kV mm $^{-1}$ . Symmetry codes are: (i)  $-x, \frac{1}{2} + y, 1 - z$ ; (ii)  $x, y, 1 + z$ ; (iii)  $1 - x, \frac{1}{2} + y, 1 - z$ ; (iv)  $x, 1 + y, 1 + z$ ; (v)  $1 - x, \frac{1}{2} + y, 1 - z$ ; (vi)  $x, 1 - y, z$ .

$\text{Li1O}_4$		$\text{Li2O}_4$		$\text{SO}_4$	
$\Delta(\text{Li1} - \text{O1}^{\text{i}})$	34.7 (3)	$\Delta(\text{Li2} - \text{O2})$	-109.8 (2)	$\Delta(\text{S} - \text{O1})$	0.5 (11)
$\Delta(\text{Li1} - \text{O3}^{\text{ii}})$	-103.3 (2)	$\Delta(\text{Li2} - \text{O2}^{\text{v}})$	33.6 (4)	$\Delta(\text{S} - \text{O2})$	10.3 (2)
$\Delta(\text{Li1} - \text{O3}^{\text{iii}})$	33.9 (2)	$\Delta(\text{Li2} - \text{O4}^{\text{vi}})$	72.0 (4)	$\Delta(\text{S} - \text{O3})$	0.5 (6)
$\Delta(\text{Li1} - \text{O4}^{\text{iv}})$	47.5 (2)	$\Delta(\text{Li2} - \text{O5})$	-9.1 (6)	$\Delta(\text{S} - \text{O4})$	12.6 (14)

**Table 4.14:** Electric-field-induced average variation of the cation-anion distances ( $10^{-5}$  Å) in the three different structural units,  $\text{Li1O}_4$ ,  $\text{Li2O}_4$  and  $\text{SO}_4$ , of  $\text{Li}_2\text{SO}_4 \cdot \text{H}_2\text{O}$ . In the last row the influence of the converse piezoelectric effect (external strain) was taken into account. The values presented refer to the electric field  $E = 5.1$  kV mm $^{-1}$  being parallel to [010].

	$\langle  \Delta(\text{Li1} - \text{O})  \rangle$	$\langle  \Delta(\text{Li2} - \text{O})  \rangle$	$\langle  \Delta(\text{S} - \text{O})  \rangle$
Internal strain	54.8 (1)	56.1 (2)	6.0 (5)
Int. & ext. strain	57.3 (1)	57.9 (2)	4.1 (8)

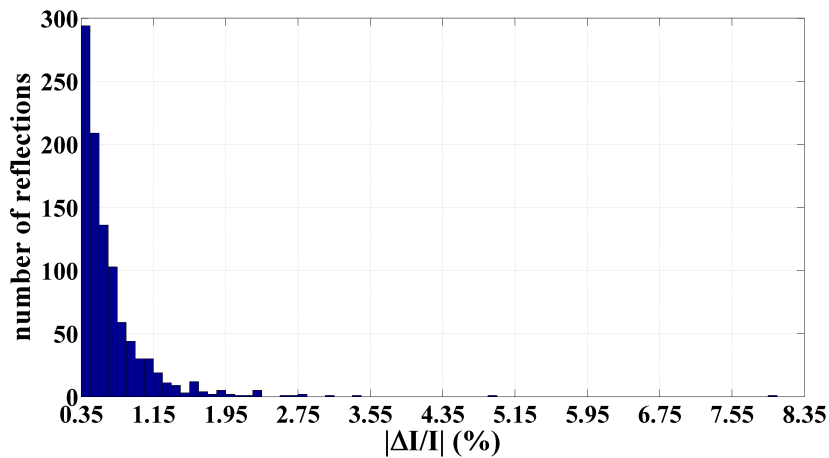


**Figure 4.12:** Using the displacements of atoms obtained for  $\mathbf{E}_+ = 5.1 \times \mathbf{e}_2$  kV mm $^{-1}$ , see Table 4.12, calculated distribution of the number of  $\text{Li}_2\text{SO}_4 \cdot \text{H}_2\text{O}$  reflections as a function of  $|\Delta I/I|$ . The calculations were based on the conditions:  $\lambda = 0.6$  Å,  $\theta < 67.5^\circ$ ,  $|F| > 0.3$  and  $|F| < 2$ . Besides, the  $\bar{h}k\bar{l}$  and  $h\bar{k}l$  reflections were omitted from the analysis.

Figure 4.12 displays a distribution of the number of  $\text{Li}_2\text{SO}_4\cdot\text{H}_2\text{O}$  reflections calculated as a function of  $|\Delta I/I|$  using the displacements of atoms obtained for the electric field  $\mathbf{E}_+ = 5.1 \times \mathbf{e}_2 \text{ kV mm}^{-1}$ , see Table 4.12. These calculations were performed for  $\lambda = 0.6 \text{ \AA}$  and all reflection with a Bragg angle  $2\theta \geq 135^\circ$  were omitted from the analysis as well as very weak ( $|F| < 0.3$ ) and relatively strong ( $|F| > 2$ ) reflections. Besides, the  $\bar{h}k\bar{l}$  reflections, which are symmetry equivalent to the  $hkl$  reflections, and the  $h\bar{k}l$  reflections were not considered, as for  $\lambda = 0.6 \text{ \AA}$  in good approximation one has:  $\Delta I/I(hkl) \approx \Delta I/I(h\bar{k}l)$ . As a result, it is well visible that there are not many reflections that are highly sensitive, showing  $\Delta I/I \geq 1\%$ , to the applied electric field. On the other hand, the diffraction intensities of most reflections are less affected by the induced changes in the atomic structure of  $\text{Li}_2\text{SO}_4\cdot\text{H}_2\text{O}$ .

### 4.1.5 Discussion

The distinctive bond-selective behavior of  $\text{Li}_2\text{SO}_4\cdot\text{H}_2\text{O}$  under an external electric perturbation reflects the bond properties, characterized by means of the topological ED analysis (see Tables 4.6, 4.7 and 4.8 in section 4.1.1 for details). In particular, the value of the Bader charge of the S pseudoatom is by a factor of about 5 larger than that for the Li atoms. For this reason, the effective force acting in an electric field on sulfur (*i.e.* the force on its atomic nucleus plus its pseudoatomic fragment of the ED) is stronger by the same factor. On the other hand, the average ED in the Li–O bond critical points is more than 10 times smaller than the corresponding value for the S–O bonds. This enormous difference is in qualitative agreement with the observed higher sensitivity of the  $\text{LiO}_4$  and  $\text{LiO}_3(\text{H}_2\text{O})$  tetrahedra to an applied external electric field. At the same time, in spite of the higher charge of the S pseudoatom, the deformation of the  $\text{SO}_4$  group is quite small, so that  $\text{SO}_4$  remains almost rigid. This feature of the internal strain may originate from the nature of the S–O and Li–O bonds. As follows from the signs of the electronic energy density and Laplacian at the bond critical points, the interactions between the Li and O atoms are of a closed-shell (ionic) type. In contrast, the S–O bonds are either of covalent (see *WIEN2k* calculation in Table 4.7) or intermediate interactions (see multipolar refinement in Table 4.6). Although the type of the S–O interactions cannot be established unambiguously, the ED for both cases is mostly (for the covalent case) or partly (for the intermediate case) relocated to the bond regions. Thus, the effective external electric field force on the isolated S pseudoatomic fragment becomes less dominant compared to the pure closed-shell interactions, which results in the small distortion of the S–O bond lengths:  $\langle |\Delta(\text{S} - \text{O})| \rangle / E = 0.8(2) \times 10^{-5} \text{ \AA (kV mm}^{-1})^{-1}$ , whereas the variation of the Li–O bond lengths is quite high:  $\langle |\Delta(\text{Li} - \text{O})| \rangle / E = 11.3(2) \times 10^{-5} \text{ \AA (kV mm}^{-1})^{-1}$ . Note that in the work on  $\alpha\text{-GaPO}_4$  by Gorfman *et al.* (2006) [14] a similar magnitude of the average Ga–O and P–O bond deformation under an external electric field,  $\langle |\Delta(\text{Ga} - \text{O})| \rangle / E = 1.5(9) \times 10^{-5} \text{ \AA (kV mm}^{-1})^{-1}$  and  $\langle |\Delta(\text{P} - \text{O})| \rangle / E = 4.3(7) \times 10^{-5} \text{ \AA (kV mm}^{-1})^{-1}$ , was found.

## 4.2 Lithium selenate monohydrate, $\text{Li}_2\text{SeO}_4\cdot\text{H}_2\text{O}$

The compound  $\text{Li}_2\text{SeO}_4\cdot\text{H}_2\text{O}$  is isostructural with  $\text{Li}_2\text{SO}_4\cdot\text{H}_2\text{O}$  and possesses the lattice parameters  $a_1 = 5.5798(3) \text{ \AA}$ ,  $a_2 = 5.0284(3) \text{ \AA}$ ,  $a_3 = 8.4521(5) \text{ \AA}$  and  $\alpha_2 = 107.634(2)^\circ$  (Johnston & Harrison (2003) [55]). Figure 4.18 illustrates the crystal structure of  $\text{Li}_2\text{SeO}_4\cdot\text{H}_2\text{O}$  projected into the  $\mathbf{a}_2\text{--}\mathbf{a}_3$  plane and the atom labeling used. Selected

geometric parameters of the  $\text{Li1O}_4$ ,  $\text{Li2O}_4 \equiv \text{Li2O}_3(\text{H}_2\text{O})$  and  $\text{SeO}_4$  groups are given in Table 4.15. In good approximation all three structural units can be considered as regular tetrahedra which do not deviate much from the perfect tetrahedral symmetry, as indicated by small  $|\mathbf{D}_{\text{tet}}|$  values in Table 4.15.

Compared with the piezoelectric and pyroelectric properties of  $\text{Li}_2\text{SO}_4 \cdot \text{H}_2\text{O}$ , the crystal  $\text{Li}_2\text{SeO}_4 \cdot \text{H}_2\text{O}$  exhibits a slightly smaller longitudinal piezoelectric effect along the two-fold screw axis ( $d_{222} = 13.3(9) \text{ pC N}^{-1}$  [66]) as well as its pyroelectric coefficient  $p_2$  is with a value of  $55.6(10) \times 10^{-6} \text{ C m}^{-2} \text{ K}^{-1}$  [57] smaller. But nevertheless, the pyroelectric effect of the non-ferroelectric  $\text{Li}_2\text{SeO}_4 \cdot \text{H}_2\text{O}$  is remarkably high.

**Table 4.15:** Average bond lengths  $\langle \mu - \text{O} \rangle$  (with  $\mu = \{\text{Li1}, \text{Li2}, \text{Se}\}$ ) and bond angles  $\langle \angle (\text{O} - \mu - \text{O}) \rangle$  plus  $|\mathbf{D}_{\text{tet}}|$  (4.1) of the tetrahedral structural units  $\text{Li1O}_4$ ,  $\text{Li2O}_4$  and  $\text{SeO}_4$ .

Tetrahedron	$\langle \mu - \text{O} \rangle$ (Å)	$\langle \angle (\text{O} - \mu - \text{O}) \rangle$ (°)	$ \mathbf{D}_{\text{tet}} $ (Å)
$\text{Li1O}_4$	1.96 (3)	109.3 (57)	0.121 (8)
$\text{Li2O}_4$	1.94 (2)	109.3 (48)	0.101 (9)
$\text{SeO}_4$	1.63 (9)	109.5 (8)	0.021 (3)

### 4.2.1 Properties of the chemical bonds

The X-ray diffraction measurements with a  $40(2) \times 30(2) \times 16(2) \mu\text{m}$  small  $\text{Li}_2\text{SeO}_4 \cdot \text{H}_2\text{O}$  crystal plate were performed in the X-ray laboratory of the Max-Planck-Institut für Kohlenforschung in Mülheim an der Ruhr using a diffractometer system composed of a Mach3 goniometer, an APEX II CCD detector and a graded multilayer mirror. A summary of the main parameters of the carried out data collection and multipole refinement of the ED in  $\text{Li}_2\text{SeO}_4 \cdot \text{H}_2\text{O}$  is presented in Table 4.16.

**Table 4.16:** Data collection and multipole refinement of the ED in  $\text{Li}_2\text{SeO}_4 \cdot \text{H}_2\text{O}$ .

Experimental parameters	
Radiation type	Mo $K\alpha$
Detection type	APEX II CCD detector
Temperature (K)	100 (2)
Size of the crystal plate	$40(2) \times 30(2) \times 16(2) \mu\text{m}$
$\mu$ ( $\text{mm}^{-1}$ )	8.25 (1)
Recorded data	
$(\sin \theta / \lambda)_{\text{max}}$ ( $\text{Å}^{-1}$ )	1.04
Observed/unique reflections	39170/2250
Redundancy	17.4
$R_{\text{sym}}(I)$	0.016
Multipole refinement	
Number of ED parameters	58
Omitted reflections	3
$R_{\text{IAM}}(F)$	0.0159
$R(F)/R_w(F)$	0.0145/0.0179
Goodness of fit	1.093

**Table 4.17:** Refined atomic positions of  $\text{Li}_2\text{SeO}_4\cdot\text{H}_2\text{O}$  at 100 (2) K. The unit-cell parameters are:  $a_1 = 5.5864(6)$  Å,  $a_2 = 5.0086(5)$  Å,  $a_3 = 8.4347(9)$  Å and  $\alpha_2 = 107.582(2)^\circ$ .

	$x$	$y$	$z$
Se	0.28418 (2)	0.10066 (2)	0.70759 (2)
Li1	0.31565 (2)	0.59906 (6)	0.49703 (2)
Li2	0.56164 (2)	0.58972 (6)	0.89753 (2)
O1	0.32222 (2)	-0.22513 (2)	0.71057 (2)
O2	0.39213 (2)	0.22833 (2)	0.56359 (2)
O3	0.44778 (2)	0.22146 (2)	0.88877 (2)
O4	-0.00962 (2)	0.18206 (2)	0.67308 (2)
O5	0.90861 (2)	0.55514 (2)	0.90801 (2)
H1	0.9370 (9)	0.4814 (3)	0.8273 (7)
H2	0.9851 (16)	0.6862 (2)	0.9335 (7)

**Table 4.18:** Anisotropic thermal parameters ( $10^{-5}$  Å<sup>2</sup>) of  $\text{Li}_2\text{SeO}_4\cdot\text{H}_2\text{O}$  at 100 (2) K. The temperature coefficients of both H atoms could not be refined.

	$U_{11}$	$U_{22}$	$U_{33}$	$U_{12}$	$U_{13}$	$U_{23}$
Se	602 (2)	410 (2)	433 (2)	20 (2)	160 (2)	7 (2)
Li1	1126 (2)	964 (2)	1015 (2)	10 (6)	360 (2)	32 (8)
Li2	1162 (2)	1002 (6)	978 (2)	116 (2)	295 (4)	-22 (4)
O1	1236 (2)	427 (2)	737 (2)	47 (2)	210 (2)	14 (2)
O2	1138 (2)	707 (2)	783 (2)	148 (2)	555 (2)	208 (2)
O3	1057 (2)	701 (2)	501 (2)	-158 (2)	59 (2)	-38 (2)
O4	643 (4)	1220 (2)	927 (2)	69 (2)	161 (4)	-213 (2)
O5	1113 (2)	1622 (2)	1620 (4)	-93 (4)	591 (4)	-336 (4)

The calculation of the diffraction intensity of measured reflections was done with the Bruker-AXS *SAINTE* v7.34a program [77]. The collected data set was corrected numerically and empirically for anisotropic absorption with the program *SADABS* [77]. In total, the experimental data were of excellent quality, which is reflected in the small values of  $R_{\text{sym}}(I) = 0.016$  and  $R_{\text{IAM}}(F) = 0.0159$ . Besides, only 3 reflections out of 39170 had to be omitted from the multipole refinement. In Tables 4.17 and 4.18 the determined atomic positions [unit-cell parameters at 100 (2) K are:  $a_1 = 5.5864(6)$  Å,  $a_2 = 5.0086(5)$  Å,  $a_3 = 8.4347(9)$  Å and  $\alpha_2 = 107.582(2)^\circ$ ] and anisotropic thermal parameters of  $\text{Li}_2\text{SeO}_4\cdot\text{H}_2\text{O}$  are displayed, whereat the temperature coefficients of the H atoms could not be refined.

The multipole expansion of the ED in  $\text{Li}_2\text{SeO}_4\cdot\text{H}_2\text{O}$  was implemented for the most part analogously to the approach applied in the case of  $\text{Li}_2\text{SO}_4\cdot\text{H}_2\text{O}$ . But, compared to  $\text{Li}_2\text{SO}_4\cdot\text{H}_2\text{O}$ , for  $\text{Li}_2\text{SeO}_4\cdot\text{H}_2\text{O}$  it is essentially more difficult to model the density distribution of the Se atom by means of the aspherical-atom formalism [32]. Therefore, all multipoles of this atom were refined by ignoring its nearly tetrahedral symmetry. But nevertheless, the features of the residual ED near Se in terms of the large peaks and holes in its vicinity are still strongly pronounced, as shown in Fig. 4.13. In addition, for all atoms the refinement of the radial parameter  $\kappa''$  (see equation (2.9) in section 2.2) did not converge as well as for the Li and H atoms the variation of  $\kappa'$  diverged. A summary of the model used and the refined values of the atomic multipole parameters are given in

**Table 4.19:** Summary of all refined atomic population coefficients ( $P_{\text{val}}$ ,  $P_{lm}$ ) and radial parameters ( $\kappa'$ ,  $\kappa''$ ) together with the  $n_l$  and  $\zeta_l$  values used in the functions  $R_l$  (2.10). The atomic  $P_{lm}$  marked by “\*\*” were excluded from the refinement of the ED distribution in  $\text{Li}_2\text{SeO}_4 \cdot \text{H}_2\text{O}$  and those marked by “-” are forbidden due to the applied local symmetry operations.

	Se	Li1/Li2	O1, O2, O3	O4	O5	H1/H2
$P_{\text{val}}$	4.304 (6)	0.467 (1)	6.661 (6)	6.582 (5)	6.519 (4)	0.839 (1)
$P_{00}$	**	**	**	**	**	-
$P_{11}$	0.067 (3)	-	-0.011 (1)	-0.026 (1)	-0.033 (1)	-
$P_{1-1}$	-0.090 (1)	-	-0.006 (1)	0.003 (1)	0.083 (1)	-
$P_{10}$	-0.173 (8)	-	-	-0.042 (1)	-	-
$P_{20}$	0.032 (1)	-	0.040 (1)	-0.104 (3)	-0.083 (2)	-
$P_{21}$	0.079 (1)	-	-	0.022 (1)	-	-
$P_{2-1}$	-0.004 (1)	-	-	0.070 (2)	-	-
$P_{22}$	0.008 (1)	-	0.029 (1)	-0.022 (1)	0.039 (2)	-
$P_{2-2}$	0.174 (1)	-	-0.016 (1)	-0.049 (1)	-0.104 (3)	-
$P_{30}$	-0.242 (3)	-	-	0.009 (1)	-	-
$P_{31}$	-0.016 (2)	-	-0.018 (1)	-0.005 (1)	-0.007 (1)	-
$P_{3-1}$	0.001 (6)	-	-0.034 (1)	-0.023 (1)	-0.080 (2)	-
$P_{32}$	-0.115 (2)	-	-	-0.037 (1)	-	-
$P_{3-2}$	0.192 (6)	-0.261 (6)	-	0.017 (1)	-	-
$P_{33}$	-0.059 (2)	-	-0.009 (1)	0.022 (1)	-0.034 (1)	-
$P_{3-3}$	0.053 (1)	-	0.026 (1)	0.004 (1)	-0.024 (1)	-
$P_{40}$	-0.345 (10)	-0.324 (16)	**	**	**	-
$P_{41}$	-0.008 (1)	-	-	**	-	-
$P_{4-1}$	0.060 (2)	-	-	**	-	-
$P_{42}$	0.137 (1)	-	**	**	**	-
$P_{4-2}$	0.147 (2)	-	**	**	**	-
$P_{43}$	0.208 (3)	-	-	**	-	-
$P_{4-3}$	0.089 (4)	-	-	**	-	-
$P_{44}$	-0.037 (6)	-0.240 (12)	**	**	**	-
$P_{4-4}$	-0.085 (1)	-	**	**	**	-
$\kappa'$	1.141 (1)	1.00	0.963 (1)	0.963 (1)	0.963 (1)	1.00
$\kappa''$	1.00	1.00	1.00	1.00	1.00	1.00
$n_0/\zeta_0$	4/4.511	2/1.279	2/4.466	2/4.466	2/4.466	0/0
$n_1/\zeta_1$	4/4.511	2/1.279	2/4.466	2/4.466	2/4.466	0/0
$n_2/\zeta_2$	4/4.511	2/1.279	2/4.466	2/4.466	2/4.466	0/0
$n_3/\zeta_3$	6/4.511	3/1.279	4/4.466	4/4.466	4/4.466	0/0
$n_4/\zeta_4$	8/4.511	4/1.279	4/4.466	4/4.466	4/4.466	0/0

Table 4.19. The extinction was treated in the same way as for  $\text{Li}_2\text{SO}_4 \cdot \text{H}_2\text{O}$ . Since for all reflections the respective extinction factor was not smaller than 0.98 [ $y \geq 0.98$ , eq. (2.8)], the X-ray data have turned out to be only slightly affected by extinction effects.

Tables 4.20, 4.21 and 4.22 present the results of the topological analysis of the ED in  $\text{Li}_2\text{SeO}_4 \cdot \text{H}_2\text{O}$  based on the density distributions that were on the one hand theoretically calculated with *WIEN2k* and on the other hand experimentally determined. On the whole, both data sets are consistent with each other. Due to the occurred model inadequacies related to the ED of the heavy Se atom (as depicted in Fig. 4.13), the

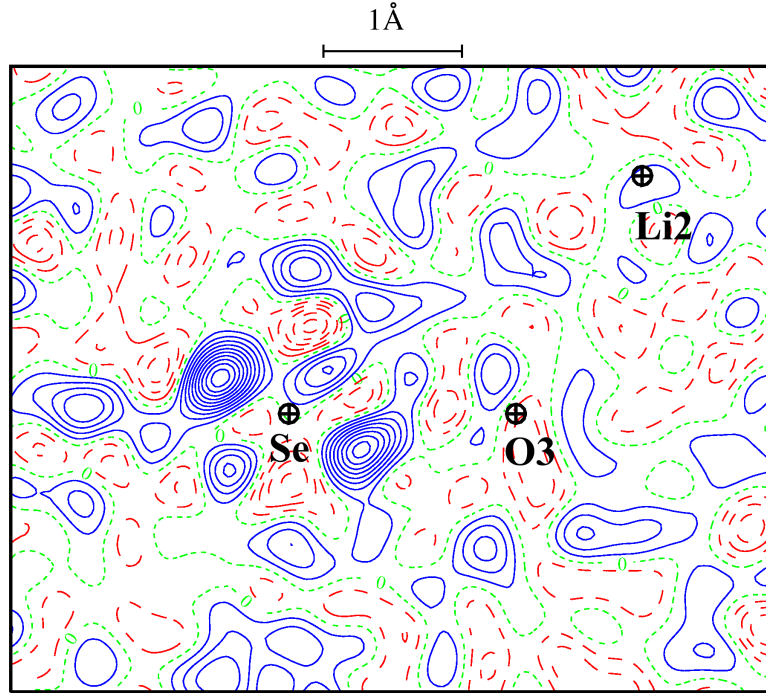


**Figure 4.13:** Residual ED map within the Se–O3–Li2 plane. Contour intervals are at  $0.05 \text{ e } \text{Å}^{-3}$ , broken red lines represent negative contours, whereas the blue lines indicate positive contours.

**Table 4.20:** Theoretical values of the ED ( $\text{e } \text{Å}^{-3}$ ), Laplacian ( $\text{e } \text{Å}^{-5}$ ), eigenvalues of the Hessian matrix ( $\text{e } \text{Å}^{-5}$ ) and electronic energy density (a.u.) at the Se–O, Li1–O, Li2–O bond critical points ( $\mathbf{r}_c$ ) averaged over the bonds within the  $\text{SeO}_4$ ,  $\text{Li1O}_4$  and  $\text{Li2O}_4$  tetrahedra.

	$\langle \rho(\mathbf{r}_c) \rangle$	$\langle \nabla^2 \rho(\mathbf{r}_c) \rangle$	$\langle \lambda_1 \rangle$	$\langle \lambda_2 \rangle$	$\langle \lambda_3 \rangle$	$\langle h \rangle$
$\text{SeO}_4$	1.56 (1)	1.7 (1)	−8.0 (1)	−8.0 (1)	17.7 (1)	−0.244 (3)
$\text{Li1O}_4$	0.16 (1)	5.2 (8)	−0.9 (2)	−0.9 (1)	6.9 (7)	0.012 (2)
$\text{Li2O}_4$	0.17 (2)	5.7 (8)	−0.9 (1)	−1.0 (1)	7.6 (8)	0.014 (2)

**Table 4.21:** Experimental values of the ED ( $\text{e } \text{Å}^{-3}$ ), Laplacian ( $\text{e } \text{Å}^{-5}$ ), eigenvalues of the Hessian matrix ( $\text{e } \text{Å}^{-5}$ ) and electronic energy density (a.u.) at the Se–O, Li1–O, Li2–O bond critical points ( $\mathbf{r}_c$ ) averaged over the bonds within the  $\text{SeO}_4$ ,  $\text{Li1O}_4$  and  $\text{Li2O}_4$  tetrahedra.

	$\langle \rho(\mathbf{r}_c) \rangle$	$\langle \nabla^2 \rho(\mathbf{r}_c) \rangle$	$\langle \lambda_1 \rangle$	$\langle \lambda_2 \rangle$	$\langle \lambda_3 \rangle$	$\langle h \rangle$
$\text{SeO}_4$	1.58 (13)	9.4 (30)	−11.2 (19)	−9.1 (14)	29.7 (19)	−0.223 (25)
$\text{Li1O}_4$	0.24 (2)	3.6 (7)	−1.3 (1)	−1.2 (1)	6.0 (6)	0.001 (1)
$\text{Li2O}_4$	0.24 (2)	3.7 (5)	−1.3 (1)	−1.2 (1)	6.2 (5)	0.002 (1)

theoretical DFT calculations are regarded as more reliable for further discussion and data treatment. Accordingly, the Se–O chemical bonds are of intermediate interactions, because:  $\langle \nabla^2 \rho(\mathbf{r}_c) \rangle > 0$  and  $\langle h \rangle < 0$  at the Se–O bond critical points, see Table 4.20. The calculated charges (first row of Table 4.22) of the individual pseudoatoms of  $\text{Li}_2\text{SeO}_4\cdot\text{H}_2\text{O}$  have all meaningful values. Figures 4.14 and 4.15 illustrate the difference ED sections in a plane containing the O2, Se and O3 atoms and the O5, Li2 and O3 atoms, respectively.

As visible in Fig. 4.15, the theoretical DFT density clearly reveals an ED redistribution within the O5–H1 bond of the water molecule of  $\text{Li}_2\text{SeO}_4 \cdot \text{H}_2\text{O}$ , which indicates a good quality of the performed DFT calculations.

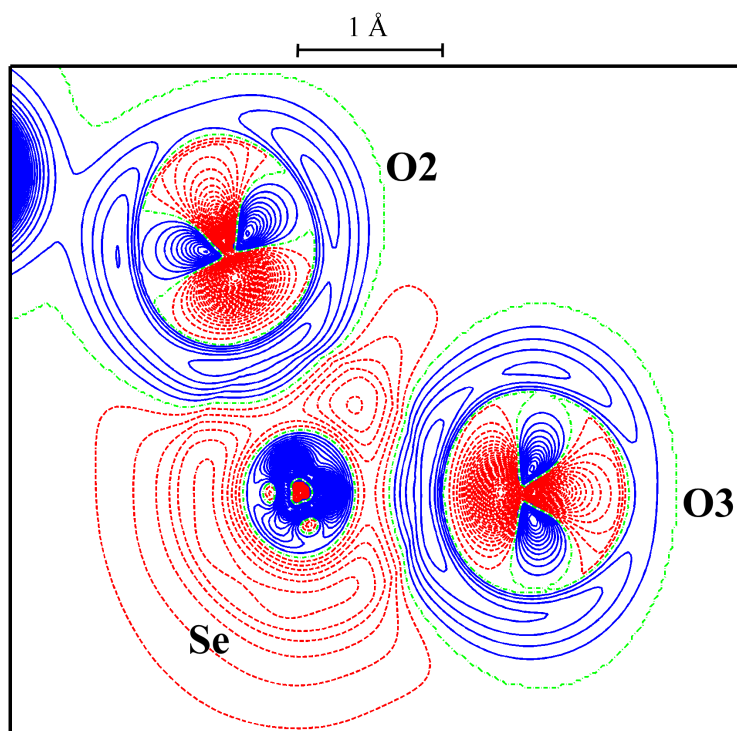


**Figure 4.14:** Theoretically calculated difference ED within the O2–Se–O3 plane. Contours are as in Fig. 4.13.

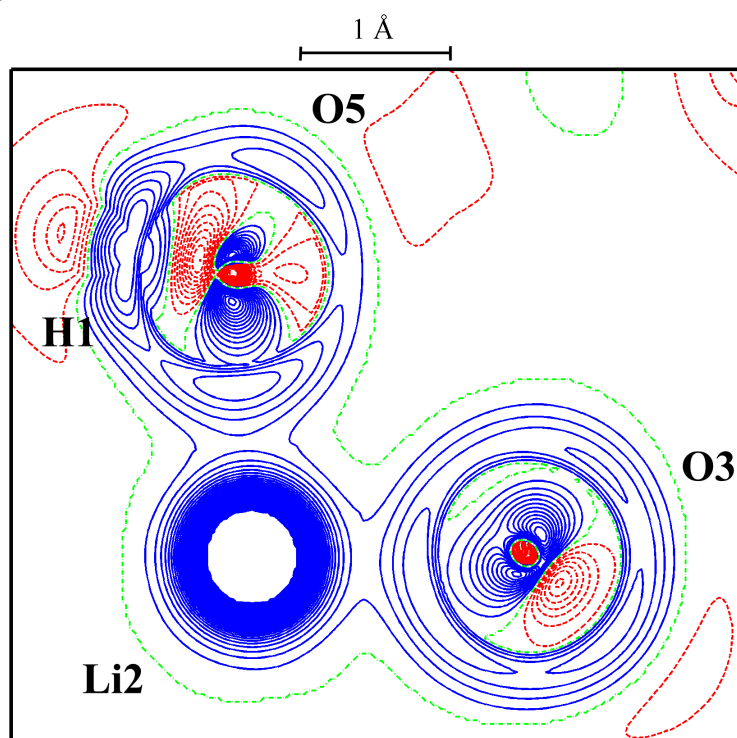


**Figure 4.15:** Theoretically calculated difference ED within the O5–Li2–O3 plane (contours are as in Fig. 4.13).

**Table 4.22:** Theoretical and experimental pseudoatomic charges of  $\text{Li}_2\text{SeO}_4\cdot\text{H}_2\text{O}$ .

	Se	Li1	Li2	O1	O2	O3	O4	O5	H1	H2
$Q_{WIEN2k}$ (e)	3.36	0.86	0.87	-1.27	-1.28	-1.29	-1.24	-1.34	0.66	0.66
$Q_{\text{EXP}}$ (e)	2.44	0.95	0.95	-1.00	-1.00	-1.00	-0.92	-1.25	0.42	0.42

## 4.2.2 Electric-field-induced atomic rearrangement

For the electric field experiment a 0.778 (2) mm thick plane-parallel  $\text{Li}_2\text{SeO}_4\cdot\text{H}_2\text{O}$  crystal plate of a (010) orientation was available. Applying the HV values  $U_{\pm} = \pm 3$  kV a maximum external electric field up to  $E = 3.9(1)$  kV mm<sup>-1</sup> could be generated in the crystal. An attempt to use a thinner sample failed, as under the applied four-step modulated HV a 0.685 (2) mm thick plate became conducting after some hours and eventually was completely destroyed. This occurrence observed also indicates that in the case of the thicker plate the measurements were conducted extremely near to the electrical breakdown condition of  $\text{Li}_2\text{SeO}_4\cdot\text{H}_2\text{O}$ .

The four piezoelectric constants  $d_{211}$ ,  $d_{222}$ ,  $d_{233}$  and  $d_{213}$  of  $\text{Li}_2\text{SeO}_4\cdot\text{H}_2\text{O}$  calculated from the measured angular shifts of rocking curve positions agree well with the values that were macroscopically obtained employing a dynamic pressure cell [66], see Table 4.23. Consequently, it can be assumed that the electric field created in the sample was homogeneous and constant throughout the crystal volume confined by the gold contacts as well as the crystal plate used for the measurements was of good quality.

**Table 4.23:** Piezoelectric constants  $d_{211}$ ,  $d_{222}$ ,  $d_{233}$  and  $d_{213}$  (pC N<sup>-1</sup>) of  $\text{Li}_2\text{SeO}_4\cdot\text{H}_2\text{O}$  measured by means of the X-ray diffraction technique (see section 2.3.1) and employing a dynamical pressure cell [66, 76] are presented.

	X-ray diffraction	Dynamic pressure cell [66]
$d_{211}$	-1.8 (2)	-3.6 (2)
$d_{222}$	14.8 (3)	13.3 (9)
$d_{233}$	0.2 (1)	0.8 (2)
$d_{213}$	-1.5 (1)	-2.8 (2)

The  $K$  absorption edge of Se has an X-ray wavelength of 0.98 Å [78], see Fig. 4.16. In order to diminish the scattering contribution of the Se atoms to the diffraction intensities of  $\text{Li}_2\text{SeO}_4\cdot\text{H}_2\text{O}$ , all measurements were performed above the Se  $K$  edge, *i.e.* mainly at  $\lambda = 0.99$  Å. In this context, Figure 4.17 demonstrates for the 040 reflection the dependence of  $|F|^2$  (2.1) on the X-ray wavelengths in the vicinity of the Se  $K$  edge. Thus, by reducing the scattering amplitude of Se to a minimum value, it became also possible to probe the displacements of the light Li and O atoms in  $\text{Li}_2\text{SeO}_4\cdot\text{H}_2\text{O}$ . Near below the Se  $K$  edge the X-ray absorption by the crystal plate was too strong to allow reasonable measurements especially of the reflections in the transmission geometry that are normally the most sensitive to the induced structural changes.

In total, the refinement of the electric-field-induced atomic displacements in  $\text{Li}_2\text{SeO}_4\cdot\text{H}_2\text{O}$  was based on the relative intensity variations measured for 53 non-symmetry-equivalent reflections, as given in Table A.2 in the appendix. Compared with the  $\text{Li}_2\text{SO}_4\cdot\text{H}_2\text{O}$  data (Table A.1), the  $\text{Li}_2\text{SeO}_4\cdot\text{H}_2\text{O}$  data set is by a factor of two smaller and therefore, a more general approach for modeling the rearrangement of atoms in  $\text{Li}_2\text{SeO}_4\cdot\text{H}_2\text{O}$  under an external electric field had to be considered. In particular, deviating from the discussion

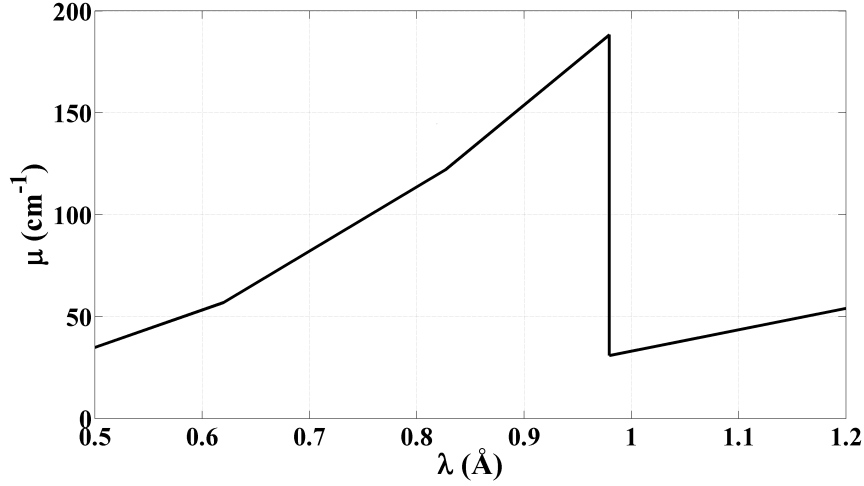


**Figure 4.16:** X-ray linear attenuation coefficient of  $\text{Li}_2\text{SeO}_4 \cdot \text{H}_2\text{O}$  in the vicinity of the  $K$  absorption edge of Se,  $\lambda(K) = 0.98 \text{ \AA}$  [78].

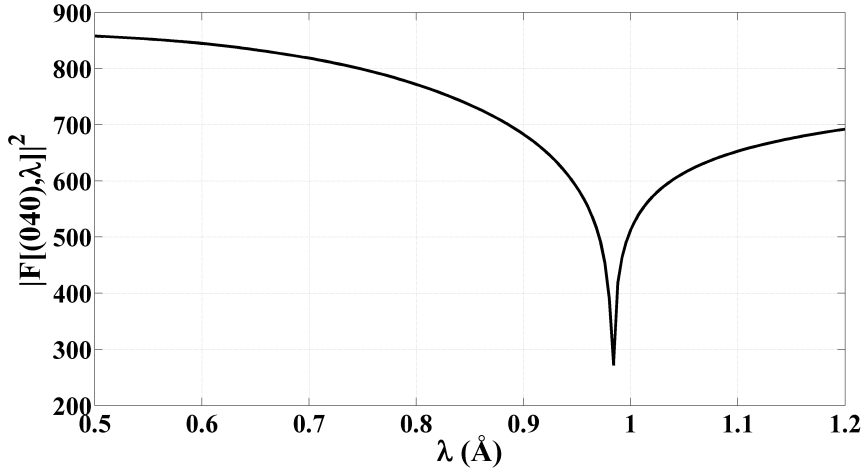


**Figure 4.17:**  $|F[(040), \lambda]|^2$  (2.1) calculated as a function of the X-ray wavelength in the range from 0.5 to 1.2  $\text{\AA}$  which includes the Se  $K$  absorption edge, see Fig. 4.16.

**Table 4.24:** Main parameters of the refinement of the atomic displacements in  $\text{Li}_2\text{SeO}_4 \cdot \text{H}_2\text{O}$  under an external electric field.

No. $(\Delta I/I)_a$	No. of variables	$R$	$R_w$	$\chi^2$	$\langle \sigma /  (\Delta I/I)_a  \rangle$
53	19	0.31	0.38	564	0.23

in section 4.1.3, the displacements of all five O atoms were refined independently from each other and without an application of any constraints. The behavior of the two crystallographically different Li atoms was constrained to be the same. But the assumption that the Li shifts are exactly parallel to  $\mathbf{E}_+ = 3.9 \times \mathbf{e}_2 \text{ kV mm}^{-1}$  ( $\mathbf{E}_+ \parallel \mathbf{a}_2$ ) had to be abandoned. As a result, the number of variables required for an adequate description of the microscopic structural changes in  $\text{Li}_2\text{SeO}_4 \cdot \text{H}_2\text{O}$  increased from 13 to 19. As displayed in Table 4.24, the  $R$  and  $R_w$  values are small but at the same time they are too high for an introduction of additional constraints beyond the model used. In Table 4.25 for all atoms regarded the refined components,  $\Delta R^i$ , of the displacement vectors are summarized. According to the values presented, the Li atoms are the most affected by the applied electric

**Table 4.25:** In  $\text{Li}_2\text{SeO}_4\cdot\text{H}_2\text{O}$  determined displacements of atoms induced by an applied electric field of the magnitude  $\mathbf{E}_+ = 3.9 \times \mathbf{e}_2 \text{ kV mm}^{-1}$ ,  $\mathbf{E}_+ \parallel \mathbf{a}_2$ . The components of the displacement vectors,  $\Delta\mathbf{R}_\mu$ , are related to the crystallographic system.

Atom	$\Delta R^1 (10^{-5})$	$\Delta R^2 (10^{-5})$	$\Delta R^3 (10^{-5})$
Se	-3.3 (2)	-111 (3)	-3.0 (2)
Li1	-85 (3)	227 (2)	111 (3)
Li2	-85 (3)	227 (2)	111 (3)
O1	48 (2)	-48 (11)	39 (1)
O2	2 (2)	-79 (3)	-12 (1)
O3	13 (1)	-86 (2)	19 (2)
O4	-0.4 (8)	-72 (2)	28 (1)
O5	-26 (2)	-58 (4)	73 (2)

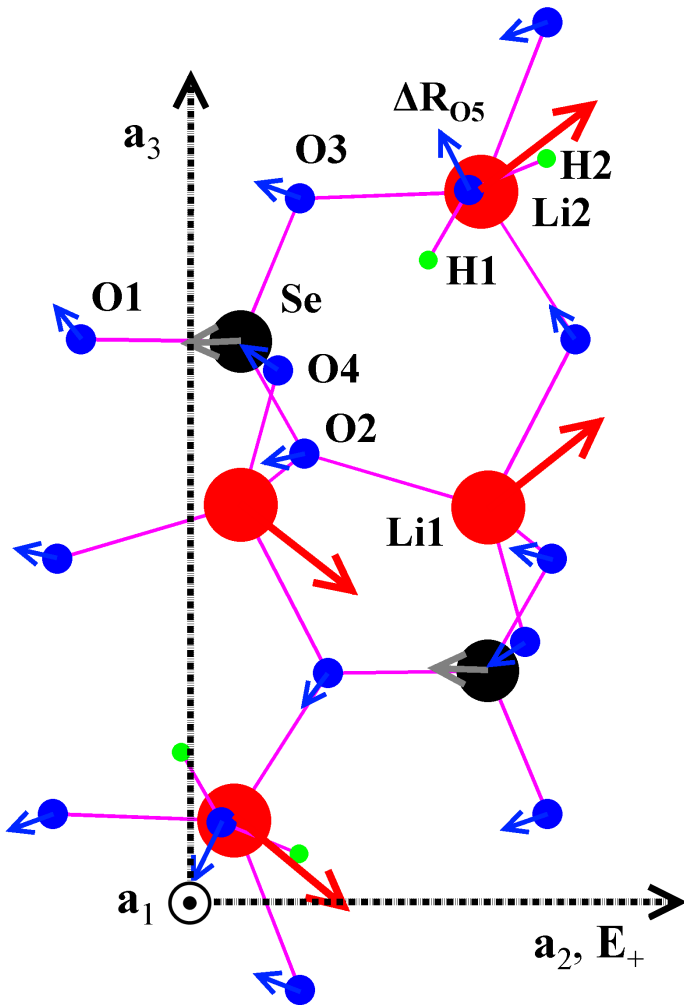


**Figure 4.18:** Schematic representation of the crystal structure of  $\text{Li}_2\text{SeO}_4\cdot\text{H}_2\text{O}$  [55] together with the determined electric-field-induced atomic displacements (see Table 4.25) viewed along the  $\mathbf{a}_1$  axis. Due to the reasons relating to a better illustration of the effect observed, the values presented in Table 4.25 were multiplied by a factor of 100. Expectedly, compared to the O and Se atoms the shifts of the Li atoms are by far the largest and mainly oriented in the direction of the applied electric field. As shown in the plot, the  $\text{LiO}_4$ ,  $\text{Li}_2\text{O}_3(\text{H}_2\text{O})$  and  $\text{SeO}_4$  groups are arranged to tetrahedral three-rings.

perturbation of the crystal and exhibit the largest component of  $\Delta\mathbf{R}$  along  $\mathbf{E}_+$ , while the Se atom is mainly displaced in the opposite direction. Figure 4.18 illustrates the absolute values and directions of the atomic  $\Delta\mathbf{R}_\mu$  vectors projected into the plane spanned by  $\mathbf{a}_2$  and  $\mathbf{a}_3$ . Note that the true lengths of  $\Delta\mathbf{R}_\mu$  are by a factor of 100 smaller than depicted in Fig. 4.18. In comparison with the  $\text{Li}_2\text{SO}_4\cdot\text{H}_2\text{O}$  results (see Table 4.12) the atomic structure of  $\text{Li}_2\text{SeO}_4\cdot\text{H}_2\text{O}$  is more strongly deformed, although the external electric field

was considerably weaker:  $E_+(\text{S}) = 5.1 \text{ kV mm}^{-1}$  and  $E_+(\text{Se}) = 3.9 \text{ kV mm}^{-1}$ .

A detailed analysis of the determined variations of the individual bond lengths in the structural units,  $\text{Li1O}_4$ ,  $\text{Li2O}_4$  and  $\text{SeO}_4$ , of  $\text{Li}_2\text{SeO}_4 \cdot \text{H}_2\text{O}$  induced by  $\mathbf{E}_+ = 3.9 \times \mathbf{e}_2 \text{ kV mm}^{-1}$  is demonstrated in Tables 4.26 and 4.27. Accordingly, the change of the Li–O distances is on average about five times larger than in the case of the Se–O bonds. Besides, since the internal strain is strongly pronounced in  $\text{Li}_2\text{SeO}_4 \cdot \text{H}_2\text{O}$ , the external strain has less effect on the deformation of the atomic bonds under an electric perturbation, as shown in the last row of Table 4.27.

**Table 4.26:** Electric-field-induced variation of the individual bond lengths ( $10^{-5} \text{ \AA}$ ) in the  $\text{Li1O}_4$ ,  $\text{Li2O}_4$  and  $\text{SeO}_4$  tetrahedra,  $\mathbf{E}_+ = 3.9 \times \mathbf{e}_2 \text{ kV mm}^{-1}$ . Symmetry codes are: (i)  $-x, \frac{1}{2} + y, 1 - z$ ; (ii)  $x, 1 + y, 1$ ; (iii)  $1 - x, \frac{1}{2} + y, 1 - z$ ; (iv)  $x, 1 + y, z$ ; (v)  $1 - x, \frac{1}{2} + y, 2 - z$ .

$\text{Li1O}_4$		$\text{Li2O}_4$		$\text{SeO}_4$	
$\Delta(\text{Li1} - \text{O2})$	-1300 (10)	$\Delta(\text{Li2} - \text{O3})$	-1270 (7)	$\Delta(\text{Se} - \text{O1})$	281 (42)
$\Delta(\text{Li1} - \text{O4}^{\text{i}})$	39 (32)	$\Delta(\text{Li2} - \text{O5})$	-520 (6)	$\Delta(\text{Se} - \text{O2})$	-143 (3)
$\Delta(\text{Li1} - \text{O1}^{\text{ii}})$	1331 (11)	$\Delta(\text{Li2} - \text{O1}^{\text{iv}})$	619 (38)	$\Delta(\text{Se} - \text{O3})$	-213 (10)
$\Delta(\text{Li1} - \text{O2}^{\text{iii}})$	-367 (6)	$\Delta(\text{Li2} - \text{O3}^{\text{v}})$	1693 (33)	$\Delta(\text{Se} - \text{O4})$	-61 (4)

**Table 4.27:** Average change of the cation-anion distances ( $10^{-5} \text{ \AA}$ ) in the three different structural units,  $\text{Li1O}_4$ ,  $\text{Li2O}_4$  and  $\text{SeO}_4$ , of  $\text{Li}_2\text{SeO}_4 \cdot \text{H}_2\text{O}$  referred to  $E_+ = 1 \text{ kV mm}^{-1}$ . The values given in the last row were calculated by taking account of the influence of the converse piezoelectric effect.

	$\langle  \Delta(\text{Li1} - \text{O})  \rangle$	$\langle  \Delta(\text{Li2} - \text{O})  \rangle$	$\langle  \Delta(\text{Se} - \text{O})  \rangle$
Internal strain	195 (3)	263 (3)	45 (3)
Int. & ext. strain	195 (3)	263 (3)	44 (3)

### 4.2.3 Comparison of the bond-selective response strength of different piezoelectric crystals

In agreement with the pure ionic Li–O interactions the average deformation of the Li–O bonds in  $\text{Li}_2\text{SeO}_4 \cdot \text{H}_2\text{O}$  (see Table 4.27) is about five times greater than the variation of the Se–O bonds, which exhibit intermediate interactions. Compared with the  $\text{Li}_2\text{SO}_4 \cdot \text{H}_2\text{O}$  results, the electric-field-induced change of the Li–O bond lengths is by a factor of about 20 larger, as given in Table 4.28. Furthermore, the distortion of the Se–O bonds is more than 50 times greater than that obtained for the S–O bonds. Indeed, the average Se–O interaction strength [ $\langle \rho(\mathbf{r}_c) \rangle (\text{Se} - \text{O}) = 1.66 (9) \text{ e \AA}^{-3}$ ] is smaller compared to that of the S–O bonds [ $\langle \rho(\mathbf{r}_c) \rangle (\text{S} - \text{O}) = 1.95 (5) \text{ e \AA}^{-3}$ ], but this difference is not such wide to give a lucid explanation about the effect observed, even if the pseudoatomic charges of S and Se are taken into account. As  $Q(\text{S}) = 4.3 (1) \text{ e}$  is larger than the charge of Se [ $Q(\text{Se}) = 2.9 (5) \text{ e}$ ] one would expect a lower electric force acting on Se in an external field, which would be in direct contradiction to the experimental results. All in all, it becomes obvious that the properties of the static electron density, such as pseudoatomic charges and strength of chemical bonds, can be well used to explain the behavior of different structural units in a crystal under an external electric perturbation. But at the same time, within this approach one cannot understand why in  $\text{Li}_2\text{SO}_4 \cdot \text{H}_2\text{O}$ ,  $\text{Li}_2\text{SeO}_4 \cdot \text{H}_2\text{O}$  and  $\text{LiH}_2\text{PO}_4$

**Table 4.28:** Electric-field-induced average change of the cation-anion distances in the  $\text{LiO}_4$  and  $\text{SO}_4$  groups of  $\text{Li}_2\text{SO}_4\cdot\text{H}_2\text{O}$ , in the  $\text{LiO}_4$  and  $\text{SeO}_4$  groups of  $\text{Li}_2\text{SeO}_4\cdot\text{H}_2\text{O}$ , in the  $\text{LiO}_4$  and  $\text{PO}_4$  groups of  $\text{LiH}_2\text{PO}_4$  [79], in the  $\text{PO}_4$  and  $\text{GaO}_4$  groups of  $\alpha\text{-GaPO}_4$  [14], in the  $\text{PO}_4$  group of  $\text{KH}_2\text{PO}_4$  [11] (measured at 167 K) and  $\text{KD}_2\text{PO}_4$  [9, 10] and in the  $\text{SiO}_4$  group of  $\alpha\text{-SiO}_2$  [13] normalized to the electric field  $E = 1 \text{ kV mm}^{-1}$ .

Crystal	Tetrahedron	$\langle  \Delta(\mu - \text{O})  \rangle$ ( $10^{-5} \text{ \AA}$ )
$\text{Li}_2\text{SO}_4\cdot\text{H}_2\text{O}$	$\text{LiO}_4$	11.3 (2)
	$\text{SO}_4$	0.8 (2)
$\text{Li}_2\text{SeO}_4\cdot\text{H}_2\text{O}$	$\text{LiO}_4$	229 (34)
	$\text{SeO}_4$	44 (3)
$\text{LiH}_2\text{PO}_4$	$\text{LiO}_4$	5.2 (2)
	$\text{PO}_4$	3.0 (8)
$\alpha\text{-GaPO}_4$	$\text{PO}_4$	4.3 (7)
	$\text{GaO}_4$	1.5 (9)
$\text{KH}_2\text{PO}_4$	$\text{PO}_4$	43 (2)
$\text{KD}_2\text{PO}_4$	$\text{PO}_4$	74 (4)
$\alpha\text{-SiO}_2$	$\text{SiO}_4$	331 (160)

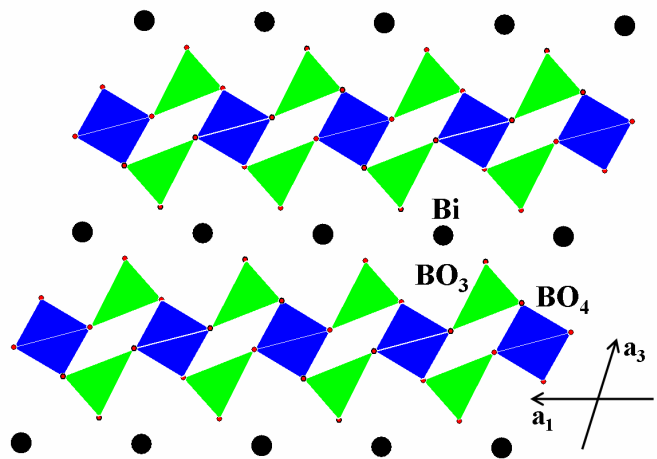
[79] the Li–O bonds differ such strongly in their response, as shown in Table 4.28. The  $\text{LiO}_4$  structural units are in each of the three crystal structures of a nearly identical size and small degree of tetrahedral distortion: See Tables 4.1 and 4.15 for  $\text{Li}_2\text{SO}_4\cdot\text{H}_2\text{O}$  and  $\text{Li}_2\text{SeO}_4\cdot\text{H}_2\text{O}$ , respectively and for  $\text{LiH}_2\text{PO}_4$  one has [80]:  $\langle \text{Li} - \text{O} \rangle = 1.96 (2) \text{ \AA}$  and  $|\mathbf{D}_{\text{tetr}}| = 0.034 (2) \text{ \AA}$  [see eq. (4.1)]. All these crystals are Li-ion conductors and therefore, the magnitude of the Li displacements induced by an external electric field depends on the strength of the hydrogen bonds in the crystals and on how compact their crystal structure is [81]. As the  $\text{SO}_4$  tetrahedra [ $\langle \text{S} - \text{O} \rangle = 1.47 (1) \text{ \AA}$ ] are smaller than the  $\text{SeO}_4$  groups [ $\langle \text{Se} - \text{O} \rangle = 1.63 (1) \text{ \AA}$ ] there are greater vacancies in the structure of  $\text{Li}_2\text{SeO}_4\cdot\text{H}_2\text{O}$ , thus the Li ions can much easier move within the crystal. On the other hand, in the case of  $\text{LiH}_2\text{PO}_4$  with  $\langle \text{P} - \text{O} \rangle = 1.54 (1) \text{ \AA}$  the detected effect seems to originate mainly from the major differences in the hydrogen-bonding scheme within  $\text{LiH}_2\text{PO}_4$  and  $\text{Li}_2\text{SO}_4\cdot\text{H}_2\text{O}$ . Finally, the average P–O bond deformation measured in  $\text{KD}_2\text{PO}_4$  [9, 10] is almost equal to that determined for the Se–O bonds, but it is at the same time by one order of magnitude larger than for the P–O bonds in  $\alpha\text{-GaPO}_4$  and  $\text{LiH}_2\text{PO}_4$ . This is another indication that under an electric perturbation the distortion of similar tetrahedral groups is strongly dependent on the specific properties of their chemical environment in contrast to the findings reported in hydrostatic high-pressure studies [82]. In this context, it is quite evident that the electric-field-induced average change of the P–O bond lengths in  $\text{KH}_2\text{PO}_4$  (studied at 167 K) [11] is different from the results obtained for  $\text{KD}_2\text{PO}_4$ , see Table 4.28. Besides, as the dielectric and piezoelectric properties of a crystal are normally anisotropic, the direction of an external electric field with respect to the crystal structure also has a large influence on the distortion of the chemical bonds in the crystal. This aspect will be treated in more detail in the next section where the properties of the internal strain in  $\text{BiB}_3\text{O}_6$  are studied as a function of the electric field direction. Neglecting the experimental value of the Si–O bond deformation in  $\alpha\text{-SiO}_2$  (displayed in the last row of Table 4.28), which does not seem to be very reliable, the deduced average distortion of the ionic Li–O bonds in  $\text{Li}_2\text{SeO}_4\cdot\text{H}_2\text{O}$  is the largest among the essentially covalent P–O, S–O, Ga–O and Se–O bonds.

### 4.3 Bismuth triborate, $\text{BiB}_3\text{O}_6$

The X-ray determination of the piezoelectric constants of  $\text{BiB}_3\text{O}_6$  was the main part of my diploma thesis [83]. Therefore, this subject will be briefly outlined in this work only. In contrast, the analysis of the internal strain induced in differently oriented  $\text{BiB}_3\text{O}_6$  crystal plates has been completely revised and strongly extended. All remaining sections deal with topics that bear no relation to my diploma thesis.

The crystal structure of  $\text{BiB}_3\text{O}_6$  (space group  $C2$ ,  $a_1 = 7.116(2) \text{ \AA}$ ,  $a_2 = 4.993(2) \text{ \AA}$ ,  $a_3 = 6.508(3) \text{ \AA}$  and  $\alpha_2 = 105.62(3)^\circ$ ) consists of alternating borate and Bi sheets arranged parallel to the (001) Miller plane [56]. The borate sheets are intersected by layers of Bi atoms and are built up by corner-sharing tetrahedral,  $\text{BO}_4$ , and trigonal,  $\text{BO}_3$ , structural units, as shown in Figs. 4.19 and 4.21. Bismuth has a six-fold oxygen coordination of a strongly irregular shape. The unit cell of  $\text{BiB}_3\text{O}_6$  contains 6 symmetry-independent atoms (Bi, B1, B2, O1, O2 and O3), where two of them occupy special positions with the point group symmetry 2: Bi at the site 2a and B1 at the site 2b [56].

**Figure 4.19:** Crystal structure of  $\text{BiB}_3\text{O}_6$  viewed along the two-fold axis,  $\mathbf{a}_2$ . The alternating borate sheets, which consist of two-dimensional networks of the  $\text{BO}_4$  and  $\text{BO}_3$  groups, and the Bi layers are well visible in this schematic representation.



$\text{BiB}_3\text{O}_6$  is a non-linear optical crystal [84] known for its exceptional physical properties. Among non-ferroelectric polar materials it ranges as a crystal that exhibits one of the highest piezoelectric effect [85]. The absolute value of the piezoelectric constant  $d_{222} = -39.5(10) \text{ pC N}^{-1}$ , which describes the maximum longitudinal piezoelectric effect along the two-fold axis, is more than 17 times larger than  $d_{111} = 2.3 \text{ pC N}^{-1}$  [67] of  $\alpha$ -quartz. In addition, the piezoelectric tensor of  $\text{BiB}_3\text{O}_6$  is strongly anisotropic as well as the elastic [85] and thermal expansion [86] behavior of this crystal. The extreme anisotropy of these macroscopic physical properties correlates well with the sheet structure of  $\text{BiB}_3\text{O}_6$ , the mutual interconnection of the  $\text{BiO}_6$ ,  $\text{B1O}_4$  and  $\text{B2O}_3$  groups and the orientation of the lone-pair electrons at the Bi ion [85, 87].

Large single crystals of  $\text{BiB}_3\text{O}_6$  were grown by P. Becker using the top-seeding technique [88]. The measurements were performed with crystals of the morphology illustrated in Fig. 4.20 [88], where additionally the face indices of  $\text{BiB}_3\text{O}_6$  and the mutual relation of the crystallographic system,  $\{\mathbf{a}_i\}$ , the Cartesian coordinate system,  $\{\mathbf{e}_i\}$ , and the reciprocal system,  $\{\mathbf{b}_i\}$  are presented ( $\mathbf{e}_2 \parallel \mathbf{a}_2 \parallel \mathbf{b}_2$ ,  $\mathbf{e}_3 \parallel \mathbf{a}_3$  and  $\mathbf{e}_1 = \mathbf{e}_2 \times \mathbf{e}_3 \parallel \mathbf{b}_1$ ). In the case of these left-handed crystals the sign of the longitudinal piezoelectric constant  $d_{222}$  is negative. For the X-ray diffraction experiments three crystal plates (see Table 4.29) were cut from a crystal parallel to the (100), (010) and (001) Miller plane. Since the boron isotope  $^{10}\text{B}$  is a strong neutron absorber, for the neutron diffraction studies two additional plane-parallel (010) plates of different thickness (as shown in Table 4.29) were

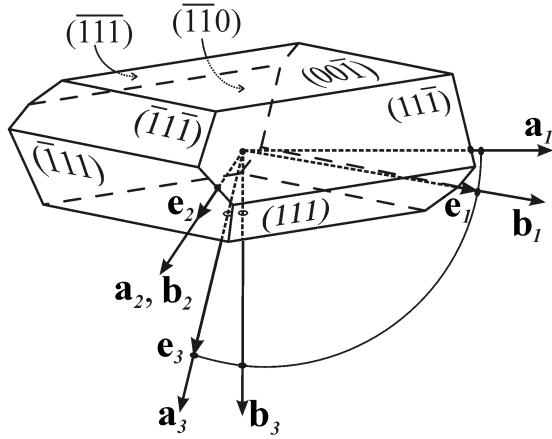


**Figure 4.20:** Typical morphology of a left-handed  $\text{BiB}_3\text{O}_6$  crystal [88] together with the face indices, the crystallographic system ( $\mathbf{a}_1$ ,  $\mathbf{a}_2$  and  $\mathbf{a}_3$ ), the Cartesian system ( $\mathbf{e}_1$ ,  $\mathbf{e}_2$  and  $\mathbf{e}_3$ ) and the reciprocal system ( $\mathbf{b}_1$ ,  $\mathbf{b}_2$  and  $\mathbf{b}_3$ ).

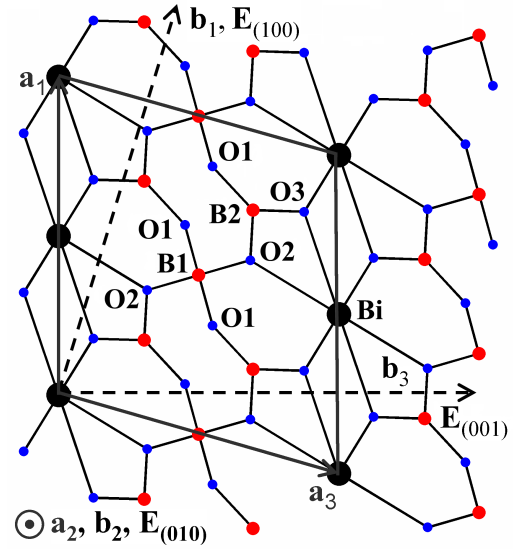


**Figure 4.21:** In this plot of the crystal structure of  $\text{BiB}_3\text{O}_6$  viewed along the  $\mathbf{a}_2$  axis the directions of the electric field vectors  $\mathbf{E}_{(100)}$ ,  $\mathbf{E}_{(010)}$  and  $\mathbf{E}_{(001)}$  are displayed with respect to the orientation of the  $\mathbf{a}_i$  and  $\mathbf{b}_i$  axes and the  $\text{B1O}_4$  and  $\text{B2O}_3$  groups.

prepared from  $\text{BiB}_3\text{O}_6$  crystals containing the element  $^{11}\text{B}$  exclusively. The opposite faces  $(0 \pm 1 0)$  of these two samples were fully sputtered with gold. That way, it was possible to illuminate the plates completely with a maximum beamsize, which made a maximum neutron flux at the specimens available in the experiments. In Table 4.29 for each plate the thickness ( $d$ ) and the maximum absolute value of an applied external electric field ( $|\mathbf{E}|_{\text{max}}$ ) are given. Figure 4.21 shows the directions of the electric field vectors  $\mathbf{E}_{(100)}$ ,  $\mathbf{E}_{(010)}$  and  $\mathbf{E}_{(001)}$  with respect to the orientation of the  $\mathbf{a}_i$  and  $\mathbf{b}_i$  axes.

**Table 4.29:** Summary of the  $\text{BiB}_3\text{O}_6$  crystal plates used in the X-ray and neutron diffraction experiments: The orientation of the plates, their thickness ( $d$ ) and the respective maximum absolute value of an applied electric field ( $|\mathbf{E}|_{\text{max}}$ ) are presented.

	$^{10}\text{B}/^{11}\text{B}$ plates			$^{11}\text{B}$ plates	
	(100)	(010)	(001)	(010)	(010)
$d$ (mm)	0.570 (2)	0.533 (2)	0.295 (2)	0.718 (2)	0.218 (2)
$ \mathbf{E} _{\text{max}}$ (kV mm $^{-1}$ )	4.4 (1)	3.8 (1)	5.1 (1)	4.2 (1)	6.9 (2)

### 4.3.1 X-ray determination of the piezoelectric constants

All eight independent piezoelectric tensor components (1.30) of  $\text{BiB}_3\text{O}_6$  were determined on the basis of expression (2.40). Using the (100) plate, from measured Bragg peak shifts with  $\mathbf{E}_{100} \parallel \mathbf{e}_1$  the piezoelectric constants  $d_{123}$  and  $d_{112}$  were refined. From the (010) plate data the four constants  $d_{211}$ ,  $d_{222}$ ,  $d_{233}$  and  $d_{213}$  were experimentally accessible,  $\mathbf{E}_{010} \parallel \mathbf{e}_2$ . In the case of the (001) plate the vector  $\mathbf{E}_{001}$  is parallel to  $\mathbf{e} = 0.27 \times \mathbf{e}_1 + 0.96 \times \mathbf{e}_3$ , thus the measurements performed with this sample enabled the determination of the last two missing constants  $d_{312}$  and  $d_{323}$ , which were in this approach also dependent on  $d_{123}$

and  $d_{112}$ . Figures 4.22 and 4.23 demonstrate how the piezoelectric constants  $d_{211}$ ,  $d_{222}$ ,  $d_{233}$ ,  $d_{213}$  and the independent coefficients  $R_{212}$ ,  $R_{213}$ ,  $R_{223}$  of the rotation tensor  $[R_{2jk}]$  converge with an increasing number of linear equations of the over-determined system (2.40), respectively.

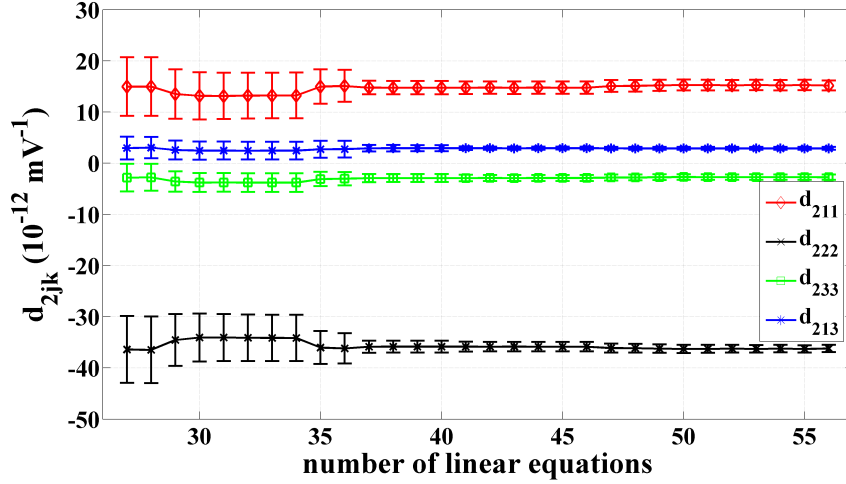


**Figure 4.22:** Four piezoelectric constants  $d_{211}$ ,  $d_{222}$ ,  $d_{233}$  and  $d_{213}$  of  $\text{BiB}_3\text{O}_6$  calculated as a function of the number of linear equations (2.40) forming an over-determined system. The standard deviation of the parameters  $d_{2jk}$  decreases with an increasing number of linear equations.

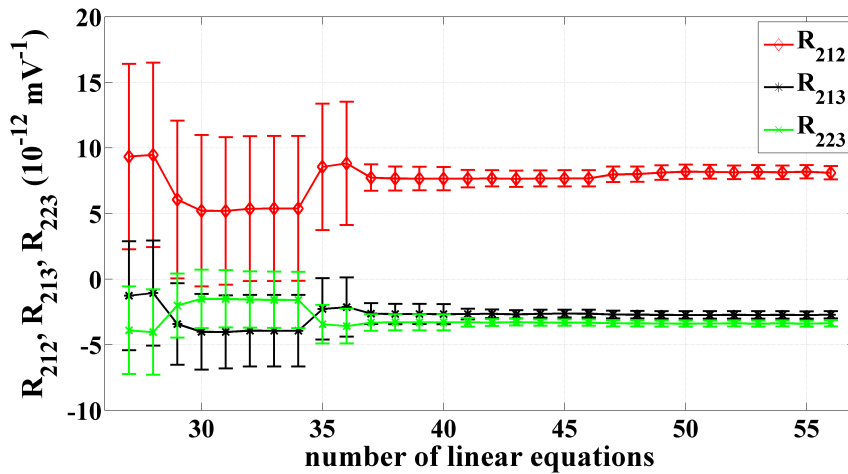


**Figure 4.23:** Three independent components  $R_{212}$ ,  $R_{213}$  and  $R_{223}$  of the rotation tensor  $[R_{2jk}]$  refined together with the piezoelectric constants  $d_{211}$ ,  $d_{222}$ ,  $d_{233}$  and  $d_{213}$  (see Fig. 4.22). With an increasing number of linear equations (2.40) all seven constants start to converge.

The piezoelectric constants of  $\text{BiB}_3\text{O}_6$  refined from the X-ray diffraction data and those obtained by means of the Michelson interferometer [85] are shown in Table 4.30, both data sets are in good agreement. The components of the rotation tensor for each of the three samples are presented in Table 4.31. As discussed in section 2.3.1 of chapter 2, the tensor  $[R_{ijk}]$  has its physical significance only for the given individual setup conditions of a crystal plate. In the case of the (001) plate the tensor coefficients  $R_{3jk}^* = 0.27 \times R_{1jk} + 0.96 \times R_{3jk}$  were considered. Especially, both coefficients  $R_{112} = 16.8$  (1)  $\text{pC N}^{-1}$  and  $R_{323}^* = -16.2$  (13)  $\text{pC N}^{-1}$  are relatively large, which indicates that the rotation contribution of the (100) and (001) plate to the angular shift of a Bragg peak position is of a

significant order and therefore cannot be neglected in the refinement of the piezoelectric constants.

**Table 4.30:** Piezoelectric constants  $d_{ijk}$  ( $\text{pC N}^{-1}$ ) of  $\text{BiB}_3\text{O}_6$  obtained in the X-ray diffraction experiment (second column) and by means of the Michelson interferometer in [85] (third column).

	X-ray diffraction	Michelson interferometer
$d_{123}$	-6.3 (4)	-6.8 (6)
$d_{112}$	-9.2 (7)	-8.4 (15)
$d_{211}$	13.7 (5)	15.6 (6)
$d_{222}$	-35.8 (8)	-39.5 (10)
$d_{233}$	-2.9 (2)	-3.8 (4)
$d_{213}$	2.9 (2)	5.1 (3)
$d_{312}$	-5.4 (3)	-6.2 (6)
$d_{313}$	-14.2 (12)	-16.3 (20)

**Table 4.31:** Independent components  $R_{ijk}$  ( $\text{pC N}^{-1}$ ) of the rotation tensor refined for each of the three crystal plates together with the according piezoelectric constants. In the case of the (001) plate the tensor coefficients  $R_{3jk}^* = 0.27 \times R_{1jk} + 0.96 \times R_{3jk}$  were determined.

(100) plate		(010) plate		(001) plate	
$R_{112}$	16.8 (1)	$R_{212}$	-2.7 (1)	$R_{312}^*$	-0.9 (2)
$R_{113}$	-3.3 (1)	$R_{213}$	-2.7 (1)	$R_{312}^*$	-3.4 (11)
$R_{123}$	1.1 (1)	$R_{223}$	-3.3 (2)	$R_{323}^*$	-16.2 (13)

In general, in comparison with the Michelson interferometry method the X-ray diffraction technique has on the one hand the advantage of making measurements at much smaller samples. On the other hand, it provides the possibility to study the spatial homogeneity of the piezoelectric properties of a crystal.

### 4.3.2 Internal strain induced in $\text{BiB}_3\text{O}_6$ by external electric fields applied in different crystallographic directions

The performed X-ray diffraction studies of the electric-field-induced atomic displacements in three differently oriented  $\text{BiB}_3\text{O}_6$  crystal plates (see  $^{10}\text{B}/^{11}\text{B}$  plates in Table 4.29) were severely complicated by the presence of the heavy element Bi with the atomic number 83. The first main problem occurred in the experiments was related to the high X-ray attenuation by the crystal, as illustrated in Fig. 4.24. Thus, even with the high intense synchrotron radiation we had access only to the reflections in the Bragg geometry, although the samples used were relatively thin. Secondly, the scattering amplitude of Bi is significantly larger compared to that of B and O. Therefore, the biggest contribution to the diffraction intensity of a reflection stems from the Bi sublattice, see red curve in Fig. 4.25. The best way to overcome this drawback is to focus on those reflections for that the structure factor is the most sensitive to the small displacements of the B and O atoms with respect to the Bi sublattice. Furthermore, for some reflections it was possible to exploit the effect of anomalous dispersion to the form factor of the Bi atom in choosing the X-ray wavelength near to its  $L_{\text{I}}$ ,  $L_{\text{II}}$  and  $L_{\text{III}}$  absorption edges ( $\lambda_{\text{I}} = 0.76 \text{ \AA}$ ,  $\lambda_{\text{II}} = 0.79 \text{ \AA}$  and  $\lambda_{\text{III}} = 0.92 \text{ \AA}$ ). This procedure reduces the scattering power of Bi in

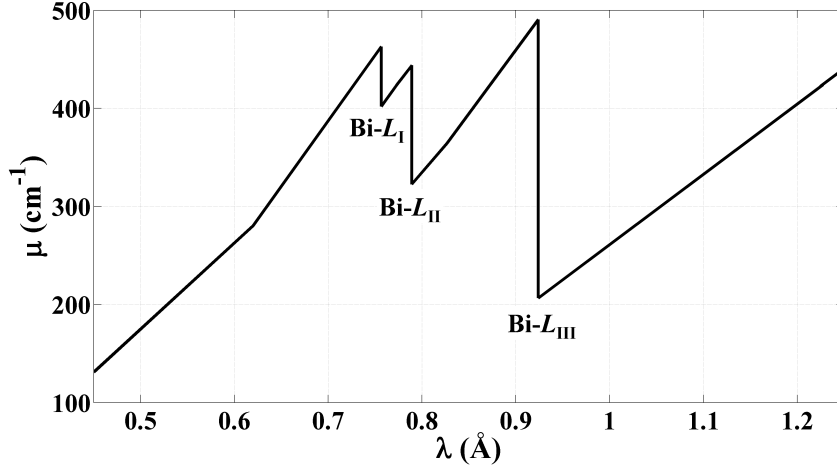


**Figure 4.24:** X-ray linear attenuation coefficient of  $\text{BiB}_3\text{O}_6$  in the X-ray wavelength range from 0.45 to 12.5 Å [78]. The three  $L$  absorption edges of Bi are located at  $\lambda_{\text{I}} = 0.76$  Å,  $\lambda_{\text{II}} = 0.79$  Å and  $\lambda_{\text{III}} = 0.92$  Å.

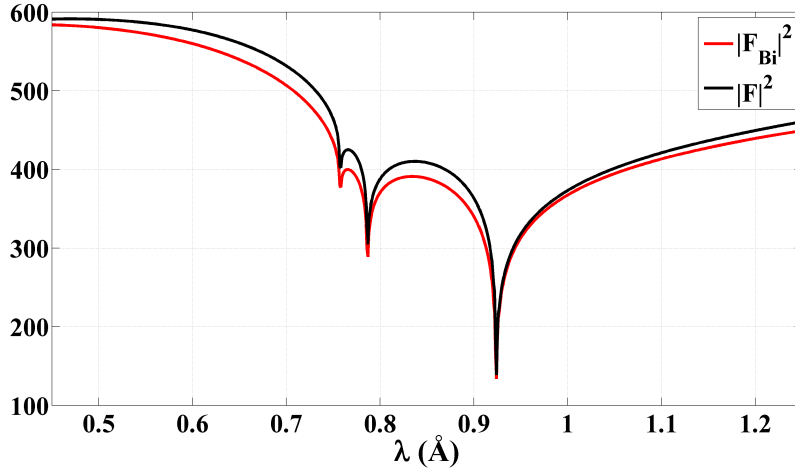


**Figure 4.25:**  $|F|^2$  (2.1) of  $\text{BiB}_3\text{O}_6$  and  $|F_{\text{Bi}}|^2$  of the Bi sublattice calculated for the  $\bar{9}\bar{1}11$  reflection as a function of the X-ray wavelength. According to the red curve, the major contribution to the diffraction intensity comes from the Bi atoms.

**Table 4.32:** Main experimental parameters: Maximum absolute value of the applied electric fields,  $|\mathbf{E}|_{\text{max}}$ ; measured average relative change of diffraction intensities,  $\langle |(\Delta I/I)_a| \rangle$ ; their average relative uncertainty,  $\langle \sigma / |(\Delta I/I)_a| \rangle$ ; total number of independent observations, No.  $(\Delta I/I)_a$ , *i.e.* those with different values of  $hkl$  or  $\lambda$  (see Table A.3).

Plate	$ \mathbf{E} _{\text{max}}$ (kV mm $^{-1}$ )	$\langle  (\Delta I/I)_a  \rangle$ (%)	$\langle \sigma /  (\Delta I/I)_a  \rangle$	No. $(\Delta I/I)_a$
(100)	4.4 (1)	0.22	0.25	19
(010)	3.8 (1)	0.33	0.20	22
(001)	5.1 (2)	0.37	0.23	17

relation to that of the remaining atoms within the unit cell, as demonstrated in Fig. 4.25 for the  $\bar{9}\bar{1}11$  reflection (close to  $L_{\text{III}}$   $f'(\text{Bi})$  reaches a value of  $-10$  [31]). However, even for the most promising reflections the relative change of diffraction intensities has never exceeded 1.2%, see Fig. 4.26 presenting the biggest effect observed. Considering the reasons mentioned above, for all three  $\text{BiB}_3\text{O}_6$  crystal plates the total number of the Bragg

reflections that showed a measurable effect in  $\Delta I/I$  was not more than 48, as given in Table A.3 in the appendix. Where for 10 reflections the measurements were conducted at two different wavelengths. Figure 4.27 displays as a function of  $\sin \theta/\lambda$  the complete experimental data [*i.e.* all  $(\Delta I/I)_a$  values, as defined by equation (3.2)]. In Fig. 4.28 a stereographic projection of the directions of the respective scattering vectors is illustrated. Accordingly, the reflections collected are equally spread over the whole half-angular space and not biased by certain crystallographic directions.

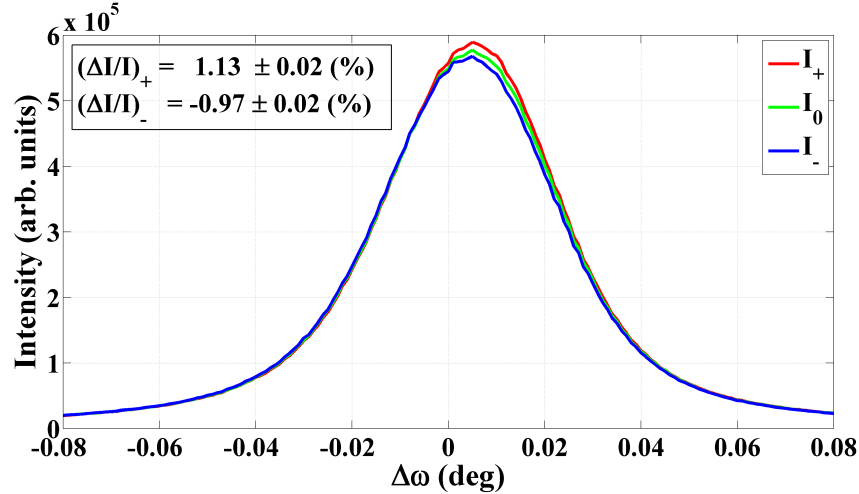


**Figure 4.26:** Three  $\omega$  rocking curves  $I_+$ ,  $I_0$  and  $I_-$  of the  $\text{BiB}_3\text{O}_6$  (001) crystal plate  $\bar{9}111$  reflection ( $\lambda = 0.95 \text{ \AA}$ ) measured simultaneously employing the four-step modulation-demodulation technique, described in section 3.1. The curves correspond to the  $U_+$ ,  $U_0$  and  $U_-$  states of the applied HV,  $|U_{\pm}| = 1.5 \text{ kV}$ .

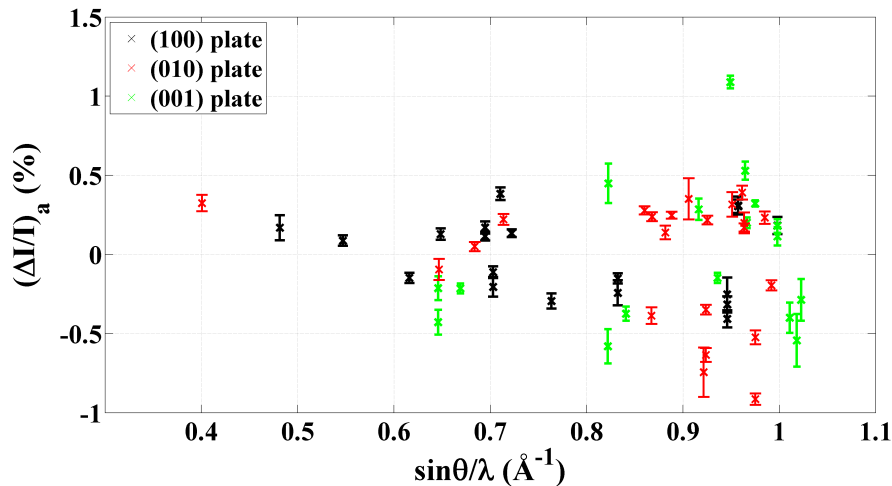


**Figure 4.27:** Overview of all  $(\Delta I/I)_a$  values [see eq. (3.2)] that were used in the refinements of the atomic rearrangement in the  $\text{BiB}_3\text{O}_6$  (100), (010) and (001) crystal plate. The data are plotted as a function of  $\sin \theta/\lambda$ .

In the case of  $\text{BiB}_3\text{O}_6$  the only non-translational symmetry operation is presented by a 2-fold rotation axis parallel to  $\mathbf{a}_2$ . Consequently, for an atom  $\mu^*$  that is related to an atom  $\mu$  by the 2-fold rotation axis the displacement tensor,  $[a_j^i(\mu^*)]$ , referred to the tensor  $[a_j^i(\mu)]$  has according to equation (2.46) the following coefficients in the crystallographic

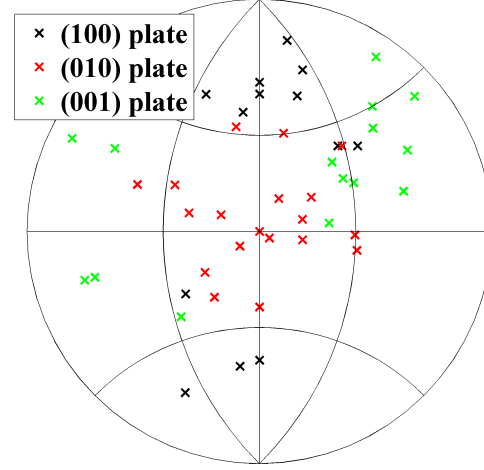


**Figure 4.28:** Stereographic projection of the directions of all in the refinements of the atomic structural changes in  $\text{BiB}_3\text{O}_6$  considered X-ray reflections. Here  $\mathbf{a}_2$  is the main axis of the projection.

coordinate system:

$$[a_j^i(\mu^*)] = \begin{pmatrix} a_1^1 & -a_2^1 & a_3^1 \\ -a_1^2 & a_2^2 & -a_3^2 \\ a_1^3 & -a_2^3 & a_3^3 \end{pmatrix}, \quad \text{with } [a_j^i(\mu)] = \begin{pmatrix} a_1^1 & a_2^1 & a_3^1 \\ a_1^2 & a_2^2 & a_3^2 \\ a_1^3 & a_2^3 & a_3^3 \end{pmatrix}. \quad (4.11)$$

Since in the crystal structure of  $\text{BiB}_3\text{O}_6$  the atoms Bi and B1 occupy sites of symmetry 2,  $[a_j^i(\text{Bi})]$  and  $[a_j^i(\text{B1})]$  only have five non-vanishing components ( $\mu_{\text{SP}} = \mu^* = \mu$ ):

$$[a_j^i(\mu_{\text{SP}})] = \begin{pmatrix} a_1^1 & 0 & a_3^1 \\ 0 & a_2^2 & 0 \\ a_1^3 & 0 & a_3^3 \end{pmatrix}, \quad (4.12)$$

as both tensors  $[a_j^i(\mu^*)]$  and  $[a_j^i(\mu)]$  defined by (4.11) have to be equal. Furthermore, because  $F_E$  (2.44) does not change under a translation of the whole unit cell, in the refinements of the displacements of the six symmetry-independent atoms of  $\text{BiB}_3\text{O}_6$  the Bi atom was fixed at its original position:

$$\Delta R_{\text{Bi}}^i = a_j^i(\text{Bi})E^j = 0. \quad (4.13)$$

Thus, the model parameters to be refined were reduced to the shifts of the B and O atoms relative to the Bi sublattice. In Table 4.33 the independent vector components  $\Delta R_{\mu}^i$  of the individual atoms within the unit cell are given in dependence on the direction of the applied external electric fields.

**Table 4.33:** Displacement vectors of the atoms  $\mu$ ,  $\mu^*$  and  $\mu_{\text{SP}}$  (here B1 atom at the site 2b) in the unit cell of  $\text{BiB}_3\text{O}_6$  for the cases when the external electric field is parallel or perpendicular to the 2-fold rotation axis. The model parameters are the non-zero vector components  $\Delta R^i$  of the five symmetry-independent B and O atoms, with  $\Delta \mathbf{R}_{\text{Bi}} = 0$ .

$\mathbf{E}$	$[a(\mu)]\mathbf{E}$	$[a(\mu^*)]\mathbf{E}$	$[a(\mu_{\text{SP}})]\mathbf{E}$
$\mathbf{E} \parallel \mathbf{a}_2$	$[\Delta R_{\mu}^1, \Delta R_{\mu}^2, \Delta R_{\mu}^3]$	$[-\Delta R_{\mu}^1, \Delta R_{\mu}^2, -\Delta R_{\mu}^3]$	$[0, \Delta R_{\mu_{\text{SP}}}^2, 0]$
$\mathbf{E} \perp \mathbf{a}_2$	$[\Delta R_{\mu}^1, \Delta R_{\mu}^2, \Delta R_{\mu}^3]$	$[\Delta R_{\mu}^1, -\Delta R_{\mu}^2, \Delta R_{\mu}^3]$	$[\Delta R_{\mu_{\text{SP}}}^1, 0, \Delta R_{\mu_{\text{SP}}}^3]$

In order to apply in the refinements the constraint (1.24) (which relates the dielectric constants of a crystal to the induced atomic structural changes) on the  $\Delta R_{\mu}^i$  coefficients,

**Table 4.34:** Pseudoatomic charges of the symmetry-independent atoms of  $\text{BiB}_3\text{O}_6$ .

	Bi	B1	B2	O1	O2	O3
$Q$ (e)	1.92	2.53	2.46	-1.66	-1.59	-1.44

the necessary pseudoatomic charges were estimated on the basis of the topological analysis of the static ED distribution in  $\text{BiB}_3\text{O}_6$ , see Table 4.34. Considering the relativistic effects in Bi due to the spin-orbit coupling, the ED was calculated with the program *WIEN2k*. In these calculations the radii of the atomic muffin-tin spheres were chosen as:

$$R(\text{Bi}) = 1.81 a_0, R(\text{O}) = 1.26 a_0, \text{ and } R(\text{B}) = 1.26 a_0, \quad (4.14)$$

where  $a_0 = 0.53 \text{ \AA}$  is the Bohr radius. As specified by P. Blaha's instructions in the *WIEN2k-FAQ: How to select RMT radii?* [89], it is not recommended to make the muffin-tin radii too different, especially in the case of the atoms with d and f states. Therefore, with  $R(\text{Bi}) = 1.81 a_0$  for Bi the smallest possible value, with that the *WIEN2k* software run stable, was taken. On the other hand, the radii of the O and B spheres could not be increased further, as with  $R(\text{O}, \text{B}) = 1.26 a_0$  the limit of almost touching spheres was reached. The cut-off energy  $E = -8.31 \text{ Ry}$  was used for the separation of the core and valence states of the Bi, O, and B atoms. That way, by adding the Bi-5P states to the valence states the leakage of the core charge out of the Bi sphere could be significantly reduced to  $N \approx 0.006 e$ . The *Generalized Gradient Approximation* by Perdew, Burke and Ernzerhof (1996) [90] was selected as approximation of the exchange-correlation functional, see section 2.2.2. Besides, inside the first Brillouin zone 200 k-points were chosen together with  $K_{\max} \times R_{\min} = 4.5$ . Since with *WIEN2k* it is not possible to perform relativistic calculations and structural optimizations simultaneously, the structural relaxation (determination of the theoretical equilibrium positions of the atoms in the unit cell) was done by neglecting the spin-orbit interactions in Bi. Afterwards fully relativistic calculations, which converged according to the total energy convergence criteria of  $10^{-4} \text{ Ry}$ , were carried out.

**Table 4.35:** Summary of the model refinements of the atomic displacements in the three differently oriented  $\text{BiB}_3\text{O}_6$  crystal plates together with the corresponding agreement indices.

Plate	No. $(\Delta I/I)_a$	No. of parameters	$R$	$R_w$	$\chi^2$
(100)	19	12	0.19	0.20	19
(010)	22	12	0.30	0.33	202
(001)	17	12	0.26	0.16	34

Table 4.35 summarizes the main parameters of the conducted refinements of the atomic redistribution in  $\text{BiB}_3\text{O}_6$  induced by an external electric field applied to crystal plates of three different orientations. As displayed in Table 4.35, for each of the three crystal plates not more than about 20 different reflections showing a change in the integrated intensities could be collected. But the obtained  $R$  and  $R_w$  values are not too high, thus the quality of the refined atomic  $\Delta\mathbf{R}$  vectors may be considered as reliable. Because of these reasons, we restricted the analysis of the determined internal strain in  $\text{BiB}_3\text{O}_6$  to the average deformation of the Bi–O, B1–O and B2–O bond lengths and average displacement,

$$\mathbf{r}_{\text{BO}} = \sum_{\mu=\text{B},\text{O}}^{\text{unit cell}} \Delta\mathbf{R}_\mu, \quad (4.15)$$

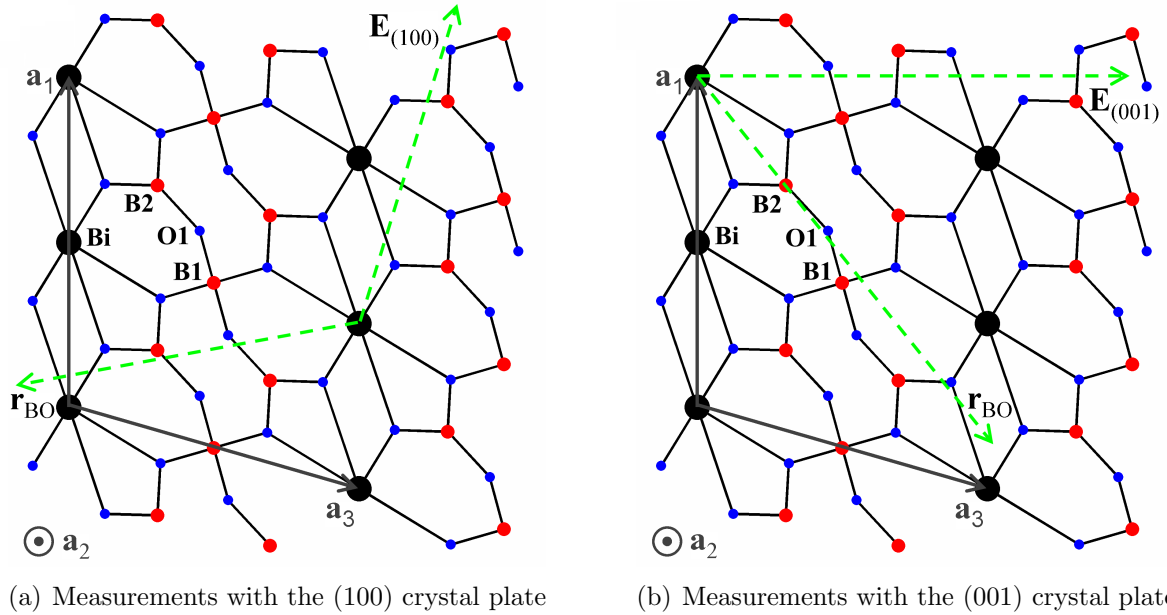


**Figure 4.29:** Direction of the applied electric field strength  $\mathbf{E}_{(100)}$  and  $\mathbf{E}_{(001)}$  compared to the direction of the induced average displacement ( $\mathbf{r}_{\text{BO}}$  vector) of the  $\text{B}_3\text{O}_6$  sublattice with respect to the Bi layers.

of the boron-oxygen ( $\text{B}_3\text{O}_6$ ) sublattice relative to the Bi one.

In the case of the (100) plate the orientation of the vector  $\mathbf{r}_{\text{BO}}$  (4.15) is illustrated in Fig. 4.29 (a). The angle between the [100] crystallographic direction and  $\mathbf{r}_{\text{BO}}$  is  $100 \pm 2^\circ$ . Hence, the average shift of the  $\text{B}_3\text{O}_6$  sublattice takes place almost perpendicular to the Bi (001) layers. In the case of the (001) plate, see Fig. 4.29 (b),  $\mathbf{r}_{\text{BO}}$  has an angle of  $141 \pm 23^\circ$  with respect to [100] and shows approximately in the direction of the B2–O–B1 connection of the  $\text{B1O}_4$  and  $\text{B2O}_3$  groups (bonding angle is  $133^\circ$ ). The sensitivity of the crystal structure of  $\text{BiB}_3\text{O}_6$  for structural deformation in the directions where the corner-sharing  $\text{B1O}_4$  and  $\text{B2O}_3$  polyhedra are arranged was also reported in the work by Haussühl *et al.* (2006) [85] for the direction of the maximum positive transverse piezoelectric effect, the maximum negative transverse elastic compliance, a local positive maximum of the longitudinal elastic compliance and in the work by Becker & Bohatý (2001) [86] for the direction of the maximum negative thermal expansion. Due to the crystal symmetry (see Table 4.33), for the (010) plate the corresponding vector  $\mathbf{r}_{\text{BO}}$  is oriented parallel to [010].

The average distortions of the different cation-anion bond lengths in  $\text{BiB}_3\text{O}_6$  under the external electric perturbations exerted are given in Table 4.36. It is clearly visible that the atomic structural changes are dependent on the direction of an applied electric field vector. In particular, the  $\text{BiO}_6$  group is the most affected by the electric field when  $\mathbf{E}$  shows along the  $\mathbf{a}_2$  axis, which is the direction of the maximum longitudinal piezoelectric effect. The application of  $\mathbf{E}$  in the  $\mathbf{b}_1$  or  $\mathbf{b}_3$  direction results in the biggest deformation of the  $\text{B1O}_4$  group. On the other hand, the  $\text{B2O}_3$  triangles are stronger deformed for  $\mathbf{E}_{(100)}$  and  $\mathbf{E}_{(010)}$ . Besides, as expected, in all three experiments the  $\text{B2O}_3$  structural unit is revealed to be the most electric-field-deformed, thus the weakest one, as displayed in the last column of Table 4.36. In contrast to the studies of the crystal structure of  $\text{BiB}_3\text{O}_6$  under high pressure [1] and at different temperatures [87], both  $\text{B1O}_4$  and  $\text{B2O}_3$  borate groups change under an applied electric field their shape and therefore do not behave as rigid structural units. Since we do not know the electric-field-affected ED distribution in

$\text{BiB}_3\text{O}_6$ , the analysis of the induced response of the lone electron pair localized at the Bi ion in the  $\text{BiO}_6$  polyhedron is not of a tenable significance.

**Table 4.36:** Average deformation of the Bi–O, B1–O and B2–O bond lengths in  $\text{BiB}_3\text{O}_6$  determined for three different directions of an applied external electric field. All values are normalized to an electric field of the magnitude  $|\mathbf{E}| = 1 \text{ kV mm}^{-1}$ .

Plane	$\langle  \Delta(\text{Bi-O})  \rangle$ ( $10^{-5} \text{ \AA}$ )	$\langle  \Delta(\text{B1-O})  \rangle$ ( $10^{-5} \text{ \AA}$ )	$\langle  \Delta(\text{B2-O})  \rangle$ ( $10^{-5} \text{ \AA}$ )
(100)	69 (1)	99 (1)	126 (1)
(010)	127 (1)	53 (2)	162 (1)
(001)	70 (9)	100 (3)	105 (4)

### 4.3.3 Neutron diffraction study of the internal strain

As previously discussed, the investigations of the internal strain in  $\text{BiB}_3\text{O}_6$  by means of X-ray diffraction suffered a lot from the large difference in the number of electrons of the Bi atom compared to that of the B and O atom. Therefore, the diffraction intensities of most reflections were not affected at all by an applied electric field and if, then the measured effect in  $\Delta I/I$  was rarely greater than 1%, see Fig. 4.27.

In the case of neutron diffraction the incident neutrons interact with atomic nuclei that act as point scatterers [22]. Since the neutron scattering length,  $b$ , of an atomic nucleus is independent of the scattering vector,  $\mathbf{H}$ , the structure factor of a neutron reflection has the form [22]

$$F(\mathbf{H}) = \sum_j b_j T_j(\mathbf{H}) \exp(2\pi i \mathbf{H} \mathbf{r}_j). \quad (4.16)$$

The respective  $b$  values of the elements  $^{10}\text{B}$ ,  $^{11}\text{B}$ ,  $^{16}\text{O}$  and  $^{209}\text{Bi}$  are [91]:

$$\begin{aligned} b(^{10}\text{B}) &= (-0.1 - i1.07) \text{ fm}, & b(^{11}\text{B}) &= 6.65 \text{ fm}, \\ b(^{16}\text{O}) &= 5.80 \text{ fm} & \text{and} & & b(^{209}\text{Bi}) &= 8.53 \text{ fm}. \end{aligned} \quad (4.17)$$

Thus, in contrast to  $^{11}\text{B}$  the isotope  $^{10}\text{B}$  of boron is a strong neutron absorber and that is why for the neutron diffraction measurements  $\text{BiB}_3\text{O}_6$  crystals were required that exclusively contained the element  $^{11}\text{B}$ . According to the  $b$  values given above, the neutron scattering power of  $^{11}\text{B}$  and  $^{16}\text{O}$  is comparable to that of  $^{209}\text{Bi}$ . Consequently, a neutron diffraction experiment should provide a much better method for the study of the electric-field-induced displacements especially of the B and O atoms in  $\text{BiB}_3\text{O}_6$ , unlike the X-ray diffraction experiment.

All measurements with neutrons were conducted at the 5C-2 beamline of LLB (Laboratoire Léon Brillouin) equipped with a four-circle diffractometer [92]. At LLB a fission reactor is used to produce beams of hot and cold neutrons [93]. The experiment was carried out with a hot incident neutron beam of the wavelength  $\lambda = 0.83 \text{ \AA}$ . For this wavelength the maximum neutron flux at a specimen amounts to  $4.5 \times 10^6 \text{ neutrons/cm}^2/\text{sec}$ . Besides, the size of the neutron beam was adjusted to 1.5 cm, which represents a maximum possible value.

In  $\text{BiB}_3\text{O}_6$  the intensity of an incident neutron beam is attenuated by a factor of  $1/e$  after a path length of about  $L_{1/e} = 2.15 \text{ cm}$ , as calculated from the atomic coherent/incoherent scattering cross sections and absorption cross sections with the scattering length

density calculator [94]. Because of the relatively weak neutron flux available and small scattering volume of the 0.718 thick (010) crystal plate (which was of excellent quality) even for the strongest reflections about 3 to 4 hours of data collection were needed to reach sufficiently high counting statistics. Therefore, in the experiment strong reflections could be considered only. The extinction depth,  $\Lambda_{\text{ext}}$  (2.6), of such  $\text{BiB}_3\text{O}_6$  reflections has an order of magnitude of  $10 \mu\text{m}$  and thus is about a factor of  $10^3$  smaller than the  $L_{1/e}$  length (2.15 cm). Even for the weakest reflections  $\Lambda_{\text{ext}}$  is not larger than 1 cm. Hence, the collected diffraction intensities were heavily influenced by primary extinction effects. Consequently, the small contribution of the atomic rearrangement to the measured change in the integrated intensities of strong reflections was completely masked by the much greater impact of an external electric field on the mosaic block structure of the crystal. In the work by Stein (2007) [95] (dealing with a temperature-dependent neutron diffraction study of the crystal structure of  $\text{BiB}_3\text{O}_6$ ) the extinction of the neutron data could be significantly reduced by using bad quality crystals with optically visible defects. But for an electric field experiment such crystals do not represent an adequate option, because they cannot be treated anymore as homogeneous with respect to their piezoelectric and dielectric properties.

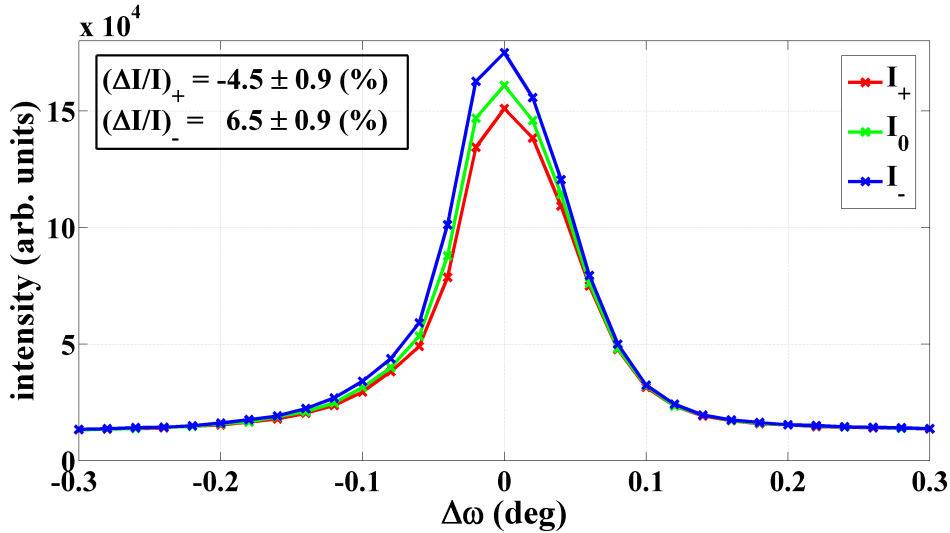


**Figure 4.30:** Three rocking curves,  $I_+$ ,  $I_0$  and  $I_-$ , of the  $60\bar{2}$  reflection measured with the four-step field-switching technique as a function of the applied electric field strengths  $\mathbf{E}_{\pm} = \pm 4.2 \times \mathbf{e}_2 \text{ kV mm}^{-1}$ .

As shown in Fig. 4.30, the observed response of the  $60\bar{2}$  reflection in terms of  $\Delta I/I$  to the applied electric fields  $\mathbf{E}_{\pm} = \pm 4.2 \times \mathbf{e}_2 \text{ kV mm}^{-1}$  is well pronounced and is almost linear with  $\mathbf{E}$ . But on the other hand, there is a small variation of the width of the rocking curve in dependence on the external electric field, which indicates some induced changes in the crystal mosaic structure. In this context, Figures 4.31 and 4.32 demonstrate the effect of extinction on the collected neutron data. In particular, in Fig. 4.31 the recorded profiles of the  $20\bar{2}$  reflection are illustrated. In this case the  $(\Delta I/I)_{\pm}$  values are asymmetric with the fields  $\mathbf{E}_{\pm}$ . The  $\psi$  angle of this reflection, which defines the rotation about the scattering vector, amounted to  $0^\circ$ . In order to vary the beam propagation direction with respect to the plate geometry and the beam path length through the crystal, in a further experiment the crystal plate was rotated about the scattering vector  $\mathbf{H} = [20\bar{2}]$  by the angle  $\psi = 90^\circ$ . As a result, a completely reverse effect in  $\Delta I/I$  of the  $20\bar{2}$  reflection was recorded as a

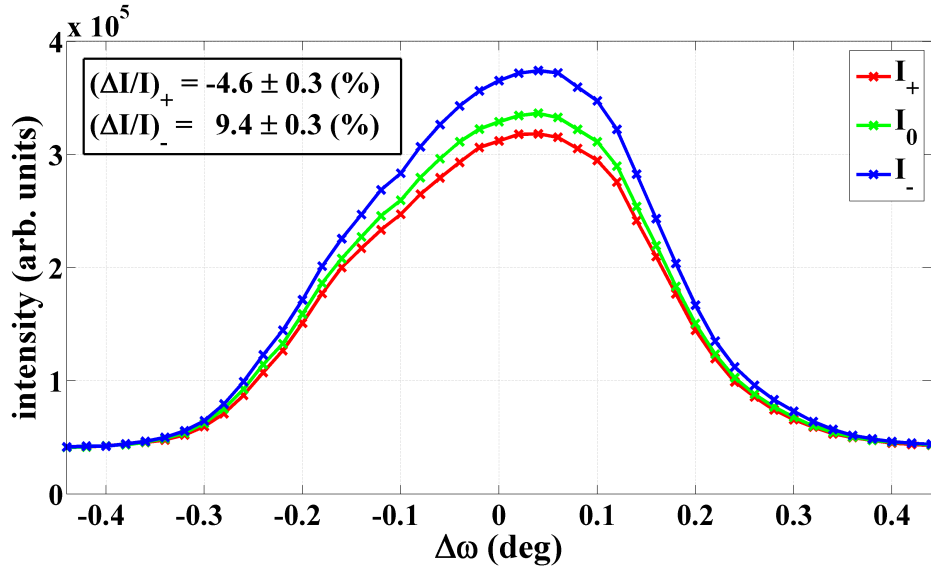


**Figure 4.31:**  $I_+$ ,  $I_0$  and  $I_-$  profiles of the  $20\bar{2}$  reflection recorded at the  $\psi$  angle  $0^\circ$  applying  $\mathbf{E}_\pm = \pm 4.2 \times \mathbf{e}_2$  kV mm $^{-1}$ .

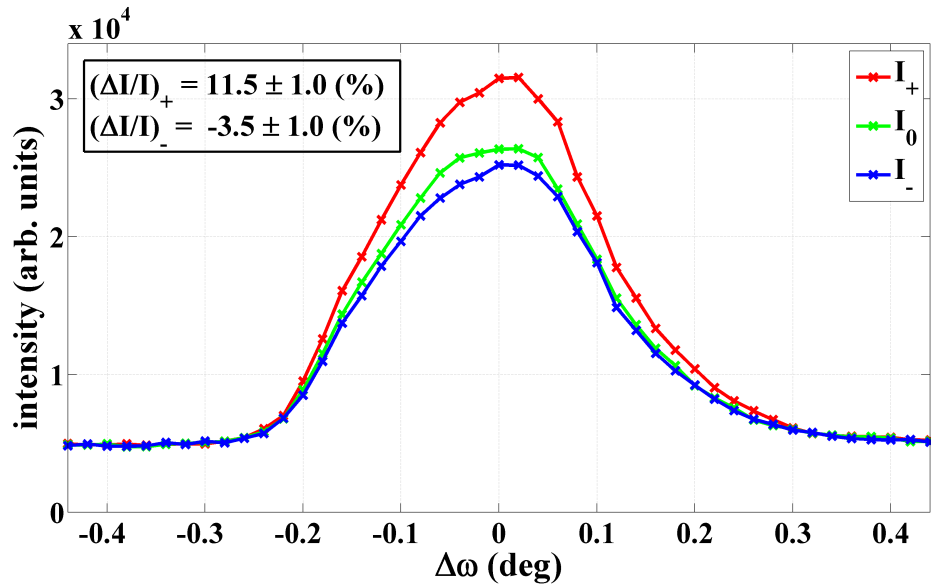


**Figure 4.32:** Compared to Fig. 4.31, in the case presented the crystal plate was rotated by the angle  $\psi = 90^\circ$  about the scattering vector  $\mathbf{H} = [20\bar{2}]$ . Then for the new plate orientation with respect to the incident beam the rocking curves were measured in dependence on the applied electric field strengths  $\mathbf{E}_\pm = \pm 4.2 \times \mathbf{e}_2$  kV mm $^{-1}$ .

function of the applied electric fields, as displayed in Fig. 4.32. Many reflections showed this behavior, *e.g.* the diffraction geometry of the  $60\bar{2}$  and  $20\bar{2}$  ( $\psi = 0^\circ$ ) reflection was not much different and therefore, the signs of the  $(\Delta I/I)_\pm$  values are the same for both reflections, compare Fig. 4.30 with Fig. 4.31.

According to the effects measured, one may conclude that there is a strong anisotropy in the response of the mosaic structure of  $\text{BiB}_3\text{O}_6$  to an external electric perturbation, which represents a distinctive feature of all reported physical properties of this crystal [85, 86]. Due to the high divergence of the neutron beam, it was not possible to resolve the electric-field-induced angular shifts ( $\Delta\omega < 0.01^\circ$ ) of the rocking curve positions. Normally, in a

scan the width of an  $\omega$  step was either  $0.02^\circ$  or  $0.03^\circ$  depending on the Bragg angle.

The second electric field experiment with neutrons was performed with a 0.218 mm thick (010) plate (see Table 4.29) employing the experimental technique developed for the time-resolved measurements. All measurements of diffraction curves were conducted with a time resolution of 100 ns. In order to increase the counting statistics, we applied the four-step modulated HV (red curve in Fig. 4.34) with a frequency of 1.5 kHz. As the charging and discharging current through the HV electronics has to be kept small, the maximum HV values were limited to  $U_{\pm} = \pm 1.5$  kV. Nevertheless, since the plate was extremely thin, a relatively high external electric field  $E = 6.9$  kV  $\text{mm}^{-1}$  could be generated within the crystal.

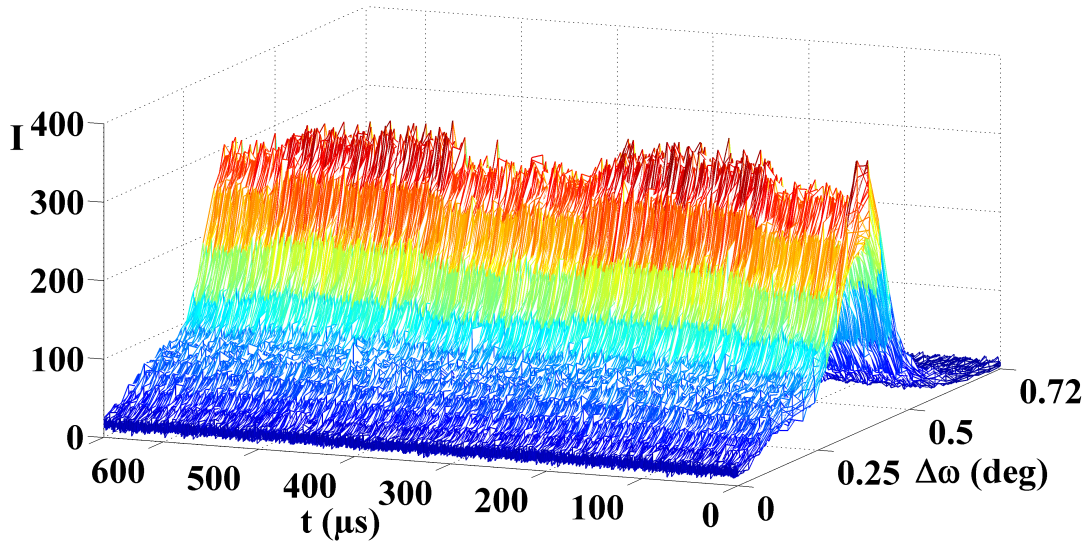


**Figure 4.33:** Raw data of a time-resolved scanning of the  $60\bar{2}$  reflection measured within the basic HV period consisting of the four-step HV modulation, see red curve in Fig. 4.34.

Figure 4.33 shows the raw data of a time-resolved scanning of the  $60\bar{2}$  reflection. The time evolution of  $\Delta I/I$  (see Fig. 4.34) within the basic HV period reveals two major effects accompanied by the application of an electric field: Firstly, by comparing the time behavior of  $\Delta I/I$  with the time structure of the HV within the basic period (as done in Fig. 4.34), one sees that there is a one to one correlation between the HV spikes and the spikes in  $\Delta I/I$  as well as the jumps of the HV to the zero states also coincide with small spikes in  $\Delta I/I$ . Secondly, there is a retardation of about  $90 \mu\text{s}$  between the HV and the corresponding crystal response in terms of  $\Delta I/I$ . Because no aluminum dome was used to shield the environment from the electromagnetic dipole radiation of the crystal linked to the fast HV switching processes, the first phenomenon may be most likely explained by a caused electromagnetic strong influence of the neutron  $^3\text{He}$  detector. In contrast, the second phenomenon is related to the finite velocity

$$v = \frac{h}{\lambda m_n} = 4.8 \times 10^3 \text{ m s}^{-1} \quad (4.18)$$

of the diffracted hot neutrons and the distance ( $d \simeq 0.4$  m) that they have to cover from the specimen to the detector. For this distance the neutrons available need a time of about  $84 \mu\text{s}$ . Taking into account that the detection process of a neutron in the detector itself takes some time to produce an electric signal, one finally gets the observed time shift in  $\Delta I/I$  of  $90 \mu\text{s}$ .

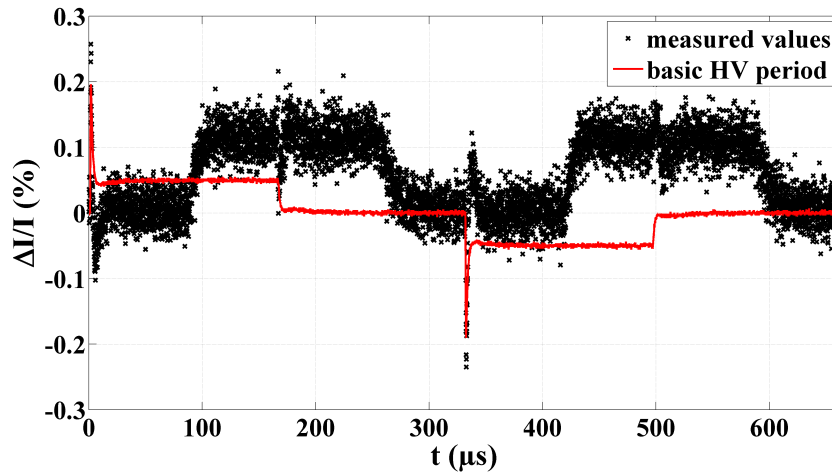


**Figure 4.34:** Basic period of the four-step modulation of the HV (applied with a frequency of 1.5 kHz,  $|U_{\pm}| = 1.5$  kV) together with the time evolution of the relative intensity change of the  $60\bar{2}$  reflection extracted from the  $\omega$  rocking curves shown in Fig. 4.33.

As depicted in Fig. 4.34, in the case of the  $60\bar{2}$  reflection  $\Delta I/I$  detected for the  $U_+$  HV state is approximately equal to  $\Delta I/I$  obtained for the  $U_-$  state. Accordingly, the measured effect is independent of the electric field direction and thus, it is obvious that it cannot originate from the induced atomic displacements in the crystal. In summary, by reducing the thickness of a  $\text{BiB}_3\text{O}_6$  crystal plate from 0.7 to 0.2 mm the extinction problem could not be solved. In fact, it seems that with a thickness of 0.2 mm the crystal plate is still far too thick to diminish the dynamical diffraction by the crystal.

## 5 Time-resolved X-ray diffraction study of the dynamic piezoelectric response of crystals

In general, as stated in section 3.2, the 200 ns jumps between different HV states within a HV basic period applied to a piezoelectric crystal are sufficiently fast to excite several superimposed vibrational modes of the crystal. Therefore, in the case of the crystal vibrations, such as thickness vibrations, changing the lattice spacings the time-resolved measurements of diffraction intensities as a function of the specially modulated external electric field enable a simultaneous and separate study of the atomic displacements within the unit cell that were induced on the one hand by the applied electric perturbation and on the other hand by the stress accompanied by the vibrational deformations of the crystal. Consequently, in one and the same experiment one has a unique possibility to combine piezoelectric measurements with those under external pressure exerted to the crystal. In the following, this novel experimental access to the atomistic origin of the macroscopic properties of a crystal will be analyzed in terms of its physical significance by considering  $\text{Li}_2\text{SO}_4\cdot\text{H}_2\text{O}$  and  $\text{BiB}_3\text{O}_6$  single crystals.

The investigations of the  $\text{Li}_2\text{SO}_4\cdot\text{H}_2\text{O}$  response to a fast change of an applied electric field were based mainly on two rectangular (010) crystal plates of slightly different dimensions, as shown in Figs. 5.1 and 5.2. All edges of the plane-parallel plates are oriented parallel to the axes of the crystal physical basic system,  $\{\mathbf{e}_i\}$ . In this context, the longest edge of the first plate lies along the  $\mathbf{e}_3$  axis (see Fig. 5.1) and in the case of the second plate the  $\mathbf{e}_1$  direction represents the largest dimension (see Fig. 5.2). The well-defined geometry of the crystal plates allows for the calculation of their respective resonance frequency spectrum in a relatively easy way, which makes an analysis of the observed electric-field-induced dynamic processes in the crystals possible.

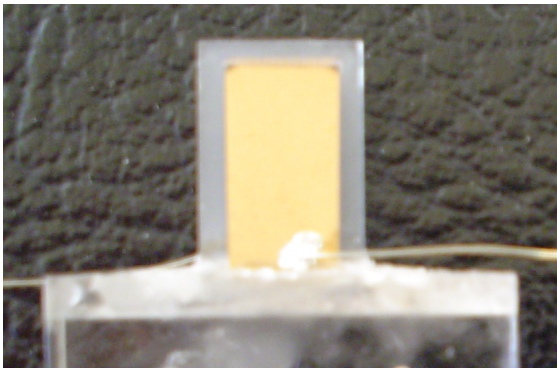


**Figure 5.1:** First rectangular  $\text{Li}_2\text{SO}_4\cdot\text{H}_2\text{O}$  (010) crystal plate with the dimensions  $8.5 \times 0.64 \times 13.5$  mm.

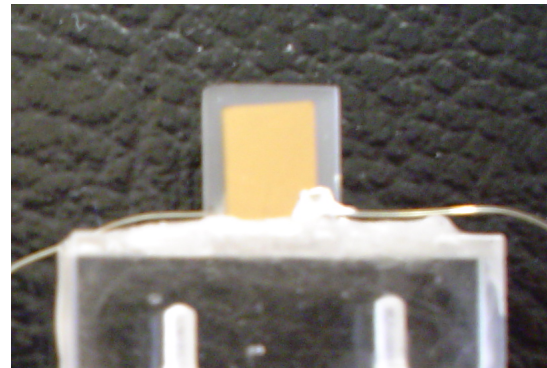


**Figure 5.2:** Second rectangular  $\text{Li}_2\text{SO}_4\cdot\text{H}_2\text{O}$  (010) crystal plate with the dimensions  $9.1 \times 0.59 \times 7.5$  mm.

## 5.1 Measurements with the first rectangular $\text{Li}_2\text{SO}_4 \cdot \text{H}_2\text{O}$ (010) crystal plate

The study of the macroscopic and microscopic strains induced in the first  $\text{Li}_2\text{SO}_4 \cdot \text{H}_2\text{O}$  (010) crystal plate (Fig. 5.1) by a fast change of an external electric field state was carried out at the BM01A beamline of ESRF. All measurements were performed using a four-step modulated HV, as illustrated in Fig. 5.3. During the experiment the HV frequency was kept constant at 1 kHz and the HV states  $U_+$  and  $U_-$  were of the order of  $\pm 1.5$  kV. In comparison with the HV jumps from  $U_{0\mp}$  to the  $U_{\pm}$  states, which took place within 200 ns, the switching process in the opposite direction from  $U_{\pm}$  to  $U_{0\pm}$  took with  $1 \mu\text{s}$  a little longer. In Fig. 5.4 the time behavior of the rocking curve of the  $\bar{1}201$  reflection within the applied HV basic period is presented. The time resolution used amounted to 100 ns and the width of the  $\omega$  steps was  $0.001^\circ$ . The raw data displayed in Fig. 5.4 were collected continuously during the course of a whole day resulting in 29 successive  $\omega$  scans.

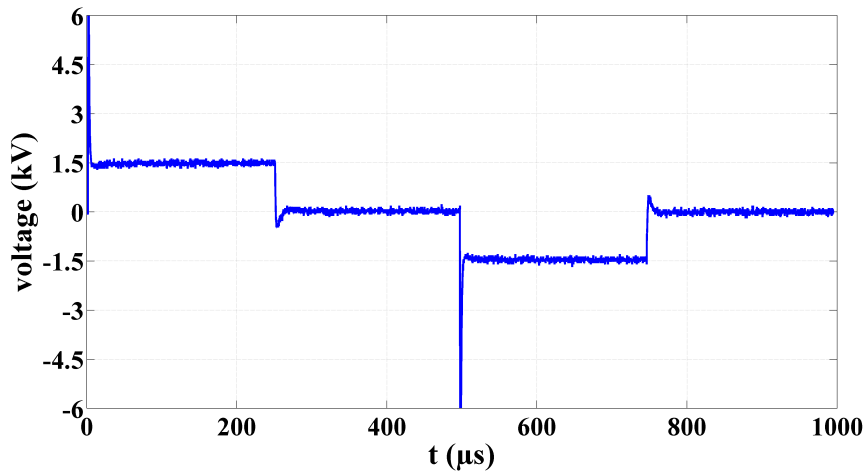


**Figure 5.3:** Four-step modulation of the HV applied in the experiment to the first  $\text{Li}_2\text{SO}_4 \cdot \text{H}_2\text{O}$  (010) crystal plate (see Fig. 5.1). The HV states  $U_+$  and  $U_-$  were of the order of  $\pm 1.5$  kV and the frequency of the basic HV period amounted to 1 kHz.

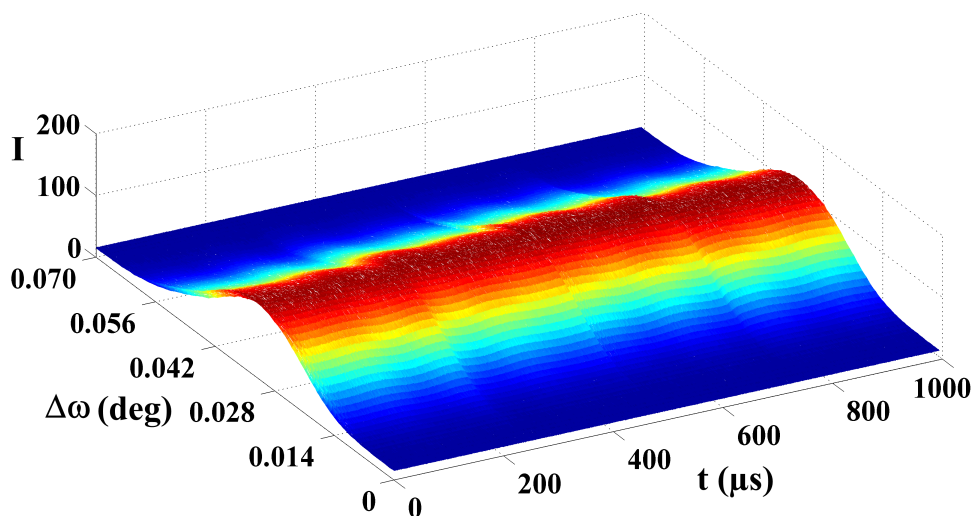


**Figure 5.4:** Time-resolved behavior of the rocking curve of the  $\bar{1}201$  reflection measured as a function of the four-step modulated HV (see Fig. 5.3) with a time-resolution of 100 ns.

The angular shift ( $\Delta\omega$ ) of the peak position of an  $\omega$  rocking curve is dependent on the time ( $t$ ) within the basic HV period and the X-ray beam position ( $\mathbf{r}$ ) on the crystal. Normally, as depicted in Figs. 5.5 and 5.7,  $\Delta\omega$  consists of a piezoelectric contribution,  $\Delta\omega_{\text{piezo}}$ , and a vibrational contribution,  $\Delta\omega_{\text{vibr}}$ :

$$\begin{aligned}\Delta\omega(t, \mathbf{r}) &= \Delta\omega_{\text{piezo}}[\text{HV}(t), \mathbf{r}] + \Delta\omega_{\text{vibr}}(t, \mathbf{r}) \\ &= \Delta\omega_{\text{piezo}}[\text{HV}(t), \mathbf{r}] - \varepsilon_{ij}(t, \mathbf{r}) \left( \tan\theta \frac{H_i H_j}{H^2} + Y_i \frac{H_j}{H} \right) + r_{ij}(t, \mathbf{r}) Y_i \frac{H_j}{H},\end{aligned}\quad (5.1)$$

here  $\Delta\omega_{\text{piezo}}$  is defined by equation (2.40). In all,  $\Delta\omega_{\text{piezo}}$  reflects the time structure of the HV and vanishes outside the crystal volume not confined by the contacts, where the external electric field is zero within the crystal. In contrast, the second term  $\Delta\omega_{\text{vibr}}$  describes the displacements of a reciprocal lattice vector,  $\mathbf{H}$ , from its exact diffraction position due to the elastic vibrations of the crystal volume illuminated by the incident X-ray beam. In this context,  $[\varepsilon_{ij}]$  stands for the strain tensor that deforms  $\mathbf{H}$  and thus changes the spacing of the corresponding lattice planes, see discussion in section 2.3.1. On the other hand, the tensor  $[r_{ij}]$  describes a pure rotation of  $\mathbf{H}$  arising from the rotation of the whole crystal volume that diffracts the incident X-rays. Note that in this special case  $\Delta\omega_{\text{vibr}}$  is not related to any deformations of the crystal lattice. In summary, by extracting the frequencies of the  $\Delta\omega$  oscillations of a reflection one gets the possibility to qualify the excited vibrational modes of a crystal plate.

Below, the time behavior of  $\Delta\omega$  (see Figs. 5.5 and 5.7) and of  $\Delta I/I$  (see Figs. 5.6 and 5.8) is analyzed as a function of the time within the period of the four  $U_+$ ,  $U_{0+}$ ,  $U_-$  and  $U_{0-}$  HV states for the  $\bar{1}201$  and  $\bar{6}56$  reflection, respectively. As shown in the plots, these two reflections were considered, because they are sensitive to the internal strain as well as to the external strain, so that both phenomena could be simultaneously probed. Concerning the time dependence of the relative change of the integrated intensity, the obtained counting statistics was for both not really weak reflections by far not good enough, as visible in Figs. 5.6 and 5.8 by the broad distribution of  $\Delta I/I$ . However, all attempts of a significant improvement of the statistics would definitely go beyond the scope of a typical beamtime, as the measurements of the  $\bar{1}201$  and  $\bar{6}56$  reflection have been already performed for one day, respectively.

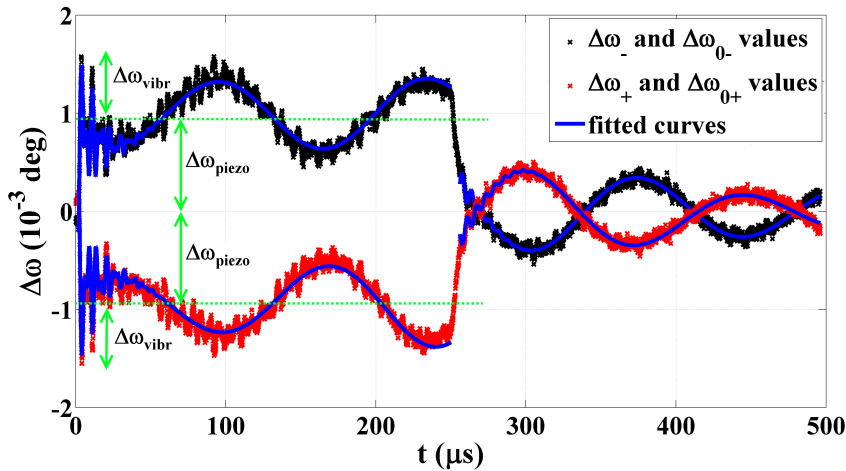


**Figure 5.5:** Angular shift of the Bragg peak position of the  $\bar{1}201$  reflection within the basic HV period (see Fig. 5.3) applied to the crystal. The black curve ( $\Delta\omega_-$  and  $\Delta\omega_{0-}$  values) was referred to  $t = 0 \mu\text{s}$  instead of  $t = 497 \mu\text{s}$  to visualize the symmetry of the effect. Using the approach (5.2), the blue curves were fitted to the experimental data.

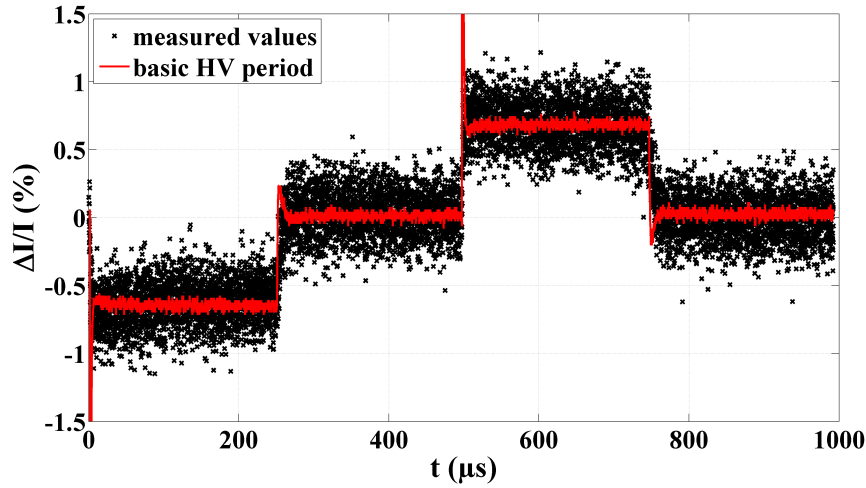


**Figure 5.6:** Relative intensity change of the  $\bar{1}201$  reflection together with the time dependence of the four  $U_+$ ,  $U_{0+}$ ,  $U_-$  and  $U_{0-}$  HV states within the basic HV period.

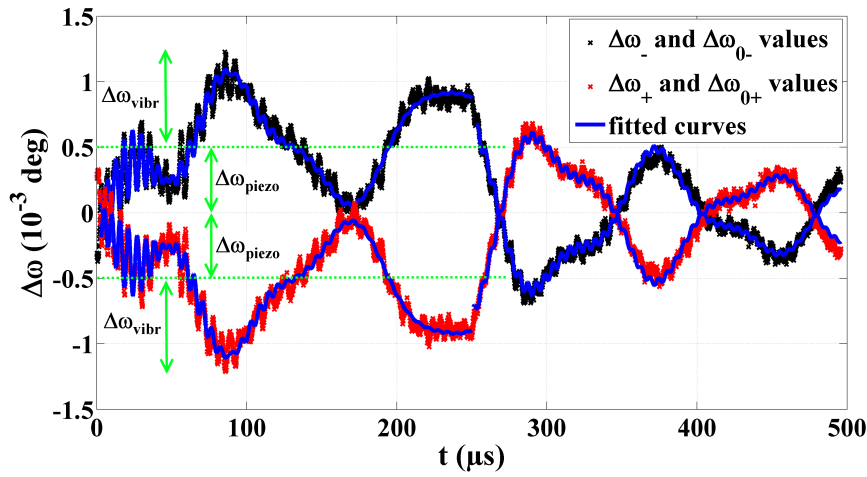


**Figure 5.7:** Angular shift of the Bragg peak position of the  $\bar{6}56$  reflection within the basic HV period shown in Fig. 5.3. Analogous to Fig. 5.5, the black curve ( $\Delta\omega_-$  and  $\Delta\omega_{0-}$  values) was referred to  $t = 0 \mu\text{s}$  and the blue curves represent fits of the model (5.2) to the recorded data.

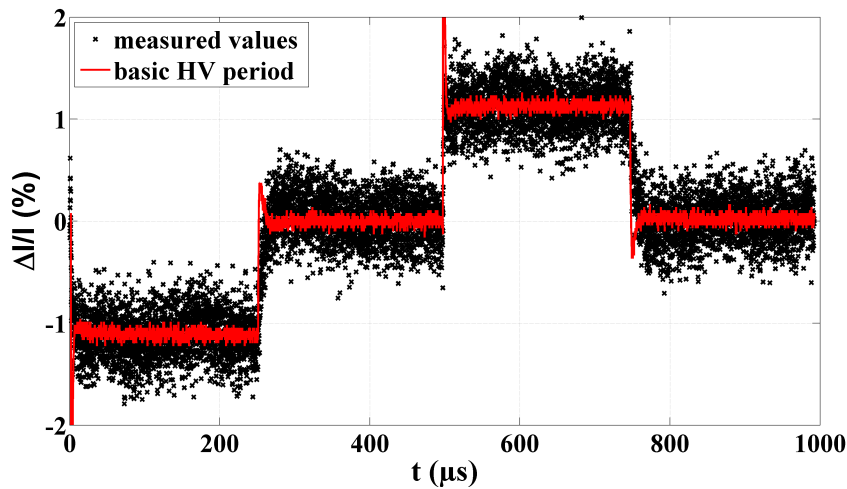


**Figure 5.8:** Relative intensity change of the  $\bar{6}56$  reflection together with the time dependence of the  $U_+$ ,  $U_{0+}$ ,  $U_-$  and  $U_{0-}$  HV states within the basic HV period.

### 5.1 Measurements with the first rectangular $\text{Li}_2\text{SO}_4 \cdot \text{H}_2\text{O}$ (010) crystal plate

In the absence of an electric perturbation the piezoelectric offset,  $\Delta\omega_{\text{piezo}}$ , in an extracted response function  $\Delta\omega$  of the crystal is zero and thus, according to equation (5.1),  $\Delta\omega$  is completely defined by  $\Delta\omega_{\text{vibr}}$ . Consequently, the  $\Delta\omega_{0+}$  and  $\Delta\omega_{0-}$  values (see time interval between 250 and 500  $\mu\text{s}$  in Figs. 5.5 and 5.7) oscillate around  $\Delta\omega = 0^\circ$ , as measured during  $U_{0+}$  and  $U_{0-}$ , respectively. In addition, both Figures 5.5 and 5.7 reveal that depending on whether  $U_{\pm}$  or zero HV states are applied  $\Delta\omega_{\text{vibr}}$  varies significantly in the amplitude of the oscillations, compare, for instance, the time range 0 – 50  $\mu\text{s}$  with that between 250 and 300  $\mu\text{s}$ . Obviously, the slower changes from  $U_{\pm}$  to  $U_{0\pm}$  result in a smaller amplitude of especially fast  $\Delta\omega_{\text{vibr}}$  oscillations during the period of the  $U_{0\pm}$  states. This is a good example how the switching time between different HV states affects the crystal response induced. For further data analysis the measured  $\Delta\omega$  curves are interpreted by means of a model describing several superimposed harmonic and damped vibrational modes of crystal plates excited each time when the HV is changed. In order to extract all different modes of the plate vibrations, the experimental data are fitted by

$$\sum_{i=1}^n A_i \exp(-\gamma_i t) \cos(\omega_i t - \delta_i) + a, \quad (5.2)$$

where  $a$  (piezoelectric offset,  $\Delta\omega_{\text{piezo}}$ ),  $\delta$  (phase),  $\omega$  (angular frequency),  $\gamma$  (damping factor) and  $A$  (amplitude) are the model parameters that are simultaneously refined. Besides, with  $n$  the number of independent vibrational modes is adjusted in a refinement.

**Table 5.1:** Oscillation frequencies determined from the  $\Delta\omega$  curve of the  $\bar{1}\bar{2}01$  reflection. The analysis of the experimental data was done separately for each of the four different HV states.

	$\nu_1$ (kHz)	$\nu_2$ (kHz)	$\nu_3$ (kHz)	$\nu_4$ (kHz)
$U_+$	7.01 (1)	16.84 (3)	159.5 (3)	183.2 (3)
$U_{0+}$	7.12 (1)	16.64 (3)	–	178.6 (3)
$U_-$	7.11 (2)	16.95 (3)	159.7 (3)	182.8 (3)
$U_{0-}$	7.04 (1)	16.75 (3)	–	178.6 (3)

**Table 5.2:** Oscillation frequencies determined from the  $\Delta\omega$  curve of the  $\bar{6}56$  reflection as a function of the respective HV state.

	$\nu_1$ (kHz)	$\nu_2$ (kHz)	$\nu_3$ (kHz)
$U_+$	7.03 (2)	162.6 (8)	263.9 (7)
$U_{0+}$	6.87 (1)	160.5 (10)	–
$U_-$	7.20 (1)	162.9 (5)	264.6 (7)
$U_{0-}$	7.09 (1)	161.8 (10)	–

As summarized in Tables 5.1 and 5.2, five different modes of the piezoelectrically excited plate vibrations could be extracted from the recorded  $\Delta\omega$  curves of the  $\bar{1}\bar{2}01$  and  $\bar{6}56$  reflection. There are in total the following effects that can be deduced from the data given: Firstly, the measurements of the two reflections reveal both same and different vibrational modes. This observation is associated with the completely different orientation of the respective lattice planes with respect to  $\mathbf{E}$ , so that the electric-field-induced in general anisotropic crystal response is probed as a function of certain crystal directions. Therefore, there is a difference in the observed  $\nu_1$  amplitude of the same modes, as different projections

of the crystal vibrations are regarded in the performed X-ray diffraction experiments. Secondly, the oscillation frequencies determined for the zero HV states are by tendency a little bit smaller than for  $U_+$  and  $U_-$ . The origin of this effect may be accounted for by the absence of a piezoelectric deformation of the crystal in the case of the  $U_{0\pm}$  states. Thirdly, in consequence of the slower switching process to  $U_{0\pm}$  some modes are missing or could not be resolved for the zero HV states.

In comparison with the  $\Delta\omega$  oscillations,  $\Delta I/I$  reflects within the statistical noise the time dependence of the  $U_+$ ,  $U_{0+}$ ,  $U_-$  and  $U_{0-}$  states of the basic HV period, as illustrated in Figs. 5.6 and 5.8. In this context, the corresponding static value of  $\Delta I/I$ ,

$$(\Delta I/I)_a = [\langle(\Delta I/I)_+\rangle - \langle(\Delta I/I)_-\rangle] / 2, \quad (5.3)$$

is for the  $\bar{1}201$  reflection equal to  $(\Delta I/I)_a^{\text{dyn}} = -0.66$  (11)% and for the  $\bar{6}5\bar{6}$  reflection one has  $(\Delta I/I)_a^{\text{dyn}} = -1.13$  (7)%. These results refer to  $\mathbf{E}_+ = -2.34 \times \mathbf{e}_2$  kV mm $^{-1}$  and were measured using  $\lambda = 0.75$  Å. The static measurements performed with a different crystal plate under  $\mathbf{E}_+ = 5.08 \times \mathbf{e}_2$  kV mm $^{-1}$  and at  $\lambda = 0.60$  Å yielded in the case of the symmetry equivalent reflections  $12,0,\bar{1}$  and  $65\bar{6}$   $(\Delta I/I)_a^{\text{stat}} = 1.61$  (13)% and  $(\Delta I/I)_a^{\text{stat}} = 2.52$  (20)%, respectively (see Table A.1 in the appendix). The normalization of the effect to the absolute value of  $\mathbf{E}_+$  results in  $|(\Delta I/I)_a^{\text{dyn}}| = 0.28$  (5)% and  $(\Delta I/I)_a^{\text{stat}} = 0.32$  (3)% for the  $12,0,\bar{1}$  reflection. In the case of the  $65\bar{6}$  reflection one gets  $|(\Delta I/I)_a^{\text{dyn}}| = 0.48$  (3)% and  $(\Delta I/I)_a^{\text{stat}} = 0.50$  (4)%. The observed effect differs in the signs, because of the defined positive direction of the electric fields. Accordingly, the time-resolved dynamic measurements are in the static limit within the experimental errors absolutely comparable with the experiment under a static external electric field concerning the induced changes in the atomic structure of  $\text{Li}_2\text{SO}_4 \cdot \text{H}_2\text{O}$ . Besides, neither in  $\Delta\omega$  nor in  $\Delta I/I$  a measurable delay with respect to the time structure of the HV jumps could be observed.

Next, for the evaluation of the time behavior of  $\Delta I/I$  the mode shapes of the plate vibrations are considered. The resonant mode frequencies calculated with the program *RUS*, introduced in section 1.1, assuming free boundary conditions of the available crystal plate were used to assign the measured frequencies to the corresponding vibrational mode shapes, see Figs. 5.9 – 5.13. In the plots presented the colors on the plate surface indicate the direction of the displacements normal to the surface. At this, red areas indicate bulges, blue areas stand for indentations and non-deformed areas are green.

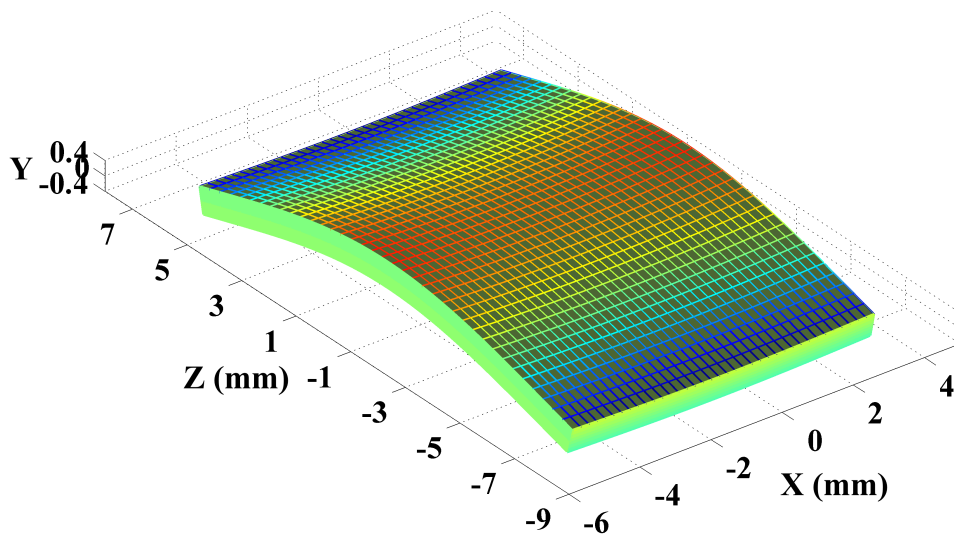


**Figure 5.9:** Resonant vibrational mode of the first crystal plate at 16 kHz,  $\mathbf{E} \parallel \text{Y-axis}$ .

5.1 Measurements with the first rectangular  $\text{Li}_2\text{SO}_4 \cdot \text{H}_2\text{O}$  (010) crystal plate

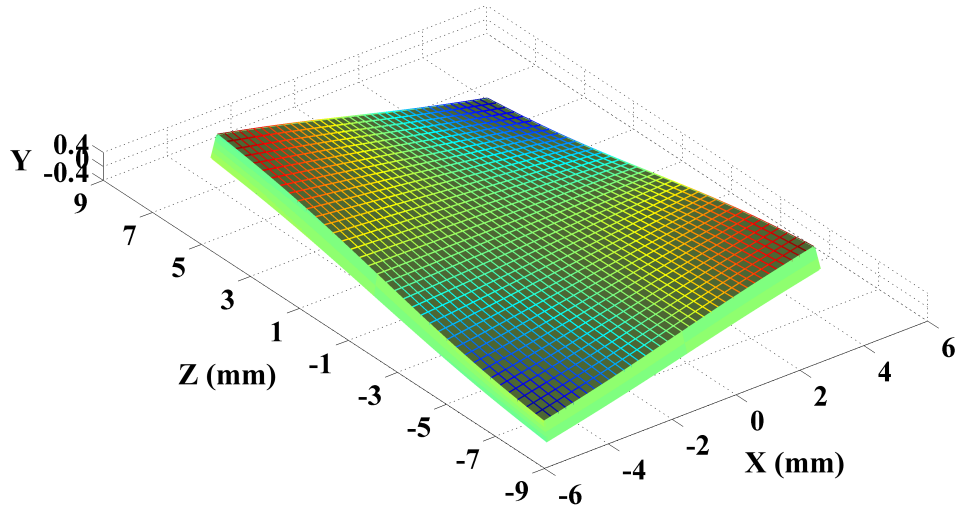


Figure 5.10: Resonant vibrational mode of the first crystal plate at 17 kHz,  $\mathbf{E} \parallel \text{Y-axis}$ .

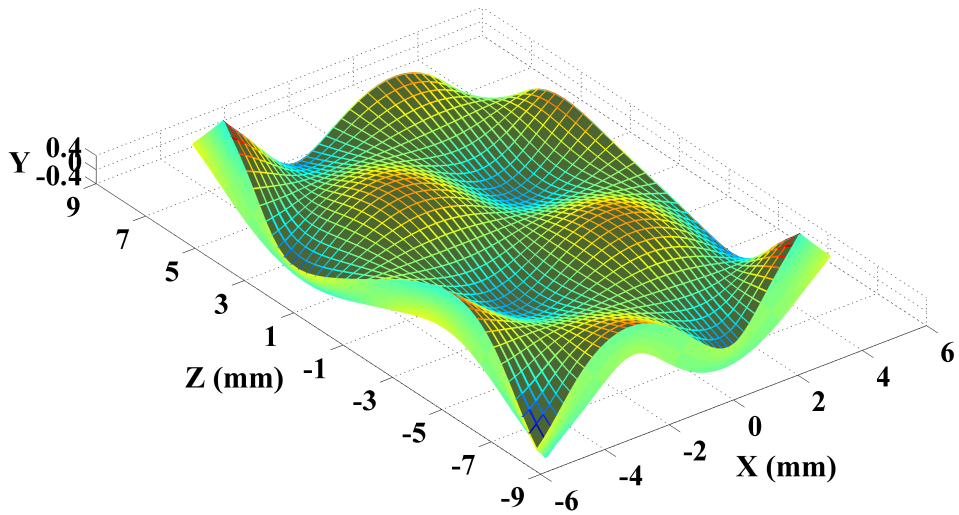


Figure 5.11: Resonant vibrational mode of the first crystal plate at 167 kHz,  $\mathbf{E} \parallel \text{Y-axis}$ .

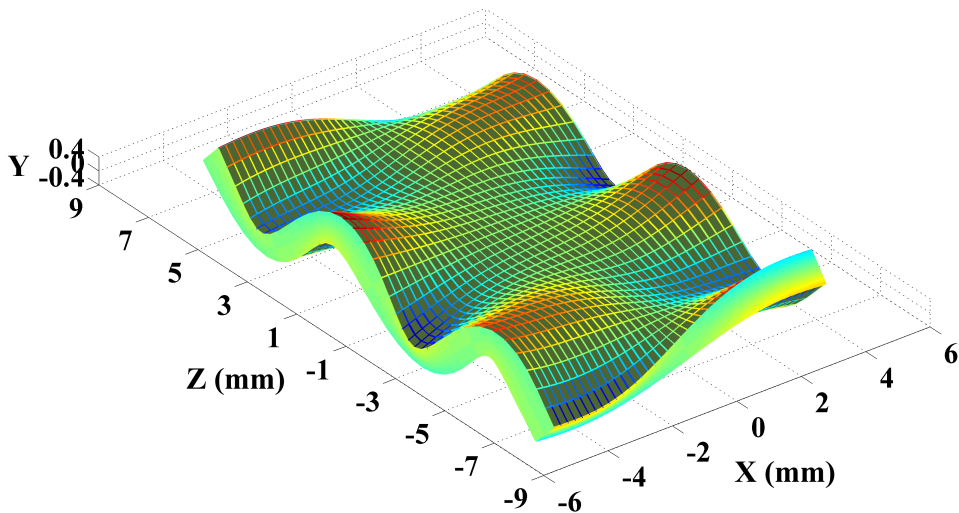
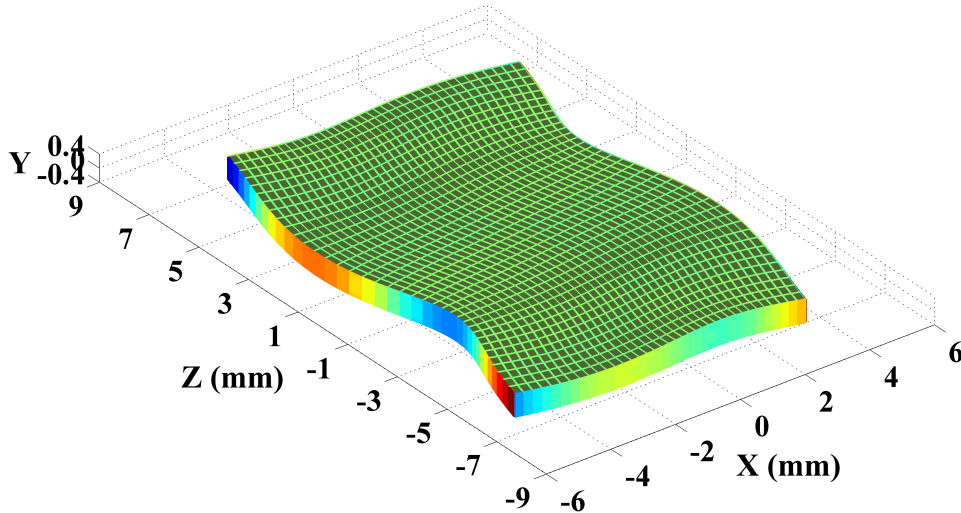


Figure 5.12: Resonant vibrational mode of the first crystal plate at 193 kHz,  $\mathbf{E} \parallel \text{Y-axis}$ .



**Figure 5.13:** Resonant vibrational mode of the first crystal plate at 271 kHz,  $\mathbf{E} \parallel \text{Y-axis}$ .

In all, the vibration frequencies obtained by the theoretical calculations overestimate the experimental values, see Table 5.3. That is because the plate was not free but rather one-sided fixed with candle wax, as illustrated in Fig. 5.1. On the other hand, the smallest frequency of the bending vibrations of a fixed crystal plate [96]

$$\nu_n = a_n(2n + 1)^2 \frac{\pi}{16\sqrt{3}} \frac{d}{l^2} \sqrt{\frac{c_{22}}{\rho}} \quad \text{with } n = 0, 1, 2, \dots, \quad a_0 \simeq 1.4 \text{ and } a_n \simeq 1 \quad (5.4)$$

is with 2.9 kHz too small compared to the corresponding experimental value ( $\nu_1 = 7$  kHz). In above equation  $\rho$  ( $2.053 \text{ g cm}^{-3}$  [75]) denotes the density of  $\text{Li}_2\text{SO}_4 \cdot \text{H}_2\text{O}$ ,  $c_{22}$  (54.2 GPa [75]) is an elastic constant of the crystal,  $d$  is the thickness and  $l$  is the length of the plate. It seems that due to the soft mechanical properties of wax the crystal plate has more degrees of freedom concerning its elastic deformations. Moreover, the mass of the 100 nm thin gold contacts is with about  $2.6 \times 10^{-4} \text{ g}$  by a factor of 577 smaller than the mass of the crystal (0.15 g). Therefore, the effect of the gold mass on the resonant frequencies of the plate can be neglected as well as the influence of the sputtered gold layers in the case of coupled oscillations with the plate [97]. This is why, in good approximation one may make use of the calculations for a free-vibrating plate to qualify the measured mode frequencies. Besides, as  $\text{Li}_2\text{SO}_4 \cdot \text{H}_2\text{O}$  exhibits a moderate piezoelectric response, according to (1.34) the error due to neglecting any interactions between the elastic, piezoelectric and dielectric properties of the crystal is negligibly small in the calculations performed.

**Table 5.3:** Comparison of the observed frequencies of resonant modes of the first crystal plate (see Fig. 5.1) with those theoretically calculated assuming a free-vibrating crystal plate.

	$\nu_1$ (kHz)	$\nu_2$ (kHz)	$\nu_3$ (kHz)	$\nu_4$ (kHz)	$\nu_5$ (kHz)
$\nu_{\text{EXP}}$	7.1 (1)	16.8 (1)	161 (1)	181 (3)	264.3 (5)
$\nu_{\text{CALC}}$	16	17	162/166/167	193	271/277

### 5.1.1 Discussion

From the determined time dependence of the relative change of diffraction intensities (see Figs. 5.6 and 5.8) two main questions arise: Firstly, it has to be clarified why the

induced elastic deformations of the crystal do not have a back influence on the fractional atomic positions within the unit cell. If this would be the case  $\Delta I/I$  would show an oscillating behavior exactly correlated to the oscillations in  $\Delta\omega$ . Secondly, one has to discuss why in addition to the elastic strain in the crystal no dynamic response could be resolved associated with the eigenvibrations of the internal strain. The latter effect does not occur, because the electric-field-induced displacements of atoms within the non-elastically deformed unit cell of a crystal are related to the optical phonons, the vibration periods of which lie commonly in the picosecond time range [44]. Therefore, with a 100 ns time resolution of the experiment such fast processes in the atomic structure cannot be detected. In contrast, the first issue is more difficult to deal with. First of all, the performed theoretical calculations do not allow for an unambiguous assignment of the observed  $\Delta\omega$  frequencies to the corresponding mode shapes, see  $\nu_3$  and  $\nu_5$  in the last row of Table 5.3. Thus, due to this uncertainty, it is well conceivable that primarily bending vibrations of the crystal plate are excited by a fast change of an applied electric perturbation, as illustrated in Figs. 5.9 – 5.13. In all these cases the major contribution to  $\Delta\omega_{\text{vibr}}$  stems from the rotation tensor  $[r_{ij}]$ , see equation (5.1). But on the other hand, as displayed in Fig. 5.14, it cannot be excluded that vibrational modes changing the dimensions of the crystal plate are generated as well. In theory, the first resonant mode strongly influencing the lattice spacings in the crystal has a frequency of 123 kHz, whereas in Fig. 5.14 the second mode having  $\nu = 162$  kHz is shown. In general, only in the case of such mode shapes the introduced field-switching X-ray diffraction experiment can be compared with measurements under high pressure.

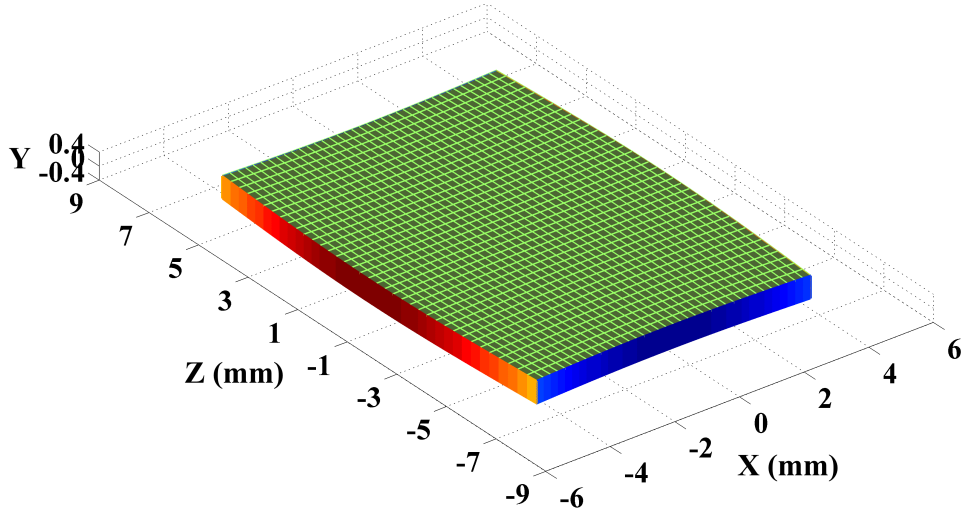


**Figure 5.14:** Resonant vibrational mode of the first crystal plate at 162 kHz,  $\mathbf{E} \parallel \text{Y-axis}$ .

Assuming that the fast  $\Delta\omega_{\text{vibr}}$  oscillations of the  $\bar{1}201$  reflection (see first 20  $\mu\text{s}$  in Fig. 5.5) with a maximum amplitude of about  $0.5 \times 10^{-3\circ}$  originate exclusively from a specific thickness vibration of the crystal plate, one may estimate the induced elastic impact on the atomic positions within the crystal. In this case according to (5.1) and with  $r_{ij} = 0$  the absolute value of  $\Delta\omega_{\text{vibr}}$  is in good approximation given by

$$\begin{aligned}
 |\Delta\omega_{\text{vibr}}(t)| &= |\Delta\omega(t) - \Delta\omega_{\text{piezo}}(t)| = |\varepsilon_{ij}(t) \left( \tan\theta \frac{H_i H_j}{H^2} + Y_i \frac{H_j}{H} \right)| \\
 &\approx |\varepsilon_{ij}(t) \tan\theta \frac{H_i H_j}{H^2}| \leq 5 \times 10^{-4\circ}.
 \end{aligned} \tag{5.5}$$

Therefore, for the  $\bar{1}201$  reflection the maximum value of the constant  $\varepsilon_{13}$  is equal to

$$\max(\varepsilon_{13}) = \frac{H^2}{2 \tan \theta |H_1| |H_3|} \times 5 \frac{\pi}{180} 10^{-4} = 5 \times 10^{-5} \quad (5.6)$$

and the maximum component of the corresponding stress,  $[\sigma_{ij}]$ , within the crystal is

$$\max(\sigma_{ij}) = \sigma_{13} = c_{1313} \varepsilon_{13} = 1 \text{ MPa}. \quad (5.7)$$

This means that the stress created in the crystal is roughly four orders of magnitude smaller than that normally accessible in modern high-pressure experiments [1]. For this reason, the elastically induced internal redistribution of atoms within the unit cell of  $\text{Li}_2\text{SO}_4 \cdot \text{H}_2\text{O}$  is negligibly small. In this context, in a very rough model a simultaneous variation of the relative  $x$  and  $z$  coordinates of the Li atoms by  $-\max(\varepsilon_{13})/2$  and those of S by  $\max(\varepsilon_{13})/20$  within the unit cell yielded that the expected effect in  $\Delta I/I$  is smaller than the magnitude of the statistical noise in the data displayed in Figs. 5.6 and 5.8,  $\Delta I/I < 0.1\%$ . Consequently, even these assumed unrealistically large Li and S displacements in  $\text{Li}_2\text{SO}_4 \cdot \text{H}_2\text{O}$  compared to the change of the lattice parameters are too small to be detected in an X-ray diffraction experiment.

Figure 5.15 shows a measurement carried out with a 0.533 mm thin  $\text{BiB}_3\text{O}_6$  (010) crystal plate. For the 060 reflection having  $\theta = 67.72^\circ$  till now the greatest oscillations of  $\Delta\omega_{\text{vibr}}$  ( $|\Delta\omega_{\text{vibr}}| \leq 1.7 \times 10^{-2^\circ}$ ) resulting in

$$\max(\varepsilon_{22}) = \frac{1}{\tan \theta} \times 1.7 \frac{\pi}{180} 10^{-2} = 1 \times 10^{-4} \quad (5.8)$$

and

$$\max(\sigma_{ij}) = \sigma_{11} = c_{1122} \varepsilon_{22} = 7.4 \times 10^6 \text{ Pa} \quad (5.9)$$

could be observed, as the piezoelectric effect of  $\text{BiB}_3\text{O}_6$  is much larger than that of  $\text{Li}_2\text{SO}_4 \cdot \text{H}_2\text{O}$ . But even in this case the maximum value of the stress components within the  $\text{BiB}_3\text{O}_6$  crystal lies in the range of MPa. Therefore, future experiments should be performed with crystals possessing much greater piezoelectric constants.

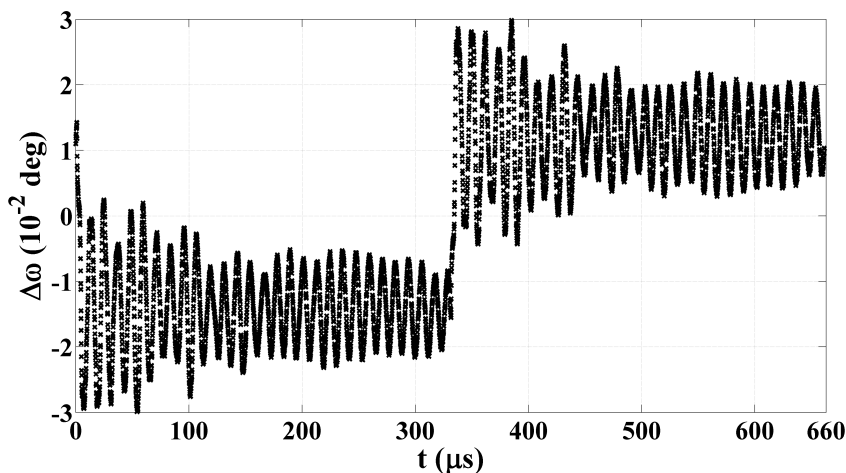


**Figure 5.15:** Using a 0.533 mm thin  $\text{BiB}_3\text{O}_6$  (010) crystal plate, for the  $\text{BiB}_3\text{O}_6$  060 reflection till now within the experimental limits detected maximum displacements of  $\Delta\omega_{\text{vibr}}$ .

## 5.2 Measurements with the second rectangular $\text{Li}_2\text{SO}_4\cdot\text{H}_2\text{O}$ (010) crystal plate

Applying a 100 ns time resolution the measurements with the second  $\text{Li}_2\text{SO}_4\cdot\text{H}_2\text{O}$  crystal plate (see Fig. 5.2) subjected to fast periodic changes of an external electric field were conducted using a high-resolution diffractometer of the home X-ray laboratory. Unlike the experiment with the first plate, this time the applied basic HV period consisted solely of a  $U_+$  and  $U_-$  HV state, as depicted in Fig. 3.5. Because of the strong absorption of the Cu  $K\alpha$  radiation by the crystal, the strongest reflections in the Bragg geometry, such as 130, 031 and 020, were considered only. The curves  $\Delta\omega_+$  and  $\Delta\omega_-$  measured for the asymmetric reflections 130 and 031 are presented in Figs. 5.16 and 5.17. The used frequency of the basic HV period was 1.5 kHz and the HV magnitudes amounted to  $U_{\pm} = \pm 1.5$  kV. As demonstrated by the blue curves, the introduced model (5.2) is well applicable for extracting all superimposed frequencies in the  $\Delta\omega$  data, although the damping of the oscillations deviates from the assumed exponential behavior.

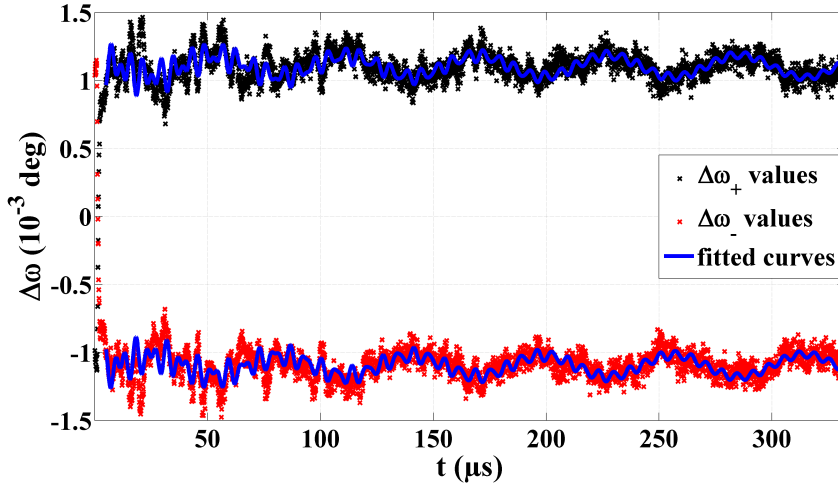


**Figure 5.16:** Angular shift of the Bragg peak position of the 130 reflection within the basic HV period consisting of a  $U_+$  and  $U_-$  state, as shown in Fig. 3.5. The red curve ( $\Delta\omega_-$  values) was referred to  $t = 0 \mu\text{s}$  instead of  $t = 333 \mu\text{s}$  to visualize the symmetry of the effect. Using the approach (5.2), the blue curves were fitted to the experimental data.

**Table 5.4:** Oscillation frequencies determined from the recorded  $\Delta\omega$  curves of the 130, 031 and 020 reflection. The experimental data were analyzed separately for the  $U_+$  and  $U_-$  HV state.

Reflection	HV state	$\nu_1$ (kHz)	$\nu_2$ (kHz)	$\nu_3$ (kHz)
130	$U_+$	17.24 (3)	146.4 (2)	219.3 (5)
	$U_-$	17.27 (3)	146.4 (2)	218.8 (5)
031	$U_+$	17.00 (3)	145.6 (2)	220.5 (5)
	$U_-$	16.98 (3)	145.6 (2)	220.5 (5)
020	$U_+$	16.89 (3)	147.1 (2)	218.3 (5)
	$U_-$	16.91 (3)	147.3 (2)	219.3 (5)

In total, three different modes of the crystal plate vibrations could be determined, see Table 5.4. Expectedly, the frequencies do not differ much either between the HV

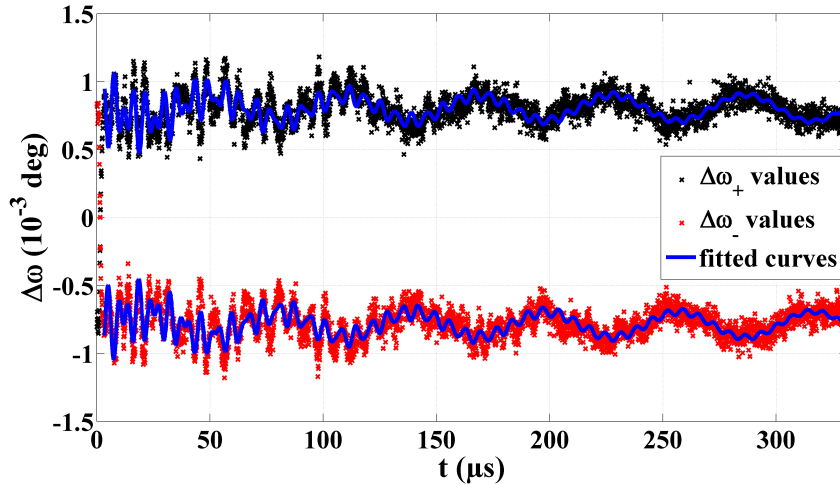


**Figure 5.17:** Angular shift of the Bragg peak position of the 031 reflection within the 2-step modulated basic HV period, see Fig. 3.5. Analogous to Fig. 5.16, the red curve ( $\Delta\omega_-$  values) was referred to  $t = 0 \mu\text{s}$  and the blue curves represent fits of the model (5.2) to the recorded experimental data.

states  $U_+$  and  $U_-$  or between the reflections 130, 031 and 020. In Table 5.5 the observed frequencies are compared with those of the resonant vibrational modes of a free-vibrating plate. Again, also in the case of the second plate the theoretical values are by about 10 kHz larger. The shape of the first mode ( $\nu_1 = 17 \text{ kHz}$ ) is similar to that presented in Fig. 5.10, the shape of the second mode ( $\nu_2 = 147 \text{ kHz}$ ) is comparable with the situation shown in Fig. 5.12 and the shape of the third mode ( $\nu_3 = 220 \text{ kHz}$ ) is either of the form plotted in Fig. 5.13 or in Fig. 5.14. Besides, due to the different dimensions of both  $\text{Li}_2\text{SO}_4 \cdot \text{H}_2\text{O}$  crystal plates the frequencies of their vibrational modes excited in the experiments are similar but not the same, as shown in the last row of Table 5.5.

**Table 5.5:** Comparison of the observed frequencies of resonant modes of the second  $\text{Li}_2\text{SO}_4 \cdot \text{H}_2\text{O}$  crystal plate (Fig. 5.2) with those on the one hand theoretically calculated and on the other hand measured in the case of the first plate (Fig. 5.1).

	$\nu_1$ (kHz)	$\nu_2$ (kHz)	$\nu_3$ (kHz)
$\nu_{\text{EXP}}$	17.0 (2)	146.6 (6)	219.5 (9)
$\nu_{\text{CALC}}$	26	155	228/230
$\nu_{\text{EXP, 1st plate}}$	7/17	161/181	264

### 5.3 X-ray diffraction investigations of the piezoelectrically induced crystal vibrations

Using the second  $\text{Li}_2\text{SO}_4 \cdot \text{H}_2\text{O}$  crystal plate, by means of the measurements of the 020 reflection the time behavior of  $\Delta\omega$  within the basic HV period was investigated as a function of the magnitude of the  $U_+$  and  $U_-$  state (see Fig. 5.18) and frequency of the HV period (see Fig. 5.19). Furthermore, in order to probe the Bragg angle dependence of  $\Delta\omega$ , the reflections 020, 040 and 060 of the second plate were considered, as summarized in Fig. 5.20.

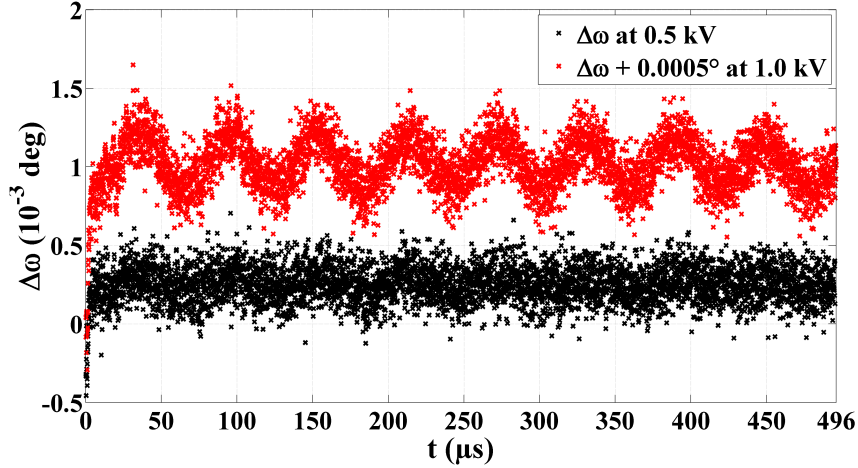


**Figure 5.18:** Angular shift of the Bragg peak position of the 020 reflection measured for  $U_{\pm} = \pm 0.5$  kV and  $U_{\pm} = \pm 1.0$  kV. In this data representation the  $\Delta\omega_{+}$  curves of the  $U_{+}$  period are shown only and the  $\Delta\omega_{+}$  values recorded under  $U_{+} = 1.0$  kV were increased by  $5 \times 10^{-4}$ .

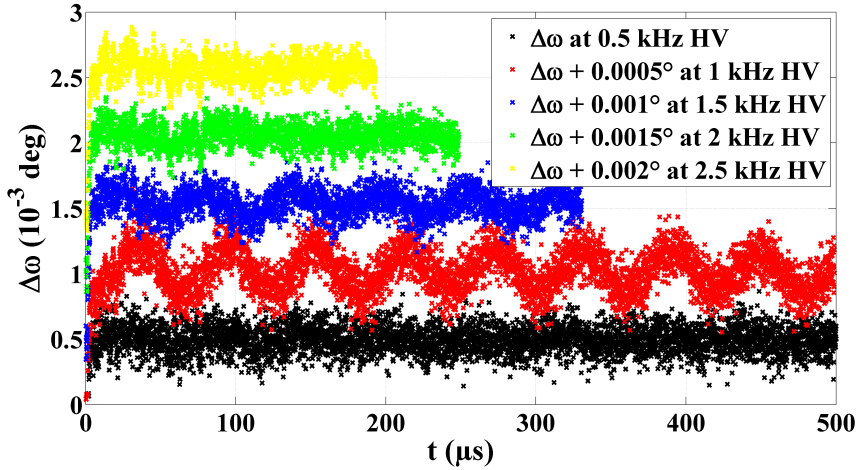


**Figure 5.19:** Angular shift of the Bragg peak position of the 020 reflection as a function of the frequency of the HV applied to the crystal plate. Note that the  $\Delta\omega_{+}$  curves are displayed only. In order to demonstrate the effect observed, the  $\Delta\omega_{+}$  values were appropriately increased.

The first measurements (Fig. 5.18) performed with a HV frequency of 1 kHz revealed that the induced dynamic response of the crystal increases strongly with the  $U_{\pm}$  values. This behavior is logical as the external perturbation, applied strength of the piezoelectric “punch” on the crystal plate, scales with the magnitude of the HV. The second measurements (Fig. 5.19) showed that the 1 kHz HV frequency is the most favorable to an excitation of the vibrational mode at 17 kHz (see Fig. 5.10) of the plate. This pronounced resonant response of the crystal to individual HV frequencies confirms the approach introduced in section 3.2.1. The analysis of the third measurements (shown in Fig. 5.20 and carried out applying  $\nu(\text{HV}) = 2.5$  kHz and  $U_{\pm} = \pm 1.0$  kV) presented in Fig. 5.21 explicitly illustrates that in the X-ray diffraction experiment conducted the piezoelectric deformation of the crystal and the excited elastic vibrations are really detected as two different physical effects. While  $\Delta\omega_{\text{piezo}}$  is strongly dependent on  $\tan \theta$ , the  $\tan \theta$  dependence of the  $\max(|\Delta\omega_{\text{vibr}}|)$  values is much less pronounced, as the piezoelectric deformation of the corresponding  $\mathbf{H}$  vectors is normally not equal to their induced elastic variation.

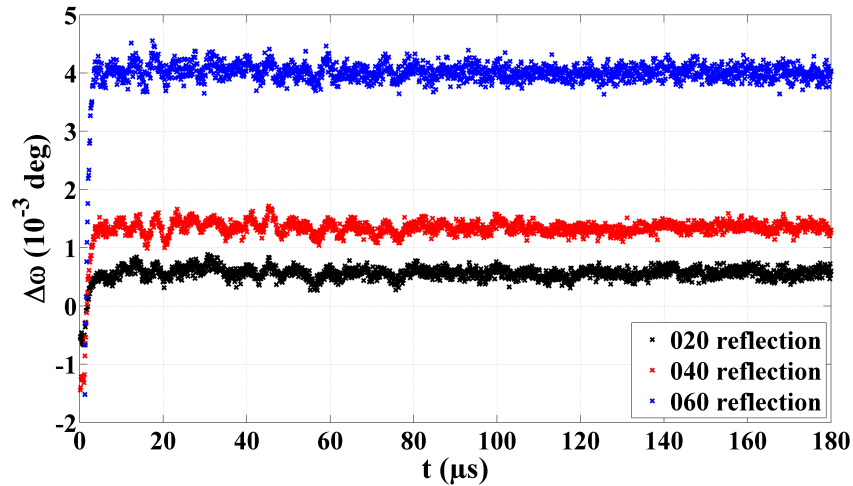


**Figure 5.20:** Angular shifts (here the  $\Delta\omega_+$  data) of the Bragg peak position of the 020, 040 and 060 reflection are compared with each other.

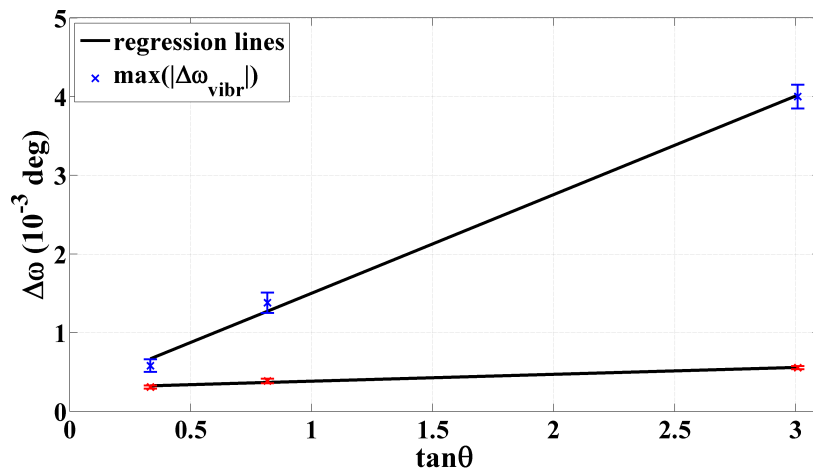


**Figure 5.21:** From the  $\omega_+$  curves displayed in Fig. 5.20 extracted contribution of  $\Delta\omega_{\text{piezo}}$  [see eq. (5.1)] and maximum absolute value of  $\Delta\omega_{\text{vibr}}$  plotted against  $\tan\theta$ .

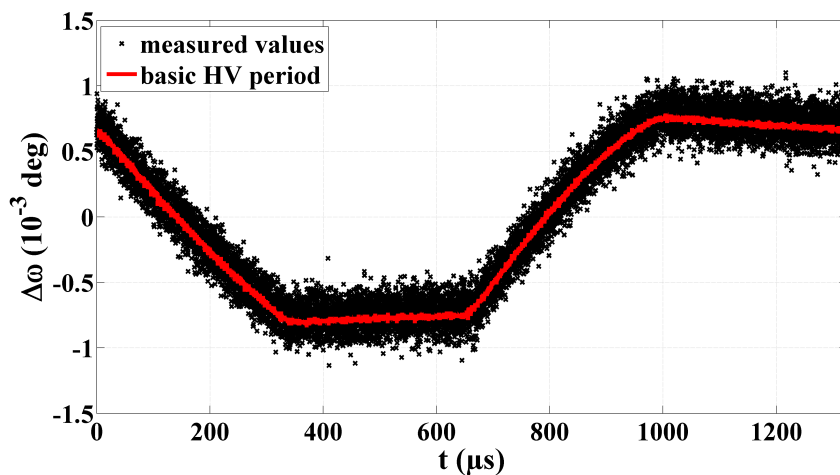


**Figure 5.22:** Angular shift of the Bragg peak position of the 031 reflection within the basic HV period modulated according to the red curve.

Another measurement (Fig. 5.22) performed with a changed modulation of the basic HV period makes clear that the fast switching time between different HV states is the crucial parameter of the experiment described. In the example depicted in Fig. 5.22 the frequency of the basic HV period was 0.75 kHz and the HV states  $U_+$  and  $U_-$  were of the magnitudes  $U_{\pm} = \pm 1.0$  kV. The switching time between  $U_{\pm}$  and  $U_{\mp}$  amounted to very slow 0.3 ms and consequently, the  $\Delta\omega$  curve measured for the 031 reflection does not possess an oscillatory behavior but rather exactly reflects the time structure of the HV.

### 5.3.1 Supplementary measurements performed with other $\text{Li}_2\text{SO}_4 \cdot \text{H}_2\text{O}$ and $\text{BiB}_3\text{O}_6$ crystal plates

From a broad range of the time-resolved measurements conducted with other differently shaped  $\text{Li}_2\text{SO}_4 \cdot \text{H}_2\text{O}$  and  $\text{BiB}_3\text{O}_6$  crystal plates the most interesting two will be discussed in this section.

In Fig. 5.23 the  $\Delta\omega_+$  curves of the 020, 040 and 060 reflection measured using a 0.718 mm thin  $\text{BiB}_3\text{O}_6$  (010) crystal plate are presented. Here the oscillations in  $\Delta\omega$  are not only very pronounced but also strongly dependent on  $\tan\theta$  in comparison with the results illustrated in Figs. 5.20 and 5.21. The maximum amplitude of  $\Delta\omega_{\text{vibr}}$  is even larger than the piezoelectric offset ( $|\Delta\omega_{\text{piezo}}|$ ) of the  $\Delta\omega_+$  curves, see Fig. 5.24. It is quite amazing that the  $\tan\theta$  dependence of  $|\Delta\omega_{\text{piezo}}|$  and  $\max(|\Delta\omega_{\text{vibr}}|)$  is almost equal, although both effects have a completely different physical background. Unfortunately, due to the not well-defined dimensions of this plate, it was not possible to assign the  $\Delta\omega_{\text{vibr}}$  oscillations to a vibrational mode of the crystal.

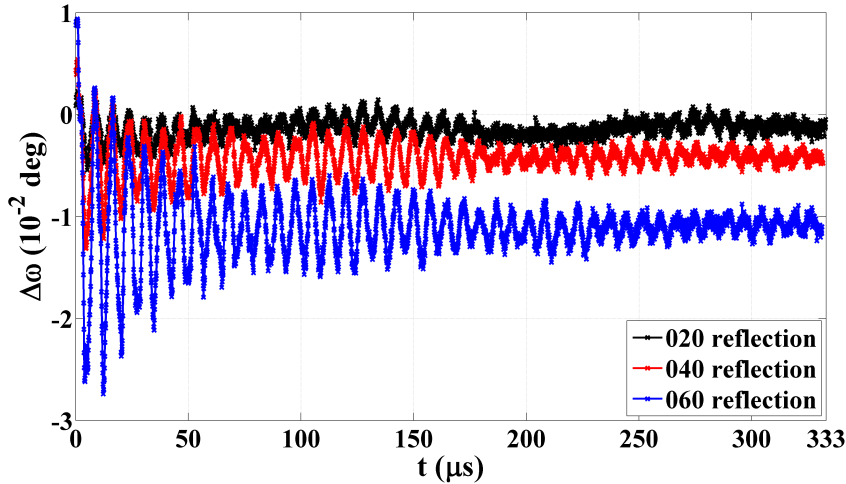


**Figure 5.23:** Angular shifts of the  $\omega$  rocking curve position of the 020, 040 and 060 reflection of a 0.718 mm thin  $\text{BiB}_3\text{O}_6$  (010) crystal plate. Note that the  $\Delta\omega$  curves measured during the  $U_+$  HV period are presented only.

In the second experiment by means of the 040 reflection of a 0.617 mm thin  $\text{Li}_2\text{SO}_4 \cdot \text{H}_2\text{O}$  (010) crystal plate  $\Delta\omega$  was recorded dependent on the X-ray spot position on the plate. For that, outside the region of the gold contacts three different  $z$  positions at an interval of 2 mm along the longest plate dimension were considered. As depicted in Fig. 5.25, the  $\Delta\omega_+$  curve changes its phase and amplitude as a function of  $z$ . These observations agree well with the spatial dependence of the mode shapes of the resonant plate vibrations displayed in Figs. 5.9 – 5.12.

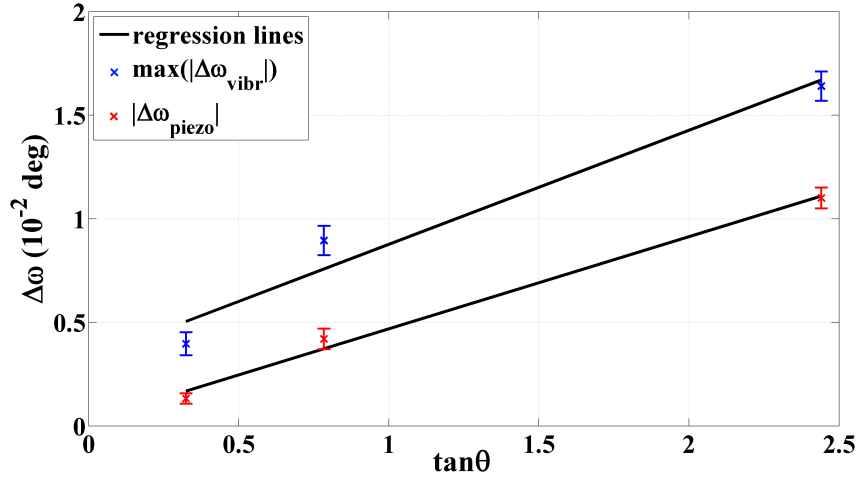


**Figure 5.24:** From the raw data shown in Fig. 5.23 extracted  $\max(|\Delta\omega_{\text{vibr}}|)$  and  $|\Delta\omega_{\text{piezo}}|$  values plotted against  $\tan\theta$ .

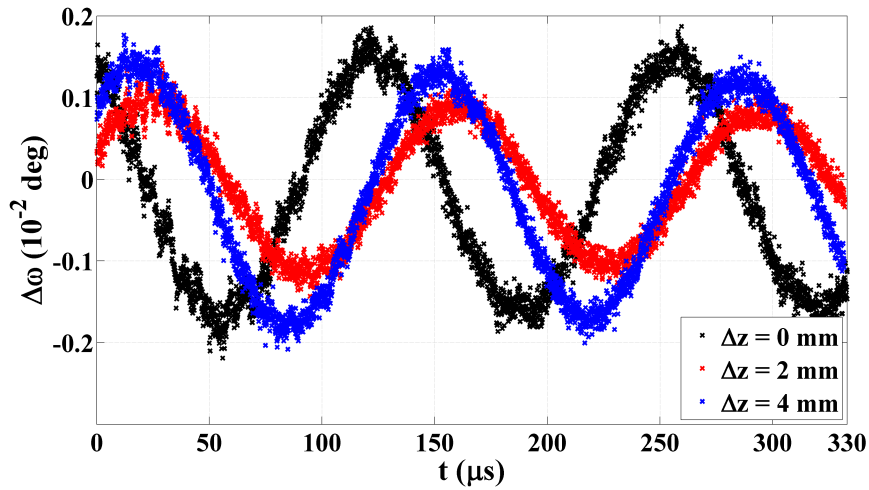


**Figure 5.25:**  $\Delta\omega_+$  curve of the 040 reflection of a 0.617 mm thin  $\text{Li}_2\text{SO}_4\cdot\text{H}_2\text{O}$  crystal plate recorded as a function of the X-ray spot position,  $z$  value, on the plate ( $\nu(\text{HV}) = 1.5$  kHz and  $U_{\pm} = \pm 1.5$  kV). All three  $z$  positions were outside the region of the gold contacts, thus the piezoelectric offset,  $\Delta\omega_{\text{piezo}}$ , is zero in the data.

## 6 Summary

The work presented covers a broad range of modern research on the response of piezoelectric crystals to a periodically applied external electric perturbation both on the macroscopic and microscopic scale. Apart from the X-ray diffraction technique as a standard probe of the electric-field-induced atomic displacements in a crystal, an approach to the internal strain by means of neutron diffraction was tested and analyzed in terms of its feasibility. In addition, a novel concept of an X-ray diffraction experiment for the time-resolved measurements of the external and internal strain in piezoelectric crystals based on the detector pulse processing with a 100 MHz FPGA chip was realized in collaboration with the electronic workshop of the University of Siegen. In particular, by reducing the switching time between different HV states to fast 200 ns within the modulation of the basic HV period applied to a crystal dynamic processes in the crystal were excited, the properties of which could be successfully investigated by performing X-ray measurements of diffraction curves with a time resolution of 100 ns. All measurements benefit substantially from the X-ray (neutron) diffraction technique, as it enables a simultaneous as well as a separate study of the electric-field-induced vibrational modes, piezoelectric deformation, changes in the mosaic and atomic structure of a crystal.

In detail, the investigations of the  $\text{Li}_2\text{SO}_4\cdot\text{H}_2\text{O}$ ,  $\text{Li}_2\text{SeO}_4\cdot\text{H}_2\text{O}$  and  $\text{BiB}_3\text{O}_6$  piezoelectric single crystals under an external electric field yielded three main results concerning the nature of the internal strain in a crystal: Firstly, based on the measurements using three differently oriented  $\text{BiB}_3\text{O}_6$  crystal plates the induced deformation of the atomic polyhedra was confirmed to be strongly dependent on the direction of an applied electric field with respect to the crystal structure. Secondly, the measurements with  $\text{Li}_2\text{SO}_4\cdot\text{H}_2\text{O}$  and  $\text{Li}_2\text{SeO}_4\cdot\text{H}_2\text{O}$  showed that the bond-selective distortion observed within these crystals depends on the strength of a chemical bond and the charges of the respective pseudoatoms bonded to each other, as extracted from a topological analysis of the static electron density. Thirdly, these two parameters have proved to be by far not sufficient for an adequate explanation of the electric-field-induced much greater average Li–O bond deformation in  $\text{Li}_2\text{SeO}_4\cdot\text{H}_2\text{O}$  compared to the magnitude of the effect measured in  $\text{Li}_2\text{SO}_4\cdot\text{H}_2\text{O}$ . These findings were referred to the larger vacancies in the structure of the lithium ion conducting  $\text{Li}_2\text{SeO}_4\cdot\text{H}_2\text{O}$  that significantly facilitate the movement of the lithium ions within the crystal under an applied electric field. Furthermore, one has also to consider the chemical environment surrounding the structural units in a crystal, as derived from a comparison with other reported studies on piezoelectric compounds. In total, it seems that the strength of hydrogen bonds has a huge influence on the electric-field-induced atomic rearrangement in a crystal. But the understanding of such complicated interdependences in a crystal is still far beyond the scope of present theories.

Finally, the dynamic response of two rectangular-shaped and plane-parallel  $\text{Li}_2\text{SO}_4\cdot\text{H}_2\text{O}$  crystal plates was deduced from the recorded time behavior of the peak position and integrated intensity of X-ray reflections. It has turned out that mainly superimposed vibrational modes of the crystals are excited by fast periodical changes between different HV states applied. Besides, it was shown that the crystal vibrations have a strong de-

## 6 Summary

pendence on the HV switching time and a pronounced resonance of one mode relating to the HV frequency was proved. In contrast, the diffraction intensity and thus, the internal strain did not exhibit as a function of time an oscillatory behavior but rather replicated the time structure of the basic HV period analogous to the time-averaged static measurements. The origin of this effect is related on the one hand to the 100 – 20 ns time resolution of the experiment that does not enable the detection of the fast processes associated with the electric-field-excited resonant optical phonon modes within a non-elastically deformed crystal. Moreover, on the other hand, the performed estimations revealed that within the experimental limits even in the case of  $\text{BiB}_3\text{O}_6$ , the piezoelectric effect of which is much stronger than that of  $\text{Li}_2\text{SO}_4\cdot\text{H}_2\text{O}$ , the pressure exerted on the atoms within the crystal by its elastic deformations lies in the range of MPa only and therefore is about three orders of magnitude smaller than that normally accessible in modern high-pressure experiments. Consequently, for an X-ray diffraction experiment the elastically induced internal redistribution of atoms in  $\text{Li}_2\text{SO}_4\cdot\text{H}_2\text{O}$  and  $\text{BiB}_3\text{O}_6$  was negligibly small. In order to overcome this drawback, future experiments should be conducted with crystals having much greater piezoelectric constants. For instance, an interesting field-switching experiment may be done with ferroelectric crystals that are cooled down or heated up to the close vicinity of their respective Curie temperature. In total, the measurements carried out well demonstrate the broad possible fields of application of the developed technique for the time-resolved studies not only of the elastic, piezoelectric and dielectric properties of a crystal under an external electric perturbation.

# Appendix

## A.1 Publications arising from the thesis

- Gorfman, S.; Schmidt, O.; Pietsch, U.; Becker, P.; Bohatý, L.: X-ray diffraction study of the piezoelectric properties of  $\text{BiB}_3\text{O}_6$  single crystals. *Z. Kristallogr.* **222** (2007), 396-401.
- Schmidt, O.; Gorfman, S.; Pietsch, U.: Electric-field-induced internal deformation in piezoelectric  $\text{BiB}_3\text{O}_6$  crystals. *Cryst. Res. Technol.* **43** (2008), 1126-1132.
- Schmidt, O.; Gorfman, S.; Bohatý, L.; Neumann, E.; Engelen B.; Pietsch, U.: Investigations of the bond-selective response in a piezoelectric  $\text{Li}_2\text{SO}_4\cdot\text{H}_2\text{O}$  crystal to an applied external electric field. *Acta Cryst.* **A65** (2009), 267-275.
- Gorfman, S.; Schmidt, O.; Ziolkowski, M.; von Kozirowski, M.; Pietsch, U.: Time-resolved X-ray diffraction studies of piezoelectric crystal response to a fast change of an applied electric field. *J. Appl. Phys.* (2010), submitted.

## A.2 Talks given at conferences, colloquiums and workshops

- Schmidt, O.; Gorfman, S.; Pietsch, U.: *Röntgenbeugungsuntersuchungen an Wismuttriborat,  $\text{BiB}_3\text{O}_6$* . 15. Jahrestagung der Deutschen Gesellschaft für Kristallographie, Bremen, Germany, 2007.
- Schmidt, O.: *Röntgenbeugungsuntersuchungen an Wismuttriborat,  $\text{BiB}_3\text{O}_6$ , und Lithiumsulfat-Monohydrat,  $\text{Li}_2\text{SO}_4\cdot\text{H}_2\text{O}$ , im äußeren elektrischen Feld*. Institut für Kristallographie, Universität zu Köln, Germany, 2007.
- Schmidt, O.; Gorfman, S.; Pietsch, U.: *Effect of the choice of radial function coefficients of Zn on the electron density refinement of  $\text{ZnSiP}_2$* . Workshop: Electron Density Reconstruction from Diffraction Experiments on Compounds of Heavy Elements, Dresden, Germany, 2007.
- Schmidt, O.; Gorfman, S.; Pietsch, U.; Bohatý, L.; Becker, P.: *Röntgenbeugungsuntersuchungen der durch ein äußeres elektrisches Feld induzierten strukturellen Verzerrungen in  $\text{Li}_2\text{SO}_4\cdot\text{H}_2\text{O}$* . 16. Jahrestagung der Deutschen Gesellschaft für Kristallographie, Erlangen, Germany, 2008.
- Schmidt, O.; Gorfman, S.; Pietsch, U.: *X-ray diffraction study of the external-electric-field-induced internal strain in piezoelectric  $\text{Li}_2\text{SO}_4\cdot\text{H}_2\text{O}$  and  $\text{Li}_2\text{SeO}_4\cdot\text{H}_2\text{O}$  single crystals*. 5th European Charge Density Meeting, Gravedona, Italy, 2008.

- Schmidt, O.; Pietsch, U.; Bohatý, L.; Becker, P.: *Zeitaufgelöste Röntgenbeugungsuntersuchungen der piezoelektrisch induzierten elastischen Wellen in  $\text{Li}_2\text{SO}_4\cdot\text{H}_2\text{O}$  und  $\text{BiB}_3\text{O}_6$* . 17. Jahrestagung der Deutschen Gesellschaft für Kristallographie, Hannover, Germany, 2009.
- Schmidt, O.; Gorfman, S.; Pietsch, U.; Becker, P.; Bohatý, L.: *Time-resolved X-ray diffraction study of  $\text{BiB}_3\text{O}_6$  and  $\text{Li}_2\text{SO}_4\cdot\text{H}_2\text{O}$  response to a fast change of an external electric field state*. 25th European Crystallographic Meeting, Istanbul, Turkey, 2009.

### A.3 Financing

This work was financially supported by Deutsche Forschungsgemeinschaft (Special Priority Program II/III 1178: Experimental charge density determination as the key for understanding chemical interactions).

### A.4 All $(\Delta I/I)_a$ data observed and calculated for $\text{Li}_2\text{SO}_4\cdot\text{H}_2\text{O}$ , $\text{Li}_2\text{SeO}_4\cdot\text{H}_2\text{O}$ and $\text{BiB}_3\text{O}_6$

**Table A.1:** Summary of all in the case of  $\text{Li}_2\text{SO}_4\cdot\text{H}_2\text{O}$  observed relative variations,  $(\Delta I/I)_a$ , of diffraction intensities together with the corresponding calculated model values.

$h, k, l$	$\lambda$ (Å)	$[(\Delta I/I)_a]_{\text{OBS}}$ (%)	$[(\Delta I/I)_a]_{\text{MOD}}$ (%)	$[(\text{OBS}-\text{MOD})/\sigma]^2$
0,-1,12	0.60	-1.63 (11)	-1.26	11.38
10,0,-6	0.60	-1.31 (10)	-0.91	15.03
10,-4,-6	0.60	-1.93 (13)	-2.26	6.58
10,-5,-2	0.60	-2.41 (14)	-1.89	14.05
11,2,0	0.60	-0.75 (7)	-0.9	4.73
11,4,0	0.60	-1.70 (9)	-1.28	19.42
11,-1,-1	0.60	0.68 (7)	0.78	1.87
11,-1,-6	0.60	2.52 (11)	1.62	63.51
11,-2,-5	0.60	-1.28 (9)	-0.96	12.8
12,0,-1	0.60	1.61 (13)	2.31	27.31
12,0,-6	0.60	1.57 (9)	1.17	18.22
12,-1,-5	0.60	-1.13 (10)	-0.71	16.33
3,2,9	0.60	-0.96 (10)	-0.54	17.17
4,0,12	0.60	-1.27 (8)	-1.3	0.09
4,1,11	0.60	-3.75 (22)	-2.62	26.98
5,-8,-1	0.60	-1.65 (14)	-2.3	20.6
6,-2,0	0.60	-2.63 (12)	-1.35	107.01
6,8,-5	0.60	-1.63 (10)	-1.62	0.0
6,8,-7	0.60	-1.40 (11)	-2.08	40.31
6,-8,-5	0.60	-1.84 (20)	-1.64	0.93
8,1,-4	0.60	-1.72 (15)	-1.61	0.62
9,0,-2	0.60	3.91 (22)	3.24	9.13
9,0,-4	0.60	-0.83 (9)	-1.09	7.26
9,6,-2	0.60	1.86 (11)	1.29	27.72

A.4 All  $(\Delta I/I)_a$  data observed and calculated for  $\text{Li}_2\text{SO}_4 \cdot \text{H}_2\text{O}$ ,  $\text{Li}_2\text{SeO}_4 \cdot \text{H}_2\text{O}$  and  $\text{BiB}_3\text{O}_6$

9,-7,-1	0.60	-1.84 (12)	-1.19	27.58
-9,7,1	0.60	-2.01 (15)	-1.18	29.01
-2,4,-8	0.60	1.89 (10)	1.93	0.21
-3,-3,-10	0.60	-1.52 (15)	-2.09	13.98
-4,-1,-11	0.60	-3.50 (13)	-2.72	36.44
-5,0,-8	0.60	-1.15 (8)	-0.96	6.29
-5,-3,-7	0.60	-1.29 (11)	-0.25	82.64
-6,0,-4	0.60	-1.66 (9)	-0.72	113.9
-6,-4,-7	0.60	-2.59 (14)	-3.43	37.12
-7,0,-3	0.60	-2.23 (11)	-1.97	6.0
-7,1,-2	0.60	2.51 (12)	3.06	20.71
-7,3,-7	0.60	1.09 (14)	1.03	0.15
-7,-1,-2	0.60	2.94 (15)	3.12	1.44
-7,-2,-11	0.60	1.19 (8)	0.78	24.08
-7,-5,-5	0.60	0.97 (7)	1.09	3.03
-8,0,-9	0.60	-1.95 (17)	-2.2	2.3
-8,1,-8	0.60	-1.22 (10)	-1.04	3.66
-8,2,-7	0.60	2.16 (9)	1.22	103.3
-8,2,-9	0.60	-1.52 (9)	-1.43	0.79
-8,3,-8	0.60	0.88 (11)	0.77	1.04
-8,-1,9	0.60	-1.42 (12)	-0.99	12.42
-8,-1,-1	0.60	-1.26 (8)	-0.77	34.84
-9,0,12	0.60	-1.37 (10)	-1.8	16.83
-9,0,-1	0.60	1.99 (13)	0.93	69.29
-9,1,-4	0.60	-1.92 (19)	-2.3	4.02
-9,-2,-3	0.60	1.67 (15)	1.13	14.0
6,5,-6	0.60	2.52 (20)	2.79	1.8
6,-5,-6	0.60	2.30 (10)	2.77	22.2
-3,3,-3	0.60	0.99 (11)	0.14	60.41
-7,4,-1	0.60	3.05 (15)	2.53	12.59
-2,8,-8	0.60	-1.64 (16)	-0.66	39.63
7,-3,-8	0.60	-1.48 (13)	-1.18	5.45
-8,0,-2	0.60	-2.42 (12)	-3.43	73.45
0,-4,-1	0.60	0.81 (9)	1.67	91.17
0,9,1	0.60	-0.61 (10)	-0.13	22.87
10,0,3	0.60	-0.24 (5)	-0.24	0.0
-10,-1,0	0.60	-0.31 (10)	-0.3	0.02
3,7,-4	0.60	0.57 (7)	0.53	0.39
5,-3,-12	0.60	0.68 (8)	1.18	39.68
6,0,5	0.60	0.56 (8)	0.36	6.42
-6,0,5	0.60	-0.80 (10)	-0.99	3.8
-2,6,9	0.60	0.87 (10)	1.61	55.39
-4,8,4	0.60	0.54 (8)	0.51	0.16
0,8,2	0.60	0.22 (4)	0.22	0.0
0,-8,2	0.60	0.37 (4)	0.27	6.21
4,6,5	0.60	-0.14 (14)	-1.13	50.1
-4,-6,-5	0.60	-0.48 (7)	-1.12	83.93
0,-8,4	0.60	0.14 (4)	0.47	66.28

Appendix

-7,-5,0	0.60	0.22 (6)	0.35	4.72
7,7,0	0.60	1.20 (19)	1.57	3.89
3,5,1	0.60	0.40 (8)	0.69	13.34
-2,5,-7	0.60	-1.13 (7)	-1.76	80.97
-1,-8 3	0.60	-0.56 (5)	-0.27	34.34
10,0,-3	0.60	0.14 (7)	0.43	16.79
5,4,-3	0.60	0.17 (15)	0.43	2.89
2,-5,7	0.60	-3.10 (9)	-2.33	72.49
4,8,-7	0.60	0.24 (10)	0.56	10.18
-7,7,-4	0.60	-1.95 (15)	-1.02	41.86
3,8,2	0.60	0.34 (11)	0.47	1.48
3,-8,2	0.60	0.35 (6)	0.49	5.23
7,0,8	0.60	-2.84 (22)	-4.51	58.74
11,0,0	0.60	-4.24 (21)	-4.08	0.54
3,-8,9	0.60	3.27 (09)	2.02	184.91
0,5,1	0.60	0.54 (7)	0.22	20.48
0,8,4	0.60	0.27 (3)	0.4	21.13
0,-5,1	0.60	0.29 (6)	0.31	0.10
10,0,-8	0.60	1.20 (18)	0.66	8.63
7,5,0	0.60	0.35 (14)	0.35	0.0
9,0,3	0.60	1.20 (4)	1.59	84.5
-8,6,3	0.60	0.82 (13)	2.38	150.22
9,0,-2	0.60	3.04 (23)	3.24	0.73
5,0,-6	0.60	-7.91 (6)	-7.97	1.08
6,0,0	0.60	-1.94 (5)	-1.95	0.04
0,0,11	0.60	-2.83 (11)	-2.8	0.07
-5,0,-6	0.60	-1.67 (6)	-1.36	30.03
-6,0,-7	0.60	-2.13 (15)	-1.86	3.31
1,7,-4	0.60	1.62 (18)	0.46	39.81
5,-5,-4	0.60	0.49 (5)	0.16	44.45
7,-5,-12	0.60	0.81 (13)	0.14	27.71
1,-4,-5	0.60	-0.90 (10)	-1.82	91.72
5,7,-5	0.60	-1.55 (9)	-0.69	99.6
8,7,-9	0.60	-1.08 (10)	-1.06	0.03
-8,-7,-3	0.60	0.91 (11)	1.56	38.12
8,-1,-4	0.60	-2.32 (16)	-2.13	1.48
-6,-8,7	0.60	-1.20 (16)	-2.46	61.7
3,-8,-8	0.60	-0.51 (8)	-0.22	13.26
-7,-7,0	0.60	1.72 (21)	1.5	1.11
7,5,-12	0.60	0.88 (10)	0.16	52.53
-8,2,-7	0.60	2.16 (9)	1.22	103.3

---

A.4 All  $(\Delta I/I)_a$  data observed and calculated for  $\text{Li}_2\text{SO}_4\cdot\text{H}_2\text{O}$ ,  $\text{Li}_2\text{SeO}_4\cdot\text{H}_2\text{O}$  and  $\text{BiB}_3\text{O}_6$

**Table A.2:** Summary of all in the case of  $\text{Li}_2\text{SeO}_4\cdot\text{H}_2\text{O}$  observed relative variations,  $(\Delta I/I)_a$ , of diffraction intensities together with the corresponding calculated model values.

$h, k, l$	$\lambda$ (Å)	$[(\Delta I/I)_a]_{\text{OBS}}$ (%)	$[(\Delta I/I)_a]_{\text{MOD}}$ (%)	$[(\text{OBS}-\text{MOD})/\sigma]^2$
2,-2,-11	0.99	-1.13 (6)	-0.78	34.88
-2,2,11	0.99	-0.88 (7)	-0.86	0.05
-2,3,10	0.99	-0.93 (10)	-0.97	0.18
2,-3,-10	0.99	-1.02 (7)	-0.91	2.43
3,0,-10	0.99	0.65 (4)	0.69	0.72
4,-3,-8	0.99	-1.17 (7)	-1.13	0.36
10,-1,-7	0.99	0.72 (25)	0.47	1.01
3,0,-8	0.99	0.30 (7)	0.24	0.62
10,0,-9	0.99	0.23 (10)	0.19	0.2
3,-4,-3	0.99	-0.39 (11)	-0.65	5.58
4,0,-2	0.99	-0.59 (10)	-0.78	3.59
4,0,-7	0.99	0.36 (13)	0.28	0.35
4,0,-9	0.99	0.36 (7)	0.37	0.04
6,-2,-7	0.99	-0.69 (9)	-0.54	2.67
-6,2,7	0.99	-0.70 (9)	-0.57	2.02
-6,3,6	0.99	-0.74 (8)	-0.44	13.82
7,-1,-5	0.99	-0.57 (10)	-0.26	9.36
7,-1,-7	0.99	-0.89 (11)	-0.95	0.28
4,2,3	0.99	-1.10 (9)	-0.75	15.33
-4,-2,-3	0.99	-0.53 (9)	-0.74	5.34
-5,-2,-4	0.99	-0.53 (7)	-0.52	0.03
5,2,4	0.99	-0.67 (7)	-0.6	1.11
3,-3,-9	0.99	-0.96 (17)	-1.08	0.53
-3,3,9	0.99	-0.51 (31)	-1.13	3.98
-6,-1,-1	0.99	-0.50 (7)	-0.67	6.23
5,-4,-1	0.99	-0.34 (12)	-0.36	0.02
-5,4,1	0.99	-0.49 (14)	-0.45	0.07
-3,-5,-3	0.99	-0.29 (8)	-0.24	0.32
4,-5,-3	0.99	-0.91 (21)	-0.36	6.92
-4,5,3	0.99	-1.06 (25)	-0.46	5.77
4,-4,-9	0.99	-0.29 (21)	-0.25	0.04
-4,4,9	0.99	-0.60 (33)	-0.55	0.02
-7,2,6	0.99	0.48 (13)	0.33	1.26
2,4,6	0.99	0.68 (7)	0.29	30.29
-2,-4,-3	0.99	0.22 (8)	0.78	49.08
-2,-4,-6	0.99	0.09 (7)	0.33	11.33
0,-2,-6	0.99	0.90 (26)	0.49	2.51
7,-7,-2	0.99	-0.28 (8)	-0.47	5.77
4,3,-8	0.99	-1.21 (15)	-1.33	0.62
10,0,-5	0.99	0.56 (8)	0.68	2.29
2,-4,-4	0.99	1.01 (19)	0.92	0.22
0,2,6	0.99	0.45 (24)	0.62	0.49
7,-2,-6	0.99	0.98 (13)	0.21	34.63
9,-4,-4	0.99	0.06 (5)	0.07	0.02

Appendix

6,3,1	0.99	-0.46 (8)	-0.28	4.87
2,0,8	0.98	0.36 (4)	0.54	21.13
2,0,8	0.99	0.48 (4)	0.59	7.48
2,0,8	1.00	1.31 (6)	0.54	164.27
2,4,8	1.00	0.77 (4)	0.47	56.65
2,-4,8	1.00	0.27 (4)	0.44	18.51
4,2,3	0.99	-0.37 (9)	-0.75	17.6
-6,-3,6	0.99	-0.31 (4)	-0.44	10.86
-6,-3,6	1.00	-0.37 (5)	-0.41	0.71

**Table A.3:** Summary of all in the case of  $\text{BiB}_3\text{O}_6$  observed relative variations,  $(\Delta I/I)_a$ , of diffraction intensities together with the corresponding calculated model values. The data sets of the crystal plates (100), (010) and (001) are separated by solid lines.

$h, k, l$	$\lambda$ (Å)	$[(\Delta I/I)_a]_{\text{OBS}}$ (%)	$[(\Delta I/I)_a]_{\text{MOD}}$ (%)	$[(\text{OBS}-\text{MOD})/\sigma]^2$
8,4,-1	0.90	0.12 (3)	0.11	0.1
8,4,-1	0.92	0.17 (4)	0.19	0.36
7,3,2	0.90	0.13 (4)	0.15	0.3
7,-3,1	0.90	-0.15 (3)	-0.16	0.1
9,3,0	0.90	0.13 (2)	0.11	0.98
11,3,3	0.92	-0.41 (5)	-0.42	0.04
11,3,3	0.97	-0.32 (5)	-0.31	0.01
3,-5,5	0.90	0.38 (4)	0.36	0.41
6,2,0	0.94	0.17 (8)	0.25	1.03
10,4,0	0.70	-0.24 (8)	-0.13	1.96
10,4,0	0.80	-0.15 (3)	-0.19	1.52
5,5,8	0.93	0.30 (4)	0.33	0.48
5,5,8	0.97	0.31 (6)	0.31	0.0
6,6,7	0.93	0.18 (5)	0.16	0.15
7,1,1	0.80	0.09 (3)	0.10	0.28
8,-2,4	0.70	-0.29 (5)	-0.17	6.77
-9,-3,3	0.80	-0.20 (6)	-0.11	2.51
-9,-3,3	0.90	-0.11 (4)	-0.14	0.62
-11,5,0	0.70	-0.25 (11)	-0.13	1.25
3,9,-4	0.92	0.39 (4)	0.11	40.9
4,-6,-8	0.92	0.24 (3)	0.13	13.93
-2,-8,-5	0.92	-0.35 (3)	-0.37	0.48
-2,-8,-5	0.94	-0.64 (4)	-0.39	29.96
-5,7,-4	0.92	0.25 (2)	0.27	1.28
-8,-6,-2	0.92	0.14 (4)	0.12	0.22
4,4,5	0.70	0.05 (3)	0.02	0.92
0,4,0	0.45	0.32 (5)	0.09	20.06
3,9,2	0.45	0.32 (8)	0.31	0.0
2,-6,4	0.92	0.22 (4)	0.41	29.88
2,-8,-4	0.50	0.28 (3)	0.22	4.23
7,-7,0	0.70	-0.39 (5)	-0.35	0.49

A.4 All  $(\Delta I/I)_a$  data observed and calculated for  $\text{Li}_2\text{SO}_4 \cdot \text{H}_2\text{O}$ ,  $\text{Li}_2\text{SeO}_4 \cdot \text{H}_2\text{O}$  and  $\text{BiB}_3\text{O}_6$

-3,7,9	0.92	0.23 (4)	0.29	2.59
-4,-8,7	0.94	-0.52 (4)	-0.71	18.28
-4,-8,7	0.92	-0.91 (4)	-0.84	3.68
-7,-7,8	0.92	-0.20 (3)	-0.10	9.21
-10,-6,2	0.95	0.22 (3)	0.11	13.56
-7,-5,10	0.95	0.17 (3)	0.19	0.53
-7,-5,10	0.97	0.20 (7)	0.19	0.04
1,-9,2	0.924	-0.74 (16)	-0.67	0.21
1,-9,-1	0.924	0.35 (13)	0.42	0.3
0,6,3	0.80	-0.10 (7)	-0.32	11.49
<hr/>				
0,-2,10	0.80	0.45 (13)	0.84	9.98
2,6,8	0.70	0.28 (7)	0.41	3.42
3,7,8	0.70	-0.40 (10)	-0.24	2.86
5,7,7	0.80	-0.29 (13)	-0.34	0.15
-1,7,6	0.80	-0.37 (4)	-0.36	0.05
0,4,11	0.95	0.53 (6)	0.43	3.31
2,2,7	0.95	-0.43 (8)	-0.27	4.13
2,2,7	1.00	-0.21 (7)	-0.26	0.4
5,1,8	0.80	-0.58 (11)	-0.63	0.21
6,4,9	0.92	-0.54 (17)	-0.05	8.88
0,2,-8	0.90	-0.22 (3)	-0.22	0.0
-6,6,-7	0.70	+0.11 (6)	0.15	0.3
-6,6,-7	0.91	+0.18 (4)	0.18	0.0
-7,-3,-8	0.95	+0.20 (3)	0.20	0.0
-9,-1,11	0.95	+1.05 (8)	1.07	0.21
-9,-1,-7	0.95	+0.32 (2)	0.32	0.0
-9,-3,10	0.90	-0.15 (3)	-0.15	0.01

## A.5 VHDL source code

Main part of the software that controls the time-resolved detector pulse processing by the FPGA board. This VHDL source code was written mainly by Marc von Kozierowski and Dr. Michael Ziolkowski. I have further improved and optimized the interplay between different processes running on the FPGA chip, so that the accessible time resolution of the developed data acquisition system could be increased to 20 ns.

```
-----
-- Design Name:   EventBuilder
-- Module Name:   EventBuilder - Behavioral
-----

library IEEE;
use IEEE.STD_LOGIC_1164.ALL;
use IEEE.STD_LOGIC_ARITH.ALL;
use IEEE.STD_LOGIC_UNSIGNED.ALL;
use ieee.numeric_std.all;

entity EventBuilder is
    GENERIC
    (
        ADDRESS_WIDTH           : integer := 18;
        DATA_WIDTH             : integer := 32;
        us_in_perioden          : integer := 10;
    );
    Port
    (
        PosIn                   : in  STD_LOGIC := '0';
        NPosIn                  : in  STD_LOGIC := '0';
        NegIn                    : in  STD_LOGIC := '0';
        NNegIn                  : in  STD_LOGIC := '0';
        Adr1                     : out STD_LOGIC_VECTOR (ADDRESS_WIDTH-1 downto 0);
        Datenout1               : out STD_LOGIC_VECTOR (DATA_WIDTH-1 downto 0);
        WE1                      : out STD_LOGIC := '0';
        CE1                     : out STD_LOGIC := not '0';
        read_adr                : out STD_LOGIC_VECTOR (ADDRESS_WIDTH-1 downto 0);
        ram_data                 : in  STD_LOGIC_VECTOR (DATA_WIDTH-1 downto 0);
        Ramfull                  : inout STD_LOGIC := '0';
        lesen                   : out BOOLEAN := false;
        Ramread                  : in  STD_LOGIC := '0';
        Clock                    : in  STD_LOGIC;
        DatenIn1                 : INTEGER;
        DatenIn2                 : INTEGER;
        Reset1                   : out STD_LOGIC := '0';
        Reset2                   : out STD_LOGIC := '0';
        hand                     : in  STD_LOGIC;
        handretard               : inout STD_LOGIC := '0';
        reading                  : in  BOOLEAN;
        Nullunterd               : in  BOOLEAN := true;
        Sumup                    : in  BOOLEAN := false;
        reset_clock              : in  Boolean := false;
        periods_in               : in  integer := 1;
        period_size              : in  integer;
    );
end EventBuilder;
```

```
end EventBuilder;
```

```
architecture Behavioral of EventBuilder is
```

```
constant sync_shift          : integer := 1;

signal s_timestamp, s_timestamp_1us    : integer range -1 to 65534 := -1;
signal s_time                    : integer := 0;
signal s_ergebnis, akt_ergebnis       : integer range 0 to 16383 := 0;
signal takte_in_dieser_us          : integer range 0 to 20000 := 0;
signal time_1us                   : boolean := false;
signal usesum1                    : boolean := true;
signal x                            : integer := -1;
signal s_hvzustand                 : STD_LOGIC_VECTOR (0 to 3) := "0000";
signal s_hvzustand_1us             : STD_LOGIC_VECTOR (0 to 3) := "0000";
signal tmp_adr1                     : Integer range 0 to 2**ADDRESS_WIDTH := 1;
signal output_buffer1              : STD_LOGIC_VECTOR (DATA_WIDTH-1 downto 0);
signal s_posin_alt                  : STD_LOGIC := '0';
signal header_gesetzt, header_gesetzt2 : STD_LOGIC := '0';
signal tail_gesetzt                 : STD_LOGIC := '0';
signal tmp_sumup                     : BOOLEAN := sumup;
signal tmp_read_adr                  : STD_LOGIC_VECTOR (ADDRESS_WIDTH-1 downto 0);
signal neue_daten                    : BOOLEAN := true;
signal tmp_ramread, ramread_alt      : std_logic := '0';
signal k, u, u1                      : integer := 0;
signal neue_periode                  : BOOLEAN := false;
signal ram_deleted                    : BOOLEAN := false;
signal ready                          : BOOLEAN := false;
signal tmp_reset_clock                : boolean := false;
```

```
begin
```

```
    timing : process (clock)
    begin
        if rising_edge(clock) then
            takte_in_dieser_us <= takte_in_dieser_us + 1;
            if takte_in_dieser_us = us_in_perioden -1 then
                time_1us <= true;
                usesum1 <= (not usesum1);
                takte_in_dieser_us <= 0 ;
            else
                time_1us <= false;
```

```
        end if;
    end if;
end process;
```

```
    Resette_Summierer: process (clock)
    begin
        if rising_edge(clock) then
            Reset1 <= '0';
            Reset2 <= '0';
            if takte_in_dieser_us = us_in_perioden -1 then
                if usesum1 then
                    Reset2 <= '1';
                else
                    Reset1 <= '1';
                end if;
            end if;
```

```

        end if;
    end if;
end process;

Lese_Ergebnisse_aus : process (clock)
begin
    if rising_edge(clock) then
        if takte_in_dieser_us = sync_shift then
            if usesum1 then
                s_ergebnis <= DatenIn2;
            else
                s_ergebnis <= DatenIn1;
            end if;
            s_timestamp_1us <= s_timestamp;
            s_hvzustand_1us <= s_hvzustand;
        end if;
        if takte_in_dieser_us = 2 then
            s_timestamp <= s_timestamp+1;
            s_hvzustand(3) <= posin;
            s_hvzustand(2) <= nposin;
            s_hvzustand(1) <= negin;
            s_hvzustand(0) <= nnegin;
            s_posin_alt <= posin;
            neue_periode <= false;
            if s_posin_alt /= posin and posin = '1' then
                s_timestamp <= 0;

                neue_periode <= true;
            end if;
        end if;
    end if;
    if time_1us then
        if x=999 then
            s_time <= s_time + 1;
            x<=0;
        else
            x <= x+1;
        end if;
        if x=999 AND s_time = 3599999 then
            s_time <= 0;
            x<=0;
        end if;
    end if;
    if reset_clock then
        tmp_reset_clock <= true;
    end if;
    if s_timestamp_1us = 0 and tmp_reset_clock then
        s_time <= 0;
        x<=0;
        tmp_reset_clock <= false;
    end if;
end if;
end process;

write_data : process ( clock )
variable sum          : integer := 0;
variable tmp_adr2     : Integer range 0 to 2**ADDRESS_WIDTH:= 1;
begin

```

```

if rising_edge (clock) then
  if ramread = '1' then
    tmp_ramread <= '1';
  end if;
  if hand = '1' AND reading = false then
    handretard <= '1';
  end if;
  if hand = '0' AND reading = true then
    handretard <= '0';
  end if;
  if hand = '1' AND reading = true then
    handretard <= '0';
  end if;
  if hand = '0' AND reading = false then
    handretard <= '0';
  end if;
  we1 <= '0';
  ce1 <= '1';
  if sumup then
    if tmp_ramread = '1' AND ready = false then
      if u < period_size*4+3 then
        Ramfull <= '0';
        if u1 = 0 then
          adr1 <= CONV_STD_LOGIC_VECTOR(u,
ADDRESS_WIDTH);
          we1 <= not '1';
          ce1 <= not '1';
          u1 <= u1 + 1;
        elsif u1 = 1 then
          u1 <= u1 + 1;
        end if;
        if u1 = 2 then
          Datenout1 <= (others => '0');
          u <= u + 1;
          u1 <= 0;
        end if;
      else
        u <= 0;
        u1 <= 0;
        ram_deleted <= true;
        tmp_ramread <= '0';
      end if;
    end if;
  end if;
  if ram_deleted AND handretard = '1' AND neue_periode AND takte_in_dieser_us =
us_in_perioden-1 then
    header_gesetzt <= '0';
    header_gesetzt2 <= '0';
    tail_gesetzt <= '0';
    ready <= true;
  end if;
  if ready then
    if k = 0 then
      if takte_in_dieser_us = 2 then
        adr1 <= CONV_STD_LOGIC_VECTOR(0,
ADDRESS_WIDTH);
        we1 <= not '1';
        ce1 <= not '1';

```

```

        header_gesetzt <= '1';
        output_buffer1 (7 downto 0) <= "01000010";
        output_buffer1 (15 downto 8) <= "10000001";
        output_buffer1 (23 downto 16) <= "10000001";
        output_buffer1 (31 downto 24) <= "10000001";
    end if;
    if takte_in_dieser_us = 4 then
        Datenout1 <= output_buffer1;
        output_buffer1 <= (others => '0');
    end if;
    if takte_in_dieser_us = 5 then
        adr1 <= CONV_STD_LOGIC_VECTOR(1,
ADDRESS_WIDTH);

        we1 <= not '1';
        ce1 <= not '1';
    end if;
    if takte_in_dieser_us = 6 then
        output_buffer1 (11 downto 0) <=
STD_LOGIC_VECTOR(to_unsigned(s_ergebnis, 12));
        output_buffer1 (15 downto 12) <= s_hvzustand_1us;
        output_buffer1 (31 downto 16) <=
STD_LOGIC_VECTOR(to_unsigned(s_timestamp_1us, 16));
    end if;
    if takte_in_dieser_us = 7 then
        tmp_adr1 <= s_timestamp_1us +2;
        Datenout1 <= output_buffer1;
        k <= k + 1;
    end if;
end if;
if k = 1 then
    if header_gesetzt = '1' then
        if takte_in_dieser_us = 2 then
            adr1 <=
CONV_STD_LOGIC_VECTOR(period_size*4+1, ADDRESS_WIDTH);
            output_buffer1 (7 downto 0) <= "01000010";
            output_buffer1 (15 downto 8) <= "01000010";
            output_buffer1 (23 downto 16) <= "01000010";
            output_buffer1 (31 downto 24) <= "01000010";
            we1 <= not '1';
            ce1 <= not '1';
        end if;
        if takte_in_dieser_us = 4 then
            Datenout1 <= output_buffer1;
            output_buffer1 <= (others => '0');
            header_gesetzt <= '0';
        end if;
    end if;
    if takte_in_dieser_us = 5 then
        adr1 <= CONV_STD_LOGIC_VECTOR(tmp_adr1,
ADDRESS_WIDTH);

        we1 <= not '1';
        ce1 <= not '1';
    end if;
    if takte_in_dieser_us = 6 then
        output_buffer1 (11 downto 0) <=
STD_LOGIC_VECTOR(to_unsigned(s_ergebnis, 12));
        output_buffer1 (15 downto 12) <= s_hvzustand_1us;

```

```

                                output_buffer1 (31 downto 16) <=
STD_LOGIC_VECTOR(to_unsigned(s_timestamp_1us, 16));
                                end if;
                                if takte_in_dieser_us = 7 then
                                    Datenout1 <= output_buffer1;
                                    if neue_periode then
                                        tmp_adr1 <= 1;
                                        k <= k + 1;
                                    else
                                        tmp_adr1 <= s_timestamp_1us +2;
                                    end if;
                                end if;
                                if takte_in_dieser_us = 8 then
                                    if k > periods_in then
                                        Ramfull <= '1';
                                        lesen <= true;
                                        ram_deleted <= false;
                                        ready <= false;
                                        k <= 0;
                                    end if;
                                end if;
                                end if;
                                if k > 1 then
                                    if takte_in_dieser_us = 2 then
                                        read_adr <= CONV_STD_LOGIC_VECTOR(tmp_adr1,
ADDRESS_WIDTH);
                                        tmp_read_adr <= CONV_STD_LOGIC_VECTOR(tmp_adr1,
ADDRESS_WIDTH);

                                        we1 <= not '0';
                                        ce1 <= not '1';
                                    end if;
                                    if takte_in_dieser_us = 6 then
                                        if neue_periode then
                                            tmp_adr1 <= 1;
                                            k <= k + 1;
                                        else
                                            tmp_adr1 <= s_timestamp_1us +2;
                                        end if;
                                        adr1 <= tmp_read_adr;
                                        we1 <= not '1';
                                        ce1 <= not '1';
                                    end if;
                                    if takte_in_dieser_us = 7 then
                                        sum := s_ergebnis + CONV_INTEGER (ram_data(11 downto
0));
                                        output_buffer1 (11 downto 0) <=
STD_LOGIC_VECTOR(to_unsigned(sum, 12));
                                        output_buffer1 (15 downto 12) <= s_hvzustand_1us;
                                        output_buffer1 (31 downto 16) <=
STD_LOGIC_VECTOR(to_unsigned(s_timestamp_1us, 16));
                                        end if;
                                        if takte_in_dieser_us = 8 then
                                            Datenout1 <= output_buffer1;
                                            if k > periods_in then
                                                Ramfull <= '1';
                                                lesen <= true;
                                                ram_deleted <= false;

```

```
ready <= false;
k <= 0;
end if;
end if;
end if;
end if;
end if;
end if;
end process;
end Behavioral;
```

# Bibliography

- [1] DINNEBIER, R. E. ; HINRICHSSEN, B. ; LENNIE, A. ; JANSEN, M.: High-pressure crystal structure of the non-linear optical compound  $\text{BiB}_3\text{O}_6$  from two-dimensional powder diffraction data. *Acta Cryst.* **B65** (2009), 1–10.
- [2] ISTOMIN, K. ; KOTAIDIS, V. ; PLECH, A. ; KONG, Q.: Dynamics of the laser-induced ferroelectric excitation in  $\text{BaTiO}_3$  studied by x-ray diffraction. *Appl. Phys. Lett.* **90** (2007), 022905.
- [3] KOVALEVSKY, A. Y. ; KING, G. ; BAGLEY, K. A. ; COPPENS, P.: Photoinduced Oxygen Transfer and Double-Linkage Isomerism in a *cis*-(NO)(NO<sub>2</sub>) Transition-Metal Complex by Photocrystallography, FT-IR Spectroscopy and DFT Calculations. *Chem. Eur. J.* **11** (2005), 7254–7264.
- [4] STAHN, J. ; PIETSCH, U. ; BLAHA, P. ; SCHWARZ, K.: Electric-field-induced charge-density variations in covalently bonded binary compounds. *Phys. Rev. B* **63** (2001), 165205.
- [5] NYE, J. F.: *Physical Properties of Crystals: Their Representation by Tensors and Matrices*. Oxford, New York : Clarendon Press, 1984.
- [6] HAUSSÜHL, S.: *Physical Properties of Crystals*. Weinheim : WILEY-VCH Verlag, 2007.
- [7] FUJIMOTO, I.: Direct Detection of Electric-Field-Induced Microscopic Structural Changes in  $\text{LiNbO}_3$  by Modulation X-ray Diffraction. *Phys. Rev. Lett.* **40** (1978), 941–944.
- [8] GRAAFSMA, H. ; COPPENS, P. ; MAJEWSKI, J. ; CAHEN, D.: Ionic Displacements and Piezoelectric Constants of  $\text{AgGaS}_2$  from X-Ray Diffraction of a Crystal in an External Electric Field. *J. Solid State Chem.* **105** (1993), 520–527.
- [9] REEUWIJK, S. J. ; PUIG-MOLINA, A. ; GRAAFSMA, H.: Electric-field-induced structural changes in deuterated potassium dihydrogen phosphate. *Phys. Rev. B* **62** (2000), 6192–6197.
- [10] REEUWIJK, S. J. ; VONK, V. ; PUIG-MOLINA, A. ; GRAAFSMA, H.: Electric-field-induced structural changes measured with a CCD-coupled X-ray image intensifier. *J. Appl. Cryst.* **33** (2000), 1422–1429.
- [11] REEUWIJK, S. J. ; PUIG-MOLINA, A. ; GRAAFSMA, H.: Electric-field-induced structural changes in  $\text{KH}_2\text{PO}_4$  at room temperature and at 167 K. *Phys. Rev. B* **64** (2001), 134105.
- [12] DAVAASAMBUU, J. ; PUCHER, A. ; KOCHIN, V. ; PIETSCH, U.: Atomistic origin of the inverse piezoelectric effect in  $\alpha\text{-SiO}_2$  and  $\alpha\text{-GaPO}_4$ . *Europhys. Lett.* **62** (2003), 834–840.

## Bibliography

- [13] GUILLOT, R. ; FERTEY, P. ; HANSEN, N. K. ; ALLÉ, P. ; ELKAIM, E. ; LECOMTE, C.: Diffraction study of the piezoelectric properties of low quartz. *Eur. Phys. J. B* **42** (2004), 373–308.
- [14] GORFMAN, S. ; TSIRELSON, V. ; PUCHER, A. ; MORGENROTH, W. ; PIETSCH, U.: X-ray diffraction by a crystal in a permanent external electric field: electric-field-induced structural response in  $\alpha$ -GaPO<sub>4</sub>. *Acta Cryst. A* **62** (2006), 1–10.
- [15] HANSEN, N. K. ; FERTEY, P. ; GUILLOT, R.: Studies of electric field induced structural and electron-density modifications by X-ray diffraction. *Acta Cryst. A* **60** (2004), 465–471.
- [16] PATURLE, A. ; GRAAFSMA, H. ; SHEU, H.-S. ; COPPENS, P. ; BECKER, P.: Measurement of the piezoelectric tensor of an organic crystal by the X-ray method: The nonlinear optical crystal 2-methyl 4-nitroaniline. *Phys. Rev. B* **43**( 18) (1991), 14683–14691.
- [17] BRANDT, S. ; DAHMEN, H. D.: *Elektrodynamik: Eine Einführung in Experiment und Theorie*. Berlin, Heidelberg, New York : Springer-Verlag, 1997.
- [18] FLIESSBACH, T.: *Mechanik: Lehrbuch zur Theoretischen Physik I*. Heidelberg, Berlin : Spektrum Akademischer Verlag, 1999.
- [19] VISSCHER, W. M. ; MIGLIORI, A. ; BELL, T. M. ; REINERT, R. A.: On the normal modes of free vibration of inhomogeneous and anisotropic elastic objects. *J. Acoust. Soc. Am.* **90** (1991), 2154–2162.
- [20] FIG, M.: *Introduction to Resonant Ultrasound Spectroscopy and the RUS program*. MATLAB Central: An open exchange for the MATLAB and Simulink user community. – <http://www.mathworks.com/matlabcentral/fileexchange/11399-resonant-ultrasound-spectroscopy-rus>.
- [21] WARREN, B. E.: *X-ray Diffraction*. New York : DOVERPUBLICATIONS, INC., 1968.
- [22] COPPENS, P.: *X-ray Charge Densities and Chemical Bonding*. New York : Oxford University Press, 1997.
- [23] ALS-NIELSEN, J.: *Elements of Modern X-Ray Physics*. Chichester : John Wiley & Sons Ltd, 2001.
- [24] AUTHIER, A.: *Dynamical Theory of X-ray Diffraction*. New York : Oxford University Press, 2003.
- [25] ZACHARIASEN, W. H.: A General Theory of X-ray Diffraction in Crystals. *Acta Cryst.* **23** (1967), 558–564.
- [26] COPPENS, P. ; HAMILTON, W. C.: Anisotropic Extinction Corrections in the Zachariassen Approximation. *Acta Cryst. A* **26** (1970), 71–83.
- [27] BECKER, P. J. ; COPPENS, P.: Extinction within the Limit of Validity of the Darwin Transfer Equations. I. General Formalisms for Primary and Secondary Extinction and Their Application to Spherical Crystals. *Acta Cryst. A* **30** (1974), 129–147.

- [28] SABINE, T. M.: A Reconciliation of Extinction Theories. *Acta Cryst.* **A44** (1988), 368–373.
- [29] SU, Z. ; COPPENS, P.: Relativistic X-ray elastic scattering factors for neutral atoms  $Z = 1-54$  from multiconfiguration Dirac-Fock wavefunctions in the  $0-12 \text{ \AA}^{-1} \sin \theta / \lambda$  range, and six-Gaussian analytical expressions in the  $0-6 \text{ \AA}^{-1}$  range. *Acta Cryst.* **A53** (1997), 749–762.
- [30] KISSEL, L. ; ZHOU, B. ; ROY, S. C. ; GUPTA, S. K. S. ; PRATT, R. H.: The Validity of Form-Factor, Modified-Form-Factor and Anomalous-Scattering-Factor Approximations in Elastic Scattering Calculations. *Acta Cryst.* **A51** (1995), 271–288.
- [31] *Anomalous Scattering Factors*. Lawrence Livermore National Laboratory. – <http://adg.llnl.gov/Research/scattering/asf.html>.
- [32] HANSEN, N. K. ; COPPENS, P.: Testing Aspherical Atom Refinements on Small-Molecule Data Sets. *Acta Cryst.* **A34** (1978), 909–921.
- [33] CLEMENTI, E. ; ROETTI, C.: Roothaan-Hartree-Fock Atomic Wavefunctions: Basis Functions and Their Coefficients for Ground and Certain Excited States of Neutral and Ionized Atoms,  $Z \leq 54$ . *Atomic Data and Nuclear Data Tables* **14** (1974), 177–478.
- [34] CLEMENTI, E. ; RAIMONDI, D. L.: Atomic screening constants from SCF functions. *J. Chem. Phys.* **38** (1963), 2686–2689.
- [35] EL HAOUZI, A. ; HANSEN, N. K. ; HÉNAFF, C. L. ; PROTAS, J.: The Phase Problem in the Analysis of X-ray Diffraction Data in Terms of Electron-Density Distributions. *Acta Cryst.* **A52** (1996), 291–301.
- [36] TSIRELSON, V. G. ; OZEROV, R. P.: *Electron Density and Bonding in Crystals*. Institute of Physics Publishing, Bristol, England / Philadelphia, USA, 1996.
- [37] COTTENIER, S.: *Density Functional Theory and the Family of (L)APW-methods: a step-by-step introduction*. K.U.Leuven, Belgium: Instituut voor Kern- en Stralingsfysica, 2002. – [http://www.wien2k.at/reg\\_user/textbooks](http://www.wien2k.at/reg_user/textbooks).
- [38] BLAHA, P. ; SCHWARZ, K. ; MADSEN, G. K. H. ; KVASNICKA, D. ; LUITZ, J.: *WIEN2k: An Augmented Plane Wave + Local Orbitals Program for Calculating Crystal Properties*. Techn. Universität Wien, Wien, Austria, 2002
- [39] HOHENBERG, P. ; KOHN, W.: Inhomogeneous Electron Gas. *Phys. Rev* **136** (1964), 864–871.
- [40] KOHN, W. ; SHAM, L. J.: Self-Consistent Equations Including Exchange and Correlation Effects. *Phys. Rev* **140** (1965), 1133–1138.
- [41] BADER, R. F. W.: *Atoms in molecules: a quantum theory*. Oxford University Press, Oxford, 1990.
- [42] GATTI, C.: Chemical bonding in crystals: new directions. *Z. Kristallogr.* **222** (2005), 399–457.

## Bibliography

- [43] ESPINOSA, E. ; ALKORTA, I. ; ELGUERO, J. ; MOLINS, E.: From weak to strong interactions: A comprehensive analysis of the topological and energetic properties of the electron density distribution involving X-H...F-Y systems. *J. Chem. Phys.* **117** (2002), 5529–5542.
- [44] BORN, M. ; HUANG, K.: *Dynamical Theory of Crystal Lattices*. New York : Oxford Clarendon Press, 1954.
- [45] BARSCH, G. R.: X-ray Determination of Piezoelectric Constants. *Acta Cryst.* **A32** (1976), 575–586.
- [46] GRAAFSMA, H.: Accurate Determination of Strain Tensors from Small Shifts of Reflections Measured on a Four-Circle Diffractometer. *J. Appl. Cryst.* **25** (1992), 372–376.
- [47] BUSING, W. R. ; LEVY, H. A.: Angle Calculations for 3- and 4-circle X-ray and neutron diffractometers. *Acta Cryst.* **A22** (1967), 457–464.
- [48] EICHHORN, K. D. ; MORGENROTH, W.: *DIF4 Users Guide*. DESY, Hamburg, Germany, 2003.
- [49] ANGEL, R. J.: Automated profile analysis for single-crystal diffraction data. *J. Appl. Cryst.* **36** (2003), 295–300.
- [50] SEBER, G. A. F. ; WILD, C. J.: *Nonlinear Regression*. Hoboken, New Jersey : Wiley-Interscience, 2003.
- [51] TSIRELSON, V. G. ; GORFMAN, S. V. ; PIETSCH, U.: X-ray scattering amplitude of an atom in a permanent external electric field. *Acta Cryst.* **A59** (2003), 221–227.
- [52] GORFMAN, S. V. ; TSIRELSON, V. G. ; PIETSCH, U.: X-ray diffraction by a crystal in a permanent external electric field: general considerations. *Acta Cryst.* **A61** (2005), 387–396.
- [53] FLETCHER, R.: *Practical Methods of Optimization*. Hoboken, New Jersey : John Wiley and Sons, 1980.
- [54] LUNDGREN, J.-O. ; KVICK, A. ; KARPPINEN, M. ; LIMINGA, R. ; ABRAHAMS, S. C.: Neutron diffraction structural study of pyroelectric  $\text{Li}_2\text{SO}_4 \cdot \text{H}_2\text{O}$  at 293, 80 and 20 K. *J. Chem. Phys.* **80** (1984), 423–430.
- [55] JOHNSTON, M. G. ; HARRISON, W. T. A.: Dilithium selenate hydrate,  $\text{Li}_2\text{SeO}_4 \cdot \text{H}_2\text{O}$ . *Acta Cryst.* **E59** (2003), i25–i27.
- [56] FRÖHLICH, R. ; BOHATÝ, L. ; LIEBERTZ, J.: Die Kristallstruktur von Wismutborat,  $\text{BiB}_3\text{O}_6$ . *Acta Cryst.* **C40** (1984), 343–344.
- [57] BECKER, P. ; AHRWEILER, S. ; HELD, P. ; SCHNEEBERGER, H. ; BOHATÝ, L.: Thermal expansion, pyroelectricity and linear optical properties of  $\text{Li}_2\text{SeO}_4 \cdot \text{H}_2\text{O}$  and  $\text{Li}_2\text{SO}_4 \cdot \text{H}_2\text{O}$ . *Cryst. Res. Technol.* **38** (2003), 881–889.
- [58] PUGET, R. ; GODEFROY, L. J.: Contribution to study of ionicity of bonds in rutile. *J. Appl. Cryst.* **8** (1975), 297–303.

- [59] *Xilinx Virtex-4 FPGA board*. – FPGA and CPLD Solutions from Xilinx, Inc. - <http://www.xilinx.com>
- [60] REEUWIJK, S. J. ; PUIG-MOLINA, A. ; MATHON, O. ; TUCOULOU, R. ; GRAAFSMA, H.: Time-resolved x-ray diffraction study of the relaxation process of electric-field-induced strain in  $\text{KD}_2\text{PO}_4$ . *J. Appl. Phys.* **94** (2003), 6708–6716.
- [61] BARON, A. Q. R. ; KISHIMOTO, S. ; MORSE, J. ; RIGAL, J.-M.: Silicon avalanche photodiodes for direct detection of X-rays. *J. Synchrotron Rad.* **13** (2006), 131–142.
- [62] SVITELSKIY, O. ; SUSLOV, A. V. ; BETTS, J. B. ; MIGLIORI, A. ; YONG, G. ; BOATNER, L. A.: Resonant ultrasound spectroscopy of  $\text{KTa}_{1-x}\text{Nb}_x\text{O}_3$  ferroelectric relaxor crystals. *Phys. Rev. B* **78** (2008), 064113.
- [63] SCHWARZ, R. B. ; VUORINEN, J. F.: Resonant ultrasound spectroscopy: applications, current status and limitations. *J. Alloys Comp.* **310** (2000), 243–250.
- [64] SCHREUER, J.: Elastic and Piezoelectric Properties of  $\text{La}_3\text{Ga}_5\text{SiO}_{14}$  and  $\text{La}_3\text{Ga}_{5.5}\text{Ta}_{0.5}\text{O}_{14}$ : An Application of Resonant Ultrasound Spectroscopy. *IEEE Trans. Ultrason. Ferroelectr. Freq. Control* **49** (2002), 1474–1479.
- [65] KARPPINEN, M. ; LIMINGA, R. ; LUNDGREN, J.-O. ; KVICK, A. ; ABRAHAMS, S. C.: Charge density in pyroelectric lithium sulfate monohydrate at 80 and 298 K. *J. Chem. Phys.* **85** (1986), 5521–5527.
- [66] OCHROMBEL, R.: *Temperaturabhängige optische, elektrooptische und piezoelektrische Untersuchungen ausgewählter azentrischer Kristalle*. Cologne, Germany, Mathematisch-Naturwissenschaftliche Fakultät, Universität zu Köln, Diss., 2007.
- [67] BECHMANN, R.: Elastic and Piezoelectric Constants of Alpha-Quartz. *Phys. Rev.* **110** (1958), 1060–1061.
- [68] WILKE, K.-Th. ; BOHM, J.: *Kristallzüchtung*. VEB Deutscher Verlag der Wissenschaft, Berlin, 1988.
- [69] ZIEGLER, G. E.: The crystal structure of lithium sulphate mono-hydrate,  $\text{Li}_2\text{SO}_4 \cdot \text{H}_2\text{O}$ . *Z. Kristallogr.* **89** (1934), 456–461.
- [70] LARSON, A. C.: The Crystal Structure of  $\text{Li}_2\text{SO}_4 \cdot \text{H}_2\text{O}$ . A Three-Dimensional Refinement. *Acta Cryst.* **18** (1965), 717–724.
- [71] PETRICEK, V. ; DUSEK, M.: *JANA2000*. The Crystallographic Computing System, Institute of Physics, Praha, Czech Republic, 2000.
- [72] GUILLOT, R. ; HANSEN, N. K.: *DIFMOL*. Internal computer programs of LCM3B, Université Henri Poincaré - Nancy I, France, 2003.
- [73] DIEDERICHS, K. ; KARPLUS, P. A.: Improved *R*-factors for diffraction data analysis in macromolecular crystallography. *Nature Struct. Biol.* **4** (1997), 269–275.
- [74] STASH, A. ; TSIRELSON, V.: WinXPRO: a program for calculating crystal and molecular properties using multipole parameters of the electron density. *J. Appl. Cryst.* **35** (2002), 371–373.

## Bibliography

- [75] BOHATÝ, L. ; BECKER, P. ; EICHLER, H. J. ; HANUZA, J. ; MACZKA, M. ; TAKAICHI, K. ; UEDA, K. ; KAMINSKII, A. A.: Efficient Stimulated Raman Scattering and Cascaded Nonlinear  $\chi^{(3)} \rightarrow \chi^{(2)} \rightarrow \chi^{(3)}$  Lasing Effects in Noncentrosymmetric  $\text{Li}_2\text{SO}_4 \cdot \text{H}_2\text{O}$  Single crystals. *Laser Physics* **15** (2005), 1509–1522.
- [76] OCHROMBEL, R. ; LINDNER, M. ; BOHATÝ, L.: Dynamic method for measurement of piezoelectric coefficients. *Acta Cryst. A* **62** (2006), 212.
- [77] BRUKER: *SMART, SAINT and SADABS*. 2003.
- [78] HUBBELL, J. H. ; COURSEY, J. S. ; HWANG, J. ; ZUCKER, D. S.: *Bibliography of Photon Total Cross Section (Attenuation Coefficient) Measurements*. National Institute of Standards and Technology, Gaithersburg, MD, 2003. – <http://physics.nist.gov/PhysRefData/XrayMassCoef/tab3.html>.
- [79] WAGNER, S.: *Röntgenbeugungsmessungen an Lithiumdihydrogenphosphat Einkristallen*. Siegen, Festkörperphysik, Universität Siegen, Diplomarbeit, 2010.
- [80] CATTI, M. ; IVALDI, G.: Crystal structure of  $\text{LiH}_2\text{PO}_4$ , structural topology and hydrogen bonding in the alkaline dihydrogen orthophosphates. *Z. Kristallogr.* **146** (1977), 215–226.
- [81] KREUER, K.-D.: Proton Conductivity: Materials and Applications. *Chem. Mater.* **8** (1996), 610–641.
- [82] HAZEN, R. M. ; DOWNS, R. T.: *High-Temperature and High-Pressure Crystal Chemistry*. Mineralogical Society of America, Washington, DC, 2000.
- [83] SCHMIDT, O.: *Bestimmung der piezoelektrischen Konstanten von Wismuttriborat,  $\text{BiB}_3\text{O}_6$ , aus Röntgenbeugungsmessungen*. Siegen, Festkörperphysik, Universität Siegen, Diplomarbeit, 2007.
- [84] HELLWIG, H. ; LIEBERTZ, J. ; BOHATÝ, L.: Exceptional large nonlinear optical coefficients in the monoclinic bismuth borate  $\text{BiB}_3\text{O}_6$  (*BIBO*). *Solid State Commun.* **109** (1999), 249–251.
- [85] HAUSSÜHL, S. ; BOHATÝ, L. ; BECKER, P.: Piezoelectric and elastic properties of the nonlinear optical material bismuth triborate,  $\text{BiB}_3\text{O}_6$ . *Appl. Phys. A* **82** (2006), 495–502.
- [86] BECKER, P. ; BOHATÝ, L.: Thermal Expansion of Bismuth Triborate. *Cryst. Res. Technol.* **36** (2001), 1175–1180.
- [87] STEIN, W.-D. ; COUSSON, A. ; BECKER, P. ; BOHATÝ, L. ; BRADEN, M.: Temperature-dependent X-ray and neutron diffraction study of  $\text{BiB}_3\text{O}_6$ . *Z. Kristallogr.* **222** (2007), 680–689.
- [88] BECKER, P. ; LIEBERTZ, J. ; BOHATÝ, L.: Top-seeded growth of bismuth triborate,  $\text{BiB}_3\text{O}_6$ . *J. Cryst. Growth.* **203** (1999), 149–155.
- [89] BLAHA, P. ; SCHWARZ, K. ; LUITZ, J.: *WIEN2k-FAQ: How to select RMT radii?* 2001. – [http://www.wien2k.at/reg\\_user/faq/](http://www.wien2k.at/reg_user/faq/).

- [90] PERDEW, J. P. ; BURKE, K. ; ERNZERHOF, M.: Generalized Gradient Approximation Made Simple. *Phys. Rev. Lett.* **77** (1996), 3865–3868.
- [91] SEARS, V. F.: Neutron scattering lengths and cross sections. *Neutron News* **3** (1992), 29–37.
- [92] *5C-2 Hot Neutron Four-Circle Diffractometer*. – Laboratoire Léon Brillouin (LLB) - <http://www-llb.cea.fr/fr-en/spectro/5c2/5c2.html>.
- [93] *Description of the Reactor*. – Laboratoire Léon Brillouin (LLB) - [http://www-llb.cea.fr/en/Web/part\\_2\\_e.pdf](http://www-llb.cea.fr/en/Web/part_2_e.pdf).
- [94] *Scattering Length Density Calculator*. – NIST Center for Neutron Research - <http://www.ncnr.nist.gov/resources/sldcalc.html>.
- [95] STEIN, W.-D.: *Struktur und Gitterdynamik in azentrischen Boraten*. Cologne, Germany, Mathematisch-Naturwissenschaftliche Fakultät, Universität zu Köln, Diss., 2007.
- [96] CLASSEN, J.: *Theorie der Biegeschwingung*. Heidelberg, Physikalisches Institut, Ruprecht-Karls-Universität Heidelberg, Diplomarbeit, 2000.
- [97] BRANDT, S. ; DAHMEN, H. D.: *Mechanik: Eine Einführung in Experiment und Theorie*. Berlin, Heidelberg, New York : Springer-Verlag, 1996.



# Acknowledgments

At this point I would like to thank all the people from whom I got support in the course of my doctoral dissertation:

- First of all, I would like to thank my dissertation advisor Prof. Dr. U. Pietsch for giving me the great opportunity to work in an exciting research field. His fruitful ideas have often led to a solution of many problems that I faced during my work.
- Next, I would like to thank Dr. S. Gorfman who gave me a comprehensive introduction to the theoretical and experimental issues in the study of the piezoelectric crystals under an external electric perturbation on the atomic scale. The long discussions we had resulted in a deeper understanding on my part of the crystal processes induced by an applied electric field.
- In addition, I would like to thank Prof. Dr. L. Bohatý and Prof. Dr. P. Becker for all the excellent crystals that they provided for my experiments. It should not be forgotten that without samples of good quality this work would not be possible. The interpretation of the time-resolved measurements is for the most part based on the discussions I had with Prof. Dr. L. Bohatý and Prof. Dr. P. Becker.
- In the case of the experimental determination of the electron-density distribution in  $\text{Li}_2\text{SO}_4\cdot\text{H}_2\text{O}$  I would like to thank Dr. E. Neumann for performing the X-ray diffraction measurements and for his good advices in many conversations we made.
- I would like to thank Dr. M. Ziolkowski, Dipl.-Ing. A. Wiese and M. von Kozirowski for their major contributions to the time-resolved electric-field experiment. Besides, Dr. M. Ziolkowski and Dipl.-Ing. A. Wiese took an active part in all the beamtimes that I had at ESRF and LLB.
- I would like to thank B. Dostal for the technical support at HASYLAB.
- Concerning the determination of the electron-density distribution in  $\text{Li}_2\text{SeO}_4\cdot\text{H}_2\text{O}$  I would like to thank Prof. Dr. C. Lehmann and A. Dreier for making an excellent experimental data set available.
- For assistance with my experiments I would like to thank Dr. W. Morgenroth and Dr. M. Tolkiehn (beamline scientists at the D3 beamline of HASYLAB), Dr. P. Pattison and Dr. D. Chernyshov (beamline scientists at the Swiss-Norwegian BM01A beamline of ESRF), Prof. Dr. M. Braden and Dr. A. Cousson (beamline scientist at the 5C2 beamline of LLB) and A. Biermanns (person in charge of the high resolution X-ray diffractometer in the home laboratory).
- Finally, I would like to thank my family, especially my parents and my grandma, for their great support upon that I can always rely.



# Abstract

Within the scope of this work the piezoelectric response of the crystals  $\text{Li}_2\text{SO}_4\cdot\text{H}_2\text{O}$ ,  $\text{Li}_2\text{SeO}_4\cdot\text{H}_2\text{O}$  and  $\text{BiB}_3\text{O}_6$  to a periodically applied external electric perturbation both on the macroscopic and microscopic scale was investigated. It was shown that the bond-selective distortion observed within these crystals is dependent on the strength of a chemical bond and the charges of the respective pseudoatoms bonded to each other. The electric-field-induced much greater average Li–O bond deformation in  $\text{Li}_2\text{SeO}_4\cdot\text{H}_2\text{O}$  compared to that measured in  $\text{Li}_2\text{SO}_4\cdot\text{H}_2\text{O}$  was referred to the larger vacancies in the structure of the lithium ion conducting  $\text{Li}_2\text{SeO}_4\cdot\text{H}_2\text{O}$  crystal. In addition, a novel concept of an X-ray diffraction experiment for the time-resolved measurements of the strains generated in piezoelectric crystals based on the detector pulse processing with a 100 MHz FPGA chip was realized. By reducing the switching time between different HV states to fast 200 ns within the modulation of the basic HV period applied to  $\text{Li}_2\text{SO}_4\cdot\text{H}_2\text{O}$  crystal plates, superimposed vibrational modes of the plates could be excited, the properties of which were studied by performing X-ray measurements of diffraction curves with a time resolution of 100 ns. In contrast, the induced internal redistribution of atoms within the unit cell of  $\text{Li}_2\text{SO}_4\cdot\text{H}_2\text{O}$  was negligibly small. This effect is accounted for by the low pressure in the range of MPa exerted on the atoms within the crystal by its elastic deformations.



# Kurzzusammenfassung

Im Rahmen dieser Arbeit wurde das Verhalten der piezoelektrischen Kristalle  $\text{Li}_2\text{SO}_4 \cdot \text{H}_2\text{O}$ ,  $\text{Li}_2\text{SeO}_4 \cdot \text{H}_2\text{O}$  und  $\text{BiB}_3\text{O}_6$  unter einer periodisch angelegten äußeren elektrischen Störung sowohl auf der makroskopischen als auch der mikroskopischen Skala untersucht. Es konnte gezeigt werden, dass innerhalb dieser Kristalle die beobachtete selektive Verzerrung einer chemischen Bindung von der Stärke der Bindung und den Ladungen der jeweils miteinander gebundenen Pseudoatome abhängig ist. Die durch das elektrische Feld induzierte viel größere mittlere Deformation der Li–O-Bindungen in  $\text{Li}_2\text{SeO}_4 \cdot \text{H}_2\text{O}$  im Vergleich zu der gemessenen in  $\text{Li}_2\text{SO}_4 \cdot \text{H}_2\text{O}$  wurde auf die größeren Lücken in der Struktur des Lithium-Ionen-leitenden  $\text{Li}_2\text{SeO}_4 \cdot \text{H}_2\text{O}$ -Kristalls zurückgeführt. Darüber hinaus wurde ein neuartiges Konzept eines Röntgenbeugungsexperiments, das auf der Verarbeitung von Detektorpulsen mit einem 100 MHz FPGA-Chip beruht, für zeitaufgelöste Messungen der in einem piezoelektrischen Kristall generierten Verzerrungen realisiert. Durch die Reduzierung der Schaltzeit zwischen verschiedenen Hochspannungszuständen innerhalb der verwendeten Modulation der Grundperiode der Hochspannung auf schnelle 200 ns konnten in  $\text{Li}_2\text{SO}_4 \cdot \text{H}_2\text{O}$ -Kristallplatten überlagerte Schwingungsmoden angeregt werden, deren Eigenschaften mit Hilfe von durchgeführten Messungen der Rockingkurven mit einer zeitlichen Auflösung von 100 ns untersucht wurden. Im Gegensatz dazu war die induzierte innere Umverteilung der Atome innerhalb der Einheitszelle von  $\text{Li}_2\text{SO}_4 \cdot \text{H}_2\text{O}$  vernachlässigbar klein. Dieser Effekt hat seinen Ursprung im niedrigen Druck im Bereich von MPa, dem die Atome innerhalb des Kristalls aufgrund seiner elastischen Deformationen ausgesetzt waren.

# ERKLÄRUNGEN

gemäß § 6 der Promotionsordnung vom 14. August 1996

Ich erkläre,

1. dass mir die Promotionsordnung vom 14. August 1996 bekannt ist.
2. dass ich die Dissertation selbständig verfaßt und alle benutzten Hilfsmittel und Quellen angegeben habe.
3. dass ich weder früher noch gleichzeitig bei einer anderen Hochschule oder in einem anderen Fachbereich ein Promotionsverfahren beantragt habe.
4. dass ich der Öffentlichkeit der mündlichen Prüfung – nicht – widerspreche<sup>1</sup>.
5. dass in meiner Dissertation Forschungsergebnisse verwendet sind, die in Zusammenarbeit mit den folgenden Wissenschaftlern gewonnen wurden (Namen, akademische Grade und Anschriften):

---

---

---

---

(Unterschrift)

---

<sup>1</sup>Nichtzutreffendes streichen